UNIVERSITÀ DEGLI STUDI DI MILANO

PhD course in MOLECULAR AND CELLULAR BIOLOGY
XXXIII cycle

DEPARTMENT OF BIOSCIENCES

MOLECULAR DETERMINANTS UNDERLYING PROTEIN MISFOLDING AND AGGREGATION

LUCA BROGGINI
R12057

Scientific tutor:
Prof. STEFANO RICAGNO

INDEX

ABSTRACT (ITA)

Le proteine sono macromolecole biologiche che svolgono attività essenziali per l'organismo. Affinché esse possano svolgere le loro funzioni fisiologiche, è necessario che raggiungano e conservino la loro struttura tridimensionale. Quando ciò non succede si può assistere a un processo di misfolding e aggregazione. Infatti una proteina parzialmente o completamente denaturata può interagire con altre molecole e formare aggregati potenzialmente dannosi per l'organismo. Allo stesso tempo, la mancanza di proteina correttamente ripiegata, e quindi attiva, altera i processi biochimici in cui essa è inserita.

Con il termine 'malattie conformazionali' si intendono tutte quelle patologie caratterizzate da errato ripiegamento delle proteine o dalla loro aggregazione successivamente alla loro sintesi. Anche se negli ultimi anni la ricerca scientifica ha fatto grandi progressi in questo campo, la complessità e varietà dei processi che portano alla formazione di aggregati proteici rende queste patologie ancora oggi incurabili. Identificare i fattori che favoriscono la conversione di proteine stabili e funzionali in aggregati proteici è fondamentale per sviluppare trattamenti per queste patologie.

Questo progetto di dottorato si è concentrato per ottenere una panoramica più esaustiva delle basi molecolari associate alla conversione di proteine in aggregati potenzialmente tossici.

In particolare, l'utilizzo di diverse tecniche biochimiche, biofisiche e strutturali su due sistemi modello, neuroserpina e beta2-microglobulina, ha permesso di studiare nel dettaglio i processi di misfolding e aggregazione.

I risultati qui riportati hanno evidenziato come tali processi dipendano da molti fattori, tra cui la sequenza primaria della proteina, la stabilità termica, la compattezza dello stato denaturato, e la presenza di modifiche post traduzionali.

I dati contenuti in questa tesi di dottorato forniscono importanti nuove informazioni utili alla descrizione e alla comprensione dei processi del misfolding e dell'aggregazione proteica.

ABSTRACT (ENG)

Proteins have evolved to adopt distinctive and well-defined functional states under physiological conditions, either as monomers or complexes. The achievement of a three-dimensional structure allows proteins to exert their physiological functions. Nevertheless, when proteins lose – or fail to acquire – their spatial organization, they can convert into aggregated species that can be harmful to the organism.

Conformational diseases gather all those pathologies characterized by the misfolding and aggregation of proteins. Indeed, while the formation and deposition of proteinaceous aggregates can be toxic to cells, the lack of active folded protein disrupts normal physiological pathways.

Although considerable progresses have been made in the recent years, to date conformational diseases are still incurable. Indeed, the incomplete understanding of the causes guiding protein misfolding and aggregation prevents the development of efficient treatments. At the same time, the complexity and the diversity of the processes leading to the formation of aggregated species make the task extremely challenging.

This PhD project was developed to provide a more comprehensive overview of the molecular bases underlying the conversion of soluble and functional states into aggregated and potentially toxic species.

To reach such aims, we applied an integrative approach on two model systems, neuroserpin (NS) and beta-2 microglobulin (β2m). In particular, we combined a series of biophysical, biochemical and structural techniques to study these two proteins which have been largely used as model systems for serpin polymerization and amyloid formation, respectively.

We found that protein misfolding and aggregation processes depend on several molecular properties, including primary sequence, denatured state compactness, thermal stability, ability to form oligomers under physiological conditions, and the presence of post-translation modifications.

The data presented in this PhD thesis add valuable information to depict the complex framework of protein misfolding and aggregation.

1 INTRODUCTION

1.1 PROTEIN FOLDING AND MISFOLDING

1.1.1 PROTEIN TERTIARY STRUCTURE AND FOLDING

Proteins are the molecular machines that control our vital cellular activities. Proteins fold into unique and intricate conformations that remain functional within the complex environment of living systems. Indeed, proteins' biological functions are determined by their three-dimensional native structures, which are encoded in their primary sequences.

The theoretical number of conformations that a sequence of amino-acid can adopt is astronomically large and, accordingly, a systematic search of the native structure is not feasible as it would require a monumental length of time (Anfinsen's dogma) (1). Nevertheless, any protein is able to reach in a rapid and efficient way its functional conformations. From a thermodynamical point of view, this process can be described as a diffusional search on a free energy surface (2) (Fig. 1). The energy landscape is, indeed, encoded by the amino-acid sequence of the protein and in this way the polypeptide chain samples only a restricted number of ensembles during its way to the lowest-energy structure (3).

The specificity of the folding process arises from the heterogeneity of the protein chain: the distinct energies associated with positioning different residues enable some structures to be more stable than others (4). Even minor changes in the primary sequence, *e.g.*, point mutations, can cause modification of the energy landscape and, accordingly, lead to distinct native conformations (5).
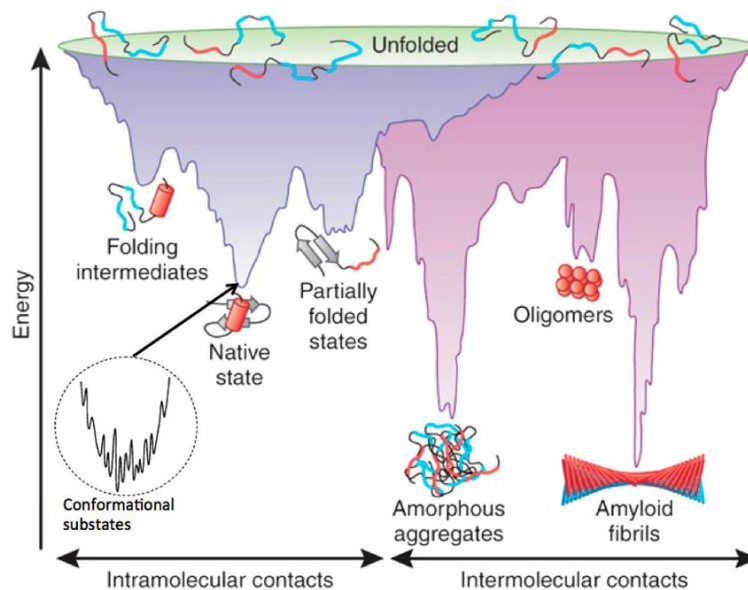
Figure 1. Energy landscape scheme of protein folding and aggregation. The polypeptide chain can assume an infinite number of conformations. The native state represents the local minimum when intramolecular contacts prevail. However, conversion into aggregated state can occur as a consequence of destabilization of the native state and formation of intermolecular contacts. Figure edited from (5).

However, besides their functional three-dimensional structures, in physiological conditions proteins can adopt different conformational states that are in equilibrium with their native states. These ensembles are differently populated and, depending on their structural

diversity, have kinetic barriers that hamper the transition from one to the other. For example, internal and external factors, *e.g.,* intrinsic dynamics, presence of binding partners or thermal fluctuations, can induce changes in the structural features, leading to the population of alternative conformations (6).

Moreover, the biologically active conformation can often be only marginally stable under physiological conditions, due to several reasons including high local concentration, presence of partners, and a crowded cellular environment (7). Indeed, in many cases it does not represent the most stable conformation thermodynamically but it is rather similar to a kinetically trapped intermediate that is prone to rearrange (Fig. 1).

1.1.2 CELL CAPABILITY TO CONTROL PROTEIN FOLDING

Although many aspects of the folding are intrinsic to the biophysical properties of the protein sequence, the process is complex and susceptible to errors. Indeed, while acquiring their tertiary structure, the polypeptide chain inevitably exposes to solvent hydrophobic regions that are then buried in the native state and that are prone to establish inappropriate intermolecular interactions (8). In addition, the functional native state is likely to only reflect a local free energy minimum and self-association into aggregated species may lower the global free energy (9).

Failure of proteins to fold properly or to retain their fold within the crowded cellular environment is at the basis of many pathological conditions, known as misfolding diseases or conformational diseases (10). Accordingly, living systems have evolved a range of strategies to control protein folding, to facilitate protein solubility over prolonged periods of time and to prevent protein conversion into non-functional aggregates (10).

First, cells express constitutively molecular chaperones and folding catalysts to assist and promote correct protein folding. Molecular chaperones increase folding efficiency by creating a safe environment where the protein can fold or be recovered without interacting with other cellular components. Thereby, they promote efficient folding and aid misfolded protein to regain their correct conformation (11,12). Folding catalysts, instead, increase the rate of slow folding steps in order to reduce the likelihood of competing reactions, including aggregation. Disulphide isomerase is an example of folding catalyst that control the formation and reorganization of disulphide bonds, thus promoting proper protein folding (13,14).

Secondly, cells adopt a series of protein quality control systems that allow them to identify and remove irreversibly misfolded and aggregated proteins (11,12). The ubiquitin-proteasome, autophagy and ER-associated degradation are examples of systems used by the cell to degrade misfolded proteins, preventing their accumulation (15,16). Within these systems, the ER plays a major role. Indeed, it contains a large number of molecular chaperones to aid in the translation and post-translational folding of proteins. For example, modifications of the glycan group of newly synthetized proteins provide information to specific chaperones about the folding state of a protein. Moreover, the ER identifies misfolded proteins, transports them into the cytoplasm and eventually targets them for proteasomal degradation via the ER-associated degradation (ERAD) pathway (17).

Nevertheless, despite the existence of elaborate quality control systems, unfolded proteins can still be able to aggregate and form potentially toxic species. Indeed, cells need to deal with the presence of proteinaceous agglomerates and degrade them. The aggregates can either be removed by the co-operation of chaperones and proteasome or by the autophagy process. In the latter case, the insoluble cellular materials are engulfed in a double-membrane autophagosome (18). The autophagosome then fuses with the lysosome where the

aggregated species undergo conformation changes due to the drop in pH and are cleared by proteases (19).

Dysfunction of any of these quality control systems leads to aberrant protein misfolding and consequent development of pathologies. However, the onset of conformational diseases cannot be solely ascribed to the collapse of the quality processes. Indeed, protein misfolding, and aggregation, can also occur as a consequence of environmental stress, aging, sustained increases in protein concentration, the existence of mutant proteins with high propensity to aggregate or aberrant proteolytic cleavage (5).

1.1.3 PROTEIN MISFOLDING: CAUSES AND CONSEQUENCES

In physiological conditions, besides their functional conformation, proteins explore a wide range of different states. The active state of certain proteins is thermodynamically and chemically metastable, and thus the conversion into more stable but non-functional ensembles can be energetically favoured.

Metastability arises when the conformational landscape of a protein presents wells of lower free energy than that of the native state itself (20). In such cases, the native state does not correspond to the thermodynamically most stable conformation. Metastability is an important regulator of the biological functions of several proteins, including the membrane fusion protein hemagglutinin from the influenza virus (21), and inhibitory members of the serine protease inhibitor (serpin) superfamily (22).

A metastable native state is inherently at the equilibrium between conserving its fold to fulfil its physiological functions and promoting rearrangements to reach a more thermodynamically stable state. In normal healthy conditions, cell processes and components shift the equilibrium towards the protection of the native fold (23). However, in other circumstances, *i.e.,* cellular stress conditions or presence of point mutations, the formation of non-functional species is favoured. These non-functional conformations usually retain most of the structural features of the native state. However, they may facilitate protein aggregation, for example by exposing hydrophobic groups which become available for intermolecular interactions, or they may lose structural features fundamental for the activity of the protein (24).

The different conformations adopted by proteins involve a highly complex series of equilibria whose thermodynamics and kinetics are determined by their intrinsic amino acid sequence. Indeed, understanding the pathogenesis of misfolding diseases is complex and challenging, as highlighted by the huge diversity of the clinical manifestations linked to erroneously folded proteins (8).

1.1.4 MISFOLDING DISEASES

Misfolding diseases arise when the presence of non-functional conformations disrupts normal cells functions. There are two possible scenarios depending on whether the pathogenesis is ascribed to a toxic activity of the misfolded conformations (gain of toxic function) or if it is rather linked to the lack of physiological activity of the protein (loss of function) (25). In 'gain of toxic function diseases', native-like structures promote aberrant intermolecular interactions leading to the formation of aggregated species. Toxicity is attributed to the formation and accumulation of proteinaceous aggregates constituted of misfolded and/or unfolded proteins. In 'loss of function diseases', instead, protein misfolding causes the inactivation of proteins; indeed in such conformations they do not fulfil their physiological functions and often are promptly degraded (25).

Another important classification within conformational diseases regards the localization of the misfolding event. Indeed, they can be divided into two sub-groups: localized misfolding diseases with proteinaceous deposits in a single organ or tissue, typically the one where the precursor protein is expressed; systemic diseases, characterized by the presence of multiple aggregated species in various organs simultaneously (26).

The diversity of the clinical manifestations in misfolding diseases is overwhelming and mostly depends on the localization of the misfolding event. For example, Alzheimer's disease (AD) is a conformational pathology characterized by the accumulation of Aβ peptide and Tau deposits in the central nervous system (27). Accordingly, AD patients present cognitive impairment and loss of memory, symptoms commonly associated with nervous system decline. Systemic light chain amyloidosis instead is an example of systemic disease with proteinaceous deposits spread all over the body. Indeed, patients suffering from AL amyloidosis have accumulation of aggregated light chain antibodies in heart, kidney, spleen or liver, and this results in the development of a multi-symptoms pathology (28). Finally, within the large group of misfolding diseases, amyloidoses and serpinopathies are of particular interest. The first is characterized by the formation and accumulation of cross-β protein aggregates named amyloids. Most of the amyloid-related disorders are considered as gain of toxic function diseases, since that the amyloid deposits, and their precursors, can be toxic to cells, tissues and organs (5).

Serpinopathies, instead, are caused by an aberrant behaviour of serpin proteins (29). Typically serpins inhibit the activity of serine proteases playing a crucial role in several cellular pathways. However, they present a metastable native state that is susceptible to rearrangements into more stable but inactive conformations. Mutations in the serpin sequence destabilise the native state causing a drastic reduction in the capability of fulfilling its functional roles, thus leading to the disruption of normal cells pathways. Eventually, misfolded serpins accumulate as ordered polymers within the cell and may exert some degree of toxicity (30). Accordingly, serpinopathies are usually considered as both gain of toxic functions disorders, due to the accumulation of serpin polymers, and loss of active function diseases, due to the loss of active serpin within the cell (30). Nevertheless, in conformational pathologies, regardless of the causes of the diseases, the number of organs affected and the kind of macromolecules involved, the effects of protein misfolding is often very dangerous for human health (31).

In conclusion, the diversity of the clinical manifestations as well as the complexity of the molecular mechanisms underlying the processes of protein misfolding and aggregation prevent from developing efficient tools to fight these pathologies. Indeed, the majority of these diseases are still uncurable and further investigations are required to depict thoroughly the whole processes (5).

1.2 AMYLOIDOSIS

1.2.1 MAIN FEATURES OF AMYLOID RELATED DISEASES

Amyloidosis is a large class of protein misfolding diseases characterized by the accumulation of insoluble amyloid fibrils. Notably, 37 different proteins have been found to form amyloid deposits in human diseases (5). Many of them are secreted, and amyloid deposits are therefore observed in the extracellular space. The majority of these proteins have less than 150 residues and only four of them exceed 400 (5). Half of them present a globular native state, while the remaining is split into intrinsically disordered proteins (that is, the functional

native state of the protein is not globular but partially unstructured) and proteins whose structure is still unknown (32).

These pathologies are associated to several factors, including aging, as in AD (27), lifestyle or diet, like type 2 diabetes (33), or genetic, such as hereditary systemic amyloidoses (34). Moreover, they present a wide spectrum of clinical manifestations depending on the precursor protein involved and where it is expressed.

The first class of amyloidosis is represented by neurodegenerative disorders, where amyloid deposits are found within the brain: among them, Alzheimer's and Parkinson's diseases, caused by the aggregation of Aβ and α-synuclein respectively, are undoubtedly the most recurrent (35). The second category groups all those conditions associated to the accumulation of protein aggregates in various organs other than the central nervous system, *e.g.*, heart, kidney, bones, spleen, liver. Notably, there can be either single organ deposition, such as in transthyretin cardiac amyloidosis (36), or multiple-site depositions, usually named systemic amyloidosis, where deposits are found in many organs (37). All these pathologies are associated to the aberrant aggregation of misfolded proteins that eventually accumulate as insoluble amyloid fibers.

1.2.2 STRUCTURAL FEATURES OF AMYLOID FIBERS

Amyloid refers to the abnormal fibrous, extracellular, proteinaceous deposits found in organs and tissues. They are filamentous self-assembled aggregates of proteins or peptides enriched in cross-β structures. This structure is a ribbon-like β-sheet extended over the length of the fibril, in which β-strands run approximately perpendicular to the fibrillar axis. The β-strands are linked by inter-strand backbone hydrogen bonds that run parallel to the growth direction. Typically, amyloid fibrils contain two or more cross-β layers, stacked on one another with sidechain-sidechain interactions, often in an interdigitating manner (38).

As observed by cryo-electron microscopy (cryo-EM) or atomic force microscopy (AFM), the fibrils are typically 7 – 13 nm in diameter and comprise 1-8 protofilaments that usually twist around each other (39).

The cross-β architecture provides great stability to the fibrils, since it allows the formation of a continuous array of hydrogen bonds that preserves them from proteolytic cleavage or hydrolysis (40). Indeed, in many cases the amyloid state is greatly more stable than the native state even under physiological conditions (23). Accordingly, in amyloidosis pathologies, the native functional state of proteins does not represent the global free energy minimum and it is separated from the amyloid form by kinetic barriers (23).

The determinant property of amyloids is the formation of a specific X-ray pattern that is due to the formation of layered arrays of extended β-sheets (41). The formation of amyloid fibers *in vitro* is usually monitored by the binding of dyes, including Congo red, thioflavin-T (ThT), and derivatives. These dyes bind specifically to the amyloid β-sheet structure and form ordered arrays along the length of the fibril (42). Fibrillar morphology, cross-β structure and recognition by specific dyes are considered the hallmarks of amyloid structures. In order to be classified as an amyloid, a proteinaceous aggregate needs to display all these features at the same time (5).

Notably, different polypeptide chains form fibrils with similar morphological and structural features. Variations on these features, *i.e.*, diameter length, stability, and twisting properties, are mainly due to differences in the primary sequence. A peculiar feature of amyloid fibers is that they have a huge heterogeneity, with the same precursor being able to produce self-propagating fibril polymorphs with distinct molecular structures, morphologies, and

biological properties. Indeed, different fibrillar morphologies have been observed to have significantly different toxicities and have also been correlated with variations in amyloid-related diseases phenotypes (43,44). Regardless of the amino acid sequence or of the structure of the protein in its native state, such fibrils are rich in β-sheet patterns and their highly packed structures confer great stability to the three-dimensional organization(45).

However, the amyloid state is not exclusively associated with human diseases. Indeed, functional amyloids have been proposed to take part in several physiological properties, including pigmentation, antimicrobial responses, and regulated necrosis (46). In addition, their fibrous structure facilitates their use as scaffolds for biochemical processes, while their compact nature is ideal for storage of proteins. Accordingly, cells make use of amyloid structures to fulfil a wide range of physiological functions. At the same time, cells can mask or prevent the toxicity associated to amyloid formation which is instead observed in misfolding diseases (46). Notably, understanding how cells manage to prevent the harmful effects of functional amyloid could provide insights into how to prevent degeneration in amyloidoses. Moreover, almost any polypeptide chain has the ability, under favourable conditions , *e.g.*, high concentration or denaturing conditions, to adopt an amyloid structural state (47).

Thanks to the recent advances in the structural biology field, in particular on solid-state nuclear magnetic resonance (ssNMR), AFM, Cryo-EM, and X-ray crystallography (X-ray), a large number of atomistic models of amyloid structures have recently been obtained (39,48–51). This structural information are pivotal to understand the molecular determinants of protein aggregation processes to design strategies to interfere with the mechanism.

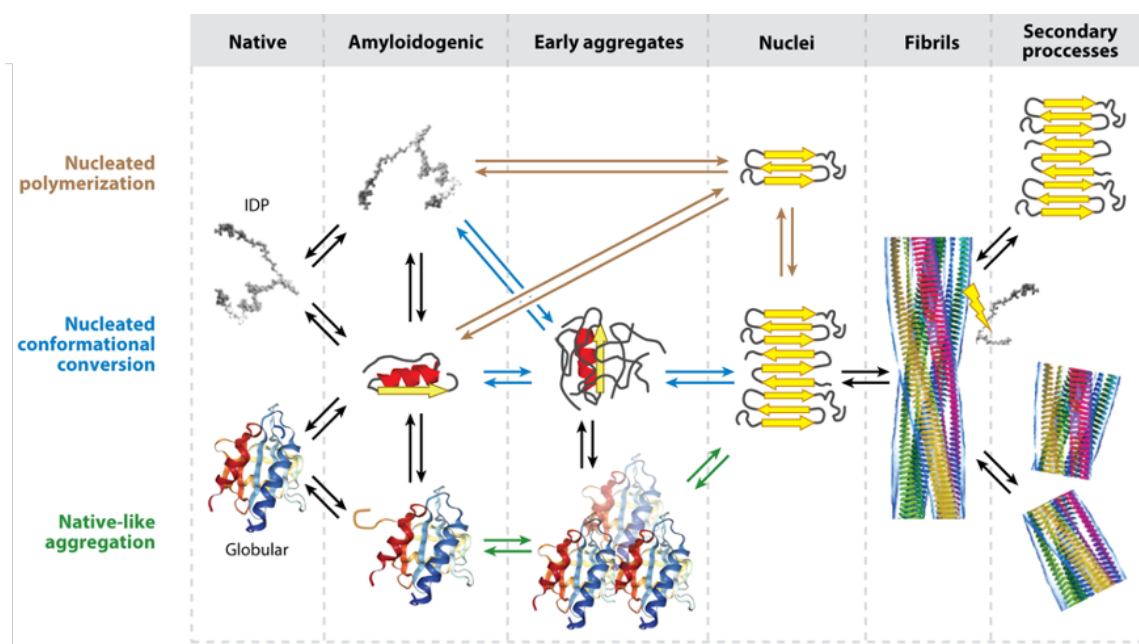### 1.2.3 MECHANISMS OF AMYLOID FIBRIL FORMATION

Understanding the mechanisms by which a soluble protein converts into insoluble aggregated species is pivotal to understand the causes of protein aggregation and to develop treatments to cure associated pathologies. The aggregation phenomenon is an extremely complex and branched process (Fig. 2) (5). Indeed, the achievement of an ordered amyloid structure is always the final step of the process. The ways towards fibril formation can vary from protein to protein and depend on several factors even though it is possible to recognise common steps (9).

The first stage of the aggregation process involves the formation of partially or totally unfolded species (50,52). While the native fold is stabilized by intramolecular interactions, in the fibrillar state the intermolecular interactions dominate. Thus, to reach the amyloid state, proteins need to lose their secondary and tertiary structure contents and deeply rearrange into β-sheet rich conformations. The conversion of a normally soluble protein into an aggregated state involves nucleation and growth steps and depends on the nature of the native state (5). Notably, reorganization of folded globular proteins into amyloid fibrils at physiological conditions is at the basis of many pathological conditions, including dialysis related amyloidosis (DRA) (53), AL amyloidosis (54) or transthyretin cardiac amyloidosis (36). The aggregation-prone regions are usually buried within the core of the protein. Thus, for globular proteins a partial or total unfolding is a necessary prerequisite of amyloid formation. On the one hand, folded globular proteins possess a significant tendency to populate native-like, partially unfolded conformations, as a consequence of local unfolding, thermal fluctuations, or ligand release (55). On the other hand, destabilization of the native fold due to mutations or environmental conditions can represent a strong driving force in the formation of aggregation-prone ensembles. These native-like states trigger the formation of

aggregates by exposing the aggregation-prone regions that are usually buried in the native fold (5,32). These conformations do not bind amyloid-specific dyes, and do not exhibit a significant content of β-sheet structure and compactness (5). Eventually, they can convert into mature, insoluble fibrils.

From a mechanistic point of view, the aggregation is a nucleated polymerization mechanism. Indeed, the first step is the conversion of monomeric proteins into nuclei. The conversion process is thermodynamically unfavourable and takes place during the lag phase. Then, during the exponential phase, addition of monomers allows the formation of the mature fibril starting from nuclei. Indeed, nuclei are defined as the smallest structures able to initiate fibril elongation and are regarded as monomeric species that are highly prone to aggregate rapidly (Fig. 2) (50). Furthermore, the number of fibrils can also increase through the secondary nucleation process: indeed, the fibril itself acts as catalyst and favours the formation of organized amyloids (56).

However, the scenario is far more complex and the whole process entails a large number of possible alternative paths that are selected depending on protein sequence or on conformational state adopted by the amyloidogenic monomers (9). For instance, in some cases monomers have been found to convert into misfolded aggregates that are not able to grow into organized fibril (57). However, a deep structural reorganization of these early aggregates leads to the generation of nuclei and, eventually, to the formation of fibrils.

Figure 2. Mechanism of amyloid fibril formation. Conversion of a soluble protein into a ordered amyloid structure requires the partial or total unfolding of the native state and rearrangement into β-sheet rich conformations. Figure edited from (5).

In conclusion, the multiplicity of aggregation processes, in which parallel pathways and reorganization steps can compete, increases the difficulties in studying the systems that are associated to the onset of pathological symptoms. However, to fully understand the pathogenesis of misfolding diseases and to efficiently tackle them, it is crucial to shed light onto the mechanisms that take a functional active protein into ordered amyloid.

1.2.4 MOLECULAR ORIGINS OF AMYLOID TOXICITY

Solid data show that the most highly pathogenic species associated with amyloid formation are not the fibrillar deposits but the prefibrillar oligomeric species (5,52,58,59). Notably, oligomers are inherently misfolded and expose hydrophobic clusters on their surface. Indeed, they are likely to interact inappropriately with a wide range of functional components of the environment they are found in. Accordingly, they exert their toxic properties by causing cellular dysfunctions (45). For example, α-synuclein oligomers were recently found to considerably interact with cellular membranes, causing leaking and disruption of the cellular homeostasis (58). Nevertheless, not all the oligomeric species formed on the way to the fibril present the same harmful properties. First of all, oligomers toxicity has been found to be strictly correlated to their size (45). In particular, small-size oligomers are generally considered to be the most toxic species as they exhibit a high diffusion coefficient which allows them to diffuse more rapidly and form aberrant interactions more readily (60). Secondly, the degree of β-sheet content is another important determinant, with the unstructured oligomers being more deleterious than the structured ones (61).

However, pathogenesis in amyloidoses is not only to be ascribed to the oligomeric species but the mature fiber itself plays a key role. First of all, extracellular amyloid deposits affect organ integrity and function. This is the case, for example, in some types of systemic amyloidosis, such as AL amyloidosis, where accumulation of fibrils within organs disrupts their normal elasticity and/or functions (62). Secondly, amyloid deposits are able to deplete key components of the protein homeostasis network. For instance, they constantly withdraw molecular chaperones and, by doing so, the total number of these molecules available for other purposes is drastically decreased (63). Then, they act as potent catalysts for the generation of new toxic oligomers through secondary nucleation mechanism. Indeed, fibrils surface can accelerate the formation of new aggregated species, increasing the number of potentially toxic species (64). Finally, there are evidences that some polymorphs of mature fibrils can have themselves significant toxicity (65).

In conclusion, the toxicity of protein aggregates is likely to be the result of a large network of aberrant interactions that misfolded proteins can generate. Thus, they exert their toxic features through multiples mechanisms of action and through the engagement of key cellular components.

1.3 SERPINOPATHIES

Serpinopathies includes a large number of conformational diseases characterized by the structural rearrangements of members of the serpin superfamily (29).

1.3.1 MAIN FEATURES OF SERPINS

Serpins are the largest class of protease inhibitors and they play crucial roles in highly controlled physiological processes, including blood coagulation, inflammation, and fibrinolysis, by regulating enzymes involved in proteolytic cascades (66).

Members of the serpin superfamily are widely distributed among the major branches of life. Indeed, serpin are found in almost all eukaryotic systems and in some viruses (67). Serpin proteins share more than a 30% sequence homology and high conservation of the tertiary structure (67). In particular, serpins fold is characterized by a metastable conformation composed of 8-9 α-helices, three β-sheet (A, B, and C), and a highly mobile and dynamic loop, named reactive centre loop (RCL) (Fig. 3) (68). The RCL is typically composed of 18-20 amino-

acids and is pivotal to the activity of the serpins. Indeed, it acts as a bait for the target protease which binds and cleaves the scissile bond (P1-P1') on it (69). Upon cleavage, the serpin forms a Michaelis complex with the proteases through an ester bond between the P1 residue and the serine of the protease active site. Formation of the covalent complex is immediately followed by a drastic conformational transition where the target protease is translocated to the other side of the serpin and inactivated. Disruption of the protease active site prevents efficient hydrolysis of the acyl-intermediate and subsequent release of the protease (70).

The serpin mechanism of action is a suicide inhibitory mechanism. Indeed, while blocking protease activity, the serpin undergoes a drastic conformational change where the RCL is cleaved and inserted into the β-sheet A forming an extra strand (s4A). This transition is termed the 'stressed (S) to relaxed (R) transition' (71). Accordingly, insertion of the RCL yields the cleaved state of the protein which is a highly stable but inactive state of the serpin (Fig. 3).

The high degree of serpins structural flexibility required to carry out the inhibitory activities entails that their native fold is not the conformation that represents the lowest-free energy conformation, but is rather a metastable, kinetically trapped state (72). Serpins metastability and their ability to undergo controlled conformational changes makes these proteins susceptible to spontaneous structural rearrangements (67). Accordingly, in addition to the native-to-cleaved transition, serpins can fold into a second stable but inactive conformation which is named latent conformation. The latent state is characterized by the spontaneous insertion of the intact RCL into the β-sheet A of the protein, where it cannot interact with the target protease (73). The achievement of such fold is a way used by serpins to control their inhibitory activity, since that hiding the RCL within the β-sheet A prevents proteases binding (Fig. 3) (74).

A third stable conformation that serpins can explore is the delta conformation. This structural rearrangement has firstly been observed for a natural mutant of a1-antichymotrypsin (75). Even though it is unlikely to be physiologically relevant, besides for some mutant variants, the delta state shows a higher chemical and thermodynamical stability than the native state but it is more prone to form polymers (75). These different biophysical features arise from structural rearrangements of the native fold: three RCL residues are inserted into the top of β-sheet A, with the remaining still flexible; in addition, helix-F rearranges and inserts into the bottom of β-sheet A (Fig. 3).

Lastly, the inherent metastability of serpins fold can also lead to the formation of soluble long-chain polymers (76). However, the intrinsic metastability is not sufficient to cause serpin polymerisation but a further destabilization factor is required. Indeed, serpin polymerization is observed *in vivo* in the presence of mutations destabilizing the serpin native state (30). In particular, even though there is not an unequivocally accepted mechanism of polymers formation, the two recognised main players involved in the achievements of long chain polymers are the β-sheet A and the RCL. Depending on the model proposed, they can either interact inter-molecularly, loop and sheet mechanism model (77), or intra-molecularly, domain-swap models (78,79). Serpin polymeric forms are inactive but stable and their accumulation within the cells are at the basis of many pathological conditions, known as serpinopathies (80).

1.3.2 DYSFUNCTIONAL SERPINS

Serpinopathies are a class of conformational diseases caused by serpin misfolding. Conformational mobility of the serpin scaffold, which is crucial as it provides a controllable

mechanism of inhibition, may be dangerous as it entails the possibility for the protein to explore several different inactive, and potentially pathological, conformations (81). Indeed, serpinopathies are simultaneously gain and loss of function diseases. On the one hand, accumulated protein, usually in the form of polymers, may be detrimental to cells. The mechanisms underlying the toxicity of these polymers are not fully understood, even though it is clear that the accumulation of long serpin chains result in cellular stress (82). On the other hand, formation of inactive alternative conformation results in the dysregulation of important proteolytic cascades (30).

Beyond the pathogenesis underlying the disease, serpinopathies result from point mutations in serpins primary sequence. They are characterized by the formation of ordered polymers that are retained within the endoplasmic reticulum of the expressing cell. The polymers accumulate into periodic acid Schiff-positive inclusions and are associated to the onset of several different symptoms (67). Analyses of the localization of the mutations within the serpin fold allowed to map the molecular switches for serpin misfolding. In particular, most of the mutations known so far cluster around specific structural elements, including the β-sheet A, the helix F and the N-terminal part of the RCL (72). All these regions are characterized by a high degree of flexibility as they are all involved in the insertion of the RCL. Indeed, it is suggested that the destabilization of the β-sheet A favors the transition to polymeric or latent states over the monomeric metastable native state (83). At the same time, modifications in these regions can have repercussions on the inhibitory activity of the serpin, since that it is primarily linked to its structural complexity (82).

The most recurrent serpinopathy arises from the misfolding and polymerization of α_1-antitrypsin (α_1AT) and is called α_1AT deficiency (84). α_1AT is expressed in the liver and fulfils its physiological functions in the lungs where it regulates neutrophil elastase, a protease that can disrupt connective tissue. Several α_1AT mutations have been identified and linked to the onset of the pathology. For example, the Glu342Lys mutation, also known as Z mutation, is responsible for α_1AT deficiency and result in the retention of polymers within the ER of hepatocytes (85). The formation of these ordered polymers is associated with cirrhosis, neonatal hepatitis, and hepatocellular carcinoma (76). In these cases, liver-related manifestations are due to the accumulation of the polymers within the expressing cells, indicating a gain of toxic function phenotypes. However, patients carrying the Z mutation usually present respiratory symptoms. Indeed, Glu342Lys α_1AT does not properly regulate neutrophil elastase in the lungs and this can give rise to shortness of breath and lung infections (85). In this latter manifestation of disease, the loss of active function phenotype is responsible for the onset of the symptoms.

Another example of serpinopathy is familial encephalopathy with neuroserpin inclusion bodies (FENIB), an autosomal dominant dementia that results from point mutations in neuroserpin (NS) (86). NS is a serpin protein expressed in the nervous system where it plays key roles in neural development and plasticity by primarily targeting tissue plasminogen activator (tPA) (87). Point mutations in NS destabilise protein fold and cause aberrant formation of polymers that accumulates within the ER of neurons as inclusion bodies. In this case, neurons damage occurs as a consequence of the formation NS polymers as well as of the loss of active NS within the cell (86). To date, six different mutations have been identified as responsible for the onset of FENIB (88). Patients suffering from FENIB present symptoms typical of neurodegenerative diseases, including loss of intellectual functions, and seizure.

In order to understand the mechanisms underlying the serpin misfolding phenomenon, it is crucial to fully characterize the all the possible conformers associated with the diseases. To

this aim, extensive studies have been conducted to elucidate the three-dimensional structures of the native (89), cleaved (89), latent (74,90), and the delta (75) form of various serpins. Unfortunately, the structural characterization of the polymeric state has still not been accomplished, preventing from the design of polymerization inhibitors.
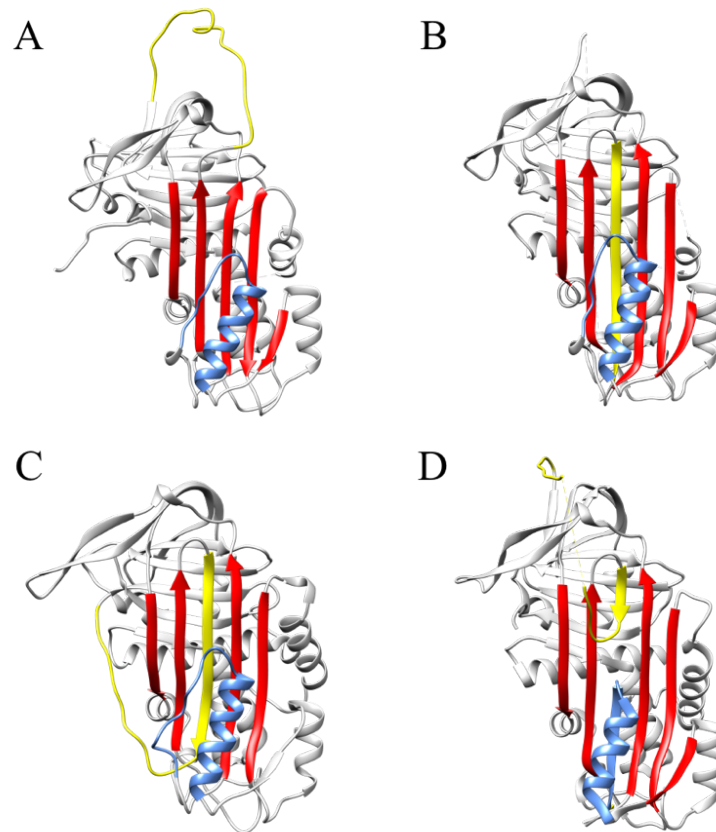
Figure 3. Monomeric serpin conformations. A) Native state. The RCL (yellow) is exposed and highly flexible (PDB ID 3F5N) (89). B) Cleaved state. Upon cleavage, the RCL (yellow) is inserted into the β-sheet A (red) forming and extra strand, strand 4A (PDB ID 3F02) (89). C) Latent state. The RCL (yellow) is inserted into the β-sheet A (red) without cleavage and is therefore protected (PDB ID 4AQH) (73). D) Delta state. The RCL (yellow) is only partially inserted into the top of β-sheet A. Helix F (blue) partially unwound and inserts into the bottom of the β-sheet A (PDB ID 3DLW) (75).

1.3.3 MECHANISMS OF SERPIN POLYMERS FORMATION

In vivo, serpin polymerization occurs when the protein presents mutations that destabilize the native fold. However, *in vitro* production of recombinant mutant variants can be difficult to achieve as mutants are generally highly unstable and tend to unfold or to associate readily into polymeric chains (67). Indeed, to efficiently characterize serpin polymers, alternative methods have been used to induce the polymerization of the wild-type serpins. In fact, under partially denaturing conditions, wild-type protein efficiently polymerises into species with morphology that recapitulates the one observed *in vivo*. In particular, high temperature, non-physiological pH or presence of denaturing agents, *i.e.,* urea and guanidinium hydrochloride, have been largely employed to obtain polymers required for an exhaustive biophysical and biochemical characterization (76,89,91,92).

Although the morphological properties of serpin polymers may vary depending on the production conditions, they share common mechanisms of formation. Indeed, the first prerequisite for serpin polymerization is the destabilization of the native state and the adoption of a non-native protein conformation (M*) prone to establish intermolecular interactions. Serpin polymerization process is considered to be a bimolecular process in which monomeric units associate one with the other. Thus, it involves the sequential addition of monomers to form a chain that can be elongated either from the head or from the tail. The process yields polymeric chain with a 'bead-on-a-string' morphology, as seen by electron microscopy (93). It should be noted that, unlike in the amyloidoses where the precursor proteins re-organize into β-sheet amyloids, in serpinopathies the polymeric state is composed of serpin monomeric subunits that retain their main structural properties (94).

Elucidating the structure of serpin polymers is an important hurdle in understanding the polymerisation process and is pivotal for rational design molecules able to interfere with it. To date, three different mechanisms have been proposed to explain the way monomeric serpin associates into larger conformations.

1.3.3.1 LOOP AND SHEET MECHANISM

The observation that serpins can incorporate RCL-like peptides lead to development of the loop and sheet hypothesis (Fig. 4A). This mechanism, originally proposed in 1990, involves the interaction between the RCL of one protomer with the β-sheet A of a second protomer (77). The first evidence supporting this model was the inability of peptide-annealed or cleaved α_1AT to polymerize *in vitro* when heated (83). Crystal structures incorporating RCL-like peptides in the s4A position of α_1AT provided another hint to support this hypothesis (95,96). In particular, these structures reported that only the middle section of the RCL (from P12 to P5) is efficiently incorporated intermolecularly and stabilizes the system by creating a new network of hydrogen bonds (97).

However, the model presents several conceptual problems. In fact, interaction between exogenous RCL and β-sheet A entails the formation of a gap at the top of strands 3A and 5A. This gap would expose a large hydrophobic area and would result in breaking of several hydrogen bonds. To fill this gap, a partial intramolecular insertion would be required, but this would create a conformation no longer able to elongate to form extended chains (98). Furthermore, this model would entail the formation of rigid polymers, as the link between the two protomers is short. This is in contrast with electron microscopy observations where *ex vivo* serpins polymers were found to be highly flexible and dynamic suggesting the present of a long linker (93).

In conclusion, the data available suggest that the loop and sheet mechanism presents some criticisms as it does not fully explain the known physical properties of serpin polymers formed either *in vivo* or *in vitro.*

1.3.3.2 S4A/S5A DOMAIN SWAP

The s4A/s5A domain swap (Fig. 4B) was firstly proposed after the elucidation of the three-dimensional structure of a closed serpin dimer. In particular, Yamasaki *et al.* managed to produce and crystallize a self-terminating dimer from plasm-derived wild-type antithrombin by heating at 37 °C in low pH conditions. They reported that the formation of the stable dimer was due to a large domain swap of more than 50 residues, including two long antiparallel β-strands inserting in the centre of the principal β-sheet of the neighbouring monomer (79).

Further evidences collected through limited proteolysis, disulphide trapping, molecular modelling, H/D mass-spectrometry and fluorescent labeling experiments on α_1AT or antithrombin gave additional confidence on the accuracy of the mechanism (79,99). However, polymers formed using these conditions were not efficiently recognised by the antibody 2C1, which is reported to specifically bind produced α_1AT polymers *in vivo* (100).

To conclude, the s4A/5A model presents some criticisms and is unlike to resemble the mechanism that occurs *in vivo*.
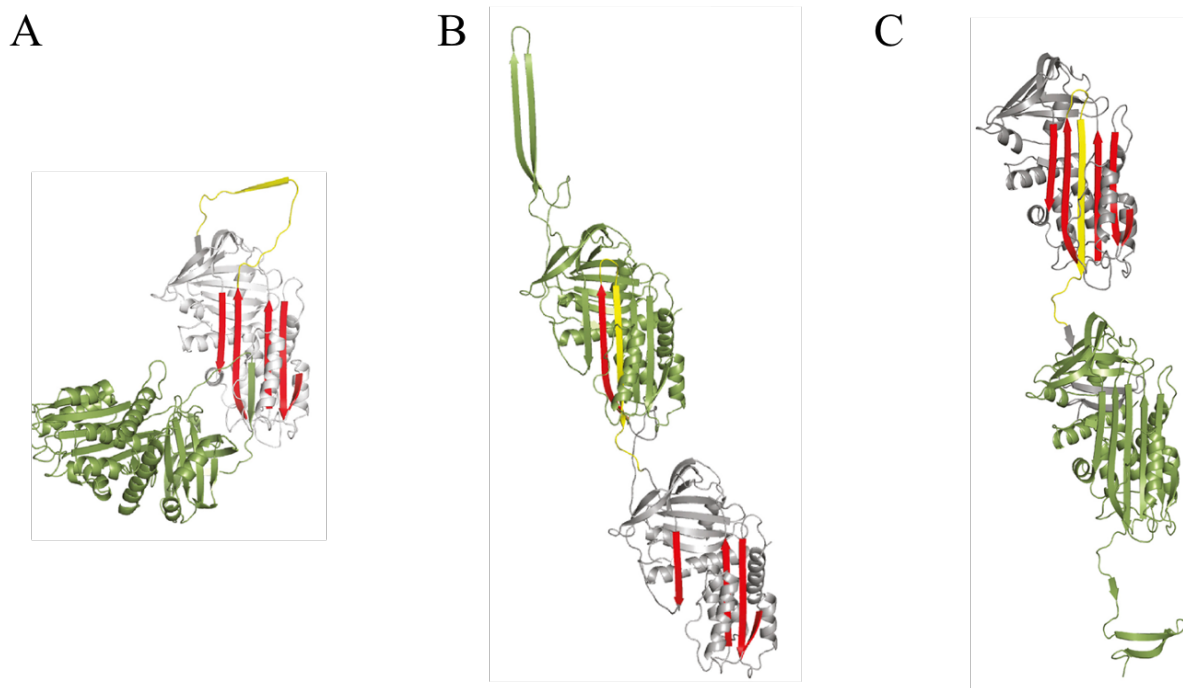
Figure 4. Proposed mechanism of serpin polymers formation. A) Loop and sheet mechanism with the insertion of part of the RCL (green) of one protomer into β-sheet A (red) of a second protomer. B) s4A/5A polymerization mechanism where the intermolecular linkage both s5A (red) and s4A(yellow) which insert into the β-sheet A of a second protomer (green). C) In the C-terminal domain swap mechanism the intermolecular interactions are performed by the C-terminal β-strands (grey) while the RCL (yellow) insert intramolecularly. Figure edited from (101).

1.3.3.3 C-TERMINAL DOMAIN SWAP

The C-terminal domain swap was hypothesized by Yamasaki *et al.* when they succeed in producing and crystallizing a α_1AT trimer stabilized by a C-terminal domain swap involving s1C, s4B and s5B (78). They engineered α_1AT by introducing cysteine residues to form a disulphide bond, thus stabilizing the super molecular trimeric complex. In the crystallographic structure, the RCL of each promoter was inserted intramolecularly and was not involved in the domain swap. The most important evidence supporting this model was that the trimer produced via disulphide trapping was efficiently recognized by the 2C1 antibody. Accordingly, their heat-induced polymers must share some important structural features with the pathological polymers of α_1AT formed *in vivo*.

To date, the C-terminal domain swap is the one that best explains several known properties of serpin polymers, including the high degree of flexibility between protomers, the hyperstability, which is due to the full insertion of the RCL, and the possibility to easily elongate thanks to persistent donor and acceptor ends (102).

2 OBJECTIVES

The general objective of this thesis is the identification of the molecular bases underlying misfolding diseases.

We intend to combine a series of biophysical and biochemical techniques on two model systems, NS and β2m, to determine the aspects favouring the self-assembly into native-like aggregates (NS) or amyloids (β2m).

In particular, the detailed objectives of this PhD thesis are:

- Characterize the denatured state of D76N and the role of this mutation in β2-microglobulin (β2m) aggregation
- Identify the biophysical and biochemical properties that prevent murine β2m aggregation
- Understand the role of β2m amyloids in the initiation and development of multiple myeloma
- Understand the importance of glycosylation in NS stability
- Identify compounds that hamper NS polymerization

3 β-2 MICROGLOBULIN

Human beta-2 microglobulin (hβ_2m) is a 11.9 kDa protein present in nearly all nucleated cells and most biological fluids, including serum, synovial fluid, and urine (103). hβ_2m constitutes the non-covalently bound light chain of the class I major histocompatibility complex (MHC-I) and other MHC-I-like structures, including neonatal Fc receptor, cluster of differentiation 1 (CD1), and human hemochromatosis protein (104).

β_2m genes are conserved across species, including mammals and birds. Although hβ_2m sharing around 50% of amino acid sequence similarity with chicken and fish β_2m and 90% with murine β_2m (mβ_2m), their overall structures are virtually identical (105,106). In particular, ten residues are conserved in all species, including two cysteine residues that form a disulphide bridge (107).

3.1 PHYSIOLOGICAL FUNCTIONS

The best-characterized physiological function of β_2m is to be part of the class I major histocompatibility complex (MHC-I), whose function is to present antigenic peptides to cytotoxic T lymphocytes (108). MHC-I is a stable ternary complex that also comprises a heavy chain (HC) and an 8-11-residue peptide (Fig. 4). It is assembled in the endoplasmic reticulum and afterwards transported to the extracellular side of the cell membrane, to which MHC-I is anchored by a short transmembrane domain (109). During its normal turnover, β_2m is continuously shed from the surface of cells displaying MHC-I molecules into the serum, where it is transported to the kidneys for degradation (110).

The function of MHC-I molecules is to bind non-self antigen peptides derived from the degradation of cytosolic proteins and display them on the cell surface for recognition by appropriate T cells (111). Identification of MHC-I by T helper lymphocytes, cytotoxic T lymphocytes, and natural killing cells activates the immune response against the presenting cells (112).

β_2m establishes non-covalent interactions with the heavy chain (HC) and is crucial for the stability of the MHC-I. In particular, the presence of β_2m is an important prerequisite for peptide binding. Although such ligands are anchored within a groove formed by the HC (Fig. 4), β_2m is essential for maintaining complex stability, and for the intracellular transport of the complex to the cell surface (113).

3.2 β2M AND AMYLOIDOSIS

hβ2m is an aggregation-prone protein responsible for at least two different types of amyloid-related diseases. In patients with kidney deficiency, wild-type hβ2m (wt hβ2m) aggregation leads to dialysis-related amyloidosis (DRA) (110), while the natural D76N genetic variant of hβ2m (D76N hβ2m) is responsible for a severe hereditary systemic amyloidosis (34). In both cases, the pathogenesis is ascribed to the formation and accumulation of proteinaceous aggregates. Indeed, β2m-related amyloidoses are usually regarded as gain of toxic function diseases.

3.2.1 DIALYSIS-RELATED AMYLOIDOSIS

In patients with renal failure undergoing hemodialysis, the concentration of hβ_2m circulating in the serum increases up to 60-fold (114). Over time, such pathologically high concentration, which can reach up to 4.3 µM (114), triggers the formation of amyloid aggregates that accumulate in the skeletal joints, bones and muscles, leading to the development of DRA (115). Depending on the location of the amyloid deposits, patients suffering from DRA may

present carpal tunnel syndrome, flexor tenosynovitis, destructive spondyloarthropathy or bone cysts (53).

Analysis of the amyloid plaques extracted from DRA patients showed that full length hβ2m is the major component of the fibrils, while a truncated form of hβ2m lacking six amino acids at the N-terminus (ΔN6 hβ2m) makes up about 20-30 % of the aggregated material (116).
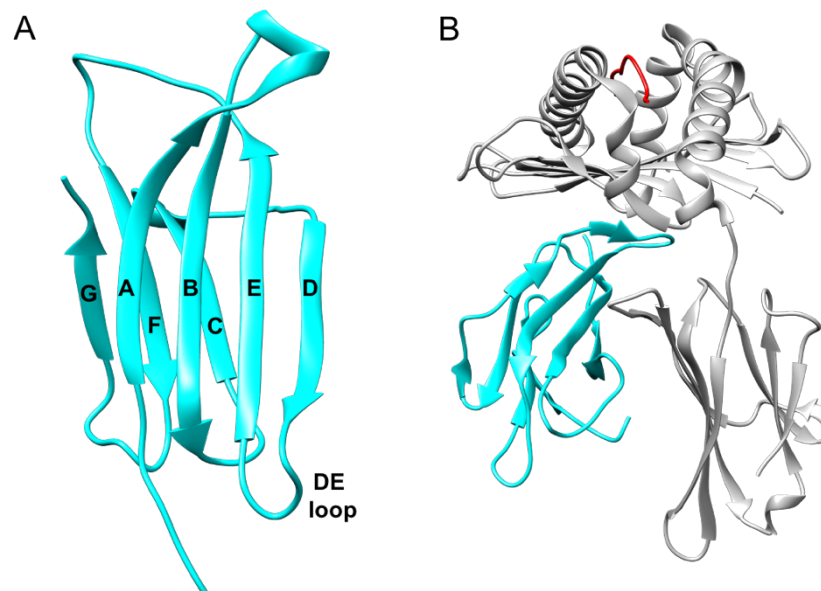
Figure 4. hβ2m and MHC-I structure. A) Crystal structure of wt hβ2m (PDB ID 5CS7). B) Crystal structure of MHC-I (PDB ID 1S9W). β2m (cyan) binds through non-covalent interactions to the HC (grey) and stabilizes the complex. The 8-11 aa long peptide (red) is localized within a groove in the HC.

3.2.2 HEREDITARY SYSTEMIC AMYLOIDOSIS

Hereditary systemic amyloidosis is, instead, linked to the natural mutant D76N hβ2m and is not triggered by an abnormally high hβ2m concentration. Indeed, D76N hβ2m aggregates spontaneously and forms amyloid deposits in several visceral organs, including liver, kidney, spleen, and heart (34). Patients carrying the mutation have normal circulating hβ2m concentrations and normal renal function, but present bowel dysfunction with extensive visceral amyloid deposits. Unlike DRA, fibrils found in patients were exclusively composed of full-length D76N hβ2m, and no truncated forms were detected (34).

3.3 PHD PROJECTS

This PhD project has been developed to study three different aspects of hβ2m.

Firstly, it focused on the role of D76N hβ2m denaturing state within the protein aggregation process. Secondly, a biochemical and biophysical comparison of mβ2m and hβ2m was performed to identify the determinants underlying hβ2m aggregation. Lastly, hβ2m has been studied in the context of multiple myeloma (MM) to understand the role of hβ2m amyloid aggregation in the initiation and development of the pathology.

3.3.1 D76N Hβ2M DENATURED STATE

The molecular bases of amyloid aggregation propensity are still poorly understood, especially for proteins that display a stable folded native structure like hβ2m (5).

Protein aggregation and subsequent amyloid formation depend on several molecular properties, *e.g.,* thermodynamic stability, dynamics, primary sequence composition, and it requires at least a partial unfolding of the native state (117). In order to understand the causes underlying hβ2m aggregation, it is crucial to get further insights into the biophysical and biochemical features of the unfolding process.

To this aim, we investigated the denatured state of D76N hβ2m, the highly amyloidogenic natural mutant responsible for a hereditary systemic amyloidosis (34). Comparison between wt and D76N hβ2m native folds revealed only minor changes, with a root mean square difference of 0.59Å, as calculated over the whole C-alpha backbone (Fig. 5). D76N hβ2m is highly aggregation-prone and *in vitro* it forms fibrils even under native conditions (118). It is less thermodynamically stable than wt hβ2m (53.2 °C vs 62.4 °C) and it showed a reduced stability to denaturing agents (midpoint concentration of guanidinium hydrochloride 1.2 M vs 1.8 M) (34,119).
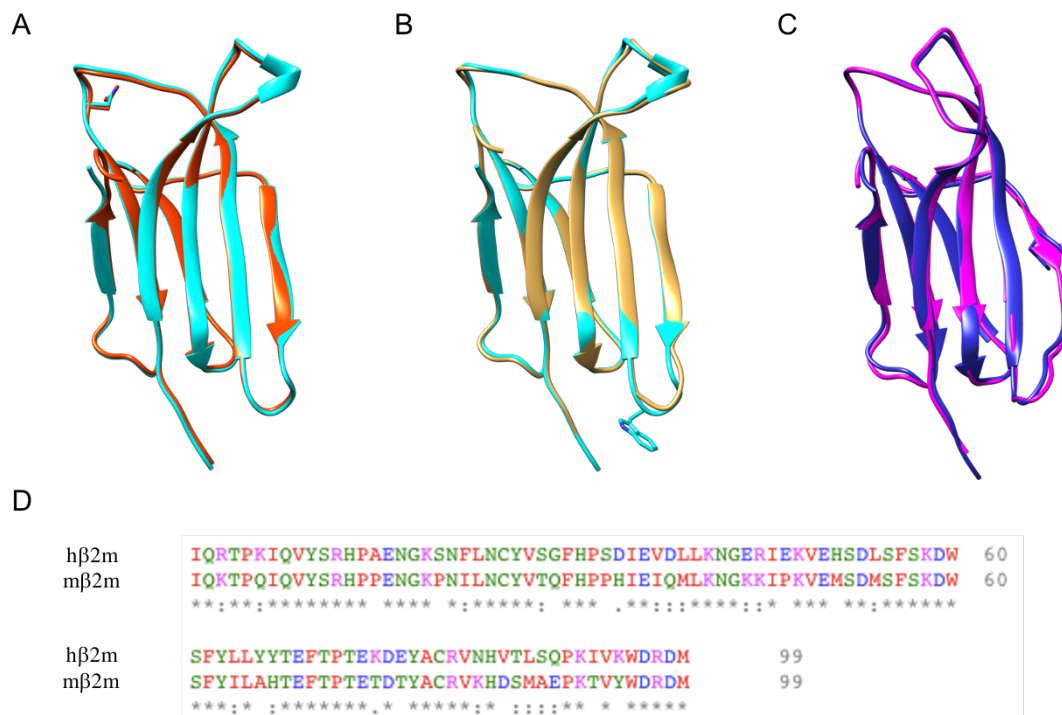
Figure 5. β2m variants. A-B) Comparison of the crystal structures of wt hβ2m (cyan, PDB ID 5CS7) with D76N hβ2m (red, PDB ID 4FXL). Asp76 and Asn76 are shown as sticks. B) Comparison of the crystal structures of wt hβ2m (cyan) with W60G hβ2m (gold, PDB ID 2Z9T). Trp60 is shown as sticks. C) Comparison of the crystal structures of the wt hβ2m from a human MHC-I complex (blue, PDB ID 1S9W) with wt mβ2m from a murine MHC-I (violet, PDB ID 1BII). D) Sequence alignment of wt hβ2m and wt mβ2m. 89 out of 99 residues are conserved between the two species.

Furthermore, the D76N mutant has been shown to present higher intrinsic dynamics than the wild-type protein under native conditions (117). In particular, even if the mutation does not affect the global protein fold, the increased protein flexibility alters the aggregation propensity by changing the accessibility to aggregation-prone conformations (117). Indeed, D76N mutation facilitates the conversion of the ground state to minor conformers

characterized by a local loss of β-strand structures and resulting exposure of aggregation-prone regions (117). In conclusion, D76N mutation introduces a general destabilization of the protein native fold, decreasing its overall stability and increasing protein dynamics (117).

Since the effect of the D76N mutation cannot solely be ascribed to direct effects on the native state, we investigated the equilibrium unfolding behaviour of the mutant in comparison to that of the wild-type. In particular, we performed equilibrium denaturation experiments to monitor changes in the accessible surface area to the solvent upon unfolding. We evaluated the changes in compactness of the denatured state, which is a defined as a transient on-pathway species that retains a considerable amount of residual structure (120). Eventually, aggregation experiments allowed to correlate the compactness of the denatured state to protein aggregation propensity ascribing a key role in the aggregation process to the protein's denatured state.

Investigating the Molecular Basis of the Aggregation Propensity of the Pathological D76N Mutant of Beta-2 Microglobulin: Role of the Denatured State

Lorenzo Visconti,†, Francesca Malagrinò,†, Luca Broggini, Chiara Maria Giulia De Luca, Fabio Moda, Stefano Gianni,*, Stefano Ricagno,* and Angelo Toto.

I contributed to this work by producing the proteins (both D76N and wt hβ2m) for unfolding experiments against denaturing agents.

Moreover, I assisted in performing the aggregation assays on D76N hβ2m.

Investigating the Molecular Basis of the Aggregation Propensity of the Pathological D76N Mutant of Beta-2 Microglobulin: Role of the Denatured State

Lorenzo Visconti [1,†], Francesca Malagrinò [1,†], Luca Broggini [2], Chiara Maria Giulia De Luca [3], Fabio Moda [3], Stefano Gianni [1,*], Stefano Ricagno [2,*] and Angelo Toto [1]

[1] Istituto Pasteur-Fondazione Cenci Bolognetti, Dipartimento di Scienze Biochimiche "A. Rossi Fanelli" and Istituto di Biologia e Patologia Molecolari del CNR, Sapienza Università di Roma, 00185 Rome, Italy; lorenzo.visconti@uniroma1.it (L.V.); francesca.malagrino@uniroma1.it (F.M.); Angelo.Toto@uniroma1.it (A.T.)

[2] Dipartimento di Bioscienze, Università degli Studi di Milano, 20133 Milano, Italy; luca.broggini@unimi.it

[3] Fondazione IRCCS Istituto Neurologico Carlo Besta, Divisione di Neurologia 5-Neuropatologia, 20133 Milano, Italy; chiara.deluca@istituto-besta.it (C.M.G.D.L.); Fabio.Moda@istituto-besta.it (F.M.)

* Correspondence: stefano.gianni@uniroma1.it (S.G.); Stefano.ricagno@unimi.it (S.R.)

† These authors contributed equally to this work.

Abstract: Beta-2 microglobulin (β2m) is a protein responsible for a pathologic condition, known as dialysis-related amyloidosis (DRA), caused by its aggregation and subsequent amyloid formation. A naturally occurring mutation of β2m, D76N, presents a higher amyloidogenic propensity compared to the wild type counterpart. Since the three-dimensional structure of the protein is essentially unaffected by the mutation, the increased aggregation propensity of D76N has been generally ascribed to its lower thermodynamic stability and increased dynamics. In this study we compare the equilibrium unfolding and the aggregation propensity of wild type β2m and D76N variant at different experimental conditions. Our data revealed a surprising effect of the D76N mutation in the residual structure of the denatured state, which appears less compact than that of the wild type protein. A careful investigation of the structural malleability of the denatured state of wild type β2m and D76N pinpoint a clear role of the denatured state in triggering the amyloidogenic propensity of the protein. The experimental results are discussed in the light of the previous work on β2m and its role in disease.

Keywords: protein stability; denatured state; protein aggregation

1. Introduction

Several types of human diseases, spanning from Alzheimer's disease to systemic amyloidosis, are caused by the incorrect folding of proteins [1]. A common factor of such pathological conditions lies in the accumulation of toxic aggregates [2]. Frequently, these aggregates are characterized by a specific type of highly ordered and stable structures, known as amyloid fibers, which are characterized by a conserved cross-beta structure and that can be identified with specific assays [3–5].

Beta-2 microglobulin (β2m) is a 99 residue protein forming part of the major histocompatibility complex class I (MHC-I). The aggregation and subsequent amyloid formation of β2m has been associated with a pathological condition known as dialysis-related amyloidosis (DRA) [6,7]. In fact, in dialyzed patients, there is an abnormally high concentration of β2m in blood. Such concentration of β2m exposes DRA patients to the risk of β2m amyloid deposition, a process that occurs mainly in joints and bones [8]. Intriguingly, β2m aggregation depends on several molecular properties and

its initiation requires at least partial unfolding of the native state [9,10]; β2m aggregation propensity correlates well with thermodynamic stability [11] but recently an important role for protein dynamics in determining amyloidogenicity was also reported [12,13]. Thus, this protein system represents a suitable candidate to investigate the links between protein folding, misfolding, and pathology.

The first naturally occurring mutant of β2m was identified in 2012 [14]. This variant is much more aggressively amyloidogenic in vitro and in vivo compared to wt β2m and corresponds to a mutation at position 76, where a D is mutated to N. Biophysical characterization of the D76N variant in vitro demonstrated that the mutation triggers remarkable effects by decreasing the thermodynamic stability of the protein and increasing its propensity to form amyloids [14,15].

A structural analysis of the D76N mutant compared to the wt β2m highlighted an interesting conundrum (Figure 1).
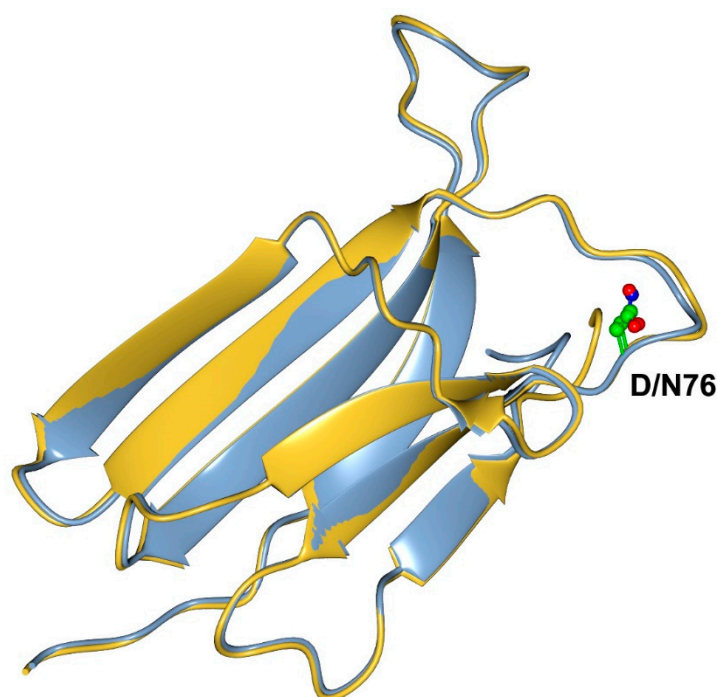
Figure 1. Three-dimensional structure of the D76N mutant (blue) in comparison to that of the wild type protein (yellow). Residue 76 is shown in ball and stick representation. It is evident that the native states of the two proteins are perfectly superimposable.

In fact, despite the dramatic effect of the mutation, residue 76 is located on a loop exposed to the solvent and the structure of the mutant is essentially identical to that of the wild type [14]. Thus, a comprehensive analysis of the biophysical and structural data available on D76N demonstrated that the destabilizing effect of the mutation is due to a complex effect involving an increased protein dynamics promoting the accumulation of a high-energy aggregation prone species [16].

Since the effect of the D76N mutation cannot be solely ascribed to direct effects on the native state, here we provide a characterization of the equilibrium folding behavior of the mutant in comparison to that of wt β2m. Data reveal that the destabilizing effect of the mutation is at least in part due to a change in its denatured state, which appears less compact than that of the wild type protein. Furthermore, by studying the equilibrium denaturation at different experimental conditions, we investigate the links between the compactness of the denatured state and the aggregation propensity of the protein. Our data are briefly discussed in the context of previous work on β2m.

2. Results

2.1. Equilibrium Unfolding Experiments

The thermodynamic stabilities of β2m wt and D76N variant were previously explored using thermal denaturations [16]. These studies showed a destabilization of the mutant, as mirrored by a ΔT_m of 10 K. In order to further compare the equilibrium unfolding of β2m wt and D76N, we conducted GdnHCl-induced equilibrium denaturation experiments. Protein denaturation was monitored by measuring the fluorescence emission of the two tryptophan residues in position 60 and 95 at different concentrations of GdnHCl. In both cases, observed fluorescence was consistent with a simple sigmoidal transition, characteristic of two-state folding. The robustness of the two-state equilibrium transition for both β2m wt and D76N was further confirmed by fitting globally the fluorescence profiles obtained at different wavelengths with shared thermodynamic parameters. The dependence of the normalized observed fluorescence signal at 330 nm versus the concentration of denaturant for wt and D76N is reported in Figure 2. It is evident that, whilst the mutant unfolds at lower concentrations of GdnHCl, the apparent cooperativity of the transition is affected by the mutation, with an increase of cooperativity for D76N as compared to that of the wild type protein.
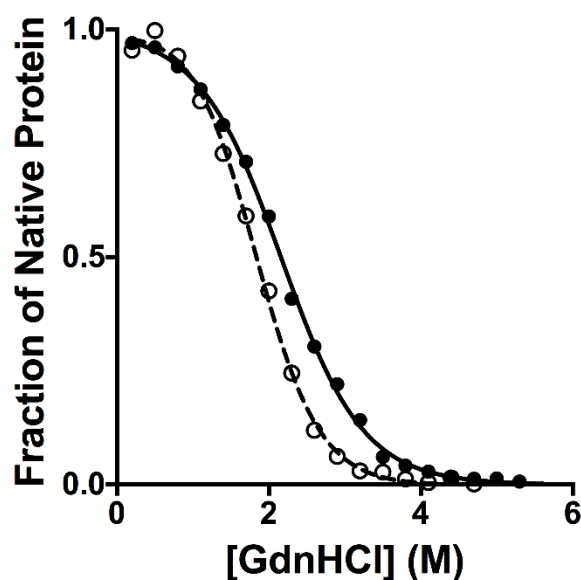
Figure 2. Equilibrium denaturations of wild type (full circles) and D76N variant (empty circles) performed in Hepes 50 mM pH 7.0 at 25 °C. The full line (for wild type) and the broken line (for D76N) are the best fit of an equation describing a two state unfolding mechanism. It is evident that the mutant displays a higher cooperativity compared to that of the wild type protein.

A powerful parameter to infer the mechanism of folding single domain proteins is the m_{D-N} value, defined as $\partial\Delta G/\partial[\text{denaturant}]$, which is the quantitative measurement of the cooperativity of the transition. In fact, the m_{D-N} value is correlated to the change in the accessible surface area to the solvent upon unfolding [17] and allows therefore detecting indirectly the overall structural transition occurring between the native and denatured states. The m_{D-N} values obtained for β2m wt and D76N were 1.08 ± 0.02 kcal mol^{-1} M^{-1} and 1.45 ± 0.04 kcal mol^{-1} M^{-1}, respectively, highlighting an effect of the mutation on the cooperativity of the unfolding reaction. Since it was previously established that β2m wt and D76N share a nearly identical native state [14], a decreased change in the accessible surface area upon denaturation can be ascribed to a more compact denatured state, highlighting the presence of a residual structure in the denatured state. Thus, on the basis of the comparison between the observed m_{D-N} values for β2m wt and D76N it may be concluded that the mutation leads to an expansion of the polypeptide chain in the denatured state.

Since the analysis of m_{D-N} values represents a signature of the residual structure in denatured states, by challenging the system at different experimental conditions, it is possible to monitor the structural malleability of the denatured state and therefore to characterize its shifts along the reaction coordinate. Thus, we resorted to perform equilibrium unfolding experiments at different experimental conditions, i.e., by varying the pH and ionic strength. The dependence of calculated m_{D-N} versus pH and the square root of the ionic strength at pH 7.0 for wt and D76N is reported in Figure 3 and the associated folding parameters are listed in Table 1.
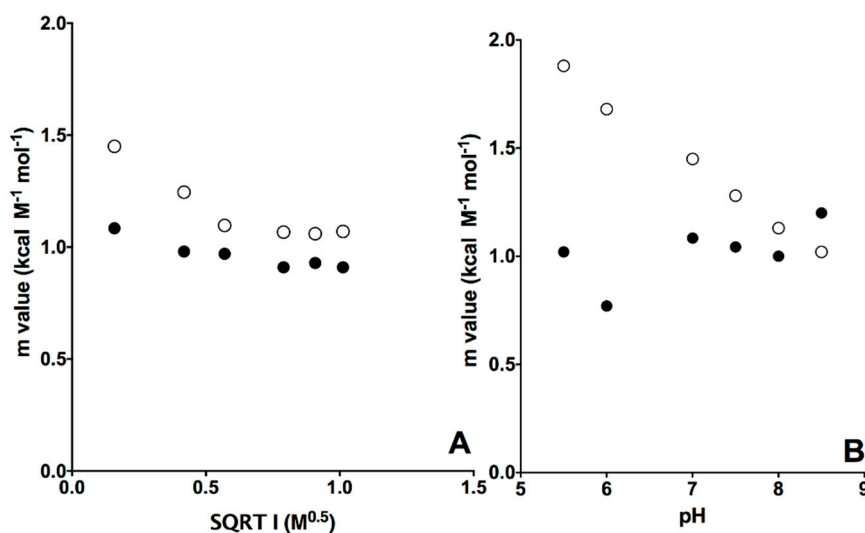
Figure 3. Dependence of m_{D-N} values calculated at different ionic strengths (panel **A**) and pH (panel **B**) for wt (full circles) and D76N variant (empty circles).

Table 1. Equilibrium folding parameters of wild type and D76N β2m.

|	β2m Wild Type		β2m D76N	
$IS^{1/2}$ ($M^{1/2}$)	[GdnHCl]$_{1/2}$ (M)	m_{value} (kcal M^{-1} mol^{-1})	[GdnHCl]$_{1/2}$ (M)	m_{value} (kcal M^{-1} mol^{-1})
0.16	2.12 ± 0.07	1.08 ± 0.03	1.82 ± 0.02	1.45 ± 0.04
0.42	2.07 ± 0.09	0.98 ± 0.03	2.13 ± 0.02	1.25 ± 0.03
0.57	2.02 ± 0.06	0.97 ± 0.05	1.95 ± 0.07	1.10 ± 0.03
0.79	2.12 ± 0.06	1.02 ± 0.02	1.79 ± 0.03	1.07 ± 0.03
0.91	2.21 ± 0.06	0.93 ± 0.01	2.03 ± 0.02	1.06 ± 0.04
1.01	1.61 ± 0.16	0.91 ± 0.06	1.42 ± 0.06	1.06 ± 0.06
	β2m Wild Type		β2m D76N	
pH	[GdnHCl]$_{1/2}$ (M)	m_{value} (kcal M^{-1} mol^{-1})	[GdnHCl]$_{1/2}$ (M)	m_{value} (kcal M^{-1} mol^{-1})
5.5	<1	1.02 ± 0.03	1.22 ± 0.02	1.88 ± 0.04
6	1.40 ± 0.16	0.77 ± 0.04	1.74 ± 0.02	1.74 ± 0.05
7	2.13 ± 0.07	1.08 ± 0.03	1.81 ± 0.02	1.45 ± 0.04
7.5	2.09 ± 0.08	1.04 ± 0.03	2.36 ± 0.02	1.28 ± 0.03
8	2.04 ± 0.09	1.00 ± 0.03	1.77 ± 0.05	1.12 ± 0.06
8.5	1.95 ± 0.04	1.23 ± 0.01	1.79 ± 0.03	1.02 ± 0.02

Inspection of the experimental data reveals that while the m_{D-N} value of wild type β2m is essentially insensitive to pH and ionic strength, for the D76N variant there is an evident decrease of the m_{D-N} value with increasing pH and ionic strength. Overall, these observations indicate the denatured state of wild type β2m to be characterized by a malleable residual structure. Such structure is perturbed in D76, but becomes more compact as the pH and ionic strength of the solution increase.

2.2. Aggregation Essays

In a recent comprehensive biophysical and structural work, it was proposed that the aggregation properties of D76N to be ascribed to the population of an aggregation-prone, highly dynamic, species, which is more compact and less aggregation prone in the wild type protein [18]. On the light on the equilibrium folding transitions described above, it is tentative to speculate that among these aggregation-prone species the denatured state of the protein may play a role, being more expanded for D76N than that of the wild type protein. A possible test to verify this hypothesis would be represented by the comparison of the aggregation propensity of D76N as a function of ionic strength and pH and the dependence of its associated unfolding m_{D-N} values.

To this aim, we performed aggregation experiments of D76N (40 μM) under continuous shaking at 37 °C under the same conditions of pH and of ionic strength, which are relevant in modifying the compactness of D76N unfolded state. The aggregation kinetics were monitored by thioflavin T showing that the aggregation lag time is increased as pH and ionic strength increase (Figure 4A,B, respectively, where the mean values of the three independent experiments subjected to nonlinear regression analysis, using Boltzmann sigmoidal equation, are reported). ThT fluorescence tends to be more intense in samples, which quickly aggregate suggesting a more abundant amyloid formation under certain conditions; however, fluorescence intensity strongly depends on experimental conditions and should be considered with care.
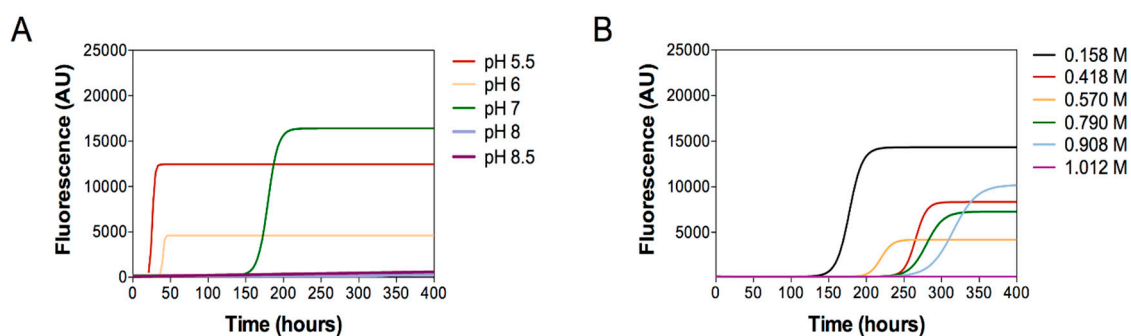
Figure 4. Aggregation experiments of D76N as function of pH (panel **A**) and of ionic strength (panel **B**). Aggregation was followed by monitoring thioflavin T (ThT) fluorescence. The mean values of the three independent experiments subjected to nonlinear regression analysis, using Boltzmann sigmoidal equation, are reported.

In summary these results clearly showed that D76N aggregation propensity is enhanced by low pH (Figure 4A) and by low ionic strength (Figure 4B). In contrast, high pH conditions or high salt concentrations delay or totally abrogate protein aggregation, even after 400 h of reaction.

3. Discussion

The denatured state of proteins has historically received considerably less consideration than the native state. In fact, the latter exerts all the biological functions and characterizing its structure is typically a key step in understanding them. Additionally, addressing denatured states is particularly difficult as they are elusive to the classical structural biology techniques and may be populated only under certain conditions.

In this context, it is important to distinguish between the unfolded state, the highly disordered conformation that may be populated in the presence of denaturant, and the denatured state, which retains a considerable amount of residual structure and represents a transient on-pathway species accumulating only at very low denaturant concentrations (or in the absence of it) [19–21]. Whilst the unfolded state often corresponds to an expanded random coil conformation, the residual structure of the denatured state is critical in sculpting the folding pathways of proteins, as well as in committing the protein to a specific topology [22–27].

The destabilization effects of the pathological D76N mutant of β2m represents a paradigmatic example on how the structural studies on the sole native state do not provide a full picture on protein stability, being the native state of both variants essentially identical [14,15]. From this angle, the experiments reported in this work are particularly informative as they point out a crucial role to the destabilizing effects in the denatured state induced by the D76N mutation. In fact, the experimental data suggest a scenario whereby the apparent ΔΔG observed in thermal denaturation experiments is most likely to arise from the expansion, and consequent increase in free energy, of the denatured state rather than changes in the native conformation.

Previous studies on the amyloidogenic properties of β2m have demonstrated that aggregation might occur only when the protein transiently escapes the thermodynamic well of its native state [9,10]. This finding would suggest that in the case of D76N, there should be a correlation between thermodynamic stability and aggregation propensity. A comparison between the equilibrium unfolding and aggregation data obtained at different pH and ionic strengths, however, shows a much more complex scenario. In fact, while the protein is mildly destabilized at high ionic strengths, it is evident that its thermodynamic stability is essentially insensitive to pH between 8.5 and 7. However, under such conditions D76N displays completely different kinetics of amyloid aggregation. Thus, we conclude that the strong correlation of the amyloidogenic propensity the thermodynamic stability underlies a strong contribution from the overall structure of the denatured state. Increasing amount of data from solid state NMR and Cryo-EM [28–31] show that proteins with an ordered native fold such as β2m and immunoglobulin light chains display a structural organization in fibrils, which is completely different from the native fold. This observation directly suggests that these proteins need to totally unfold during the aggregation pathway.

The experiments reported in this work indicate that the denatured state has a malleable structure that is perturbed from changes in experimental conditions. The overall compactness of such state correlates with the aggregation propensity of D76N. Overall, our work represents a direct demonstration on the key role of denatured states in dictating protein aggregation and reinforces the importance of their characterization.

4. Materials and Methods

4.1. Protein Expression and Purification

Recombinant wt and D76N β2m were expressed and purified as previously reported [12].

4.2. Equilibrium Experiments

Equilibrium unfolding experiments on wt and D76N β2m were performed at 25 °C using a Fluoromax single photon counting spectrofluorometer (Jobin-Yvon; Edison, NJ, USA) and a quartz cuvette with a path length of 1 cm. The native protein, at a constant concentration of 2 μM, was mixed with increasing concentrations of the denaturant agent guanidium chloride (GdnHCl), and the intrinsic tryptophan emission of the residues in position 60 and 95 was measured by excitation at 280 nm and record of emission spectra between 300 and 400 nm. Fluorescence equilibrium experiments at different pH were carried out using 50 mM sodium acetate pH 5.5, 50 mM BisTris pH 6.0 pH 6.5, 50 mM HEPES pH 7.0, 50 mM TrisHCl pH 7.5, pH 8.0, and pH 8.5 as buffers. In equilibrium denaturations at different ionic strength conditions, the buffer used was 50 mM HEPES pH 7.0 with different NaCl concentrations (0, 150 mM, 300 mM, 600 mM, 800 mM, and 1000 mM).

Data were fitted using the following equation,

$$Y_{obs} = (Y_N + Y_D) \frac{e^{m_{D-N}([GdnHCl]-[GdnHCl]_{1/2})}}{1 + e^{m_{D-N}([GdnHCl]-[GdnHCl]_{1/2})}}$$

4.3. Aggregation Assays

Aggregation assays of D76N β2m at different pH (5.5, 6, 7, 8, and 8.5) were performed in reaction mix containing D76N β2m (40 μM) and ThT (10 μM).

Aggregation assays of D76N β2m at different concentration of NaCl (0, 150 mM, 300 mM, 600 mM, 800 mM, and 1000 mM) were performed in 25 mM Na phosphate pH 7.4 containing D76N β2m (40 μM) and ThT (10 μM).

All reactions were performed in triplicate using black, clear-bottom, 96-well microplates. After sealing, the plate was incubated in a FLUOstar OPTIMA reader (BMG Labtech, Germany) at 37 °C, over a period of 400 h with continuous shaking (600 rpm, single orbital). The ThT fluorescence values are expressed in arbitrary units (AU) and were taken every hour using 450 ± 10 nm (excitation) and 480 ± 10 nm (emission) wavelengths, with a bottom read and a gain of 1000. The mean ThT fluorescence values per sample were plotted against time (hours).

The mean ThT fluorescence values of the three replicates per sample were plotted against time (hours) and the obtained curves were subjected to nonlinear regression analysis, using Boltzmann sigmoidal equation.

Author Contributions: S.G., S.R., and A.T. designed the research. L.V., F.M. (Francesca Malagrinò), L.B., C.M.G.D.L., F.M. (Fabio Moda) and A.T. performed the research. All the authors analyzed data. S.G. and S.R. wrote the first version of the manuscript. All authors revised the manuscript.

Conflicts of Interest: The authors declare no conflict of interest.

References

1. Knowles, T.P.; Vendruscolo, M.; Dobson, C.M. The amyloid state and its association with protein misfolding diseases. *Nat. Rev. Mol. Cell Biol.* **2014**, *15*, 384–396. [CrossRef] [PubMed]
2. Westermark, P.; Benson, M.D.; Buxbaum, J.N.; Cohen, A.S.; Frangione, B.; Ikeda, S.; Masters, C.L.; Merlini, G.; Saraiva, M.J.; Sipe, J.D. A primer of amyloid nomenclature. *Amyloid* **2007**, *14*, 179–183. [CrossRef] [PubMed]
3. Chiti, F.; Dobson, C.M. Protein misfolding, functional amyloid, and human disease. *Annu. Rev. Biochem.* **2006**, *75*, 333–366. [CrossRef] [PubMed]
4. Chiti, F.; Dobson, C.M. Protein Misfolding, Amyloid Formation, and Human Disease: A Summary of Progress Over the Last Decade. *Annu. Rev. Biochem.* **2017**, *86*, 27–68. [CrossRef] [PubMed]
5. Baldwin, A.J.; Knowles, T.P.; Tartaglia, G.G.; Fitzpatrick, A.W.; Devlin, G.L.; Shammas, S.L.; Waudby, C.A.; Mossuto, M.F.; Meehan, S.; Gras, S.L.; et al. Metastability of native proteins and the phenomenon of amyloid formation. *J. Am. Chem. Soc.* **2011**, *133*, 14160–14163. [CrossRef] [PubMed]
6. Stoppini, M.; Bellotti, V. Systemic amyloidosis: Lessons from beta2-microglobulin. *J. Biol. Chem.* **2015**, *290*, 9951–9958. [CrossRef] [PubMed]
7. Gejyo, F.; Yamada, T.; Odani, S.; Nakagawa, Y.; Arakawa, M.; Kunitomo, T.; Kataoka, H.; Suzuki, M.; Hirasawa, Y.; Shirahama, T.; et al. A new form of amyloid protein associated with chronic hemodialysis was identified as beta 2-microglobulin. *Biochem. Biophys. Res. Commun.* **1985**, *129*, 701–706. [CrossRef]
8. Gorevic, P.D.; Casey, T.T.; Stone, W.J.; DiRaimondo, C.R.; Prelli, F.C.; Frangione, B. Beta-2 microglobulin is an amyloidogenic protein in man. *J. Clin. Investig.* **1985**, *76*, 2425–2429. [CrossRef] [PubMed]
9. McParland, V.J.; Kad, N.M.; Kalverda, A.P.; Brown, A.; Kirwin-Jones, P.; Hunter, M.G.; Sunde, M.; Radford, S.E. Partially unfolded states of beta(2)-microglobulin and amyloid formation in vitro. *Biochemistry* **2000**, *39*, 8735–8746. [CrossRef] [PubMed]
10. Smith, D.P.; Jones, S.; Serpell, L.C.; Sunde, M.; Radford, S.E. A systematic investigation into the effect of protein destabilisation on beta 2-microglobulin amyloid formation. *J. Mol. Biol.* **2003**, *330*, 943–954. [CrossRef]

11. Ami, D.; Ricagno, S.; Bolognesi, M.; Bellotti, V.; Doglia, S.M.; Natalello, A. Structure, stability, and aggregation of beta-2 microglobulin mutants: Insights from a Fourier transform infrared study in solution and in the crystalline state. *Biophys. J.* **2012**, *102*, 1676–1684. [CrossRef] [PubMed]

12. Esposito, G.; Ricagno, S.; Corazza, A.; Rennella, E.; Gumral, D.; Mimmi, M.C.; Betto, E.; Pucillo, C.E.; Fogolari, F.; Viglino, P.; et al. The controlling roles of Trp60 and Trp95 in beta2-microglobulin function, folding and amyloid aggregation properties. *J. Mol. Biol.* **2008**, *378*, 887–897. [CrossRef] [PubMed]

13. Camilloni, C.; Sala, B.M.; Sormanni, P.; Porcari, R.; Corazza, A.; De Rosa, M.; Zanini, S.; Barbiroli, A.; Esposito, G.; Bolognesi, M.; et al. Rational design of mutations that change the aggregation rate of a protein while maintaining its native structure and stability. *Sci. Rep.* **2016**, *6*, 25559. [CrossRef] [PubMed]

14. Valleix, S.; Gillmore, J.D.; Bridoux, F.; Mangione, P.P.; Dogan, A.; Nedelec, B.; Boimard, M.; Touchard, G.; Goujon, J.M.; Lacombe, C.; et al. Hereditary systemic amyloidosis due to Asp76Asn variant beta2-microglobulin. *N. Engl. J. Med.* **2012**, *366*, 2276–2283. [CrossRef] [PubMed]

15. Halabelian, L.; Ricagno, S.; Giorgetti, S.; Santambrogio, C.; Barbiroli, A.; Pellegrino, S.; Achour, A.; Grandori, R.; Marchese, L.; Raimondi, S.; et al. Class I major histocompatibility complex, the trojan horse for secretion of amyloidogenic beta2-microglobulin. *J. Biol. Chem.* **2014**, *289*, 3318–3327. [CrossRef] [PubMed]

16. De Rosa, M.; Barbiroli, A.; Giorgetti, S.; Mangione, P.P.; Bolognesi, M.; Ricagno, S. Decoding the Structural Bases of D76N ss2-Microglobulin High Amyloidogenicity through Crystallography and Asn-Scan Mutagenesis. *PLoS ONE* **2015**, *10*, e0144061. [CrossRef] [PubMed]

17. Myers, J.K.; Pace, C.N.; Scholtz, J.M. Denaturant m values and heat capacity changes: Relation to changes in accessible surface areas of protein unfolding. *Protein Sci.* **1995**, *4*, 2138–2148. [CrossRef]

18. Le Marchand, T.; de Rosa, M.; Salvi, N.; Sala, B.M.; Andreas, L.B.; Barbet-Massin, E.; Sormanni, P.; Barbiroli, A.; Porcari, R.; Sousa Mota, C.; et al. Conformational dynamics in crystals reveal the molecular bases for D76N beta-2 microglobulin aggregation propensity. *Nat. Commun.* **2018**, *9*, 1658. [CrossRef]

19. Mittag, T.; Forman-Kay, J.D. Atomic-level characterization of disordered protein ensembles. *Curr. Opin. Struct. Biol.* **2007**, *17*, 3–14. [CrossRef]

20. McCarney, E.R.; Kohn, J.E.; Plaxco, K.W. Is there or isn't there? The case for (and against) residual structure in chemically denatured proteins. *Crit. Rev. Biochem. Mol. Biol.* **2005**, *40*, 181–189. [CrossRef]

21. Oliveberg, M.; Fersht, A.R. Thermodynamics of transient conformations in the folding pathway of barnase: Reorganization of the folding intermediate at low pH. *Biochemistry* **1996**, *35*, 2738–2749. [CrossRef] [PubMed]

22. Morrone, A.; McCully, M.E.; Bryan, P.N.; Brunori, M.; Daggett, V.; Gianni, S.; Travaglini-Allocatelli, C. The denatured state dictates the topology of two proteins with almost identical sequence but different native structure and function. *J. Biol. Chem.* **2011**, *286*, 3863–3872. [CrossRef] [PubMed]

23. Troilo, F.; Bonetti, D.; Toto, A.; Visconti, L.; Brunori, M.; Longhi, S.; Gianni, S. The Folding Pathway of the KIX Domain. *ACS Chem Biol* **2017**, *12*, 1683–1690. [CrossRef]

24. Giri, R.; Morrone, A.; Travaglini-Allocatelli, C.; Jemth, P.; Brunori, M.; Gianni, S. Folding pathways of proteins with increasing degree of sequence identities but different structure and function. *Proc. Natl. Acad. Sci. USA* **2012**, *109*, 17772–17776. [CrossRef] [PubMed]

25. Plaxco, K.W.; Gross, M. Unfolded, yes, but random? Never! *Nat. Struct. Biol.* **2001**, *8*, 659–660. [CrossRef] [PubMed]

26. Religa, T.L.; Markson, J.S.; Mayor, U.; Freund, S.M.; Fersht, A.R. Solution structure of a protein denatured state and folding intermediate. *Nature* **2005**, *437*, 1053–1056. [CrossRef] [PubMed]

27. Shortle, D.; Ackerman, M.S. Persistence of native-like topology in a denatured protein in 8 M urea. *Science* **2001**, *293*, 487–489. [CrossRef] [PubMed]

28. Iadanza, M.G.; Silvers, R.; Boardman, J.; Smith, H.I.; Karamanos, T.K.; Debelouchina, G.T.; Su, Y.; Griffin, R.G.; Ranson, N.A.; Radford, S.E. The structure of a beta2-microglobulin fibril suggests a molecular basis for its amyloid polymorphism. *Nat. Commun.* **2018**, *9*, 4517. [CrossRef]

29. Barbet-Massin, E.; Ricagno, S.; Lewandowski, J.R.; Giorgetti, S.; Bellotti, V.; Bolognesi, M.; Emsley, L.; Pintacuda, G. Fibrillar vs crystalline full-length beta-2-microglobulin studied by high-resolution solid-state NMR spectroscopy. *J. Am. Chem. Soc.* **2010**, *132*, 5556–5557. [CrossRef]

30. Liberta, F.; Loerch, S.; Rennegarbe, M.; Schierhorn, A.; Westermark, P.; Westermark, G.T.; Grigorieff, N.; Fandrich, M.; Schmidt, M. Cryo-EM structure of an amyloid fibril from systemic amyloidosis. *bioRxiv* **2018**. [CrossRef]

31. Swec, P.; Lavatelli, F.; Tasaki, M.; Paissoni, C.; Rognoni, P.; Maritan, M.; Brambilla, F.; Milani, P.; Mauri, P.; Camilloni, C.; et al. Cryo-EM structure of cardiac amyloid fibrils from an immunoglobulin light chain (AL) amyloidosis patient. *bioRxiv* **2018**. [CrossRef]

3.3.2 Biophysical and biochemical characterization of human and mouse β2m

The aggregation and amyloid formation of wt hβ2m in DRA patients is still poorly understood (53).

The main trigger of the fibril formation in DRA is the increase in concentration that occurs as a consequence of kidney dysfunction (53). Indeed, while the physiological concentration of wt hβ2m in plasma is 80 nM (34), in DRA patients it can increase by 50-60 fold, reaching 4.3 μM (114). This sustained high plasma concentration causes the deposition of wt hβ2m amyloid fibrils in joints, bones and muscles and is responsible for the development of DRA (110). However, the formation of wt hβ2m fibrils cannot exclusively be attributed to concentration effects but protein biophysical properties facilitate the formation of β-sheet rich structures (117,121,122).

In order to better understand which are the determinants of the hβ2m aggregation phenomenon, we compared from a biochemical and biophysical point of view wt hβ2m with the murine variant, wt mβ2m. mβ2m represents a conundrum: indeed, despite sharing 90% of sequence identity with wt hβ2m and having a physiological concentration 5-fold higher than the wt hβ2m concentration in DRA patients, wt mβ2m amyloids have never been observed in mice (123). Thus, in order to identify the molecular determinants that underlie wt hβ2m aggregation, we compared wt hβ2m and wt mβ2m for their aggregation propensity, ability to form soluble oligomers under native-like conditions, stability, three-dimensional structure and dynamics. In particular, we found that protein primary sequence combined with the absence of high-energy amyloid-competent conformation under native conditions plays a crucial role in protecting wt mβ2m from aggregating.

Biochemical and biophysical comparison of human and mouse beta-2 microglobulin reveals the molecular determinants of low amyloid propensity

Adnane Achour, <u>Luca Broggini</u>, Xiao Han, Renhua Sun, Carlo Santambrogio, Jeremie Buratto, Cristina Visentin, Alberto Barbiroli, Chiara Maria Giulia De Luca, Pietro Sormanni, Fabio Moda, Alfonso De Simone, Tatyana Sandalova, Rita Grandori, Carlo Camilloni and Stefano Ricagno.

I contributed to this work by producing the proteins (both hβ2m and mβ2m) required to run all the reported experiments.

Moreover, I set expression, purification and characterization of the D85V mβ2m mutant.

I assisted in performing the aggregation experiments of wt hβ2m, wt mβ2m and D85V mβ2m.

Finally, I performed thermal denaturing experiments by circular dichroism of wt hβ2m, wt mβ2m and D85V mβ2m.

Biochemical and biophysical comparison of human and mouse beta-2 microglobulin reveals the molecular determinants of low amyloid propensity

Adnane Achour[1,2], Luca Broggini[3], Xiao Han[1,2], Renhua Sun[1,2] (iD), Carlo Santambrogio[4], Jeremie Buratto[1,2], Cristina Visentin[3], Alberto Barbiroli[5], Chiara Maria Giulia De Luca[6], Pietro Sormanni[7], Fabio Moda[6], Alfonso De Simone[8], Tatyana Sandalova[1,2], Rita Grandori[4], Carlo Camilloni[3] and Stefano Ricagno[3] (iD)

1 Science for Life Laboratory, Department of Medicine Solna, Karolinska Institute, Solna, Sweden
2 Division of Infectious Diseases, Karolinska University Hospital, Solna, Sweden
3 Dipartimento di Bioscienze, Università degli Studi di Milano, Italy
4 Dipartimento di Biotecnologie e Bioscienze, Università Milano-Bicocca, Italy
5 Dipartimento di Scienze per gli Alimenti, la Nutrizione e l'Ambiente, Università degli Studi di Milano, Italy
6 Divisione di Neurologia 5 - Neuropatologia, Fondazione IRCCS Istituto Neurologico Carlo Besta, Milano, Italy
7 Department of Chemistry, University of Cambridge, UK
8 Department of Life Sciences, Imperial College London, UK

The molecular bases of amyloid aggregation propensity are still poorly understood, especially for proteins that display a stable folded native structure. A prototypic example is human beta-2 microglobulin (β2m), which, when accumulated in patients, gives rise to dialysis-related amyloidosis. Interestingly, although the physiologic concentration of β2m in mice is five times higher than that found in human patients, no amyloid deposits are observed in mice. Moreover, murine β2m (mβ2m) not only displays a lower amyloid propensity both *in vivo* and *in vitro* but also inhibits the aggregation of human β2m *in vitro*. Here, we compared human and mβ2m for their aggregation propensity, ability to form soluble oligomers, stability, three-dimensional structure and dynamics. Our results indicate that mβ2m low-aggregation propensity is due to two concomitant aspects: the low-aggregation propensity of its primary sequence combined with the absence of high-energy amyloid-competent conformations under native conditions. The identification of the specific properties determining the low-aggregation propensity of mouse β2m will help delineate the molecular risk factors which cause a folded protein to aggregate.

Abbreviations

AB, AlphaBeta collective variable; DRA, dialysis-related amyloidosis; hβ2m, human beta-2 microglobulin; M&M, metadynamics metainference; MHC-I, major histocompatibility complex class I; MS, mass spectrometry; mβ2m, murine beta-2 microglobulin; TFE, 2,2,2 trifluoroethanol; ThT, thioflavin T; wt, wild-type; β2m, beta-2 microglobulin.

Introduction

The 99-residue-long β2m protein is the invariable sub-unit, noncovalently bound to the heavy chain in major histocompatibility complex class I molecules (MHC-I). The globular β2m molecule displays a typical immunoglobulin-like fold with seven β-strands arranged in two β-sheets, ABDE and CFG, linked by a disulphide bond [1]. The overall stability of MHC-I/peptide complexes depends on the qualities and affinity of the bound antigen [2–5]. When β2m interacts with the MHC-I heavy chain, it is highly stabilized while the unbound β2m monomer may exert its amyloidogenic potential [6]. Indeed, it is well established that human β2m (h β2m) is an aggregation-prone protein responsible for at least two types of amyloid-related diseases. The aggregation of wild-type (wt) human beta-2 microglobulin (hβ2m) induces dialysis-related amyloidosis (DRA) [7]. Conversely, a severe hereditary systemic amyloidosis is linked to the D76N variant of hβ2m [8]. Physiologically, hβ2m is degraded in the kidneys. Thus, DRA patients typically suffer from kidney dysfunction with a consequent accumulation of hβ2m. Over the years, such pathologically high concentration results in aggregation and amyloid deposition in the skeletal joints, bones and muscles, leading to bone fragility and movement impairment [9]. Interestingly, while a hβ2m concentration up to 4.3 μM is typical for DRA patients [10], the physiologic concentration of murine β2m (mβ2m) is usually around 22 μM but no amyloid aggregation is observed in the mouse [11]. This indicates a much lower amyloidogenic potential for mβ2m compared to hβ2m. The picture is however more complex as Zhang *et al.* [12] showed that overexpressed hβ2m in mouse does not aggregate, suggesting that either some molecular elements necessary to aggregation are missing or that the mouse life span is not sufficient for hβ2m to successfully aggregate. *In vitro*, Pashley *et al.* [13] identified the increased solubility of mβ2m as the main reason for its lower aggregation propensity compared to hβ2m. Intriguingly, Radford and coworkers recently demonstrated that despite both hβ2m and its highly aggregation-prone truncated variant ΔN6-hβ2m can interact with mβ2m, mβ2m does not aggregate. Moreover, the murine protein is capable of inhibiting the aggregation of both hβ2m and ΔN6-hβ2m [14,15].

Altogether, a solid amount of previous work has demonstrated that hβ2m aggregation propensity stems from several specific properties, including the stability of the folded state [14,16,17] as well as the presence of several aggregation-prone residues on the surface of hβ2m [18,19]. Recent publications have also highlighted the crucial role of protein dynamics in determining hβ2m aggregation propensity by exposing aggregation-prone regions [18,20].

In order to shed further light into how mβ2m is protected from amyloid aggregation and can unexpectedly act as an inhibitor of hβ2m amyloid formation, a mixed structural, biophysical and computational approach was undertaken.

Results

mβ2m displays lower amyloid propensity compared to hβ2m

It has been previously demonstrated that mβ2m does not display the aggregation propensity typical of hβ2m [11,13]. We initiated the present study by testing two different well-established aggregation protocols to confirm these observations. Soluble hβ2m and mβ2m were incubated 100 h at 37 °C at pH 2.5 and at pH 7.4 in the presence of 20% v/v 2,2,2 trifluoroethanol (TFE). Incubations were performed both in the absence and presence of seeds prepared from preformed hβ2m fibrils [21]. Our results confirm that hβ2m aggregates abundantly under both these conditions, while mβ2m remains soluble and does not display any sign of aggregation (Fig. 1A,B). A sequence-based analysis of the solubility – and in turn aggregation propensity – of mβ2m or hβ2m using CamSol [22] revealed that the overall aggregation propensity is comparable along the two protein sequences except for the regions corresponding to amino acid residues 60–70 (E strand) and 80–90 (F, G strands). Our analysis indicated that these two regions are markedly more aggregation prone in hβ2m than in mβ2m (Fig. 1C).

Under native conditions mβ2m forms less oligomers compared to hβ2m

Native mass spectrometry (MS) was thereafter employed to assess the oligomerization propensity of hβ2m and mβ2m under nondenaturing conditions. As previously shown, hβ2m displays a pronounced tendency to oligomerize under native conditions [23], with a considerable protein fraction (~ 20%) in oligomeric states of variable stoichiometry (dimer and trimer; Fig. 2A). Under the same experimental conditions, mβ2m displays a significantly reduced propensity to form oligomers, with only a minor fraction of the population (~ 2%) detectable in the dimeric state and no higher order species (Fig. 2B). This reduced oligomerization tendency under native-like conditions could be related to the lower aggregation propensity of mβ2m
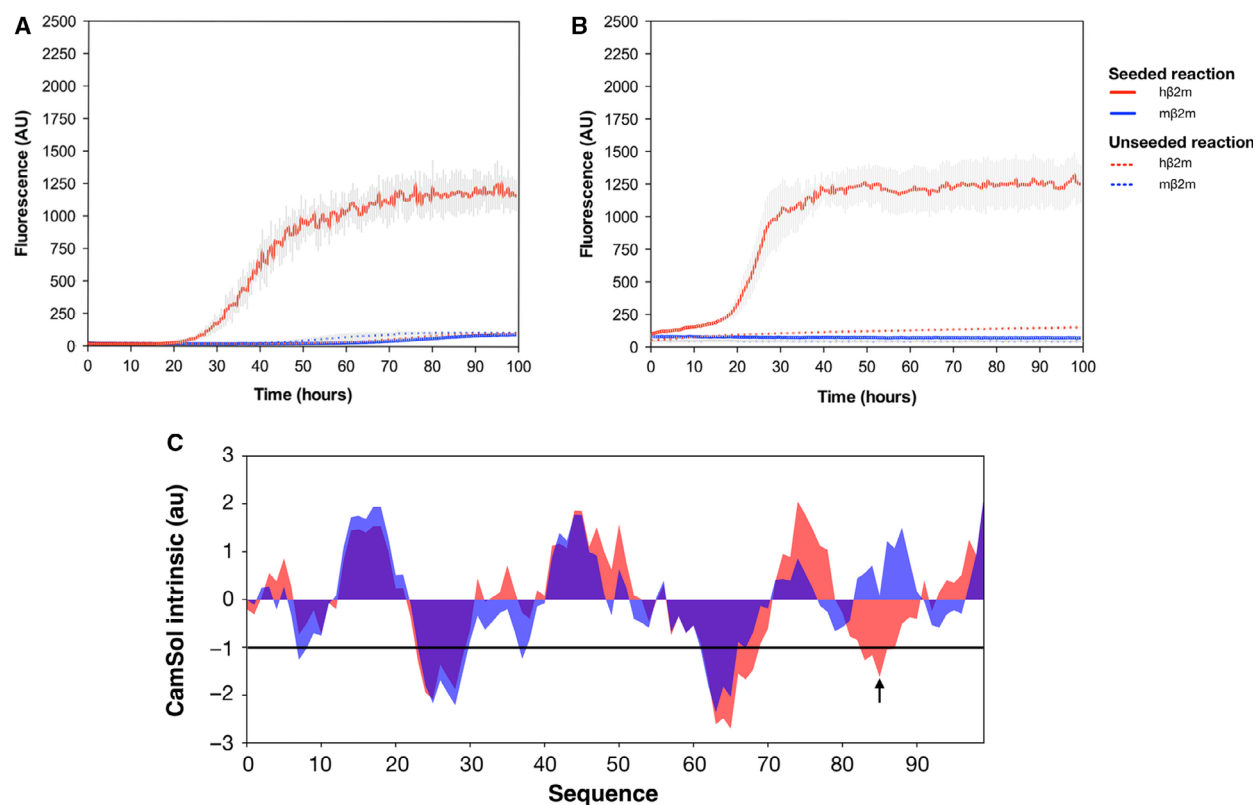
Fig. 1. (A, B) The kinetics of fibril formation were monitored by fluorescence using the ThT binding assay. Monomeric mβ2m (blue) and hβ2m (red) were incubated at 37 °C under two different aggregation conditions at pH 7.4 (A) and at pH 2.5 (B). (C) CamSol intrinsic solubility scores of hβ2m (red) and mβ2m (blue). A score greater than 1 indicates highly soluble sites while a score lower than −1 indicates aggregation-prone sites. The two profiles reveal that in contrast to mβ2m, the regions corresponding to residues 60–70 and 80–90 in hβ2m are prone to aggregation. The black arrow indicates the position of residue 85.

relative to hβ2m. The murine D85V variant (see below) presents an oligomeric pattern much more similar to hβ2m (Fig. 2D). Furthermore, the mβ2m monomer is characterized by a bimodal charge state distribution (Fig. 2B), suggesting the existence of a minor, at least partially unfolded component, which is not observed in hβ2m. These results indicate a lower conformational stability of the mβ2m variant. To rule out the effects of accidental variability in the experimental conditions, an equimolar mixture of the two β2m variants was analysed, confirming the presence of the peaks for the unfolded component only for mβ2m (Fig. 2C). Crucially the spectrum of the mixture also revealed that the oligomerization pattern of hβ2m is affected by the presence of mβ2m. β2m heterodimers are formed, but a significant decrease in the amount of hβ2m oligomers is also observed. The ability of mβ2m to interact with hβ2m and to reduce hβ2m oligomerization propensity could be related to the previously reported inhibitory effect of mβ2m on hβ2m aggregation [14,15].

The crystal structure of monomeric mβ2m reveals localized conformational changes compared to hβ2m

In order to better understand the molecular interactions occurring in the oligomers, the crystal structure of mβ2m was determined to 1.92 Å resolution, providing an electron density of excellent quality (Table 1). As expected, the three-dimensional structure of mβ2m takes a typical β-sandwich fold (Fig. 3A). Interestingly, comparison of the crystal structures of mβ2m and hβ2m reveals that mβ2m resembles more closely to hβ2m or mβ2m when bound to MHC-I [24,25], compared to soluble monomeric hβ2m [26] (Fig. 3A–C). In particular, the three-dimensional structure of the monomeric mβ2m reveals that the AlphaBeta collective variable (AB) loop, connecting the A and B strands, takes the same closed conformation as found in hβ2m when bound to MHC-I (Fig. 3B,C). Furthermore, the D-strand is bulged at residue 53 in both monomeric mβ2m and MHC-I-bound hβ2m compared
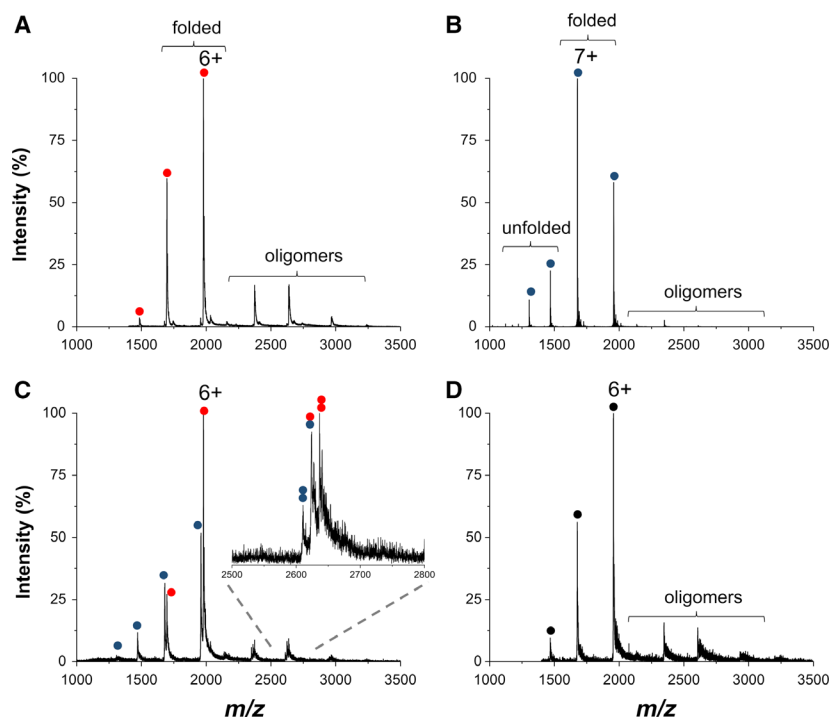
Fig. 2. (A) ESI-MS spectra of 75 μm hβ2m; (B) 75 μm mβ2m; (C) a mix of 75 μm hβ2m and 75 μm mβ2m; (D) 75 μm V85 mβ2m. The most intense peak in each panel is labelled by the corresponding charge state. In (A, B and D), the peaks corresponding to distinct species are grouped by braces. The inset of panel C is a magnification of the 9+ signals of the dimer. Red, blue and black circles correspond to the subunits of hβ2m, mβ2m and V85 mβ2m respectively.

to monomeric hβ2m (Fig. 3) [17,21,27,28]. This is reflected by the RMSD values of 0.87 Å over 99 Cα and of 1.13 Å over 90 Cα following the superposition of unbound mβ2m onto MHC-I-bound hβ2m or monomeric hβ2m respectively. Most importantly, several regions considered as highly relevant for hβ2m aggregation present analogous conformational arrangements in monomeric mβ2m. First, Pro32 is in *cis* conformation. This isomerisation from *cis* to *trans* is considered as a fundamental step towards the formation of the aggregation-prone intermediate [29]. Furthermore, the aromatic residues (Y10, Y26, F56, W60, F62, Y63), involved in Thioflavin T (ThT) binding [30] and crucial for hβ2m amyloid aggregation [19], display very similar structural conformations in both structures. Finally, a Ramachandran plot analysis of mβ2m reveals that the strained geometry of the DE loop is perfectly comparable to the one observed in monomeric hβ2m. This loop is directly involved in the destabilization of the hβ2m fold [23,31]. In summary, the monomeric structure of mβ2m does not display any major conformational changes in regions known to be relevant for amyloid formation compared to hβ2m.

mβ2m may form DD dimers

To date, several works have proposed that a head to head interaction named DD strand interface, formed

between hβ2m molecules, may be the first intermolecular interaction along the β2m aggregation pathway [15,30,32,33]. This DD interface involves several β2m regions, which are all relevant for aggregation including the D-strand as well as the BC and DE loops [32]. Using the crystal structures of monomeric mβ2m and hβ2m, hypothetical molecular models of murine and heterodimeric murine-human DD complexes were created and analysed (Fig. 3D–F). No steric clashes were observed in these molecular models, suggesting that both mβ2m and hβ2m are fully compatible with the formation of a DD interface. Indeed, mixed dimers were also formed (Fig. 2). Moreover, a PISA analysis indicated that the dimer formation between two hβ2m molecules seems to be more energetically favourable compared to the murine dimer (interface area and energy gain on complex formation corresponded 225 Å/−1.1 kcal·mol^{-1} and 171 Å/−0.2 kcal·mol^{-1} for dimeric hβ2m and mβ2m respectively). This result well correlates with the observation that, under native conditions, mβ2m forms significantly less dimers compared to hβ2m (Fig. 2).

mβ2m displays lower stability compared to hβ2m

Since β2m aggregation propensity correlates with thermodynamic stability of the native state [31], the fold stability of the two β2m orthologs was assessed by temperature ramps (temperature slope 50 °C·h^{-1})

Table 1. Data collection and refinement statistics for the structure of mβ2m.

PDB code	6I8C
Space group	$P2_12_12_1$
Cell *a, b, c* (Å)	36.24, 47.60, 64.94
Resolution (Å)	38.00–1.92 (1.95–1.92)
Number of unique reflections	8882 (572)
Completeness (%)	98.6 (96.8)
Redundancy	4.4 (4.3)
I/σ	20.1 (7.3)
R_{sym} (%)	4.4 (13.2)
Refinement statistics	
Resolution (Å)	28.85–1.92
R_{work} (%)	18.32
R_{free} (%)	22.20
Number of atoms	
All	934
Protein	842
Water	87
Ligand	5
Mean isotropic *B*-factor (Å^2)	
Protein main-chain atoms	20.46
Protein side-chain atoms	24.20
Water	32.10
Rmsd from ideal values	
Bond length (Å)	0.007
Bond angles (°)	1.152
Ramachandran plot statistics	
Residues in preferred regions (%)	98.97
Residues in allowed regions (%)	1.03
Outliers (%)	0

monitored by Far-UV CD. Thermal denaturation demonstrated that mβ2m unfolds at lower temperature compared to hβ2m (T_m values of 58.9 ± 0.8 °C and 63.6 ± 1.0 °C for mβ2m and hβ2m respectively; Fig. 4A). Unexpectedly, although significantly less amyloidogenic, mβ2m is also less stable than hβ2m.

The structural dynamics of the two protein variants were further investigated by analysis of the reduction kinetics of the internal disulphide bridge formed between the cysteine residues C25 and C80. This process is very slow under nondenaturing conditions for hβ2m, due to the buried structural environment of the disulphide bridge [23,34]. Monomeric hβ2m and mβ2m were mixed and incubated under native but strongly reducing conditions. Aliquots were collected at different time points and free thiols were alkylated by allyl bromide. The resulting samples were purified and analysed by denaturing MS (Fig. 4B). After 30 min, both variants remained completely oxidized. The presence of species with reduced/alkylated cysteine residues became evident only after 1 h of incubation, when mβ2m became highly reduced (~ 60%, estimated by the sum of single- and double-alkylated species), while

hβ2m remained prevalently in the oxidized form (~ 80%). After 3 h of incubation, ~ 90% and 70% of mβ2m and hβ2m were reduced respectively. Taken together, these results suggest a higher accessibility of the disulphide bridge within mβ2m compared to hβ2m under these conditions.

mβ2m ensemble does not show high-energy states and displays a lower aggregation propensity

In order to characterize the conformational properties of mβ2m and hβ2m, we first measured and assigned backbone chemical shifts for mβ2m as previously described (Fig. 3G) [35]. Experimental NMR data were already available in the literature for hβ2m [36]. We thereafter employed NMR chemical shifts as restraints in metadynamics metainference (M&M) simulations [37]. The resulting M&M simulations were carried out until convergence (Fig. 5) with a statistical error on the resulting conformational free energies of < 1 kJ·mol^{-1}. The resulting structural ensembles was then analysed as a function of the side-chain rotamer distribution (AB) and the antiparallel β-structure content (AntiBetaRMSD CV; anti-β; Fig. 6A). The resulting free energy surfaces (FESs) are then comparable with those formerly obtained for other β2m variants [18,20]. The FES for hβ2m and mβ2m display remarkable differences. hβ2m is characterized by a global minimum and by the presence of a high-energy low populated state. The global minimum (anti-β variable between 19 and 22, corresponding to a beta content between 38% and 44%) is structurally similar to the crystal structure (average RMSD of 1.5 Å), while the high-energy state (anti-β between 17 and 18 corresponding to a beta content between 34% and 36%) is slightly more disordered (average RMSD of 3 Å). The free energy for mβ2m displays a single minimum with slightly higher average beta content as well as larger fluctuations (anti-β between 19 and 25 corresponding to a beta content between 34% and 36%, and an average RMSD with respect to the crystal of mβ2m of 1.8 Å) compared to hβ2m. Intriguingly, the FES does not reveal the presence of any high-energy state (Fig. 6A). Notably, in a recent work, simulations and experiments indicate the presence of a high-energy state in both hβ2m and the D76N hβ2m variant characterized by loss of secondary structure [20].

The hβ2m and mβ2m conformational ensembles were subsequently used in combination with the program CamSol to generate a per-residue analysis of the aggregation propensity under native conditions (Fig. 6B). Remarkably, the most relevant difference in
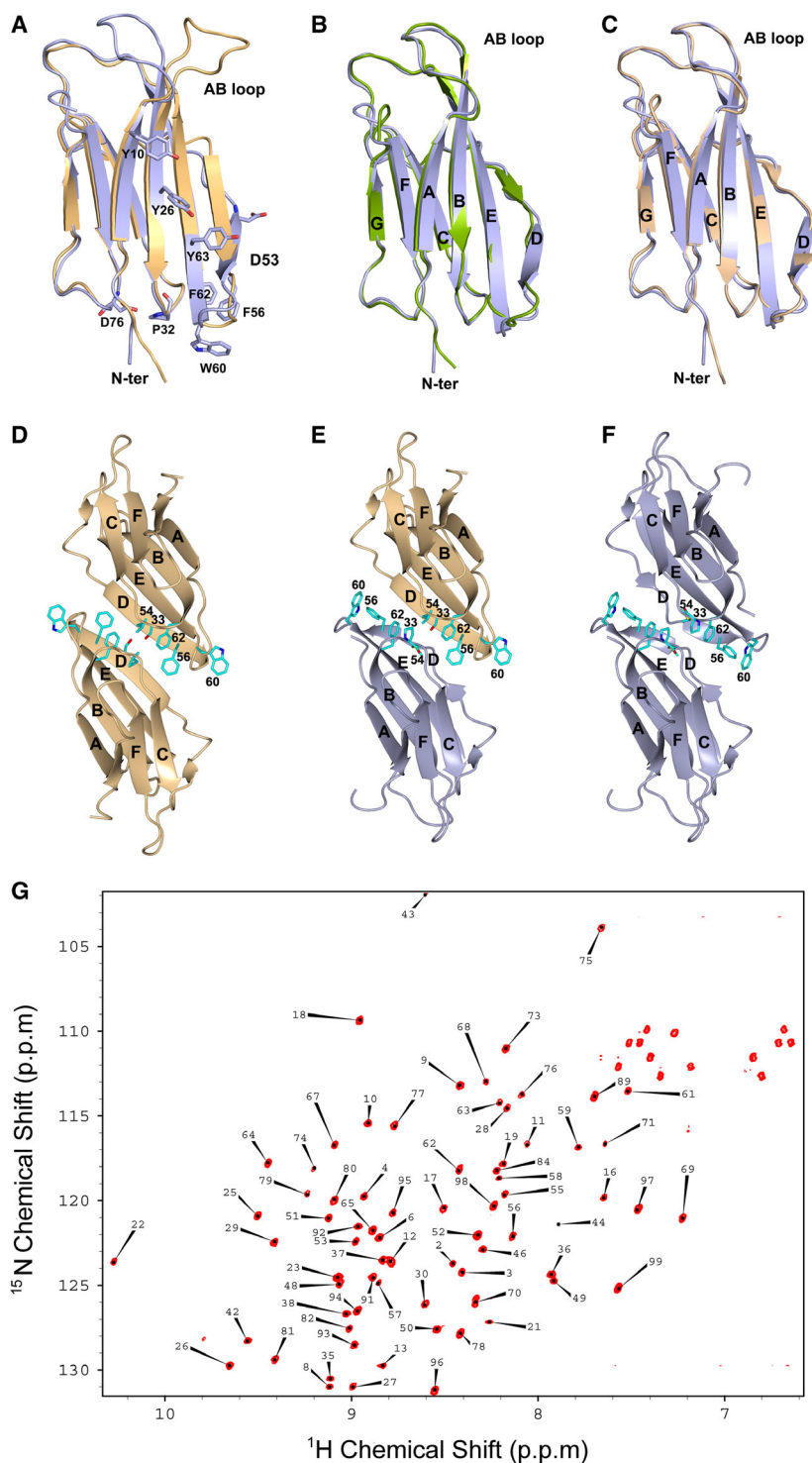
Fig. 3. (A–C) Comparisons of the crystal structures of the mβ2m in purple with (A) the structure of monomeric hβ2m in orange (pdb code: 1LDS); (B) the structure of mβ2m from an MHC I complex in green (pdb code: 1BII); (C) the structure of hβ2m from a complex with mouse MHC I, H-2Dd in beige (pdb code 2F74). (D–F) Models of DD dimers built using the structures of (D) two monomeric hβ2m; (E) one mβ2m and hβ2m; (F) two monomeric mβ2m. Main residues involved in the interface as reported in [32] are shown. These models suggest that mβ2m and hβ2m structures are compatible with the formation of homo and hetero DD dimers. (G) NMR HSQC spectrum of mβ2m at 25 °C, peaks are well resolved and 78 out of 100 can be uniquely assigned.

the obtained aggregation propensity profiles was observed for residue 85, a valine in hβ2m and an aspartic acid in mβ2m. Interestingly, this position has already been determined as crucial for hβ2m aggregation. Indeed, the rationally designed V85E hβ2m variant displays significantly less aggregation propensity compared to hβ2m with a comparable fold stability [18]. To better distinguish the role of structure and dynamics in determining the aggregation properties of β2m, we also compared the profiles averaged over the
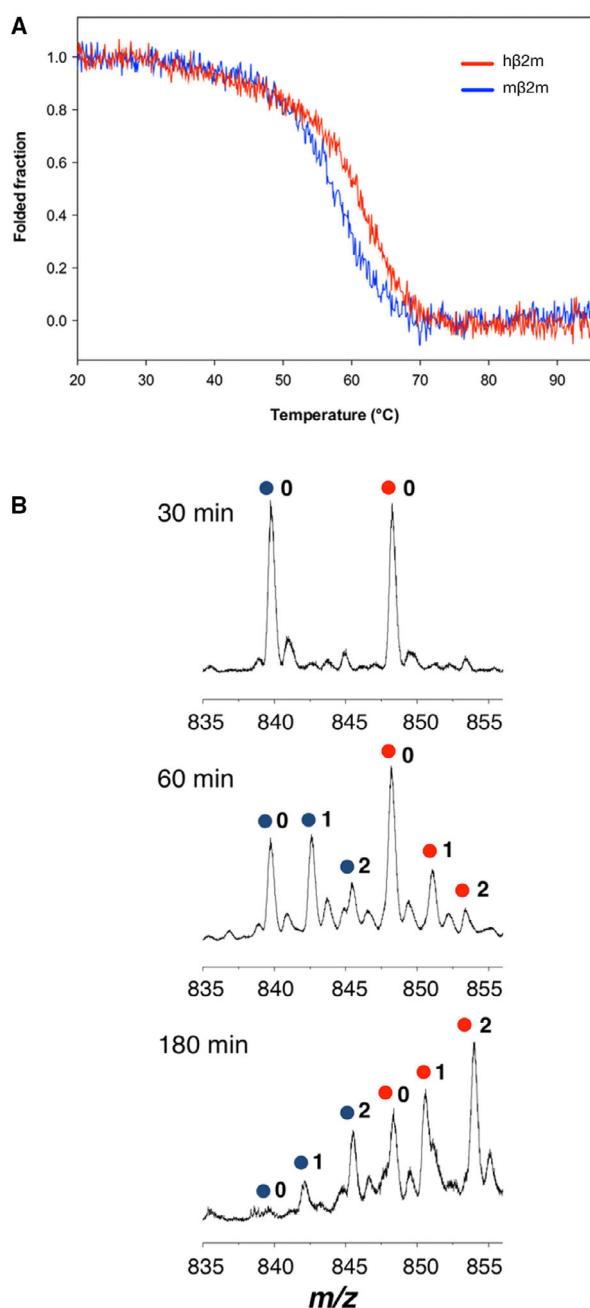
Fig. 4. (A) Thermal unfolding of 8.5 µm mβ2m and hβ2m in 50 mm sodium phosphate pH 7.4 monitored by far-UV CD at 202 nm. (B) Kinetics of disulphide bridge reduction. Magnification of the 14+ peaks of nano-ESI-MS spectra obtained from equimolar (25 µm) mixtures of hβ2m (red circle) and mβ2m (blue circle), incubated in 100 mm DTT for 30, 60 or 180 min, and alkylated by allyl bromide. Peaks are labelled according to the number of the incorporated propyl groups.

ensemble with those calculated from the crystal structures (Fig. 6B). Interestingly, in hβ2m the dynamics increase the surface aggregation propensity, while we

observe the opposite behaviour for mβ2m. In fact, the profile calculated over the ensemble for mβ2m displays much less aggregation-prone regions compared to the crystal structure.

Thus, the comparison of the M&M conformational ensembles indicates that while the aspartic acid D85 in mβ2m may be critical for its remarkably lower aggregation propensity, the relative dynamics of the two proteins also contribute to either increased (for hβ2m) or decreased (for mβ2m) overall aggregation propensity.

The presence of V85 increases the aggregation propensity of mβ2m *in vitro*

All previous studies on mβ2m aggregation propensity have focused on the D85 mβ2m variant (herein named mβ2m), but in contrast to hβ2m, several variants of mβ2m have been identified. Among these a valine residue at position 85 has been previously reported [38,39]. We therefore mutated the aspartate residue at position 85 to a valine and characterized the D85V mβ2m variant (V85 mβ2m) in order to verify the importance of this position in determining mβ2m aggregation propensity. The stability of V85 mβ2m was evaluated by monitoring its thermal denaturation by far-UV CD measurements. Our results revealed that the Tm value for V85 mβ2m is slightly higher compared to mβ2m (61.4 ± 0.8 °C and 58.9 ± 0.8 °C respectively; Fig. 7A). Thus, the aspartic acid to valine substitution at position 85 does not alter significantly the overall fold stability of the mutated variant compared to mβ2m. On the other hand, V85 mβ2m has a higher propensity to oligomerize relative to mβ2m, resulting in the formation of a dimeric population similar to the one detected for hβ2m (Fig. 2D). We then assessed the aggregation propensity of V85 mβ2m as described above. Our results demonstrate that, at pH 2.5, V85 mβ2m aggregates considerably compared to mβ2m in the presence of seeds of hβ2m (Fig. 7B). Furthermore, seeds of V85 mβ2m fibrils also successfully triggered hβ2m aggregation but not mβ2m aggregation. Finally, the fibrillar nature of V85 mβ2m aggregates was also verified using transmission electron microscopy (Fig. 7C). Altogether, our results demonstrate that the V85 mutation facilitates mβ2m aggregation, further supporting the key role of this position.

Discussion

Beta-2 microglobulin has been studied as a model for amyloid aggregation for decades [40]. This protein is of particular interest given that its fold is highly stable,
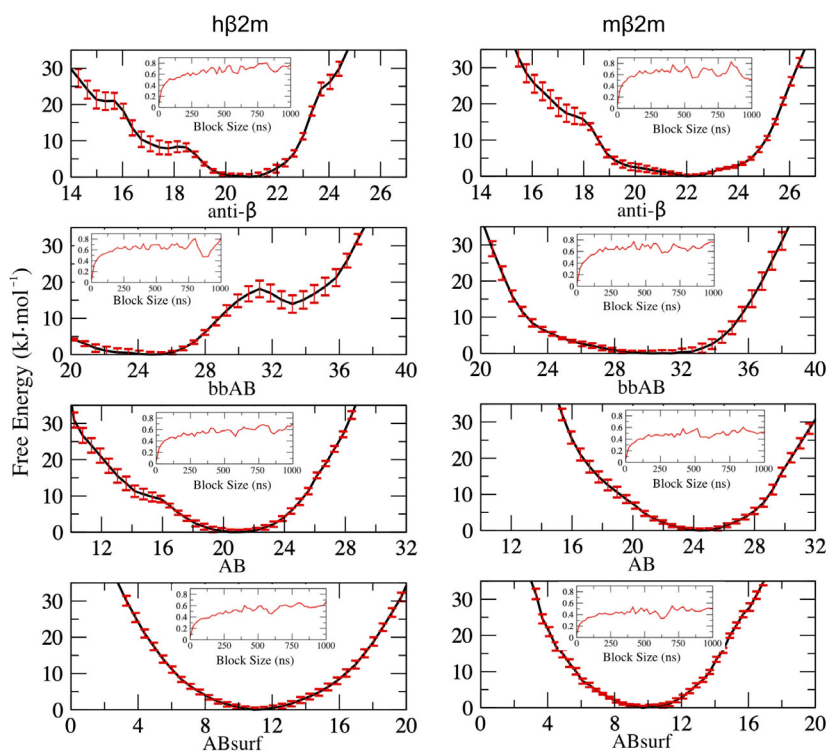
Fig. 5. Free energy profiles and error estimates (inset) in kJ·mol^{-1} for the hβ2m (left) and the mβ2m ensembles respectively. The free energy profiles are plotted as a function of the four biased collective variables (see Materials and methods). The corresponding error estimates are obtained by block analysis and plotted as a function of the block size, that is the extent in ns of the time window employed for the calculation (see Materials and methods).

which is a somehow counterintuitive property for an amyloidogenic protein. Indeed, only abnormally high hβ2m concentration over several years triggers aggregation leading to DRA. Interestingly mβ2m is not amyloidogenic *in vivo* or *in vitro* [11] and mixed oligomers of mβ2m with hβ2m seeds inhibit the aggregation capacity of hβ2m [11,15]. It is well established that mβ2m has a higher saturation concentration compared to hβ2m, resulting in a lower aggregation propensity [13]: However, the results presented within this study suggest in our opinion a more complex picture.

We have previously reported that hβ2m displays a marked tendency to form soluble oligomers under native conditions [23]. Conversely, we here demonstrate that mβ2m displays a very limited tendency to oligomerize, forming relatively small amounts of only dimers. Remarkably, hβ2m oligomerization is significantly inhibited in the presence of mβ2m, even though heterodimers are detectable in mβ2m–hβ2m mixtures. This suggests that the decreased oligomerization could be mediated by hβ2m–mβ2m protein–protein interactions. (Fig. 2). Moreover, based on the crystal structure of mβ2m, a hypothetical molecular model of a DD-mβ2m dimer was designed, indicating no major structural steric clashes upon dimer formation. Interestingly, the calculated energy gain upon dimer mβ2m formation was significantly reduced compared to hβ2m dimer models, suggesting a less optimized interface in

mβ2m dimers compared to hβ2m dimers. This observation may explain several previous results. Karamanos *et al.* [15] observed that although the hβ2m/hβ2m homodimer and the mβ2m/hβ2m heterodimer may have comparable interaction interfaces, the formation of the hβ2m/hβ2m homodimer is instrumental to amyloid formation while mβ2m/hβ2m heterodimerization results in an inhibitory complex, impairing amyloid formation. It is thus possible that mβ2m competes with the formation of hβ2m homodimers and either kinetically or thermodynamically impairs the formation of higher order oligomers. Thus altogether, our results suggest that suboptimal DD interface formed within mβ2m/mβ2m homodimers may protect mβ2m from inducing amyloid aggregation. Similarly, the DD interface formed in mβ2m/hβ2m heterodimers may also perturb the appropriate formation of hβ2m oligomers.

Our results demonstrate that specific segments of mβ2m sequence (residues: 60–70 and 80–90), and to a lesser extent the dynamics, play also crucial roles in determining its low aggregation propensity. Indeed, the analyses of the primary sequence and of the computed aggregation propensity of the conformational ensembles indicate that residue D85 plays a key role in the significant reduction of mβ2m aggregation propensity compared to hβ2m. Accordingly, the V85 mβ2m variant presents an oligomerization pattern similar to
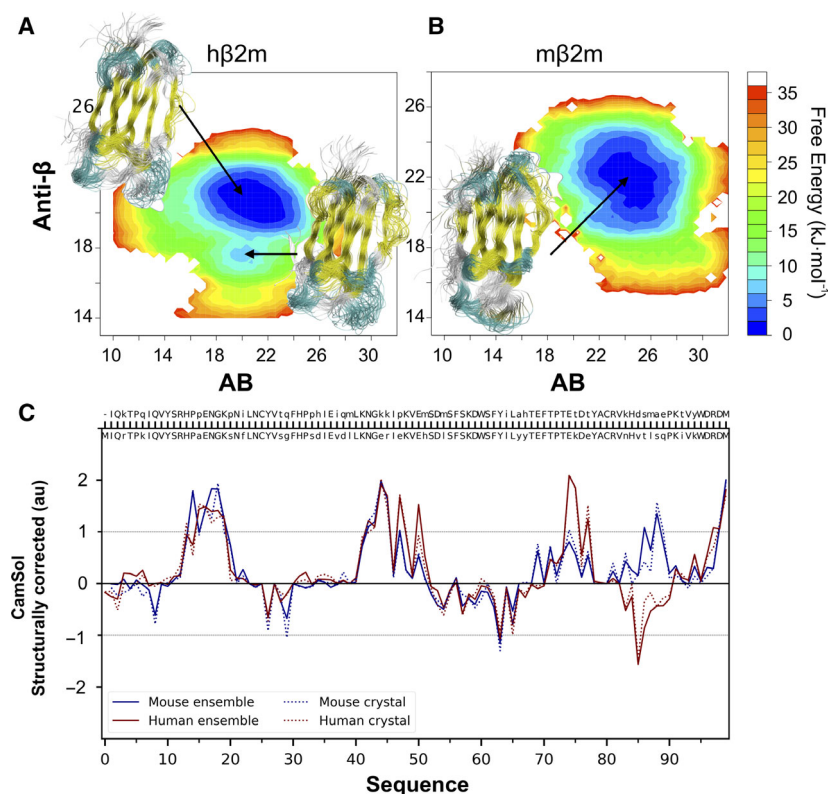
Fig. 6. (A, B) FESs for hβ2m and mβ2m respectively. The surfaces are shown as a function of the side-chain rotameric state, AB and the antiparallel β-structure content (anti-β). (C) CamSol structurally corrected solubility scores for the hβ2m (red solid) and mβ2m (blue solid) conformational ensembles as well as for the hβ2m and mβ2m crystal structures (red dotted and blue dotted, respectively). A score > 1 indicates a highly soluble site while a score lower than −1 indicates an aggregation-prone site.

human wild-type and displays an amyloidogenicity comparable to hβ2m under denaturing conditions, while mβ2m is mainly monomeric under nondenaturing conditions, and remains soluble under the same amyloidogenic conditions as previously reported [13]. This is well in line with data showing that residues 83 and 85 are crucial in determining hβ2m aggregation [18].

It thus remains to be determined if the V85 mβ2m variant would display the same amyloidogenicity as hβ2m *in vivo* or if the low oligomerization tendency observed for mβ2m is sufficient to hinder aggregation. Finally, high-energy, partially misfolded, states have been suggested to play a role in protein aggregation by providing aggregation-prone structures [29,41,42]. In a recent work on the D76N hβ2m mutant, we observed that the aggregation propensity of the high-energy state populated by D76N hβ2m is more pronounced with respect to that of the high-energy state formed by hβ2m and may explain the stronger aggregation propensity of the D76N variant [20]. Consequently, the lack of such a state for mβ2m is compatible with the different tendencies of hβ2m and mβ2m to oligomerize and for amyloid fibrils.

The results presented within this study shed additional light on the molecular bases underlying the different aggregation propensities of β2m in human and

mouse, and provide new possible mechanisms for mβ2m inhibition of hβ2m aggregation. The possibility of blocking pathologic protein misfolding by using a nonaggregative mβ2m variant may be a tantalizing and generalizable strategy to address amyloid aggregation.

Materials and methods

Preparation of the human β2m

The hβ2m was expressed and purified as previously reported in [43].

Preparation of the murine β2m

The mβ2m sequence encoding amino acids 1–99 was cloned in a pET-8c plasmid. D–V mutagenesis of mβ2m was performed using the QuikChange Lightning site-directed mutagenesis kit supplied by Agilent (Santa Clara, CA, USA) according to the manufacturer's instructions. The following primers were used: 5′-GCAGAGTTAAGCATGTCAG TATGGCCGAGCC-3′ and 5′-GGCTCGGCCATACTGA CATGCTTAACTCTGC-3′.

The expression vectors were transformed into BL21 (DE3)pLysS (Novagen, Madison, WI, USA). The protein production was IPTG induced and the product was
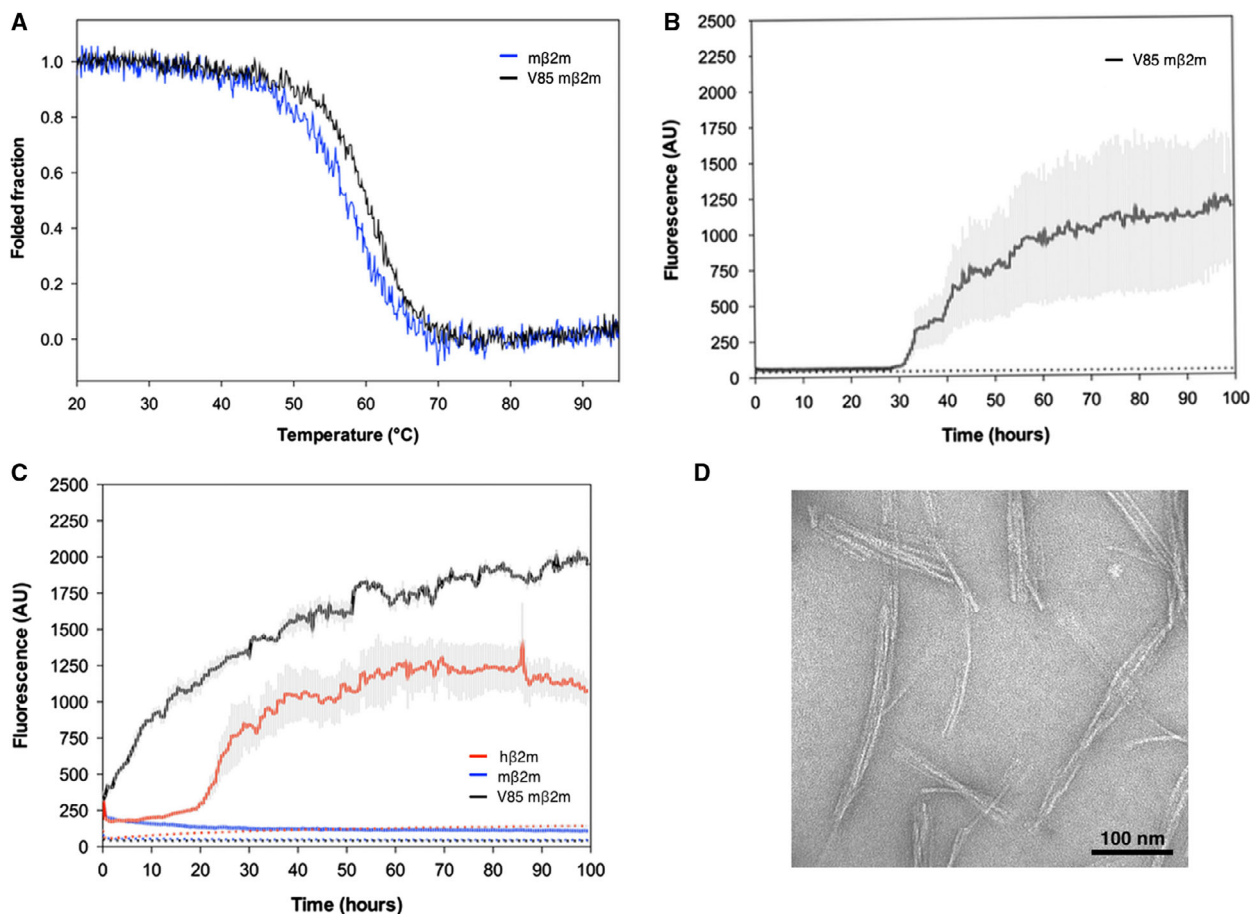
Fig. 7. (A) Thermal unfolding of 8.5 μm mβ2m and V85 mβ2m in 50 mm sodium phosphate pH 7.4 monitored by far-UV CD at 202 nm. (B, C) Kinetics of fibril formation monitored by fluorescence in the ThT binding assay. The V85 mβ2m was incubated at pH 2.5 in the presence of preformed hβ2m seeds (B); hβ2m, mβ2m and V85 mβ2m were incubated in the presence of preformed V85 mβ2m seeds at pH 2.5. Seeded and unseeded reactions are shown in solid and dashed lines respectively. (D) Transmission electron microscopy micrograph shows fibrillar aggregates of the V85 mβ2m variant.

purified as inclusion bodies as for hβ2m. The concentration of the final product was determined spectrophotometrically and purity of the product was assessed by SDS/PAGE under denaturing conditions. Refolding was performed by dialysis at 4 °C against 20 mm Tris HCl pH 7.5. After 24 h, the refolding mixture was concentrated using Amicon concentration devices. Refolded β2m was purified and buffer exchanged into 20 mm Tris HCl pH 7.0 by FPLC using Superdex 75 gel filtration (Pharmacia, Uppsala, Sweden).

Aggregation assays

Three independent aggregation tests for hβ2m, mβ2m and the V85 mβ2m variant were performed in triplicate using black, clear-bottom, 96-well microplates, the protein concentration of 100 μM was used in all experiments. Plates were incubated in a FLUOstar OPTIMA reader (BMG

LABTECH GmbH, Ortenberg, Germany) at 37 °C, over a period of 100 h with intermittent cycles of shaking (1 min, 300 r.p.m, double orbital) and rest (30 min). The ThT fluorescence intensity of the aggregates, expressed as arbitrary units, was taken every 30 min using 450 ± 10 nm (excitation) and 480 ± 10 nm (emission) wavelength, with a bottom read and a gain of 1000. All reaction mixes were freshly prepared and optimized for self-assembly or seeding experiments under two different conditions: 50 mm phosphate buffer and 100 mm NaCl, pH 7.4, in the presence of 20% v/v TFE [44]; 50 mm sodium citrate and 100 mm NaCl, pH 2.5 [45].

Transmission electron microscopy analysis

Morphological analysis of V85 mβ2m aggregates were carried out adsorbing 10 μL of sample onto carbon-coated 200-mesh grids and staining with UAR replacement

(negative staining), using a FEI Tecnai Spirit transmission electron microscope (120 kV) equipped with an Olimpus Soft imaging solutions Megaview camera (Olympus, Shinjuku, Tokyo, Japan). Images were taken at 18 500 × magnification.

Mass spectrometry

The ESI-MS spectra under nondenaturing conditions (50 mm ammonium acetate, pH 7) were acquired by direct injection on a Orbitrap Fusion instrument (ThermoFisher Scientific, Waltham, MA, USA). The main instrumental parameters were: ion-spray voltage, 3.1 kV; source dissociation, 55 V; ion transfer tube temperature, 225 °C; flow rate 2 µL·min^{-1}. Spectra were averaged over a 2-min acquisition.

Disulphide bridge reduction kinetics: mixtures of 25 µm hβ2m and 25 µm mβ2m were incubated at 37 °C in 50 mm ammonium carbonate, 100 mm DTT, pH 8, to reduce disulphide bridges. At different incubation times, 10-µL aliquots were taken and diluted in 90 µL of 20% cold trichloroacetic acid, vortexed and incubated 30 min at 4 °C. Then, the sample was centrifuged at 20000 *g*, 4 °C for 30 min and the resulting pellet washed with cold acetone. After lyophilization in a Speed Vac system (Analitica De Mori, Milan, IT, USA), the sample was resuspended in 20 µL of 50 mm ammonium carbonate, pH 8, 130 mm allyl bromide and incubated 1 h at room temperature for thiol alkylation. Finally, the sample was buffer exchanged by C18 ZipTips (Merck Millipore, Burlington, MA, USA), with elution by 50% acetonitrile, 1% formic acid followed by direct injection into the mass spectrometer. Each of the above experiments was repeated at least three times using different protein batches.

Crystallization and structure determination

Crystallization experiments were performed at 293 K using a hanging drop vapour diffusion method with 6 µL of mβ2m (4 mg·mL^{-1} in 20 mm Tris HCl, pH 7.5) mixed with 2 µL of the reservoir solution and equilibrated against 1 mL of the reservoir solution. The best crystals were obtained in 34% poly(ethylene glycol) 8000 w/v, 100 mm Tris HCl, pH 8.0 and in 40% poly(ethylene glycol) 6000 w/ v, 100 mm Tris HCl, pH 8.0. The crystal was cryoprotected by addition of 34% poly(ethylene glycol) 400 w/v. Data were collected at BL711 beam line, MAX Laboratory, Lund, Sweden the 6/9/1999 (= 1.018 Å) and were processed and scaled with DENZO and SCALEPACK [46]. The crystal diffracted up to 1.92 Å, it belongs to the space group P2$_1$2$_1$2$_1$ with unit cell dimensions of 36.24, 47.60, 64.94 Å. The data collection statistics are shown in Table 1.

The structure of mß2m was solved by molecular replacement using AMoRe [47], mβ2m from the murine MHC-I complex H-2Dd, (PDB code 1BII) was used as an initial

model. One subunits of mβ2m was found in the asymmetric unit, crystals display a 51% solvent content. Refinement was carried with X-PLOR [48] applying strict noncrystallographic symmetry. Last step of refinement was performed in Refmac5 [49]. Statistics for the final model are shown in Table 1.

NMR experiments

The NMR measurements were performed on ^{13}C-, ^{15}N-labelled mβ2m samples at a concentration of 200 µM. Assignment of the backbone resonances was performed by a combination of ^{1}H–^{15}N HSQC, CBCA(CO)NH, HNCACB, HNCO and HN(CA)CO spectra, collectively providing chemical shifts for ^{13}Cα, ^{13}Cβ, ^{1}HN, ^{13}CO and ^{15}N atoms [35].

NMR was performed at 25 °C using a Bruker AVANCE spectrometer operating at proton frequency of 700 MHz, equipped with a triple resonance cryoprobe. NMR data were processed using NMRPIPE [50] and analysed using SPARKY [51]. Data were processed using the MARS programme [52].

Ensembles determination

The simulations were carried out using GROMACS [53] and PLUMED [54] with the ISDB module [55]. The system was described using the Amber03W force field [56] in explicit TIP4P05 water [57] at 298 K. The starting conformations were taken from the 2YXF and the here reported X-ray structure for the hβ2m and mβ2m, respectively. The structures were protonated and solvated with ~ 8200 water molecules in a dodecahedron box of ~ 260 nm^3 of volume. The M&M protocol was applied using chemical shifts and a global outlier model for the noise as previously described [37,58]. Ten replicas of the system were simulated in parallel with a restraint applied on the weighted average value of the back-calculated NMR chemical shifts with a force constant determined on the fly by M&M [59].

All replicas were biased by Parallel Bias Metadynamics [60] along the following four CVs: the antiparallel beta content (the 'anti-β' CV), the AB CV defined over all the chi-1 angles for the hydrophobic side chains (the 'AB' CV), the AB CV defined over all the chi-1 angles for the surface exposed side chains (the 'ABsurf' CV), and the AB CV defined over all the phi and psi backbone dihedral angles of the protein (the 'bbAB' CV). Definition of the CVs are available in the PLUMED manual. Gaussians deposition was performed with σ values automatically determined by averaging the CV fluctuations over 2000 steps and setting a minimum value of 0.1, 0.12, 0.12 and 0.12, for anti-β, AB, ABsurf and bbAB respectively [61]; an initial energy deposition rate of 2.5 kJ·mol^{-1}·ps^{-1} and a bias-factor of 20. Furthermore, in order to limit the extent of accessible space

along each collective variable and correctly treat the problem of the borders, intervals were set to 12–30, 10–40, 0–33 and 10–42 for the four CVs respectively. Each replica has been run for a nominal time of 400 ns.

The sampling of the 10 replicas was combined using a simple reweighting scheme based on the final metadynamics bias B where the weight w of a conformation X is given by $w = \exp(+B(X)/k_BT)$, with k_B the Boltzmann constant and T the temperature, consistently with the quasi static behaviour at convergence of well-tempered metadynamics [61]. The convergence of the simulations by block analysis, including error estimates, is shown in Fig. 5. All the data and PLUMED input files required to reproduce the results reported in this paper are available on PLUMED-NEST (www.plumed-nest.org), the public repository of the PLUMED consortium as plumID:19.038 [62]. Of notice the free energy obtained for hβ2m resembles that previously determined by replica-averaged metadynamics simulations on a slightly different sequence [18,63]. The main differences being the lack of a more 'crystal'-like high-energy state and the presence of a slightly more disordered, high-energy, state. This latter was not sampled in a former work [18] because the sampling was not allowed in that region, but was more recently observed by solid-state NMR and replica-averaged metadynamics simulations [20].

CD

Thermal stability experiments were performed in triplicate using three independent batches of protein and were monitored in the far-UV region using a J-810 spectropolarimeter (JASCO Corp., Tokyo, Japan) equipped with a Peltier system for temperature control. The protein concentration was 0.1 mg·mL^{-1} in 50 mm sodium phosphate pH 7.4. The temperature ramps were carried out from 20 to 95 °C (temperature slope 50 °C·h^{-1}) in a 0.1-cm path length cuvette and monitored at 202 nm wavelength. Tm was calculated as the first-derivative minimum of the traces. Spectra before and after unfolding ramp were recorded (260–190 nm). All three β2m variants considered in this work display an irreversible unfolding under the tested conditions.

Accession number

Atomic coordinates and structure factors for mβ2m have been deposited at the Protein Data Bank, with accession code 6I8C.

Acknowledgements

Conflict of interest

The authors declare no conflict of interest.

Author contributions

AA, LB, XH, RS, CS, JB, CV, AB, CMGDL, PS, FM, ADS, TS and CC performed the experiments; AA, RG, CC and SR designed the study; AA, RG, CC and SR wrote the paper with contributions from all other authors.

References

1 Bjorkman PJ, Saper MA, Samraoui B, Bennett WS, Strominger JL & Wiley DC (1987) Structure of the human class I histocompatibility antigen, HLA-A2. *Nature* **329**, 506–512.

2 Hafstrand I, Doorduijn EM, Duru AD, Buratto J, Oliveira CC, Sandalova T, van Hall T & Achour A (2016) The MHC class I cancer-associated neoepitope Trh4 linked with impaired peptide processing induces a unique noncanonical TCR conformer. *J Immunol* **196**, 2327–2334.

3 Madhurantakam C, Duru AD, Sandalova T, Webb JR & Achour A (2012) Inflammation-associated nitrotyrosination affects TCR recognition through reduced stability and alteration of the molecular surface of the MHC complex. *PLoS ONE* **7**, e32805.

4 Uchtenhagen H, Abualrous ET, Stahl E, Allerbring EB, Sluijter M, Zacharias M, Sandalova T, van Hall T, Springer S, Nygren PA *et al.* (2013) Proline substitution independently enhances H-2D(b) complex stabilization and TCR recognition of melanoma-associated peptides. *Eur J Immunol* **43**, 3051–3060.

5 van Stipdonk MJ, Badia-Martinez D, Sluijter M, Offringa R, van Hall T & Achour A (2009) Design of agonistic altered peptides for the robust induction of CTL directed towards H-2Db in complex with the melanoma-associated epitope gp100. *Can Res* **69**, 7784–7792.

6 Halabelian L, Ricagno S, Giorgetti S, Santambrogio C, Barbiroli A, Pellegrino S, Achour A, Grandori R, Marchese L, Raimondi S *et al.* (2014) Class I major histocompatibility complex, the trojan horse for

secretion of amyloidogenic beta2-microglobulin. *J Biol Chem* **289**, 3318–3327.

7 Floege J & Ehlerding G (1996) Beta-2-microglobulin-associated amyloidosis. *Nephron* **72**, 9–26.

8 Valleix S, Gillmore JD, Bridoux F, Mangione PP, Dogan A, Nedelec B, Boimard M, Touchard G, Goujon JM, Lacombe C *et al*. (2012) Hereditary systemic amyloidosis due to Asp76Asn variant beta2-microglobulin. *N Engl J Med* **366**, 2276–2283.

9 Gejyo F, Yamada T, Odani S, Nakagawa Y, Arakawa M, Kunitomo T, Kataoka H, Suzuki M, Hirasawa Y, Shirahama T *et al*. (1985) A new form of amyloid protein associated with chronic hemodialysis was identified as beta 2-microglobulin. *Biochem Biophys Res Comm* **129**, 701–706.

10 Niwa T (1997) Beta2-Microglobulin dialysis amyloid and its formation: role of 3-deoxyglucosone and advanced glycation end products. *Nephron* **76**, 373–391.

11 Ivanova MI, Sawaya MR, Gingery M, Attinger A & Eisenberg D (2004) An amyloid-forming segment of beta2-microglobulin suggests a molecular model for the fibril. *Proc Natl Acad Sci USA* **101**, 10584–10589.

12 Zhang P, Fu X, Sawashita J, Yao J, Zhang B, Qian J, Tomozawa H, Mori M, Ando Y, Naiki H *et al*. (2010) Mouse model to study human A beta2M amyloidosis: generation of a transgenic mouse with excessive expression of human beta2-microglobulin. *Amyloid* **17**, 50–62.

13 Pashley CL, Hewitt EW & Radford SE (2016) Comparison of the aggregation of homologous beta2-microglobulin variants reveals protein solubility as a key determinant of amyloid formation. *J Mol Biol* **428**, 631–643.

14 Eichner T, Kalverda AP, Thompson GS, Homans SW & Radford SE (2011) Conformational conversion during amyloid formation at atomic resolution. *Mol Cell* **41**, 161–172.

15 Karamanos TK, Kalverda AP, Thompson GS & Radford SE (2014) Visualization of transient protein-protein interactions that promote or inhibit amyloid assembly. *Mol Cell* **55**, 214–226.

16 de Rosa M, Barbiroli A, Giorgetti S, Mangione PP, Bolognesi M & Ricagno S (2015) Decoding the structural bases of D76N ss2-microglobulin high amyloidogenicity through crystallography and Asn-scan mutagenesis. *PLoS ONE* **10**, e0144061.

17 Ricagno S, Raimondi S, Giorgetti S, Bellotti V & Bolognesi M (2009) Human beta-2 microglobulin W60V mutant structure: Implications for stability and amyloid aggregation. *Biochem Biophys Res Comm* **380**, 543–547.

18 Camilloni C, Sala BM, Sormanni P, Porcari R, Corazza A, De Rosa M, Zanini S, Barbiroli A, Esposito G, Bolognesi M *et al*. (2016) Rational design of mutations that change the aggregation rate of a protein while maintaining its native structure and stability. *Sci Rep* **6**, 25559.

19 Platt GW, Routledge KE, Homans SW & Radford SE (2008) Fibril growth kinetics reveal a region of beta2-microglobulin important for nucleation and elongation of aggregation. *J Mol Biol* **378**, 251–263.

20 Le Marchand T, de Rosa M, Salvi N, Sala BM, Andreas LB, Barbet-Massin E, Sormanni P, Barbiroli A, Porcari R, Sousa Mota C *et al*. (2018) Conformational dynamics in crystals reveal the molecular bases for D76N beta-2 microglobulin aggregation propensity. *Nat Commun* **9**, 1658.

21 Esposito G, Ricagno S, Corazza A, Rennella E, Gumral D, Mimmi MC, Betto E, Pucillo CE, Fogolari F, Viglino P *et al*. (2008) The controlling roles of Trp60 and Trp95 in beta2-microglobulin function, folding and amyloid aggregation properties. *J Mol Biol* **378**, 885–895.

22 Sormanni P, Aprile FA & Vendruscolo M (2015) The CamSol method of rational design of protein mutants with enhanced solubility. *J Mol Biol* **427**, 478–490.

23 Santambrogio C, Ricagno S, Colombo M, Barbiroli A, Bonomi F, Bellotti V, Bolognesi M & Grandori R (2010) DE-loop mutations affect beta2 microglobulin stability, oligomerization, and the low-pH unfolded form. *Protein Sci* **19**, 1386–1394.

24 Achour A, Harris RA, Persson K, Sundback J, Sentman CL, Schneider G, Lindqvist Y & Karre K (1999) Murine class I major histocompatibility complex H-2Dd: expression, refolding and crystallization. *Acta Crystallogr A* **55**, 260–262.

25 Achour A, Michaelsson J, Harris RA, Ljunggren HG, Karre K, Schneider G & Sandalova T (2006) Structural basis of the differential stability and receptor specificity of H-2Db in complex with murine versus human beta2-microglobulin. *J Mol Biol* **356**, 382–396.

26 Iwata K, Fujiwara T, Matsuki Y, Akutsu H, Takahashi S, Naiki H & Goto Y (2006) 3D structure of amyloid protofilaments of beta2-microglobulin fragment probed by solid-state NMR. *Proc Natl Acad Sci USA* **103**, 18119–18124.

27 Iwata K, Matsuura T, Sakurai K, Nakagawa A & Goto Y (2007) High-resolution crystal structure of beta2-microglobulin formed at pH 7.0. *J Biochem* **142**, 413–419.

28 Ricagno S, Colombo M, de Rosa M, Sangiovanni E, Giorgetti S, Raimondi S, Bellotti V & Bolognesi M (2008) DE loop mutations affect beta-2 microglobulin stability and amyloid aggregation. *Biochem Biophys Res Comm* **377**, 146–150.

29 Chiti F, De Lorenzi E, Grossi S, Mangione P, Giorgetti S, Caccialanza G, Dobson CM, Merlini G, Ramponi G & Bellotti V (2001) A partially structured species of beta 2-microglobulin is significantly populated under

physiological conditions and involved in fibrillogenesis. *J Biol Chem* **276**, 46714–46721.

30 Halabelian L, Relini A, Barbiroli A, Penco A, Bolognesi M & Ricagno S (2015) A covalent homodimer probing early oligomers along amyloid aggregation. *Sci Rep* **5**, 14651.

31 Ami D, Ricagno S, Bolognesi M, Bellotti V, Doglia SM & Natalello A (2012) Structure, stability, and aggregation of beta-2 microglobulin mutants: insights from a Fourier transform infrared study in solution and in the crystalline state. *Biophys J* **102**, 1676–1684.

32 Colombo M, de Rosa M, Bellotti V, Ricagno S & Bolognesi M (2012) A recurrent D-strand association interface is observed in beta-2 microglobulin oligomers. *FEBS J.* **279**, 1131–1143.

33 Rennella E, Cutuil T, Schanda P, Ayala I, Gabel F, Forge V, Corazza A, Esposito G & Brutscher B (2013) Oligomeric states along the folding pathways of beta2-microglobulin: kinetics, thermodynamics, and structure. *J Mol Biol* **425**, 2722–2736.

34 Hong DP, Gozu M, Hasegawa K, Naiki H & Goto Y (2002) Conformation of beta 2-microglobulin amyloid fibrils analyzed by reduction of the disulfide bond. *J Biol Chem* **277**, 21554–21560.

35 Patel JR, Xu Y, Capitini C, Chiti F & De Simone A (2018) Backbone NMR assignments of HypF-N under conditions generating toxic and non-toxic oligomers. *Biomol NMR Assign* **12**, 273–277.

36 Beerbaum M, Ballaschk M, Erdmann N, Schnick C, Diehl A, Uchanska-Ziegler B, Ziegler A & Schmieder P (2013) NMR spectroscopy reveals unexpected structural variation at the protein-protein interface in MHC class I molecules. *J Biomol NMR* **57**, 167–178.

37 Bonomi M, Camilloni C & Vendruscolo M (2016) Metadynamic metainference: Enhanced sampling of the metainference ensemble using metadynamics. *Sci Rep* **6**, 31232.

38 Gates FT 3rd, Coligan JE & Kindt TJ (1981) Complete amino acid sequence of murine beta 2-microglobulin: structural evidence for strain-related polymorphism. *Proc Natl Acad Sci USA* **78**, 554–558.

39 Hermel E, Robinson PJ, She JX & Lindahl KF (1993) Sequence divergence of B2m alleles of wild Mus musculus and Mus spretus implies positive selection. *Immunogenetics* **38**, 106–116.

40 Merlini G & Bellotti V (2003) Molecular mechanisms of amyloidosis. *N Engl J Med.* **349**, 583–596.

41 Chiti F, Mangione P, Andreola A, Giorgetti S, Stefani M, Dobson CM, Bellotti V & Taddei N (2001) Detection of two partially structured species in the folding process of the amyloidogenic protein beta 2-microglobulin. *J Mol Biol* **307**, 379–391.

42 Neudecker P, Robustelli P, Cavalli A, Walsh P, Lundstrom P, Zarrine-Afsar A, Sharpe S, Vendruscolo

M & Kay LE (2012) Structure of an intermediate state in protein folding and aggregation. *Science (New York, NY)* **336**, 362–366.

43 Esposito G, Michelutti R, Verdone G, Viglino P, Hernandez H, Robinson CV, Amoresano A, Dal Piaz F, Monti M, Pucci P *et al.* (2000) Removal of the N-terminal hexapeptide from human beta2-microglobulin facilitates protein aggregation and fibril formation. *Protein Sci* **9**, 831–845.

44 Yamamoto S, Yamaguchi I, Hasegawa K, Tsutsumi S, Goto Y, Gejyo F & Naiki H (2004) Glycosaminoglycans enhance the trifluoroethanol-induced extension of beta 2-microglobulin-related amyloid fibrils at a neutral pH. *J Am Soc Nephrol* **15**, 126–133.

45 Naiki H, Haschimoto N, Suzuki S, Rimura H, Nakakuki K & Gejyo F (1997) Establishment of a kinetic model of dialysis-related amyloid fibril extension *in vitro*. *Amyloid* **4**, 223–232.

46 Otwinowski Z (1993) Oscillation Data Reduction Program. Daresbury Laboratory, Warrington.

47 Navaza J (2001) Implementation of molecular replacement in AMoRe. *Acta Crystallogr A* **57**, 1367–1372.

48 Brunger AT, Adams PD, Clore GM, DeLano WL, Gros P, Grosse-Kunstleve RW, Jiang JS, Kuszewski J, Nilges M, Pannu NS *et al.* (1998) Crystallography & NMR system: A new software suite for macromolecular structure determination. *Acta Crystallogr A* **54**, 905–921.

49 Murshudov GN, Vagin AA & Dodson EJ (1997) Refinement of macromolecular structures by the maximum-likelihood method. *Acta Crystallogr A* **53**, 240–255.

50 Delaglio F, Grzesiek S, Vuister GW, Zhu G, Pfeifer J & Bax A (1995) NMRPipe: a multidimensional spectral processing system based on UNIX pipes. *J Biomol NMR* **6**, 277–293.

51 Lee W, Tonelli M & Markley JL (2015) NMRFAM-SPARKY: enhanced software for biomolecular NMR spectroscopy. *Bioinformatics* **31**, 1325–1327.

52 Jung YS & Zweckstetter M (2004) Mars – robust automatic backbone assignment of proteins. *J Biomol NMR* **30**, 11–23.

53 Abraham MJ, Murtola T, Schulz R, Pall S, Smith JC, Hess B & Lindhal E (2015) GROMACS: High performance molecular simulations through multi-level parallelism from laptops to supercomputers. *SoftwareX* **1–2**, 19–25.

54 Tribello GA, Bonomi F, Branduardi D, Camilloni C & Bussi G (2014) PLUMED 2: New feathers for an old bird. *Comput Phys Commun* **182**, 604–613.

55 Bonomi M & Camilloni C (2017) Integrative structural and dynamical biology with PLUMED-ISDB. *Bioinformatics* **33**, 3999–4000.

56 Best RB & Mittal J (2010) Protein simulations with an optimized water model: cooperative helix formation and temperature-induced unfolded state collapse. *J Phys Chem B* **114**, 14916–14923.

57 Abascal JL & Vega C (2005) A general purpose model for the condensed phases of water: TIP4P/2005. *J Chem Phys* **123**, 234505.

58 Bonomi M, Camilloni C, Cavalli A & Vendruscolo M (2016) Metainference: A Bayesian inference method for heterogeneous systems. *Sci Adv* **2**, e1501177.

59 Lohr T, Jussupow A & Camilloni C (2017) Metadynamic metainference: Convergence towards force field independent structural ensembles of a disordered peptide. *J Chem Phys* **146**, 165102.

60 Pfaendtner J & Bonomi M (2015) Efficient sampling of high-dimensional free-energy landscapes with parallel bias metadynamics. *J Chem Theory Comput* **11**, 5062–5067.

61 Branduardi D, Bussi G & Parrinello M (2012) Metadynamics with Adaptive Gaussians. *J Chem Theory Comput* **8**, 2247–2254.

62 The PLUMED consortium (2019) Promoting transparency and reproducibility in enhanced molecular simulations. *Nat Methods* **16**, 607–673.

63 Camilloni C & Vendruscolo M (2014) Statistical mechanics of the denatured state of a protein using replica-averaged metadynamics. *J Am Chem Soc* **136**, 8982–8991.

3.3.3 Hβ2M AMYLOIDS IN MULTIPLE MYELOMA

Multiple myeloma (MM) is a B-cell neoplasm characterized by the accumulation of malignant plasma cells in the bone marrow (124). The initiation as well as the progression of MM are linked to the dysregulation of inflammatory and immunological processes (125). In particular, tumor-associated macrophages (TAMs) play a crucial role by activating pro-inflammatory pathways (126). Indeed, in TAMs the activation of highly inflammatory interleukins (including IL-1β and IL-18) is regulated by cytosolic multiprotein complexes named inflammasomes, which in turn favors the progression of MM (127). Among the several complexes, the nod-like receptor family pyrin domain-containing 3 (NLRP3) has been highly studied due to its implication in several pathologies, including type 2 diabetes and Alzheimer's (128,129). Interestingly, one of the factors mediating the activation of the NLRP3 inflammasome is the formation of amyloid fibrils (130). In particular, the deposition of insoluble materials disrupts the lysosome leading to perturbation of cytosolic homeostasis (130).

hβ2m is used as biomarker for staging and prognosis of MM patients and increased levels of hβ2m usually correlates with poor prognosis (131). Nonetheless, while there is a clear correlation between hβ2m concentration and MM severity, it is to date unclear whether hβ2m has any role in MM development and progression (124).

In this study, we explored the role of hβ2m amyloids in the activation of the inflammasome. In particular, we demonstrated that macrophages can phagocytose hβ2m which is then delivered to the lysosome for degradation. However, the acidic conditions of the lysosome favour hβ2m aggregation leading to the disruption of the organelle and alteration of cytosolic homeostasis. To confirm our findings, we compared the behaviour of wt hβ2m and of W60G hβ2m, a non-natural mutant that presents reduced amyloidogenicity and increased stability (132,133) (Fig.5). Indeed, W60G hβ2m shows little aggregation under mild denaturing conditions (pH 7.4, 20% TFE), while abundant amyloid formation is observed exclusively under strong denaturing conditions (pH 2.5) (133,134). Thus, to in order to prove that wt hβ2m amyloids are involved in the activation of pro-inflammatory processes in macrophages, we compared the stability and the aggregation propensity under acidic condition of wt hβ2m and of W60G hβ2m.

β2-microglobulin - a trigger for NLRP3 inflammasome activation in tumor-associated macrophages promoting multiple myeloma cell progression

Daniel Hofbauer, Dimitrios Mougiakakos, Luca Broggini, Mario Zaiss, Maike Büttner-Herold, Frank Neumann, Savita Bisht, Jens Nolting, Robert Zeiser, Shaima'a Hamarsheh, Martin Eberhardt, Martin Böttcher, Katrin Bitterer, Simon Völkl, Andreas Mackensen, Stefano Ricagno and Heiko Bruns[*]

Muniscript submitted for publication.

I contributed to this work by producing the proteins required to run the experiments. In particular, I produced wt hβ2m and W60G β2m used for *in vitro* (fluorescence and aggregation assays) and *in vivo* studies.
I performed *in vitro* aggregation experiments in the lysosomal like conditions.
In parallel, I also carried out chemical unfolding experiments on wt hβ2m and W60G hβ2m.

1 **Title: β₂-microglobulin - a trigger for NLRP3 inflammasome activation in tumor-**

2 **associated macrophages promoting multiple myeloma cell progression**

3 Running title:

4

5 **Authors:** Daniel Hofbauer[1], Dimitrios Mougiakakos[1], Luca Broggini[2], Mario Zaiss[3], Maike

6 Büttner-Herold[4], Frank Neumann[5], Savita Bisht[6], Jens Nolting[6], Robert Zeiser[7], Shaima'a

7 Hamarsheh[7], Martin Eberhardt[8], Chiara Maria Giulia De Luca[9], Fabio Moda[9], Martin

8 Böttcher[1], Katrin Bitterer[1], Simon Völkl[1], Andreas Mackensen[1], Stefano Ricagno[2], and Heiko

9 Bruns[1*]

10

11 **Affiliations:** [1]Department of Internal Medicine 5, University Hospital Erlangen, Erlangen,

12 GER; [2]Department of Bioscience, University of Milan, Milan, ITA; [3]Department of

13 Nephropathology, University Hospital Erlangen, Erlangen, GER; [4]Department of Internal

14 Medicine 1, Saarland University Medical School, Homburg, GER; [5]Department of

15 Oncology/Hematology and Rheumatology, University Hospital Bonn, Bonn, GER;

16 [6]Department of Medicine 1, University of Freiburg, Freiburg, GER;; [7]Department of Internal

17 Medicine 3, University Hospital Erlangen, Erlangen, GER; [8]Department of Dermatology,

18 University Hospital Erlangen, Erlangen, GER; [9]Divisione di Neurologia 5 - Neuropatologia,

19 Fondazione IRCCS Istituto Neurologico Carlo Besta, Milano, Italy

20

21 *Address correspondence to Heiko Bruns, Department of Internal Medicine 5 -

22 Hematology/Oncology, FAU, Erlangen, Germany, Ulmenweg 18, D-91054 Erlangen. Phone:

23 +49 09131-85-43163, Fax: +49-9131-85-36521, E-Mail: heiko.bruns@uk-erlangen.de

24

27

1 **Abstract**

2 As significant constituents of the tumor microenvironment in multiple Myeloma (MM), pro-

3 inflammatory macrophages are key promoters of disease progression, bone destruction, and

4 immune-impairment. Consequently, the identification of endogenous mediators of these

5 inflammatory processes can open novel therapeutic avenues against major pathological

6 features of MM. Here, we identify beta-2-microglobulin (β2m) as an important driver in the

7 initiation of inflammation in myeloma-associated macrophages (MAMs). Lysosomal

8 accumulation of phagocytosed β2m in patient derived MAMs promoted β2m amyloid

9 aggregation, resulting in lysosomal rupture and ultimately in the production of active

10 interleukin (IL)-1b and IL-18. Interestingly, this process strictly depended on the activation of

11 the NALP3 inflammasome after β2m accumulation, as macrophages from NALP3-deficient

12 mice lacked efficient β2m-induced IL-1b production. Moreover, depletion or silencing of β2m

13 in MM cells abrogated inflammasome activation in a murine MM model. Finally, we

14 demonstrate that specific disruption of NLRP3 or IL-18 diminished tumor growth and

15 osteolytic bone destruction normally promoted by β2m-induced inflammasome signaling.

16 Taken together our results provide novel mechanistic evidence for β2m amyloid aggregates as

17 an NALP3 inflammasome activator during MM pathogenesis. Moreover, inhibition of

18 NALP3 highlights one potential novel therapeutic approach to combat this severe malignancy.

19

20

1 **Introduction**

2 Multiple myeloma (MM) is an incurable B-cell malignancy characterized by accumulation of

3 malignant plasma cells in the bone marrow (BM)[1], lytic bone lesions[2] and with a remarkable

4 ability to manipulate the bone marrow environment[3, 4]. It is widely accepted that dysregulated

5 inflammatory and immunological processes in the tumor microenvironment are not mere

6 bystanders but that invading leucocytes and tumor-associated macrophages (TAMs) are

7 central for the initiation and progression of MM[5, 6, 7, 8]. Studies have suggested that TAMs in

8 MM support proliferation[9] and drug resistance[10] of MM cells, and that high TAMs content

9 correlates with poor prognosis[11]. TAMs acquire a strongly pro-inflammatory transcriptional

10 profile in the myeloma microenvironment[9] and produce pro-inflammatory cytokines including

11 interleukin-6 (IL-6)[12], IL-1β[13] and tumor necrosis factor (TNF)[14], which in turn favors the

12 progression and severity of MM[13]. More recently, increased production of the inflammatory

13 cytokine IL-18 was identified as a key driver for MM progression[15]. Moreover, systemic

14 inhibition of inflammation[16, 17] or targeting of IL-1β prolongs the progression-free survival of

15 MM patients and delays disease onset[18], which indicates that pharmacological intervention in

16 inflammatory pathways, may potentially hold great therapeutic promise. Despite the central

17 function attributed to TAMs in promoting MM disease, the initiating pathways that ultimately

18 lead to the pro-inflammatory activation of macrophages remain completely unclear.

19 Because of its highly inflammatory nature, IL-1β and IL-18 production is tightly controlled by

20 cytosolic multiprotein complexes known as "inflammasomes". One of the most widely

21 studied inflammasome complexes is nod-like receptor family pyrin domain-containing 3

22 (NLRP3), which has been implicated in a wide range of diseases, including Alzheimer's

23 disease[19], gout[20], type 2 diabetes[21] and some infectious diseases[22, 23]. After being activated,

24 NLRP3 recruits the adaptor molecule ASC, which in turn binds to procaspase-1, leading to its

25 autocatalytic processing and activation. Active caspase-1 catalyzes cleavage of the pro-

26 cytokines IL-1β and IL-18, which are secreted and biologically active only in their processed

1   forms[24]. Signals and mechanisms leading to inflammasome activation are still poorly

2   understood. The NLRP3 inflammasome can be activated by microbial cell wall components

3   and toxins[25]. However, the inflammasome is also proficient in sensing stress or endogenous

4   danger signals, such as extracellular ATP[26], crystalline substances[27] or amyloid β fibrils[19].

5   The latter initiates NLRP3 activation by perturbation of cytoplasmic homeostasis due to

6   lysosomal destabilization[28]. This process, triggered by phagocytosed aggregated or insoluble

7   materials, is characterized by the cytosolic release of lysosomal contents (like cathepsins) and

8   reactive oxygen species (ROS), which results in assembly of the NLRP3 inflammasome and

9   activation of caspase-1. Despite the key role of inflammation in MM progression, little is

10   known about the relevance and initiating pathways of inflammasome activation in MM.

11   β2-microglobulin (β2m) is a non-glycosylated protein composed of 119 amino acid residues

12   with a secreted form of 99 amino acids and a molecular mass of 11,800 Dalton. β2m is

13   synthesized by all nucleated cells and forms complexes with the heavy chain of MHC class I

14   antigen through noncovalent linkage on cell surfaces[29,30]. While under physiological

15   conditions, β2m is generated at a constant rate, elevated β2m serum levels are observed in a

16   range of autoimmune, renal and hematological diseases. In particular wild type and the D76N

17   β2m variants are responsible of two amyloid related diseases indicating a clear amyloid

18   aggregation propensity for monomeric β2m in vivo[31,32]. In multiple myeloma, increased β2m

19   levels are correlated with a poor prognosis and the failure of MM patients to respond to

20   therapy[33]. Although the biological effects of β2m in MM remains enigmatic, earlier studies

21   have reported β2m uptake by myeloid cells and an induction of a pro-inflammatory immune

22   response (maybe a reference here?).

23   Here we found that the NLRP3 inflammasome is activated after phagocytosis of β2m and that

24   internalized β2m aggregates into amyloid fibrils under the acidic phagosomal conditions,

25   which results in lysosomal swelling and damage. We further demonstrated that the β2m-

26   triggered NLRP3 activation in TAMs results in the release IL-1β and IL-18 and, in turn favors

1   the growth and severity of MM. Our findings provide insight into the molecular processes

2   underlying the inflammatory conditions of MM and indicate that β2m represents a novel

3   inducer of sterile inflammation in macrophages.

4

5   **Results**

6   **β2m induces IL-1β and IL-18 release by macrophages in a caspase-1 and NLRP3-**

7   **dependent manner.** It remains unexplained how the inflammatory microenvironment in MM

8   is initiated. Given the fact that β2m concentration is increased during MM progression, as

9   well as the finding that ingested β2m triggers a pro-inflammatory immune response, we

10   hypothesized that β2m induces inflammasome activation in macrophages. Initially, we

11   investigated whether β2m treatment promotes release of IL-1β and IL-18 by human

12   macrophages. Given that pro-IL-1β is not constitutively expressed and requires transcriptional

13   induction, we primed cells with lipopolysaccharide (LPS), to ensure robust induction of pro-

14   IL-1β and to mimic the chronic activation of macrophages in inflammatory diseases. We

15   found that β2m induced a dose-dependent release of IL-1β and IL-18 in comparison to

16   controls (**Fig. 1A**), whereas protease digested β2m had no effect (IL-1β: $p=0.016$) (IL-18:

17   $p=0.0079$) (**Supplementary Fig. 1A**). In addition, IL-1β and IL-18 secretion was inhibited in

18   the presence of a β2m blocking antibody but not by control IgG (IL-1β: $p=0.016$) (IL-18:

19   $p=0.0079$) (**Supplementary Fig. 1A**), indicating that β2m is the active soluble factor

20   responsible for the release of IL-1β and IL-18.

21   To confirm the β2m-triggered inflammasome activation in macrophages, we performed

22   western blot analysis of cell lysates and supernatants (**Fig. 1B**). Firstly, we observed high

23   expression levels of NLRP3 and the concomitant adaptor oligomer ASC in cell lysates of β2m

24   - and nigericin-treated macrophages. In addition, we monitored low basal intracellular protein

25   levels of further inflammasome markers, such as pro-IL-1β (p31) and pro-caspase-1 (p45).

26   Detection of active caspase-1 (p20) in cell supernatants revealed that β2m induces specific

1   cleavage of caspase-1 to its functional subunits p10 and p20, which appeared to be partially

2   released. As expected, intracellularly processed cytokines IL-1β (p17) and IL-18 (p22) were

3   detected in cell supernatants of β2m - and nigericin-treated macrophages (**Fig. 1B**). To test

4   whether β2m actives caspase-1, we measured caspase-1 activation in β2m-treated

5   macrophages using FLICA® reagent, a cell-permeant fluorescent-labeled inhibitor specific

6   binding covalently to active caspase-1 (**Fig. 1C**). Confocal microscopy as well as flow

7   cytometry showed an increase in caspase-1-positive macrophages after treatment with β2m

8   (**Fig. 1C**, right). The significant β2m-triggered increase in caspase-1-positive macrophages

9   (89.8 ± 2.0 %, p = 0.00020) was similar to the positive control nigericin (77.3 ± 5.5 %, p =

10   0.00020) (**Fig. 1C**, middle**; Supplementary Fig. 1B**). In contrast, macrophages treated with

11   β2m$_{digest}$ (p = 0.0070) or β2m in the presence of a neutralizing antibody (α β2m) (p = 0.0070)

12   showed no activation (**Supplementary Fig. 1C**). To verify the observed impact of β2m on

13   caspase-1 activation, we treated macrophages with β2m in the presence of a caspase-1-

14   specific inhibitor z-YVAD-fmk and measured IL-1β levels in supernatants by ELISA. We

15   noted nearly complete inhibition of IL-1β release by macrophages (p = 0.0079) (**Fig. 1D**),

16   indicating that β2m-induced release of IL-1β is mediated by activated caspase-1. Next, we

17   investigated whether the inflammasome adaptor oligomer ASC might be present in

18   macrophages, since it is required for autocatalysis of pro-caspase-1 converting into active

19   caspase-1 (**Fig. 1E**). We therefore analyzed ASC oligomerization in β2m- and nigericin-

20   treated macrophages. Confocal microscopy revealed an increase in ASC oligomerization after

21   β2m treatment (82 ±3%, p=0.016) (**Fig. 1E** and **Fig. 1F**), similar to the NLRP3-dependent

22   control nigericin (84 ± 2%, p=0.016) (**Fig. 1E** and **Fig. 1F**). Finally, we examined whether

23   β2m specifically induces NLRP3 inflammasome activation. Therefore, we treated LPS-

24   primed bone marrow (BM) cells from wild-type (C57BL/6, WT) and NLRP3-deficient mice

25   (*Nlrp3-/-*, KO) with β2m as well as with NLRP3-dependent (ATP, nigericin) and NLRP3-

26   independent (poly(dA:dT) (poly(deoxyadenylic-thymidylic) acid)) stimuli (**Fig. 1G** and

1   **Supplementary Fig. 2**). Increasing the amount of β2m from 3 μg/ml up to 60 μg/ml, we

2   detected a dose-dependent IL-1β and IL-18 secretion by BM cells from wild-type mice up to

3   0.49 ± 0.17 ng/ml IL-1β (p=0.0031), as well as observed for NLRP3-independent control

4   poly(dA:dT) (0.25 ± 0.053 ng/ml, p=0.0519). In contrast, we found that IL-1β and IL-18

5   release by BM cells from NLRP3-deficient mice (*Nlrp3-/-*, KO) was nearly diminished after

6   β2m treatment, as well as observed for NLRP3-dependent controls (ATP, nigericin) (**Fig. 1G**

7   and **Supplementary Fig. 2**). To confirm that β2m specifically triggers NLRP3 inflammasome

8   activation, we treated macrophages with β2m in the presence of the NLRP3-specific inhibitor

9   MCC950[34]. Treating macrophages with nanomolar concentrations of MCC950 inhibited

10   significantly the β2m-triggered release of IL-1β (6.8-fold reduction) (p=0.0317) (**Fig. 1H**).

11   These data collectively indicate that β2m induces the release of IL-1β and IL-18 from

12   macrophages in a caspase-1 and NLRP3-dependent manner.

13

14   **Phagocytosis of β2m leads to formation of β-fibrils and subsequent lysosomal rupture.**

15   Next, we investigated the mechanism and pathway by which β2m induces NLRP3

16   inflammasome activation. Since the NLRP3 inflammasome in macrophages is known to be

17   activated by phagocytosis of crystals or peptides, we reasoned that phagocytosis is essential

18   for β2m-triggered IL-1β release. Initially, we analyzed whether β2m is internalized by

19   macrophages. Therefore, we treated macrophages with fluorescent-labeled β2m for three

20   hours in the presence or absence of the phagocytosis inhibitor cytochalasin D. Analysis by

21   confocal microscopy demonstrated that β2m is phagocytosed rapidly by macrophages (**Fig.**

22   **2A**, top), and that pretreatment of macrophages with cytochalasin D prevented β2m uptake

23   (**Fig. 2A**, bottom). Similar to monosodium urate crystals (MSU), β2m-triggered release of IL-

24   1β was also attenuated by cytochalasin D, (**Fig. 2B**), which indicated that phagocytosis is

25   required for the induction of IL-1β secretion by β2m. Cytochalasin D had no effect on the

26   release of IL-1β after stimulation with nigericin (**Supplementary Fig. 3A**). Human β2m is

1 known for its amyloid propensity *in vivo*[31, 32] and specifically it has been shown to form

2 amyloid-like fibrils under acidic conditions[35, 36] .Thus we hypothesize that after phagocytosis,

3 β2m may aggregate in lysosomes at low pH conditions (pH4 - pH5), forms cross-β-fibrils,

4 which lead to lysosomal rupture and the concomitant release of lysosomal factors into the

5 cytosol which finally activates the NLRP3 inflammasome. Firstly, we found that bafilomycin

6 a1, (an inhibitor of lysosomal acidification), prevents IL-1β release, suggesting that

7 phagolysosome acidification is necessary for β2m-mediated inflammasome activation

8 (**Supplementary Fig. 3B**). Secondly, we examined whether amyloids are present in

9 macrophages after β2m internalisation. Therefore, we analyzed fibril formation in β2m-

10 treated macrophages using AmyTracker™ reagent, a cell-permeant fluorescent marker

11 binding to fibrillar and proto-fibrillar amyloids[37]. Flow cytometry analysis of macrophages

12 revealed a significant increase in amyloid structures (37.5 ± 13.6 %, *p*=0.041) after treatment

13 with β2m (**Fig. 2C** and **Supplementary Fig. 3C**). Simultaneously, we determined caspase-1

14 activation in AmyTracker-positive macrophages (32.8 ± 9.9 %, *p*=0.065) indicating the

15 connection between β-fibril formation and inflammasome activation (**Supplementary Fig.**

16 **3D**). In order to further validate whether the formation of β2m amyloids is required for

17 inflammasome induction, we tested the effect of the mutational β2m variant β2m$_{W60G}$ (**Fig.**

18 **2D**) on lysosomal damage and inflammasome activation in macrophages. In contrast to WT,

19 β2m$_{W60G}$ is reported to have greater thermodynamic stability and an overall lower aggregation

20 propensity compared to the WT protein[38, 39, 40]. Specifically, *in vitro* experiments show that at

21 lysosomal pH between pH 4 and pH 5 β2m$_{W60G}$ displays markedly low aggregation

22 propensity and that its folded fraction is significantly higher than the one observed for WT

23 β2m (**Supplementary Fig. 4**). Initially, we investigated whether β2m and β2m$_{W60G}$ showed

24 differential formation of amyloid fibrils in lysosomes of macrophages. Therefore, we treated

25 macrophages with β2m or β2m$_{W60G}$ and analyzed these cells by electron microscopy.

26 Phagocytosed β2m led to a diffuse cellular distribution of fibrillar aggregates in the cytosol of

1   macrophages (**Fig. 2E,** left), while $\beta 2m_{W60G}$, was localized as globularly aggregates in

2   structurally intact lysosomes (**Fig. 2E**, right). To further explore whether lysosomal damage

3   occurs during the phagocytosis of β2m, we simultaneously monitored lysosomal integrity and

4   phagocytosis of labeled β2m and $\beta 2m_{W60G}$ by confocal microscopy. We identified punctuated

5   colocalization of fluorescent-labeled $\beta 2m_{W60G}$ with intact lysosomes by LysoTracker a

6   fluorescent dye, which selectively accumulates in acidic vesicular compartments,

7   predominantly in late endosomes and lysosomes (**Fig. 2F**, right). In contrast to the mutant

8   form, WT β2m-containing lysosomes were partially swollen and the lysomotropic dye was

9   also detected in cytoplasm, suggesting a destabilization of lysosomal integrity (**Fig. 2F**, left).

10 We confirmed this with a LysoSensor flow cytometry-based assay in which we quantified

11 lysosomal destabilization by the increase in LysoSensor-negative cells. Consistent with the

12 findings obtained by confocal microscopy β2m-treatment resulted in a significant loss of

13 fluorescence, whereas treatment with $\beta 2m_{W60G}$ had no effect on LysoSensor accumulation in

14 macrophages (**Fig. 2G** and **Supplementary Fig. 5A**). Accordingly, the reduced lysosomal

15 destabilization by $\beta 2m_{W60G}$ was reflected by a significant reduction in IL-1β (**Fig. 2H**) and IL-

16 18 release (*p*=0.041) (**Supplementary Fig. 5B**) in comparison to WT β2m. We reasoned that

17 the lysosomal destabilization results in the release of lysosomal factors, such as proteolytic

18 enzymes or reactive oxygen species (ROS), which are in turn activate the NLRP3

19 inflammasome[41, 42, 43]. Therefore, we treated macrophages with β2m or $\beta 2m_{W60G}$ and

20 measured intracellular cathepsin-B activity with the fluorescent substrate Magic Red-(RR)2,

21 which selectively binds to proteolytically cleaved active cathepsin B. Cathepsin B is assumed

22 to directly induce NLRP3 inflammasome activation as well as to mediate mitochondrial

23 dysfunction leading to mtROS-triggered NLRP3 inflammasome activation. In contrast to the

24 control $\beta 2m_{W60G}$, β2m treatment resulted in a diffused cellular staining pattern, which

25 demonstrates release of active cathepsin B into the cytosol (**Supplementary Fig. 6A**).

26 Pretreatment of macrophages with the cathepsin B-specific inhibitor CA-074 Me resulted in a

1   significant inhibition of IL-1β release (**Fig. 2I**) (p = 0.0317), whereas the inhibitor had no

2   effect on nigericin mediated IL-1β release (**Supplementary Fig. 6B**). In addition, we detected

3   increased level of ROS in macrophages after treatment with β2m, which could be abrogated

4   by the ROS scavenger N-acetylcysteine (NAC) (**Supplementary Fig. 6C**). However, we

5   found no significant effect on the release of IL-1β (**Supplementary Fig. 6D**). Collectively,

6   these data indicate that it is not β2m internalisation in lysosomes of macrophages but its

7   aggregation into amyloid fibrils which specifically causes lysosomal rupture and the

8   concomitant release of lysosomal factors, such as proteolytic enzyme cathepsin B, into the

9   cytosol resulting in inflammasome activation.

10

11   **β2m -mediates NLRP3 inflammasome activation in TAMs of MM patients.**

12   Based on our observation that β2m can activate the NLRP3 inflammasome in macrophages,

13   we hypothesized that MM patients with elevated β2m levels also display elevated

14   inflammasome activation. To test this hypothesis we initially correlated β2m bone marrow

15   plasma levels of MM patients with levels of IL-1β and IL-18 (n = 31). By separating IL-1β

16   and IL-18 levels into low (≤ 2.7 µg/ml), intermediate (2.8 - 9.7 µg/ml) and high (≥ 9.8 µg/ml)

17   β2m groups, we found that higher β2m concentrations resulted in significantly increased IL-

18   1β (low: 0.2 ±0.03 pg/ml vs. high: 5.3 ±1.3 pg/ml, p = 0.036) and IL-18 production (low:

19   0.29 ± 0.03 ng/ml vs. high: 1.3 ± 0.37 ng/ml, p = 0.00070) in the bone marrow plasma of MM

20   patients (**Fig. 3A** and **Supplemental Figure 7**). Since macrophages are the primary sources

21   for the release of active IL-1β and IL-18, we investigated whether these cytokines and further

22   inflammasome markers are present in TAMs of MM patients. Firstly, RNA analysis of

23   isolated TAMs of untreated MM patients showed an increased transcription of inflammasome

24   markers (AIM2, CASP1, IL1B, IL18, and NLRP3) in comparison to bone marrow

25   macrophages of healthy controls (**Fig. 3B**). Secondly, staining bone marrow samples of

26   untreated MM patients for IL-1β or caspase-1 (p20) and the macrophage marker CD68,

1   revealed an enhanced activation of caspase-1 (**Fig. 3C**, left) and high expression levels of IL-

2   1β in TAMs (**Fig. 3C**, right). Next, we compared the expression of inflammasome markers in

3   TAMs of MM patients with bone macrophages of healthy donors by flow cytometry (**Fig.**

4   **3D**). We found that, in comparison to healthy controls, TAMs displayed a significant

5   increased expression of NLRP3 (2.7-fold, $p = 0.0027$), IL-1β (1.6-fold, $p = 0.029$), IL-18 (2.6-

6   fold, $p = 0.0078$) and an enhanced caspase-1 activation (2.7-fold, $p = 0.069$). These results

7   collectively suggest TAMs of MM patients display an active inflammasome. In order to

8   analyze whether amyloid fibrils are present in TAMs of MM patients, we stained TAMs with

9   AmyTracker™ to visualize amyloid proteins and FLICA to detect simultaneously active

10   caspase-1. Analysis by flow cytometry demonstrated that amyloidogenic proteins were

11   present in TAMs of MM patients, but not in bone marrow macrophages from healthy controls

12   (MM: 28.6 ± 17.8 %, vs. HD: 3.0 ± 0.5 %) (**Fig. 3E and Supplementary Fig. 8A**).

13   Furthermore, a significant proportion of amyloid-positive TAMs displayed also an active

14   caspase-1 (39.7 ± 15.6 %), suggesting a link between the presence of amyloid proteins and

15   inflammasome activation (**Fig. 3E**; **Supplementary Fig. 8B**). To verify whether TAMs

16   contain increased amounts of amyloid fibrils, we performed dot blot analysis by using

17   conformation specific antibodies against cross-β fibrils (LOC antibody) or against soluble

18   β2m (**Supplementary Fig. 8C**). We detected high amyloid levels in cell lysates of isolated

19   TAMs, but not in the healthy controls (**Fig. 3F**), while soluble β2m was equally expressed in

20   both groups. Of note, the conformation specific antibody against amyloid fibrils recognizes

21   generic epitopes common to many amyloid fibrils and fibrillar oligomers, but not monomers,

22   prefibrillar oligomers or natively folded proteins. Next we sought to determine whether β2m

23   in human BM plasma of MM patients has the ability to activate caspase-1 and subsequent IL-

24   1β and IL-18 release. Therefore, we primed generated macrophages with LPS and treated

25   them with human BM plasma of untreated MM patients in the presence or absence of a

26   neutralizing anti- β2m antibody (αβ2m). We detected by flow cytometry a robust increase in

1 caspase-1 activation in macrophages after stimulation with BM plasma of MM patients (30.2

2 ± 5.9 %) (**Fig. 3G**). Moreover, treatment of macrophages with human BM plasma of MM

3 patients led also to an increase in IL-1β (1.4 ± 0.58 ng/ml) and IL-18 release (27.5 ± 7.3

4 ng/ml) (**Fig. 3H**). These effects were markedly inhibited in the presence of the neutralizing

5 anti- β2m antibody, whereas isotype control treatment had no effect (**Supplementary Fig. 9A**

6 **and 9B**), which indicates that β2m in the bone marrow plasma of MM patients is responsible

7 for inflammasome activation in macrophages and for the release of IL-1β and IL-18.

8

9 **β2m-triggered NLRP3 inflammasome activation *in vivo*.**

10 To elucidate whether β2m is responsible for inflammasome activation in MM, we

11 investigated the induction of the inflammasome in 5T33MM mice. 5T33M mice develop

12 spontaneously myeloma and the disease have many features in common with the human

13 disease. When transplanted myeloma cells (5TGM1) into syngeneic mice, recipients develop

14 the presence of a monoclonal protein and osteolytic bone disease, inevitably leading to hind

15 limb paralysis. Initially, syngeneic GFP$^+$ myeloma cells (5TGM1) were injected and serum

16 levels of β2m, IL-1β and IL-18 were determined weekly for four weeks (t0, t1, t2, t3) (**Fig.**

17 **4A**). Levels of β2m (7.1 ± 3.0 µg/ml, *p* = 0.029), IL-1β (735.5 ± 170.7 ng/ml, p = 0.050) and

18 IL-18 (1,692.4 ± 221.0 ng/ml, p = 0.029) significantly increased with the stage of MM (GFP$^+$

19 MM cells at t$_3$: 5.8% ± 1.2%) (**Fig. 4A** and **Supplementary Fig. 10A**), which is in accordance

20 with our observation in human. In addition, we observed an increase in IL-6 (51.1 ± 14.6

21 pg/ml, *p* = 0.029) and TNF (19.1 ± 8.8 pg/ml, *p* = 0.069) (**Supplementary Fig. 10B**). Next,

22 we analyzed mRNA expression of isolated TAMs and found that, similar to human TAMs,

23 TAMs of 5T33MM mice express high amounts of NLRP3 mRNA in comparison to controls

24 (7.9-fold) (**Fig. 4B**). Moreover, flow cytometric analysis of TAMs demonstrated high

25 expression of IL-1β and IL-18 during tumor progression, which indicates that TAMs of

26 5T33MM mice display an active inflammasome (**Fig. 4C**). Because we found that β2m forms

1   aggregates in lysosomes, leading to NLRP3 inflammasome activation, we next investigated

2   whether amyloid fibrils might be present in murine TAMs of 5T33MM mice (**Fig. 4D**). Flow

3   cytometry specifically demonstrated an increase in amyloid-positive TAMs from 5T33MM

4   mice (16.7 ± 0.23 %, $p = 0.1$), which was not the case for BM macrophages of control mice (n

5   = 3, p = 0.1) (**Supplementary Fig. 11A**). Simultaneously, we detected an enhanced caspase-1

6   activation in amyloid-positive TAMs (67.1 ± 2.6 %, $p = 0.01$), confirming the connection

7   between β2m aggregation and NLRP3 inflammasome activation in this murine myeloma

8   model (**Fig. 4D; Supplementary Fig. 11B**). To decipher whether β2m is responsible for the

9   observed inflammasome induction, we generated β2m low expressing 5TGM1 cells by

10 transduction with shRNA against β2m (**Fig. 4E** and **Supplementary Fig. 12**) and injected

11 these cells in syngeneic mice. In line with previous data, we quantified high serum levels of

12 IL-1β and IL-18 in late stage of disease. In contrast, we detected only low amounts of IL-1β

13 and IL-18 in mice challenged with β2m low expressing 5TGM1 cells (**Fig. 4F**). Compared

14 with the control group, silencing β2m in 5TGM1 cells significantly inhibited the formation of

15 amyloid aggregates in TAMs and the activation of caspase-1 (**Fig. 4G**). These data indicate

16 that β2m of myeloma cells is at least partly responsible for inflammasome activation in MM.

17

18 **Inhibition of the NLRP3 inflammasome reduces MM progression**

19 Because MM cells are critically dependent on stromal and cytokine support, we reasoned that

20 the NLRP3 inflammasome, activated by β2m aggregates, plays a pivotal role in MM

21 progression. We therefore co-cultured 5T33MM cells (5TGM1) with bone marrow of

22 NLRP3-deficient mice (Nlrp3-/-, KO) or bone marrow of control mice (C57BL/KaLwRij or

23 C57/BL6) and measured MM cell growth using flow cytometry. When MM cells were

24 cultured with autologous bone marrow or C57/BL6 wild-type mice, a significant increase

25 (3.1-fold) in cell growth was measured after 24 hours (**Fig. 5A**). In contrast, bone marrow

26 cells of NLRP3-deficient mice failed to support cell growth of MM cells (**Fig. 5B**).

1   Furthermore, activation of the AIM2 inflammasome in bone marrow of NLRP3-deficient

2   mice restored stromal growth support of MM cells, suggesting that inflammatory effector

3   molecules are required for the promotion of MM cell growth (**Fig. 5C**). To confirm the

4   requirement of an active NLRP3 inflammasome for the stromal growth support, we blocked

5   the NLRP3 inflammasome with the selective NLRP3 inhibitor MCC950[34]. Treatment of bone

6   marrow and MM cells with MCC950 results in a significant reduction of MM cell growth

7   (**Fig. 5D**). Of note, we did not observe direct cytotoxic effects of MCC950 on MM cell

8   growth (**Supplementary Fig. 13**). We next sought to address the mechanism of NLRP3-

9   dependent growth support. Bone marrow cells were incubated with MM cells in the presence

10   of various blocking antibodies (anti-IL-1β, anti-IL-6, anti-IL-18 or anti-IL-18 receptor), and

11   MM cell growth was determined by flow cytometry. Growth support was markedly inhibited

12   in the presence of an anti-IL-18 or an anti-IL-18 receptor antibody, whereas anti-isotype

13   control treatment had no effect (**Fig. 5E** and **Supplementary Fig. 14**). Conversely, the

14   inhibition of IL-1β or IL-6 in the co-culture did not result in a significant reduction of stromal

15   growth support (**Supplementary Fig. 14**). By analyzing the IL-1 receptor superfamily

16   (IL1R1, IL18R1 and IL33R) on MM cells, we found that human and murine MM cells

17   express high levels of the IL-18 receptor, indicating that IL-18 could affect MM cells

18   (**Supplementary Fig. 15A and 15B**). Treatment of 5TGM1 cells with recombinant IL-18

19   resulted in a slight increase of cell growth (**Supplementary Fig. 15C**). In summary, these

20   findings suggest that the observed stromal growth support depends on the inflammasome

21   mediated IL-18 secretion of BM cells.

22   We next investigated the effects of MCC950 on MM progression *in vivo*. Syngeneic GFP+

23   myeloma cells were injected in 5T33MM mice and subsequently treated with MCC950 (20

24   mg/kg per week, 4 weeks). Treatment with MCC950 reduced serum concentration of IL-1β

25   and IL-18 (**Fig. 5F**) but did not decrease the amount of TNF (**Supplementary Fig. 16**).

26   However, serum levels of IL-6 were also significantly reduced by MCC950 treatment

1   (**Supplementary Fig. 16**). To determine whether MCC950 treatment also reduce MM growth

2   *in vivo*, we measured the percentage of GFP+ myeloma cells in the bone marrow. Strikingly,

3   we found a significant lower percentage of myeloma cells in the bone marrow of treated mice

4   (**Fig. 5G** and **Supplementary Fig. 16**). In order to measure disease severity in 5T33MM mice

5   during MCC950 treatment, we developed a clinical scoring system ranging from 0

6   (asymptomatic) to 50 based on weight loss, motility, development of paralysis, and mortality.

7   Treatment of mice with MCC950 delayed the onset and reduced the severity of myeloma

8   (**Fig. 5H**). Remarkably, MCC950 treatment of 5T33MM mice prevented development of hind

9   limb paralysis (control: 80% vs. MCC950: 20%) (**Fig. 5I**). To examine osteolysis, we

10   analyzed the femurs for bone density and volume by micro-computed tomography (μCT)

11   (**Fig.5J**). Quantitative μCT analysis showed that injection of 5TGM1 cells induce osteolysis,

12   (decrease in trabecular bone volume, number of trabeculae, increase in trabecular separation),

13   whereas MCC950 treated mice display only small osteolytic lesions.

14   In summary, these findings strongly indicate that inflammasome activation favours myeloma

15   progression, and that therapeutic inhibition of the NLRP3 inflammasome delayed the onset

16   and reduced the severity of myeloma disease (**Fig. 6**).

17

18   **Discussion**

19   Inflammation is a key component of the tumor microenvironment in multiple myeloma.

20   Consequently, inflammatory TAMs promotes disease progression[9], bone destruction[7] and

21   immune-impairment[44]. Our work here has identified β2m amyloid aggregation as an

22   endogenous mediator that leads to NLRP3 inflammasome activation, resulting in abnormal

23   IL-1β and IL-18 secretion, which in turn promotes progression and severity of MM (**Figure**

24   **6**). Therefore, we propose, that β2m is a clinically relevant endogenous danger signal that is

25   sensed by the NLRP3 inflammasome.

1 In MM patients, high levels of β2m correlate with poor prognosis and poor therapy

2 response[33]. Here, we provide one explanation for this clinical observation, by describing a

3 β2m-triggered inflammasome activation in TAMs, which leads to increased tumor growth of

4 MM cells and osteolytic bone disease, which is a frequent complication of multiple

5 myeloma[2]. The finding that β2m induces inflammasome activation after phagocytosis is

6 supported by an earlier report that uptake of β2m by myeloid cells induce a pro-inflammatory

7 immune response[45]. Moreover, a role of the inflammasome complex in MM was previously

8 suggested by one elegant study, using Vk*MYC mice. Injection of Vk12653 MM cells in

9 NLRP3$^{-/-}$, ASC$^{-/-}$ or NLRP1$^{-/-}$ resulted in prolonged survival compared with WT mice[15].

10 Here we have shown that β2m uptake is necessary for the activation of the NALP3

11 inflammasome but its accumulation in lysosome is not *per se* sufficient, but amyloid

12 aggregation is required. Indeed, while NALP3 inflammasome is activated in macrophages

13 treated with WT β2m, the single mutant β2m$_{W60G}$ known to be highly stable and poorly

14 amyloidogenic[40, 39, 38] fails to trigger the same effect. Specific *in vitro* experiments at pH

15 values mimicking lysosomal environment show that under such conditions β2m$_{W60G}$ tends to

16 retain its native structure and form little aggregates while the WT protein is largely unfolded

17 and aggregates rapidly and abundantly (**Supplementary Fig. 4**). Moreover, specific amyloid

18 staining shows that the presence of fibrillar aggregates in macrophages treated with WT β2m

19 is accompanied by large lysosomal damage and NALP3 inflammasome activation.

20 Conversely, a clear correlation between absence of amyloids, intact lysosomes and non-

21 activation of NALP3 inflammasome is observed in macrophages treated with β2m$_{W60G}$

22 (**Figure 2**). Taking together, these data strongly support β2m amyloid aggregation as the

23 molecular event responsible for lysosomal rupture and ultimately for the activation of NALP3

24 inflammasome.

25 Our results support a model in which induction of the NLRP3 inflammasome in TAMs

26 triggered by "frustrated phagocytosis" is a critical and early step in the initiation and

16

1 progression of MM. Remarkably, the most common cancer associated with Gaucher disease, a

2 primary macrophage lysosomal storage disorder characterized by chronic macrophages

3 activation and overproduction of IL-1β by macrophages, is myeloma[46]. Along with our

4 observations, this is consistent with inflammasome induction by lysosomal damage playing a

5 key role in the development of MM. Moreover, increased β2m serum levels are also observed

6 in a range of autoimmune, renal and hematological diseases. For example, elevated serum

7 β2m levels have been reported in rheumatoid arthritis (RA)[47] or inflammatory bowel disease

8 (IBD)[48]. Interestingly, in both diseases tissue macrophages exhibit a hyper-activated NLRP3

9 inflammasome complex and increased levels of IL-1β and IL-18 are detected in active RA[49]

10 or IBD[50]. With regard to our observation, that β2m aggregation activates the NLRP3

11 inflammasome in TAMs, it is tempting to speculate that β2m amyloids may be a general

12 trigger for NLRP3 inflammasome activation in a range of otherwise unrelated inflammatory

13 diseases.

14 Both IL-1β and IL-18, which are abundant in serum of MM patients, have already been linked

15 to the pathogenesis of MM. IL-1β promotes inflammatory osteolysis, regulates the homing of

16 malignant plasma cells into the bone marrow and controls IL-6 production, which is important

17 for myeloma survival and proliferation[51]. Importantly, treatment with a recombinant IL-1R

18 antagonist (Anakinra) prolongs the progression-free survival of patients with indolent

19 myeloma, suggesting that therapeutic reduction of IL-1β activity can halt progression to

20 active myeloma[18]. In contrast, much less is known about the pathologic functions of IL-18 in

21 MM. High levels of bone marrow plasma IL-18 were associated with poor overall survival of

22 MM patients[52] and mice deficient for IL-18 were remarkably protected from Vk*MYC MM

23 progression. Moreover, IL-18 can accelerate generation of myeloid-derived suppressor cells

24 (MDSCs), which in turn inhibit T cell mediated killing of MM cells[15].

25 We observed increased cell growth of MM cells in the presence of BM cells, which was

26 abrogated by blocking IL-18 signaling and inhibition of the NLRP3 inflammasome. However,

1   treatment of 5TGM1 cells with recombinant IL-18 only resulted in a minor increase in cell

2   growth. This suggests that IL-18 alone is not sufficient to induce proliferation of MM cells.

3   However, the observation that IL-18 directly affects MM cells is supported by previous

4   findings of IL-18 injection in mice resulting in the production of self-reactive antibodies and

5   expansion of plasma cells[53]. IL-18 also facilitates bone destruction by stimulating osteoclast

6   formation through upregulation of RANKL (receptor activator of nuclear factor κB ligand)[54].

7   However, IL-18 frequently appears to act synergistically with other factors, and it is

8   frequently unclear whether IL-18 associated effects are direct and/or indirect effects.

9   Even though we demonstrate that uptake and amyloid aggregation of β2m can trigger

10   inflammasome activation in MM, the question of which factors aid in priming the

11   inflammasome in this disease remains open. Although high concentrations of β2m alone were

12   able to replace LPS as the priming agent, the amount of secreted IL-1β and IL-18 level were

13   much lower under these conditions, indicative of other factors being involved. However,

14   recent studies indicate that certain endogenous ligands, which were recognized by Toll-like

15   receptors (TLRs), were expressed in the tumor microenvironment. For example, the

16   extracellular matrix proteoglycan versican has previously been shown to activate TLR2/6

17   signaling in myeloma-associated macrophages[13]. It remains to be determined whether there

18   are other damage-associated molecular patterns (DAMPs), like syndecan-1[55] or S100

19   proteins[56], in multiple myeloma, able to induce a noninfectious inflammatory response.

20   The 5TMM mouse model revealed that activation of TAMs by β2m increased tumor growth

21   and lytic bone lesions. Importantly these effects were strongly reduced in the presence of the

22   specific NLRP3 inhibitor MCC-950[34]. These results have important practical ramifications in

23   light of ongoing clinical trials specifically investigating inhibition of inflammasome

24   components in human cancers[57]. Although one clinical trial focusing on the inhibition of the

25   downstream effector IL-1β showed promising results[58], blocking IL-1β or IL-18 individually

26   have been shown to increase the risk of infections. Theoretically, inhibition of a specific

1 inflammasome like NLRP3 (e.g. by MCC950) can block pathological effects of NLRP3

2 without compromising beneficial effects from other inflammasomes. This approach appears

3 particularly promising as our results highlight β2m-tiggered inflammasome induction as a

4 relevant pathophysiological process mediating inflammatory bone destruction. Importantly,

5 morbidity, mortality, as well as the overall quality of life of MM patients is directly linked to

6 progressive osteolytic bone disease, which is the hallmark of multiple myeloma. The results

7 from our study demonstrated that inflammasome inhibition during MM progression reduces

8 osteolytic lesions which is in accordance with earlier reports[59]. Mechanistically, IL-1β can

9 directly or indirectly induce osteoclast differentiation, and targeting IL-1β limits osteolysis in

10 inflammatory diseases[60]. Moreover, mice with an activating-mutation in the NLRP3 gene

11 exhibit systemic inflammation and severe osteopenia[61]. In this context, it is notable that

12 thalidomide, a well-established drug in the front line therapy of MM, can inhibit caspase-1,

13 which suggests that the antineoplastic effects of this agent may be mediated (at least partially)

14 through inflammasome inhibition[62]. However, given that an active inflammasome triggers

15 tumor growth, immune escape and osteolytic lesions, we expect that specific inflammasome

16 inhibition during standard treatment will improve outcome and well-being of patients with

17 myeloma.

18 Taken together, our data allow building a model describing the molecular events supporting

19 inflammation in MM (**Figure 6**). β2m is abundantly internalised by macrophages and

20 lysosomal environment facilitates β2m aggregation. The accumulation of amyloid fibrils

21 results in lysosomal damage and subsequent inflammasome induction.

22 Intriguingly, we may speculate that such molecular cascade could be relevant beyond MM,

23 and that this work may extend the understanding of the β2m-mediated inflammasome

24 activation also in other inflammatory diseases.

25

26

1

2 **Material and Methods**

3 **Cell culture reagents.** Cells were cultured in RPMI 1640 media supplemented with L-

4 glutamine (2 mM), 2-mercaptoethanol (50 nM), PenStrep (160 µIU/ml penicillin, 160 ng/ml

5 streptomycin) (GIBCO®, Thermo Fisher Scientific™, Waltham, USA), sodium pyruvate (1

6 mM), MEM-vitamin (0.4 %), MEM-NEAA (1 %) (PAN™ Biotech, Aidenbach, GER) and

7 FCS (10 %) (c.c. pro, Oberdorla, GER).

8

9 **Preparation of macrophages.** Human PBMCs were isolated from freshly drawn peripheral

10 blood of healthy donors (University Hospital of Erlangen, Department of Transfusion

11 Medicine and Haemostaseology, GER) by density gradient centrifugation using human

12 Pancoll (1.077 g/ml) (PAN™ Biotech, Aidenbach, GER) and a subsequent buffy coat

13 purification. To generate macrophages, CD14$^+$ monocytes were isolated by adherence to

14 polystyrene in CELLSTAR® cell culture flasks (Greiner Bio-One, Kremsmünster, AUT) and

15 cultured in the presence of Leucomax® GM-CSF (500 U/µl) (Novartis Pharma, Nürnberg,

16 GER). After 6-7 d of culture, macrophages were detached with EDTA (1 mM) (Sigma-

17 Aldrich®, München, GER).

18

19 **Mice.** NLRP3-deficient mice (*Nlrp3*-/-) were provided by Prof. Dr. Robert Zeiser and

20 Shaima'a Hamarsheh (Department of Medicine 1 - Medical Center, University of Freiburg,

21 Freiburg, GER). C57BL/6 mice were from The Jackson Laboratory (Bar Harbor, USA).

22 5TMM mice were from Dr. Jens Nolting and Savita Bisht-Feldmann (Department of

23 Oncology/Hematology and Rheumatology, University Hospital Bonn, Bonn, GER). Mouse

24 strains were bred and housed in pathogen-free conditions. All experiments were in accordance

25 with the guidelines set forth by the University Hospital of Erlangen and approved by the

26 Institutional Animal Care and Use Committee.

1

2 **Reagents.** ATP, MSU crystals, nigericin, poly(dA:dT) and the v-ATPase-specific inhibitor

3 bafilomycin A1 were from InvivoGen (San Diego, USA). LPS (*Escherichia coli* 0111:B4),

4 the phagocytosis inhibitor cytochalasin D, the cathepsin B-specific inhibitor CA-074 methyl

5 ester and the mtROS-inhibitor *N*-acetyl-L-cysteine (NAC) were from Sigma-Aldrich®

6 (München, GER). The NLRP3-specific inhibitor MCC950 was from Biomol (Hamburg,

7 GER). The pancaspase inhibitor z-VAD-fmk was from R&D Systems® (Minneapolis, USA)

8 and the caspase-1-specific inhibitor z-YVAD-fmk was from Abcam® (Cambridge, UK).

9

10 **Protein expression and purification.** Recombinant $\beta 2m$ and $\beta 2m_{W60G}$ were expressed and

11 purified as previously reported[63].

12

13 **Aggregation assays.** Aggregation assays at different pH (2.5, 3, 3.5, 4, 4.5, 5, 7.5) were

14 performed in reaction mix containing 50 mM sodium citrate (acidic conditions) or 50 mM

15 sodium phosphate, 15 mM NaCl, $\beta 2m$ variant (40 µM) and ThT (10 µM).

16 All reactions were performed in triplicate using black, clear-bottom, 96-well microplates.

17 Upon seeding with preformed $\beta 2m$ fibrils, plates were incubated in a FLUOstar OPTIMA

18 reader (BMG Labtech, Germany) at 37 °C, over a period of 100 h with intermittent cycles of

19 shaking (1 min, 300 rpm, double-orbital) and rest (30 min). The ThT fluorescence intensity of

20 the aggregates, expressed as arbitrary units (AU), was taken every 30 min using 450 ± 10 nm

21 (excitation) and 480 ± 10 nm (emission) wavelength, with a bottom read and a gain of 1000.

22

23 **Fluorescence experiments.** The denaturation of the $\beta 2m$ variants (8.5 µM) at different pH

24 values was followed by intrinsic Trp fluorescence under the same conditions used for

25 aggregation assays. All measurements were performed in triplicate on a Cary Eclipse

26 spectrofluorometer (Agilent) using a QS High Precision Cell (HellmaAnalytics) with

1 emission slit 5 nm. Excitation wavelength was set to 295 nm and Trp fluorescence was

2 monitored at 350 nm.

3

4 **LysoSensor™ Green DND-189.** Intralysosomal pH was detected using the LysoSensor™

5 Green DND-189 kit from Thermo Fisher Scientific™ (Waltham, USA) according to the

6 manufacturer's instructions. macrophages were seeded at 1×10^6/ml in polystyrene Falcon®

7 round bottom tubes (Corning® LifeSciences, Corning, USA), LPS-primed (1 µg/ml, 3 h) and

8 overnight-incubated with   250 µg/ml MSU crystals, 60 µg/ml B2M and 60 µg/ml B2M$_{W60G}$.

9 Cells were washed with PBS and incubated with the LysoSensor™ Green DND-189 reagent

10 (4 µM, 2 h) at 37 °C and 5 % CO_2. As assessed by flow cytometry, an increase in

11 intralysosomal pH or rather lysosomal rupture was defined as decrease in fluorescence.

12

13 **FLICA® 660 Caspase-1 assay.** Caspase-1 activity was detected using the FLICA® 660

14 Caspase-1 assay kit from ImmunoChemistry Technologies (Bloomington, USA) according to

15 the manufacturer's instructions. macrophages were seeded at 1×10^6/ml in polystyrene

16 Falcon® round bottom tubes (Corning® LifeSciences, Corning, USA) and on a 8 well

17 Permanox™ Chamber Slide™ system (Thermo Fisher Scientific™, Waltham, USA), LPS-

18 primed (1 µg/ml, 3 h) and overnight-incubated with 10 µM nigericin, 10 µg/ml β2m$_{digest}$, 10

19 µg/ml β2m pre-incubated with a β2m-neutralizing antibody (clone: 2M2) (LifeSpan

20 BioSciences, Seattle, USA) (10 µg/ml, 1 h) and β2m (10, 60 µg/ml). For pancaspase

21 inhibition, macrophages were pre-incubated with z-VAD-fmk (20 µM, 1 h). For β2m-

22 blocking, macrophages were overnight-primed with 100 ng/ml LPS and overnight-cocultured

23 with bone marrow plasma from MM patients (8 %) pre-incubated with a β2m-neutralizing

24 antibody (clone: 2M2) (LifeSpan BioSciences, Seattle, USA) and an IgG1 antibody (clone:

25 12G8G11) (BioLegend®, Minneapolis, USA) (10 µg/ml, 1 h). Cells were washed with PBS

26 and incubated with the FLICA® 660-YVAD-fmk reagent (1:150, 30 min) at 37 °C and 5 %

1   CO_2. As assessed by flow cytometry and confocal microscopy, caspase-1 activation was

2   defined as increase in fluorescence.

3

4   **CellROX® Deep Red assay.** mtROS in macrophages were detected using the CellROX®

5   Deep Red assay kit from Thermo Fisher Scientific™ (Waltham, USA) according to the

6   manufacturer's instructions. macrophages were seeded at 1×10^6/ml in polystyrene Falcon®

7   round bottom tubes (Corning® LifeSciences, Corning, USA). For mtROS inhibition, medium

8   of LPS-primed (100 ng/ml, 3 h) macrophages was removed, cells were washed with PBS and

9   incubated in medium containing 1 mM NAC and 60 µg/ml β2m for 48 h. Cells were washed

10   with PBS and incubated with the CellROX® Deep Red reagent (5 µM, 30 min) at 37 °C and 5

11   % CO_2. As assessed by flow cytometry, an increase in mtROS was defined as increase in

12   fluorescence.

13

14   **Magic Red® Cathepsin B assay.** Cathepsin B activity in macrophages was detected using

15   the Magic Red® Cathepsin B assay kit from ImmunoChemistry Technologies (Bloomington,

16   USA) according to the manufacturer's instructions. macrophages were seeded at 1×10^6/ml on

17   a 8 well Permanox™ Chamber Slide™ system (Thermo Fisher Scientific™, Waltham, USA),

18   LPS-primed (1 µg/ml, 3 h) and overnight-incubated with 250 µg/ml MSU crystals and 60

19   µg/ml β2m. Cells were washed with PBS, incubated with the Magic Red® MR-$(RR)_2$

20   substrate (1:260, 45 min) at 37 °C and 5 % CO_2 and fixed with 4 % (vol/vol)

21   paraformaldehyde. Cell membrane and nuclei staining was performed using FITC-conjugated

22   WGA (2.5 µg/ml) (Vector Laboratories, Burlingame, USA) and DAPI (Thermo Fisher

23   Scientific™, Waltham, USA). As assessed by confocal microscopy, cathepsin B activation

24   was defined as increase in fluorescence.

25

1   **FITC-Dextran.** Lysosomes in macrophages were detected using FITC-Dextran (average mol

2   wt of 70,000, FITC:glucose = 1:250) from Sigma-Aldrich® (München, GER) according to the

3   manufacturer's instructions. macrophages were seeded at 1×10^6/ml on a 8 well Permanox™

4   Chamber Slide™ system (Thermo Fisher Scientific™, Waltham, USA), LPS-primed (1

5   µg/ml, 3 h) and overnight-incubated with 250 µg/ml MSU crystals, 60 µg/ml β2m and 60

6   µg/ml β2m$_{W60G}$. Cells were washed with PBS, incubated with the FITC-Dextran reagent (250

7   µg/ml, 3 h) at 37 °C and 5 % CO_2 and fixed with 4 % (vol/vol) paraformaldehyde. Cell

8   membrane and nuclei staining was performed using AF™ 555-conjugated WGA (2.5 µg/ml)

9   (Thermo Fisher Scientific™, Waltham, USA). As assessed by confocal microscopy,

10   lysosomal detection was defined as increase in fluorescence.

11

12   **Protein labeling.** β2m and β2m$_{W60G}$ were labeled using the AF™ 647 microscale protein

13   labeling kit from Thermo Fisher Scientific™ (Waltham, USA) according to the

14   manufacturer's instructions. For analysis of β2m phagocytosis and fibril formation,

15   macrophages were seeded at 1×10^6/ml on a 8 well Permanox™ Chamber Slide™ system

16   (Thermo Fisher Scientific™, Waltham, USA), LPS-primed (1 µg/ml, 3 h) and overnight-

17   incubated with AF™ 647-labeled β2m and β2m$_{W60G}$ (60 µg/ml). For inhibition of

18   phagocytosis, macrophages were pre-incubated with cytochalasin D (5 µM, 1 h). Cells were

19   washed with PBS and fixed with 4 % (vol/vol) paraformaldehyde. Cell membrane and nuclei

20   staining was performed using FITC-conjugated WGA (2.5 µg/ml) (Vector Laboratories,

21   Burlingame, USA). As assessed by confocal microscopy, β2m phagocytosis and fibril

22   formation was defined as increase in fluorescence.

23

24   **AmyTracker™ 480.** Amyloid fibrils in macrophages were detected using the AmyTracker™

25   480 from EBBA Biotech (Solna, SWE) according to the manufacturer's instructions.

26   macrophages were seeded at 1×10^6/ml in polystyrene Falcon® round bottom tubes

1   (Corning® LifeSciences, Corning, USA), LPS-primed (1 µg/ml, 3 h) and overnight-incubated

2   with 60 µg/ml B2M. Cells were washed with PBS and incubated with the AmyTracker™ 480

3   reagent (5 µM, 1 h) at 37 °C and 5 % CO_2. As assessed by flow cytometry, an increase in

4   amyloids was defined as increase in fluorescence.

5

6   **Confocal microscopy.** Imaging was performed using the LSM 700 confocal microscope

7   (Zeiss, Oberkochen, GER) at a magnification of x630. Slides were analyzed by z-stacking to

8   generate up to 10 optical layers (0.5 µm).

9

10   **ELISA.** Cell culture supernatants were examined for human and murine cytokines IL-1β and

11   IL-18 with ELISA kits from R&D Systems® (Minneapolis, USA) and Thermo Fisher

12   Scientific™ (Waltham, USA) according to the manufacturer's instructions. macrophages and

13   bone marrow cells from NLRP3-deficient (*Nlrp3-/-*) and C57BL/ 6 mice were seeded at $1\times$

14   10^6/ml in polystyrene Falcon® 24 well plates (Corning® LifeSciences, Corning, USA), LPS-

15   primed (1 µg/ml, 3 h) and incubated with nigericin (10 µM, 30 min), ATP (5 mM, 30 min),

16   poly(dA:dT) (1 µg/ml, 24 h), β2m$_{W60G}$ (10 µg/ml, 6 h) and increasing concentrations of β2m

17   (3, 6, 10, 30, 60 µg/ml, 6 h). For inhibition assays, medium of LPS-primed (100 ng/ml, 1

18   µg/ml, 3 h) macrophages and murine bone marrow cells was removed, cells were washed with

19   PBS and incubated in medium containing appropriate inhibitors (20 µM z-YVAD-fmk, 10

20   µM MCC950, 10 µM bafilomycin A1, 5 µM cytochalasin D, 20 µM CA-074 methyl ester),

21   nigericin (10 µM, 30 min), MSU crystals (250 µg/ml, 6 h), poly(dA:dT) (1 µg/ml, 6 h) and

22   β2m (60 µg/ml, 6 h). For β2m-blocking, macrophages were seeded at $1\times$ 10^6/ml in

23   polystyrene Falcon® round bottom tubes (Corning® LifeSciences, Corning, USA), overnight-

24   primed with 100 ng/ml LPS and overnight-cocultured with bone marrow plasma from MM

25   patients (8 %) pre-incubated with a β2m-neutralizing antibody (clone: 2M2) (LifeSpan

1   BioSciences, Seattle, USA) and an IgG1 antibody (clone: 12G8G11) (BioLegend®,

2   Minneapolis, USA) (10 µg/ml, 1 h).

3

4   **Flow cytometry.** A FACSCanto™ II cytometer (BD Biosciences, Franklin Lakes, USA) was

5   used for all flow cytometric assays, data were acquired by a FACSDIVA™ software (BD

6   Biosciences, Franklin Lakes, USA) and analyzed using a FlowJo_v10 software (Tree Star,

7   Ashland, USA).

8

9   **Western blot analysis.** Cell lysates and supernatants were examined for human proteins IL-

10 1β, IL-18, NLRP3, ASC, caspase-1, β-actin and β2m. macrophages were seeded at 2×10^6/ml

11 in polystyrene Falcon® 24 well plates (Corning® LifeSciences, Corning, USA), LPS-primed

12 (1 µg/ml, 3 h) and overnight-incubated with 10 µM nigericin and 60 µg/ml β2m. Cell lysates

13 were prepared by direct lysis in 2 % (w/v) SDS lysis buffer (5 mM EDTA, 50 mM Tris/HCl,

14 150 mM NaCl, 2.2 % (wt/vol) SDS) supplemented with cOmplete™ EDTA-free (Roche

15 Diagnostics, Mannheim, GER) as protease inhibitor. Cell debris was removed by

16 centrifugation (21,382 xg, 15 min, 4 °C) and the concentration of total protein in cell extracts

17 was determined using the Qubit® protein assay kit and the Qubit® 3.0 fluorometer (Thermo

18 Fisher Scientific™). Cell culture supernatants were used purely. Protein samples were

19 resuspended in 4× Laemmli sample buffer (278 mM Tris/HCl, 355 mM 2-mercaptoethanol,

20 0.02 % (wt/vol) bromophenol blue, 4.4 % (wt/vol) lithium dodecyl sulfate, 44.4 % (vol/vol)

21 glycerol, pH (HCl) 6.8) (Bio-Rad Laboratories, München, GER) and boiled for 10 min at 95

22 °C. The protein content of cell lysates, supernatants and the Precision Plus Protein™

23 WesternC™ standard (Bio-Rad Laboratories, München, GER) was separated by SDS-PAGE

24 (10 %, 15 %, 90 µg) and transferred onto nitrocellulose membranes (0.2 µm) (GE Healthcare

25 Life Sciences, Chalfont St Giles, UK) using the semi-dry TransBlot® Turbo™ transfer

26 system (Bio-Rad Laboratories, München, GER). Membranes were blocked in 5 % (wt/vol)

1   dried milk in TBS-T (100 mM Tris/HCl, 150 mM NaCl, 0.1 % (vol/vol) Tween®-20) for 1 h

2   at room temperature. Membranes were overnight-incubated with primary antibodies diluted in

3   5 % (wt/vol) dried milk in TBS-T at 4 °C. Subsequently, membranes were incubated with the

4   appropriate HRP-conjugated secondary antibody diluted in 5 % (wt/vol) dried milk in TBS-T

5   for 1 h at room temperature. Proteins were detected by chemiluminescence using the

6   SuperSignal® ELISA femto maximum sensitivity substrate (Thermo Fisher Scientific™,

7   Waltham, USA) according to the manufacturer's instructions and the Amersham™ Imager

8   600 (GE Healthcare Life Sciences, Chalfont St Giles, UK). Membranes were stripped using

9   the Restore™ western blot stripping buffer (Thermo Fisher Scientific™, Waltham, USA)

10   before being re-examined. Primary antibodies used were β-actin (4967) (1:2,500), caspase-1

11   (clone: D7F10), IL-1β (clone: 3A6), NLRP3 (clone: D2P5E) (Cell Signaling Technology®,

12   Cambridge, UK), ASC (clone: B-3) (Santa Cruz Biotechnology®, Dallas, USA), IL-18

13   (ab191152) and β2m (ab6608) (1:1,000) (Abcam®, Cambridge, UK). Secondary HRP-

14   conjugated antibodies used were anti-mouse IgG (7076) and anti-rabbit IgG (7074) (1:2,500)

15   (Cell Signaling Technology®, Cambridge, UK).

16

17   **Immunocytochemistry.** Cells were fixed using 4 % (vol/vol) paraformaldehyde for 15 min at

18   room temperature. Cell membranes were stained using FITC- or AF™ 555-conjugated WGA

19   (2.5 μg/ml) (Vector Laboratories, Burlingame, USA) (Thermo Fisher Scientific™, Waltham,

20   USA). Cell nuclei staining was performed using DAPI (Thermo Fisher Scientific™,

21   Waltham, USA).

22

23   **ASC expression assay.** macrophages were seeded at 1×10^{6}/ml on a 8 well Permanox™

24   Chamber Slide™ system (Thermo Fisher Scientific™, Waltham, USA), LPS-primed (1

25   μg/ml, 3 h) and overnight-incubated with 10 μM nigericin and 60 μg/ml β2m. Cells were

26   washed with PBS, fixed with 4 % (vol/vol) paraformaldehyde and overnight-incubated at 4 °C

1 in a humidity chamber (LabArt, Waldbüttelbrunn, GER) with the appropriate primary ASC

2 antibody (clone: B-3) (1:200) (Santa Cruz Biotechnology®, Dallas, USA) and the secondary

3 anti-mouse IgG F(ab')2AF™ 555-conjugated antibody (4409) (1:400) (Cell Signaling

4 Technology®, Cambridge, UK) diluted in PBS containing 2 % (vol/vol) FCS and 0.5 %

5 (vol/vol) Triton® X-100. Cell membrane and nuclei staining was performed using FITC-

6 conjugated WGA (2.5 µg/ml) (Vector Laboratories, Burlingame, USA) and DAPI (Thermo

7 Fisher Scientific™, Waltham, USA). As assessed by confocal microscopy, ASC expression

8 was defined as increase in fluorescence.

9

10 **LysoTracker® Red DND-99.** Lysosomes in macrophages were detected using the

11 LysoTracker® Red-DND-99 kit from Thermo Fisher Scientific™ (Waltham, USA) according

12 to the manufacturer's instructions. macrophages were seeded at 1×10^6/ml on a 8 well

13 Permanox™ Chamber Slide™ system (Thermo Fisher Scientific™, Waltham, USA), LPS-

14 primed (1 µg/ml, 3 h) and overnight-incubated with 60 µg/ml β2m and 60 µg/ml β2m$_{W60G}$.

15 Cells were washed with PBS, incubated with the LysoTracker® Red-DND-99 reagent (50

16 nM, 1.5 h) at 37 °C and 5 % CO_2 and fixed with 4 % (vol/vol) paraformaldehyde. Cell

17 membrane and nuclei staining was performed using FITC-conjugated WGA (2.5 µg/ml)

18 (Vector Laboratories, Burlingame, USA). As assessed by confocal microscopy, lysosomal

19 detection was defined as increase in fluorescence.

20

21 **Statistical analysis.** Results are presented as average values ± SEM from multiple

22 independent experiments each performed at least in triplicate. Statistical analysis were

23 performed using a non-parametric Mann-Whitney *t*-test, an unpaired two-tailed *t*-test, using

24 the Prism software 5.03 (GraphPad Software, La Jolla, USA). Data were considered

25 significant when $P \leq 0.05$ (*), $P \leq 0.01$ (**) or $P \leq 0.001$ (***).

26

1 **Acknowledgements**

6

7

8 **Authorship Contributions**

9

10 **Disclosure of Conflicts of Interest**

11 HB received research support from Celgene and Morphosys. All other authors declared no

12 conflict of interest.

13

14

15

16

1 **Legends**

2 **Figure 1.** β2m-induces the release of IL-1β and IL-18 in a caspase-1 and NLRP3-dependent

3 matter. (**A**) IL-1β and IL-18 release [ng/ml] from macrophages cultured in absence (UT,

4 untreated) or presence of 1μg/ml LPS for 3h and treated with ATP (5 mM, 30 min) or

5 nigericin (NIG, 10 μM, 30 min) (blue bars) and increasing concentrations of β2m (3, 6, 10,

6 30, 60 μg/ml, 6 h) (red bars) as measured by ELISA (n=8). (**B**) Western blot analysis of cell

7 lysates (total protein: 90 μg) and supernatants to detect NLRP3, pro-caspase-1, pro-IL-1β,

8 ASC, β-actin, active caspase-1, IL-18 and IL-1β in macrophages cultured in absence (UT,

9 untreated) or presence of 1μg/ml LPS for 3h and overnight-treated with NIG (10 μM) or β2m

10 (60 μg/ml). (**C**) Confocal microscopy (top row) and flow cytometry (bottom row) of active

11 caspase-1 using FLICA® 660 (red) in macrophages cultured in absence (UT, untreated) or

12 presence of 1μg/ml LPS for 3h and overnight-treated with NIG (10 μM) or β2m (60 μg/ml).

13 Cell membranes and nuclei were stained using WGA (FITC, green) and DAPI (blue),

14 respectively. Scale bar: 20 μm. Grey histograms in the flow cytometry plots represent the

15 isotype/unstained control. (**D**) IL-1β release [ng/ml] from macrophages cultured in absence

16 (UT, untreated) or presence of 1μg/ml LPS for 3h and treated with NIG (10 μM) or β2m (60

17 μg/ml, 6 h) in the presence (red bars) and absence (blue bars) of caspase-1-specific inhibitor

18 z-YVAD-fmk (20 μM) as measured by ELISA (n=5). (**E**) Confocal microscopy to detect ASC

19 oligomers (AF® 555, red) in macrophages cultured in absence (UT, untreated) or presence of

20 1μg/ml LPS for 3h and overnight-treated with NIG (10μM) and β2m (60 μg/ml). Cell

21 membranes and cell nuclei were stained using WGA (FITC, green) and DAPI (blue),

22 respectively. Scale bar: 20 μm. (**F**) Quantification of confocal microscopy images in **Fig. 1E**

23 to detect frequency [%] of ASC[+] macrophages (n=4). Untreated (UT), LPS-primed and NIG-

24 treated macrophages are shown as blue bars; β2m-treated macrophages are shown as red bars.

25 (**G**) IL-1β release [ng/ml] from murine bone marrow cells of C57BL/6 (WT) (blue bars)

26 (n=10) and NLRP3-deficient (KO) (red bars) (n=7) mice left untreated (UT) or primed with

30

1   LPS and treated with ATP, NIG, poly(dA:dT) (1 µg/ml, 24 h) or increasing concentrations of

2   β2m (3, 6, 10, 30, 60 µg/ml, 6 h) as measured by ELISA. (**H**) IL-1β release [ng/ml] from

3   macrophages cultured in absence (UT, untreated) or presence of 1µg/ml LPS for 3h and

4   treated with NIG or β2m (60 µg/ml, 6 h) in the presence (red bars) and absence (blue bars) of

5   NLRP3-specific inhibitor MCC950 (10 µM) as measured by ELISA (n=5). Results are

6   expressed as mean ± SEM. *$P < 0.05$, **$P < 0.01$, ***$P < 0.001$, ns: not significant.

7

8   **Figure 2.** Phagocytosis of β2m leads to formation of amyloid fibrils and lysosomal rupture.

9   (**A**) Confocal microscopy to detect phagocytosis of β2m by macrophages primed with LPS

10 and treated with fluorescent-labeled β2m (AF® 647, red) in the presence (bottom row) and

11 absence (top row) of phagocytosis inhibitor cytochalasin D (5 µM). Cell membranes and cell

12 nuclei were stained using WGA (FITC, green) and DAPI (blue), respectively. Scale bar: 20

13 µm. (**B**) IL-1β release [ng/ml] from macrophages cultured in absence (UT, untreated) or

14 presence of 1µg/ml LPS for 3h and treated with MSU (250 µg/ml, 6 h) or β2m (60 µg/ml, 6 h)

15 in the presence (red bars) and absence (blue bars) of phagocytosis inhibitor cytochalasin D (5

16 µM) as measured by ELISA (n=5). (**C**) Flow cytometry using AmyTracker™ 480 to detect

17 amyloid fibrils and FLICA® 660 to detect active caspase-1 in LPS-primed macrophages

18 overnight-treated with β2m (60 µg/ml). (**D**) Comparison of tertiary structures of WT β2m

19 (yellow) and β2m$_{W60G}$ (green) (PDB codes: 5CS7, 2Z9T). W60 residue is represented as stick

20 model. (**E**) Electron microscopy to detect amyloid fibrils and lysosomal rupture in

21 macrophages primed with LPS and overnight-treated with β2m and β2m$_{W60G}$ (10 µg/ml).

22 Scale bar: 1µm. (**F**) Confocal microscopy to detect lysosomal rupture in macrophages primed

23 with LPS and treated with fluorescent-labeled β2m and β2m$_{W60G}$ (AF® 647, green).

24 Lysosomes, cell membranes and cell nuclei were stained using LysoTracker® Red (red),

25 WGA (FITC, light blue) and DAPI (dark blue), respectively. Scale bar: 20 µm. (**G**) Flow

26 cytometry using LysoSensor™ Green (red lines) to detect lysosomal rupture [%] in

1   macrophages cultured in absence (UT, untreated) or presence of 1µg/ml LPS for 3h and

2   overnight-treated with MSU (250 µg/ml), β2m or β2m$_{W60G}$. (**H**) IL-1β release [ng/ml] from

3   macrophages cultured in absence (UT, untreated) or presence of 1µg/ml LPS for 3h and

4   treated with β2m (blue bars) or β2m$_{W60G}$ (red bar) as measured by ELISA (n=6). (**I**) IL-1β

5   release [ng/ml] from macrophages cultured in absence (UT, untreated) or presence of 1µg/ml

6   LPS for 3h and treated with MSU or β2m in the presence (red bars) and absence (blue bars) of

7   cathepsin B-specific inhibitor CA-074 Me (10 µM) as measured by ELISA (n=5). (**J**) Flow

8   cytometry using CellROX® Deep Red (red lines) to detect mitochondrial dysfunction [%] in

9   macrophages cultured in absence (UT, untreated) or presence of 1µg/ml LPS for 3h and

10   treated with β2m in the presence or absence of anti-oxidant and free radical scavenger NAC

11   (5 mM). Results are expressed as mean ± SEM. *$P < 0.05$.

12

13   **Figure 3.** β2m-mediated NLRP3 inflammasome activation in TAMs of MM patients. (**A**) IL-

14   1β [pg/ml] and IL-18 [ng/ml] levels in human BM plasma of untreated MM patients divided

15   into low [≤ 2.7 µg/ml], intermediate [2.8 - 9.7 µg/ml] and high [≥ 9.8 µg/ml] β2m plasma

16   concentrations as measured by ELISA. The distribution of MM patients is shown as blue dots.

17   (**B**) The heat map shows the differential expression of inflammatory biomarkers estimated as

18   the log2 fold change between TAMs isolated from BM of HDs (HD1-3) or untreated MM

19   patients (MM1-3). (**C**) Confocal microscopy to detect active caspase-1 (left, p20, APC, red)

20   and IL-1β (right, PE, red) in human CD68^{+} cells (FITC, green) from BM of untreated MM

21   patients. Cell nuclei were stained using DAPI (blue). Scale bar: 20 µm (**D**) Flow cytometry to

22   detect protein expression of NLRP3, active caspase-1 (FLICA® 660), IL-1β and IL-18 as

23   MFI in human TAMs from BM of HDs (blue lines and bars) and untreated MM patients (red

24   lines and bars). The gray histogram indicates the isotype control. The top row shows

25   representative histograms of a total of n=8 samples as summarized in the bottom row. (**E**)

26   Flow cytometry using AmyTracker™ 480 to detect amyloid fibrils and FLICA® 660 to detect

1　active caspase-1 in human TAMs (CD163$^+$ and CD15$^-$) from BM of HDs and untreated MM

2　patients. The density plots show one representative example of a total of 8 experiments. (**F**)

3　Dot blot analysis of cell lysates (total protein: 50 μg) to detect β2m and amyloid fibrils in

4　isolated TAMs of HDs (HD 1-3) and untreated MM patients (MM 1-3). (**G**) Flow cytometry

5　using FLICA® 660 to detect frequency [%] of active caspase-1$^+$ macrophages primed with

6　LPS and overnight-co-cultured with human BM plasma of untreated MM patients in the

7　presence (red bar) and absence (blue bar) of a β2m-neutralizing antibody (anti-β2m) (10

8　μg/ml) (n=6). (**H**) IL-1β and IL-18 release [ng/ml] from macrophages primed with LPS and

9　overnight-co-cultured with human BM plasma of untreated MM in the presence (red bars) or

10　absence (blue bars) of a β2m-neutralizing antibody (anti-β2m) (n=6). Results are expressed as

11　mean ± SEM. *$P < 0.05$, **$P < 0.01$, ***$P < 0.001$, ns: not significant.

12

13　**Figure 4.** β2m-triggered NLRP3 inflammasome activation *in vivo*. (**A**) Levels of β2m

14　[μg/ml], IL-1β and IL-18 [ng/ml] in murine BM plasma of untreated 5TMM mice at different

15　time points during MM progression (first week = t_0, second week = t_1, third week = t_2, fourth

16　week = t_3) as measured by LEGENDplex™ or ELISA (n=4). (**B**) Flow cytometry to detect

17　frequency [%] of murine GFP$^+$ MM cells from BM of untreated 5TMM mice at different time

18　points during MM progression (n=4). (**C**) Quantitative real-time PCR to detect gene

19　expression of inflammatory biomarkers in murine TAMs from BM of C57BL/6 (blue bars)

20　(n=3) and untreated 5TMM mice (red bars) (n=3). (**D**) Flow cytometry using AmyTracker™

21　480 to detect amyloid fibrils and FLICA® 660 to detect active caspase-1 in murine TAMs

22　from BM of C57BL/6 and untreated 5TMM mice. Density plots show one representative

23　experiment of a total of 3 independent analysis. (**E**) Flow cytometric analysis of shRNA-

24　mediated generation of β2m low expressing 5TGM1 cells. (**F**) Levels of IL-1β and IL-18

25　[ng/ml] in murine BM plasma of 5TMM mice challenged with 5TGM1 cells transduced with

26　control shRNA (blue bars) (n=8) or β2m shRNA (red bars) (n=8). (**G**) Flow cytometry using

1   AmyTracker™ 480 to detect amyloid fibrils and FLICA® 660 to detect active caspase-1 in

2   murine TAMs from 5TMM mice challenged with 5TGM1 cells transduced with control

3   shRNA or β2m shRNA. Density plots show representative data of a total of 8 independent

4   experiments. Results are expressed as mean ± SEM. *$P < 0.05$, **$P < 0.01$, ***$P < 0.001$, ns:

5   not significant.

6

7   **Figure 5.** Inhibition of the NLRP3 inflammasome reduces MM progression. (**A-E**)Absolute

8   count [cells/ml] measured by flow cytemotry using 123count™ eBeads Counting Beads of

9   murine 5TGM1 cells co-cultured with murine BM cells (1:25, 96 h) from (**A**) C57BL/6 mice

10   (red bar, n=8), (**B**) C57BL/6 mice (WT) (blue bar) or NLRP3-deficient mice (KO) (red bar)

11   (n=4). (**C**) Cell count of 5TGM1 cells co-cultured with NLRP3-deficient mice in the presence

12   (red bars) and absence (blue bars) of poly (dA:dT) (1 µg/ml, 24h) (n=4). (**D**) Cell count of

13   5TGM1 cells co-cultured with BM of C57BL/6 mice in the presence (red bars) and absence

14   (blue bars) of the NLRP3-specific inhibitor MCC950 (10 µM) (n=12) or (**E**) IL-18 and IL-18

15   receptor neutralizing antibodies (aIL-18, aIL-18R) (1 µg/ml) (n=8). (**F**) Levels of IL-1β and

16   IL-18 [ng/ml] in murine BM plasma (n=8) and (**G**) frequency of GFP⁺ 5TGM1 cells in the

17   bone marrow of 5TMM mice treated with DMSO (blue bars) (n=10) or MCC950 (red bars)

18   (n=10) (20 mg/kg per week, 4 weeks). (**H**) Clinical Score of DMSO (blue, n=5) or MCC950

19   (red, n=5) treated 5TMM mice. (**I**) Clinical evaluation of hind limb paralysis of vehicle

20   (DMSO, blue bar)) or MCC950-treated (red bar) 5TMM mice (n=10). (**J**) Bone densities in

21   mice treated with DMSO (n=5) or MCC950 (n=5) as representatively shown on the left and

22   quantitatively summarized on the right depicting bone volume/total volume (%), trabecular

23   number (mm) and trabecular separation (µm). Results are expressed as mean ± SEM. *$P <$

24   0.05, **$P < 0.01$, ***$P < 0.001$.

25

1   **References**

2   1.   Palumbo, A. & Anderson, K. Multiple myeloma. *N Engl J Med* **364**, 1046-1060 (2011).
3

4   2.   Terpos, E. *et al.* International Myeloma Working Group recommendations for the treatment
5   of multiple myeloma-related bone disease. *J Clin Oncol* **31**, 2347-2357 (2013).
6

7   3.   Rutella, S. & Locatelli, F. Targeting multiple-myeloma-induced immune dysfunction to
8   improve immunotherapy outcomes. *Clin Dev Immunol* **2012**, 196063 (2012).
9

10   4.   Kawano, Y. *et al.* Targeting the bone marrow microenvironment in multiple myeloma.
11   *Immunol Rev* **263**, 160-172 (2015).
12

13   5.   Prabhala, R.H. *et al.* Elevated IL-17 produced by TH17 cells promotes myeloma cell growth
14   and inhibits immune function in multiple myeloma. *Blood* **115**, 5385-5392 (2010).
15

16   6.   Hebron, E. *et al.* MAP3K8 kinase regulates myeloma growth by cell-autonomous and non-
17   autonomous mechanisms involving myeloma-associated monocytes/macrophages. *Br J*
18   *Haematol* **160**, 779-784 (2013).
19

20   7.   Roussou, M. *et al.* Increased expression of macrophage inflammatory protein-1alpha on
21   trephine biopsies correlates with extensive bone disease, increased angiogenesis and
22   advanced stage in newly diagnosed patients with multiple myeloma. *Leukemia* **23**, 2177-2181
23   (2009).
24

25   8.   Coussens, L.M. & Werb, Z. Inflammation and cancer. *Nature* **420**, 860-867 (2002).
26

27   9.   Kim, J. *et al.* Macrophages and mesenchymal stromal cells support survival and proliferation
28   of multiple myeloma cells. *Br J Haematol* **158**, 336-346 (2012).
29

30   10.   Zheng, Y. *et al.* Macrophages are an abundant component of myeloma microenvironment
31   and protect myeloma cells from chemotherapy drug-induced apoptosis. *Blood* **114**, 3625-
32   3628 (2009).
33

34   11.   Suyani, E. *et al.* Tumor-associated macrophages as a prognostic parameter in multiple
35   myeloma. *Ann Hematol* **92**, 669-677 (2013).
36

37   12.   Durie, B.G., Vela, E.E. & Frutiger, Y. Macrophages as an important source of paracrine IL6 in
38   myeloma bone marrow. *Curr Top Microbiol Immunol* **166**, 33-36 (1990).
39

40   13.   Hope, C. *et al.* TPL2 kinase regulates the inflammatory milieu of the myeloma niche. *Blood*
41   **123**, 3305-3315 (2014).
42

43   14.   Hideshima, T., Chauhan, D., Schlossman, R., Richardson, P. & Anderson, K.C. The role of
44   tumor necrosis factor alpha in the pathophysiology of human multiple myeloma: therapeutic
45   applications. *Oncogene* **20**, 4519-4527 (2001).
46

47   15.   Nakamura, K. *et al.* Dysregulated IL-18 Is a Key Driver of Immunosuppression and a Possible
48   Therapeutic Target in the Multiple Myeloma Microenvironment. *Cancer Cell* **33**, 634-648
49   e635 (2018).
50

16. Alexanian, R., Barlogie, B. & Dixon, D. High-dose glucocorticoid treatment of resistant myeloma. *Ann Intern Med* **105**, 8-11 (1986).

17. Richardson, P.G. *et al.* A phase 2 study of bortezomib in relapsed, refractory myeloma. *N Engl J Med* **348**, 2609-2617 (2003).

18. Lust, J.A. *et al.* Induction of a chronic disease state in patients with smoldering or indolent multiple myeloma by targeting interleukin 1{beta}-induced interleukin 6 production and the myeloma proliferative component. *Mayo Clin Proc* **84**, 114-122 (2009).

19. Halle, A. *et al.* The NALP3 inflammasome is involved in the innate immune response to amyloid-beta. *Nat Immunol* **9**, 857-865 (2008).

20. Martinon, F., Petrilli, V., Mayor, A., Tardivel, A. & Tschopp, J. Gout-associated uric acid crystals activate the NALP3 inflammasome. *Nature* **440**, 237-241 (2006).

21. Masters, S.L. *et al.* Activation of the NLRP3 inflammasome by islet amyloid polypeptide provides a mechanism for enhanced IL-1beta in type 2 diabetes. *Nat Immunol* **11**, 897-904 (2010).

22. Lightfield, K.L. *et al.* Critical function for Naip5 in inflammasome activation by a conserved carboxy-terminal domain of flagellin. *Nat Immunol* **9**, 1171-1178 (2008).

23. Rathinam, V.A. *et al.* The AIM2 inflammasome is essential for host defense against cytosolic bacteria and DNA viruses. *Nat Immunol* **11**, 395-402 (2010).

24. Latz, E., Xiao, T.S. & Stutz, A. Activation and regulation of the inflammasomes. *Nat Rev Immunol* **13**, 397-411 (2013).

25. Sutterwala, F.S., Ogura, Y. & Flavell, R.A. The inflammasome in pathogen recognition and inflammation. *J Leukoc Biol* **82**, 259-264 (2007).

26. Mariathasan, S. *et al.* Cryopyrin activates the inflammasome in response to toxins and ATP. *Nature* **440**, 228-232 (2006).

27. Hornung, V. *et al.* Silica crystals and aluminum salts activate the NALP3 inflammasome through phagosomal destabilization. *Nat Immunol* **9**, 847-856 (2008).

28. He, Y., Hara, H. & Nunez, G. Mechanism and Regulation of NLRP3 Inflammasome Activation. *Trends Biochem Sci* **41**, 1012-1021 (2016).

29. Bjorkman, P.J. *et al.* Structure of the human class I histocompatibility antigen, HLA-A2. *Nature* **329**, 506-512 (1987).

30. Halabelian, L. *et al.* Class I major histocompatibility complex, the trojan horse for secretion of amyloidogenic beta2-microglobulin. *J Biol Chem* **289**, 3318-3327 (2014).

31. Gejyo, F. *et al.* A new form of amyloid protein associated with chronic hemodialysis was identified as beta 2-microglobulin. *Biochem Biophys Res Commun* **129**, 701-706 (1985).

32. Valleix, S. *et al.* Hereditary systemic amyloidosis due to Asp76Asn variant beta2-microglobulin. *N Engl J Med* **366**, 2276-2283 (2012).

33. Bataille, R., Grenier, J. & Sany, J. Beta-2-microglobulin in myeloma: optimal use for staging, prognosis, and treatment--a prospective study of 160 patients. *Blood* **63**, 468-476 (1984).

34. Coll, R.C. *et al.* A small-molecule inhibitor of the NLRP3 inflammasome for the treatment of inflammatory diseases. *Nat Med* **21**, 248-255 (2015).

35. McParland, V.J. *et al.* Partially unfolded states of beta(2)-microglobulin and amyloid formation in vitro. *Biochemistry* **39**, 8735-8746 (2000).

36. Platt, G.W. & Radford, S.E. Glimpses of the molecular mechanisms of beta2-microglobulin fibril formation in vitro: aggregation on a complex energy landscape. *FEBS Lett* **583**, 2623-2629 (2009).

37. Klingstedt, T. & Nilsson, K.P. Luminescent conjugated poly- and oligo-thiophenes: optical ligands for spectral assignment of a plethora of protein aggregates. *Biochem Soc Trans* **40**, 704-710 (2012).

38. Santambrogio, C. *et al.* DE-loop mutations affect beta2 microglobulin stability, oligomerization, and the low-pH unfolded form. *Protein Sci* **19**, 1386-1394 (2010).

39. Ami, D. *et al.* Structure, stability, and aggregation of beta-2 microglobulin mutants: insights from a Fourier transform infrared study in solution and in the crystalline state. *Biophys J* **102**, 1676-1684 (2012).

40. Camilloni, C. *et al.* Rational design of mutations that change the aggregation rate of a protein while maintaining its native structure and stability. *Sci Rep* **6**, 25559 (2016).

41. Chevriaux, A. *et al.* Cathepsin B Is Required for NLRP3 Inflammasome Activation in Macrophages, Through NLRP3 Interaction. *Front Cell Dev Biol* **8**, 167 (2020).

42. Chu, J. *et al.* Cholesterol-dependent cytolysins induce rapid release of mature IL-1beta from murine macrophages in a NLRP3 inflammasome and cathepsin B-dependent manner. *J Leukoc Biol* **86**, 1227-1238 (2009).

43. Zhou, R., Yazdi, A.S., Menu, P. & Tschopp, J. A role for mitochondria in NLRP3 inflammasome activation. *Nature* **469**, 221-225 (2011).

44. Minnie, S.A. & Hill, G.R. Immunotherapy of multiple myeloma. *J Clin Invest* **130**, 1565-1575 (2020).

45. Miyata, T. *et al.* Involvement of beta 2-microglobulin modified with advanced glycation end products in the pathogenesis of hemodialysis-associated amyloidosis. Induction of human monocyte chemotaxis and macrophage secretion of tumor necrosis factor-alpha and interleukin-1. *J Clin Invest* **93**, 521-528 (1994).

46. Ayto, R. & Hughes, D.A. Gaucher disease and myeloma. *Crit Rev Oncog* **18**, 247-268 (2013).

47. Sjoblom, K.G., Saxne, T. & Wollheim, F.A. Plasma levels of beta 2-microglobulin in rheumatoid arthritis. *Ann Rheum Dis* **39**, 333-339 (1980).

48. Descos, L., Andre, C., Beorghia, S., Vincent, C. & Revillard, J.P. Serum levels of beta-2-microglobulin--a new marker of activity in Crohn's disease. *N Engl J Med* **301**, 440-441 (1979).

49. Guo, C. *et al.* NLRP3 inflammasome activation contributes to the pathogenesis of rheumatoid arthritis. *Clin Exp Immunol* **194**, 231-243 (2018).

50. Zhen, Y. & Zhang, H. NLRP3 Inflammasome and Inflammatory Bowel Disease. *Front Immunol* **10**, 276 (2019).

51. Lust, J.A. & Donovan, K.A. The role of interleukin-1 beta in the pathogenesis of multiple myeloma. *Hematol Oncol Clin North Am* **13**, 1117-1125 (1999).

52. Alexandrakis, M.G. *et al.* Interleukin-18 in multiple myeloma patients: serum levels in relation to response to treatment and survival. *Leuk Res* **28**, 259-266 (2004).

53. Enoksson, S.L. *et al.* The inflammatory cytokine IL-18 induces self-reactive innate antibody responses regulated by natural killer T cells. *Proc Natl Acad Sci U S A* **108**, E1399-1407 (2011).

54. Dai, S.M., Nishioka, K. & Yudoh, K. Interleukin (IL) 18 stimulates osteoclast formation through synovial T cells in rheumatoid arthritis: comparison with IL1 beta and tumour necrosis factor alpha. *Ann Rheum Dis* **63**, 1379-1386 (2004).

55. Yang, Y. *et al.* The syndecan-1 heparan sulfate proteoglycan is a viable target for myeloma therapy. *Blood* **110**, 2041-2048 (2007).

56. De Veirman, K. *et al.* Extracellular S100A9 Protein in Bone Marrow Supports Multiple Myeloma Survival by Stimulating Angiogenesis and Cytokine Secretion. *Cancer Immunol Res* **5**, 839-846 (2017).

57. Karki, R. & Kanneganti, T.D. Diverging inflammasome signals in tumorigenesis and potential targeting. *Nat Rev Cancer* **19**, 197-214 (2019).

58. Ridker, P.M. *et al.* Effect of interleukin-1beta inhibition with canakinumab on incident lung cancer in patients with atherosclerosis: exploratory results from a randomised, double-blind, placebo-controlled trial. *Lancet* **390**, 1833-1842 (2017).

59. Mbalaviele, G., Novack, D.V., Schett, G. & Teitelbaum, S.L. Inflammatory osteolysis: a conspiracy against bone. *J Clin Invest* **127**, 2030-2039 (2017).

60. Dinarello, C.A., Simon, A. & van der Meer, J.W. Treating inflammation by blocking interleukin-1 in a broad spectrum of diseases. *Nat Rev Drug Discov* **11**, 633-652 (2012).

61. Qu, C. *et al.* NLRP3 mediates osteolysis through inflammation-dependent and -independent mechanisms. *FASEB J* **29**, 1269-1279 (2015).

62. Keller, M., Sollberger, G. & Beer, H.D. Thalidomide inhibits activation of caspase-1. *J Immunol* **183**, 5593-5599 (2009).

63. Esposito, G. *et al.* The controlling roles of Trp60 and Trp95 in beta2-microglobulin function, folding and amyloid aggregation properties. *J Mol Biol* **378**, 887-897 (2008).

Figure 1

Figure 2

A)

B)

C)

D)

E)

F)

G)

H)

I)

J)
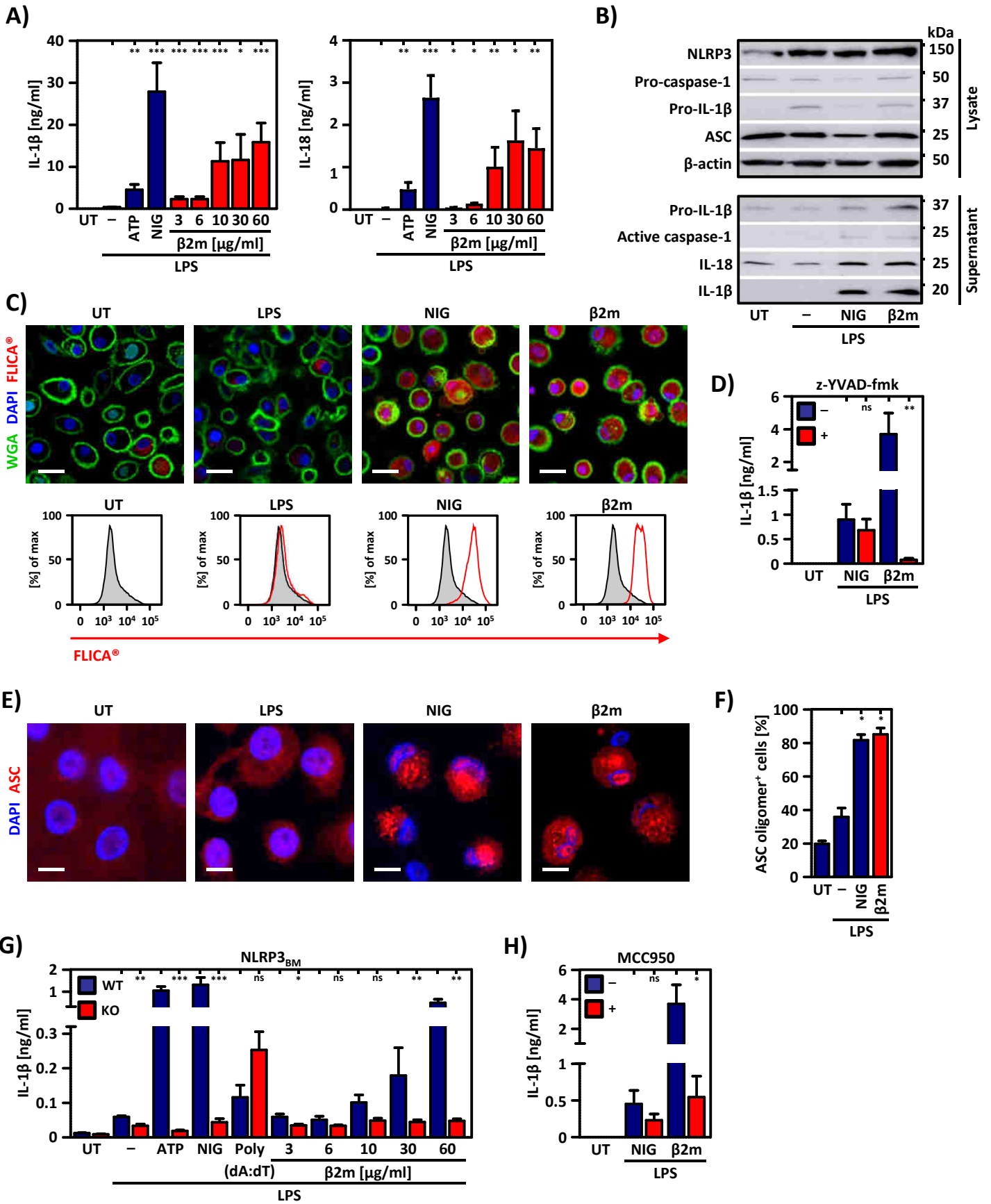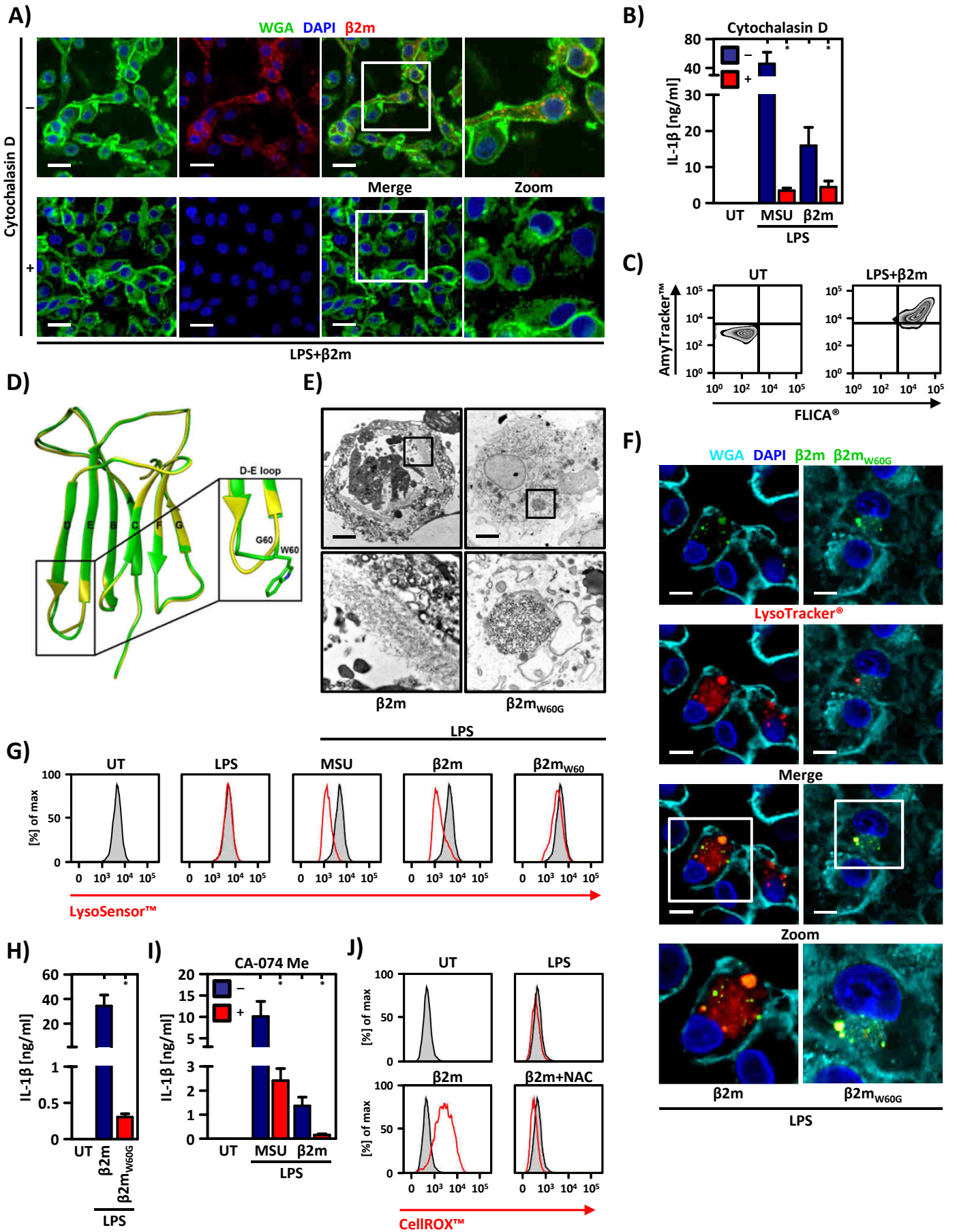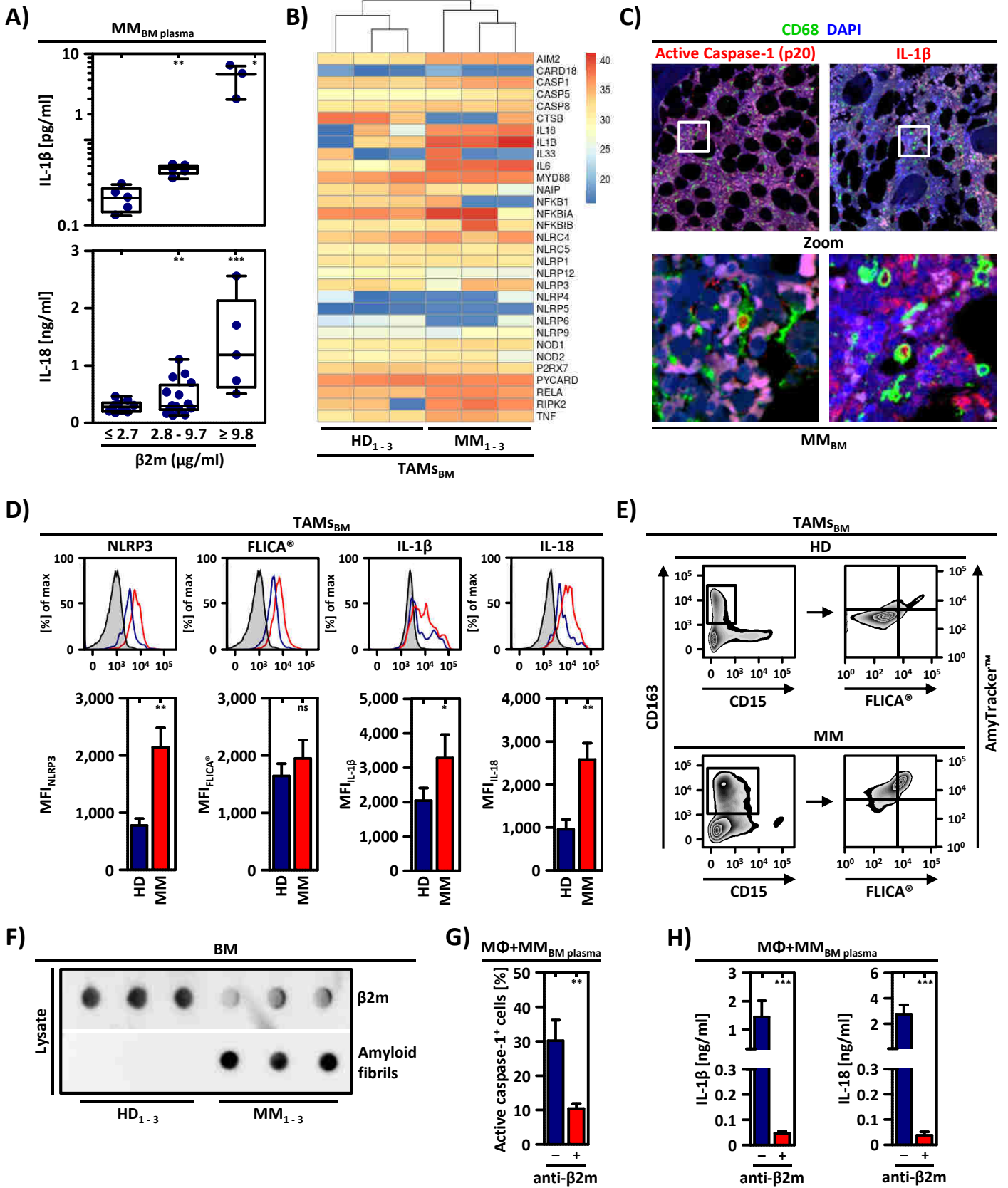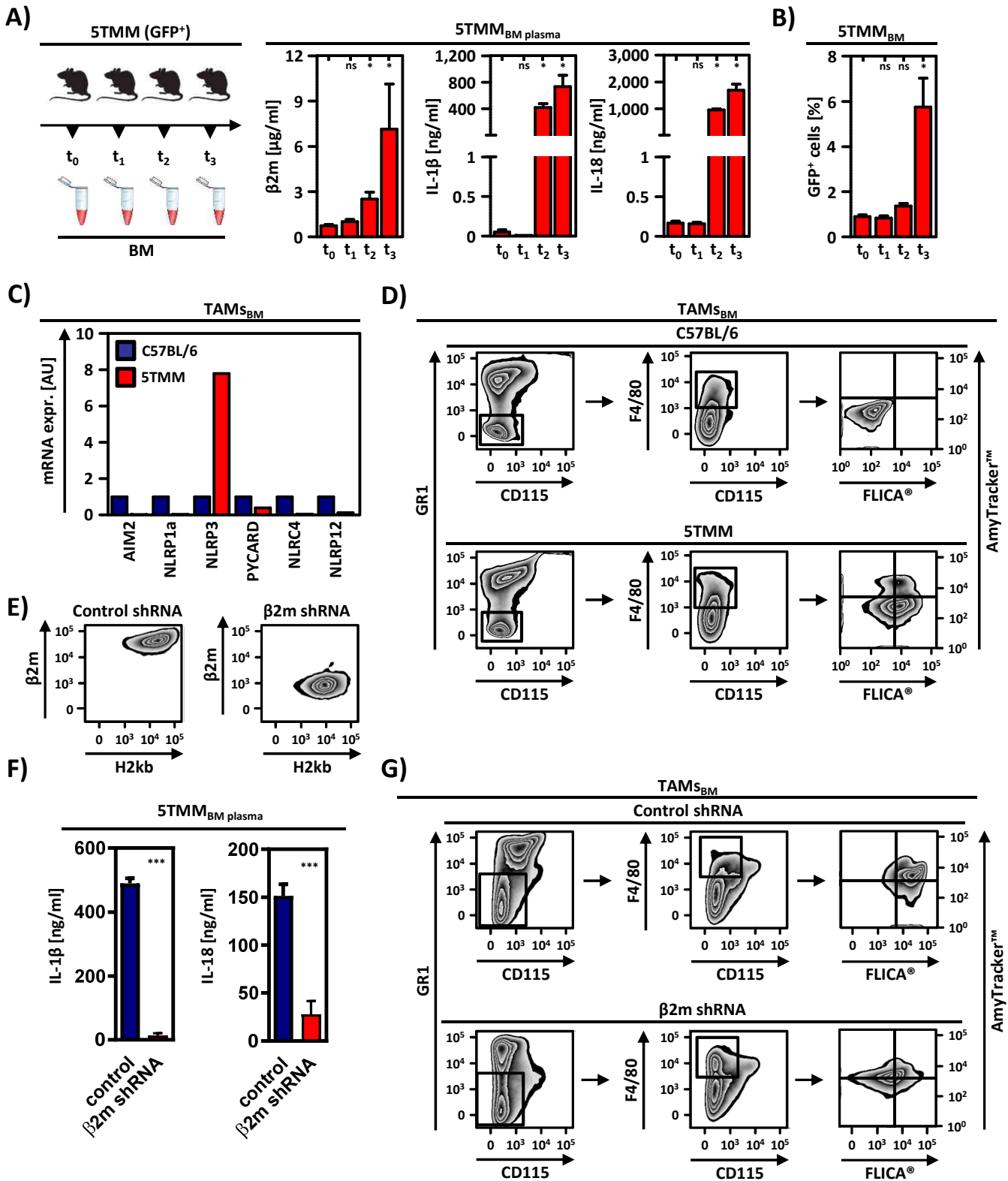
Figure 3

Figure 4

Figure 5
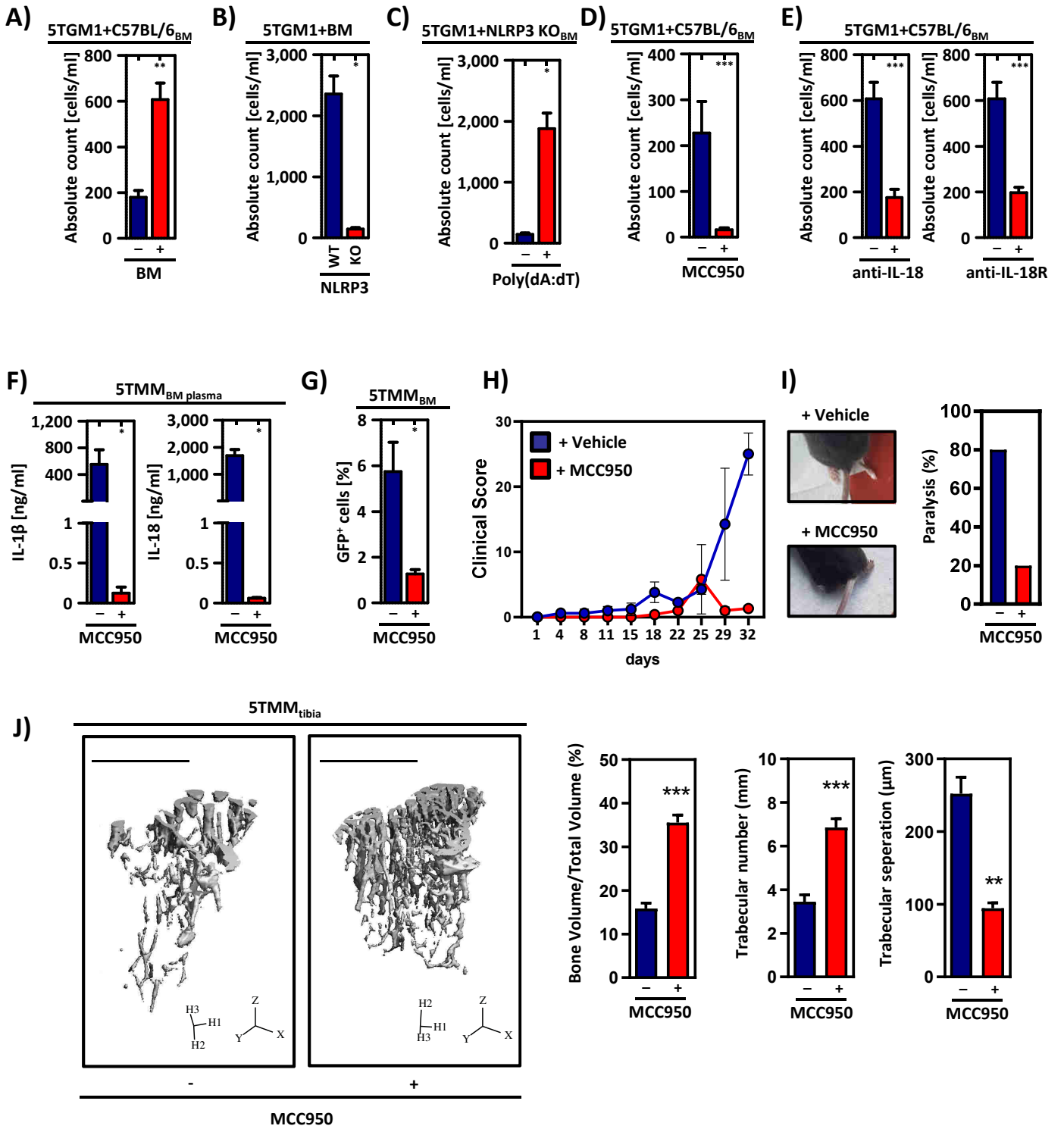
Figure 6 or graphical abstract
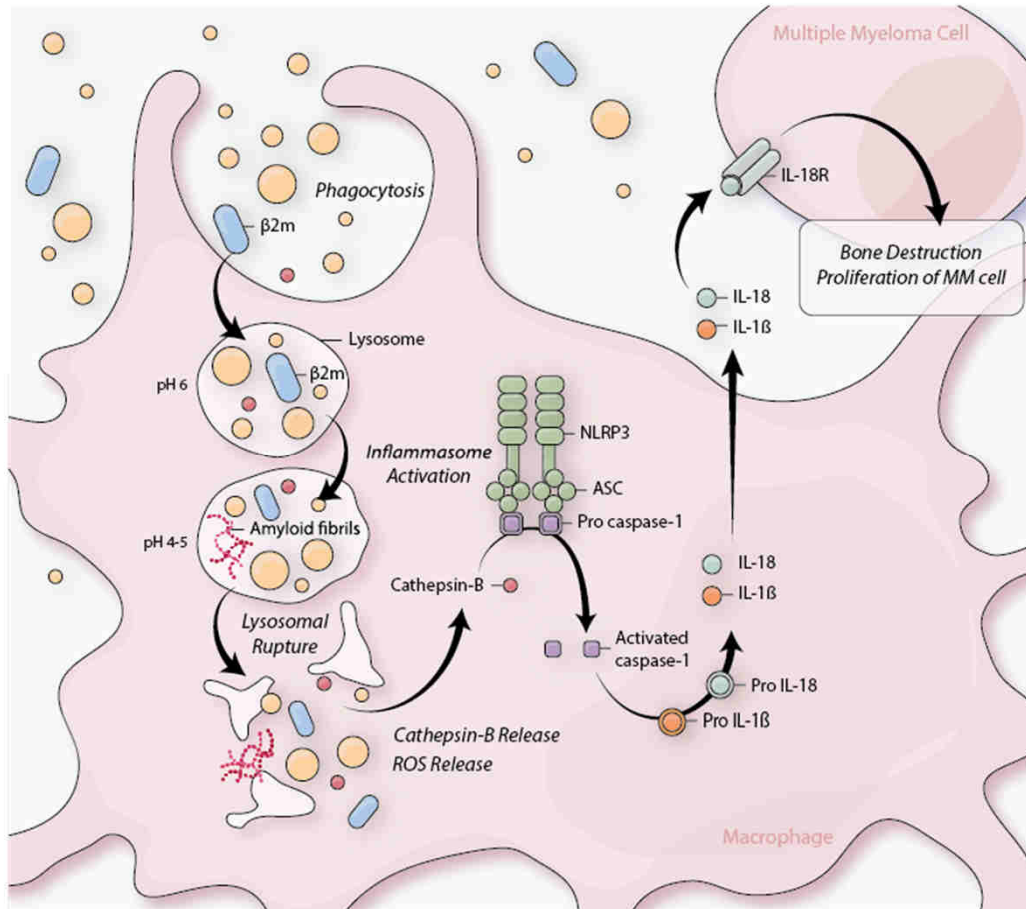
Supplementary Figures
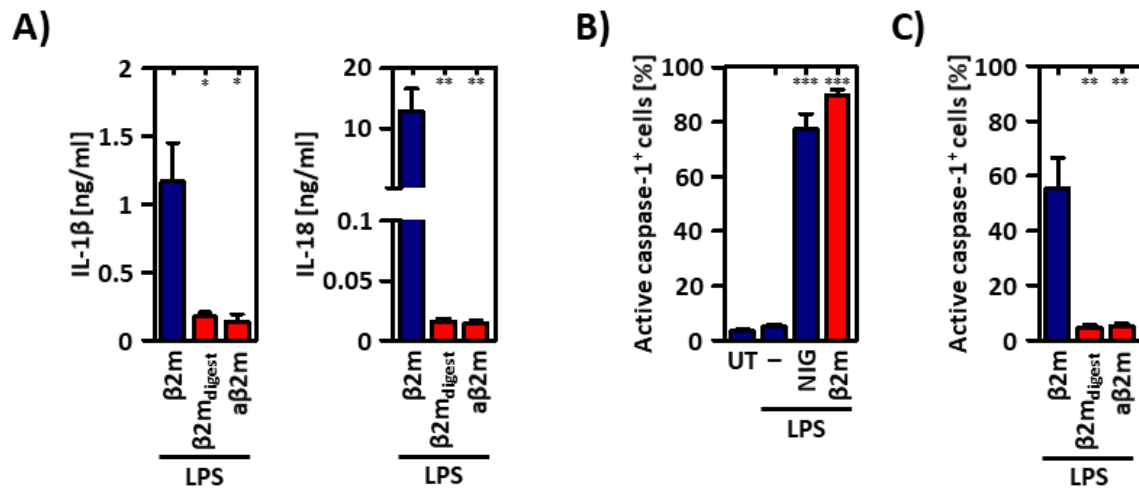
Supplementary Figure 1

β2m-induced IL-1β and IL-18 release from MΦs in a caspase-1 -dependent matter. (**A**) IL-1β and IL-18 release [ng/ml] from MΦs primed with LPS (1 µg/ml, 3 h) and treated with β2m (blue bar), β2mdigest and β2m (10 µg/ml, 6 h) in the presence of a β2m-neutralizing antibody (aβ2m) (10 µg/ml) (red bars) as measured by ELISA. Data representative of five independent experiments are shown. (**B**) Flow cytometry using FLICA® 660 to detect percentage [%] of active caspase-1+ (**A**) MΦs left untreated (UT) or primed with LPS (1 µg/ml, 3 h) and overnight-treated with NIG (10 µM) (blue bars) and β2m (60 µg/ml) (red bar) as well as (**C**) MΦs primed with LPS (1 µg/ml, 3 h) and overnight-treated with β2m (blue bar), β2mdigest and β2m (10 µg/ml, 6 h) in the presence of a β2m-neutralizing antibody (aβ2m) (10µg/ml) (red bars). Results are expressed as mean ± SEM. Data representative of at nine (**B**) or seven (**C**) independent experiments are shown. *P < 0.05, **P < 0.01, ***P < 0.001.
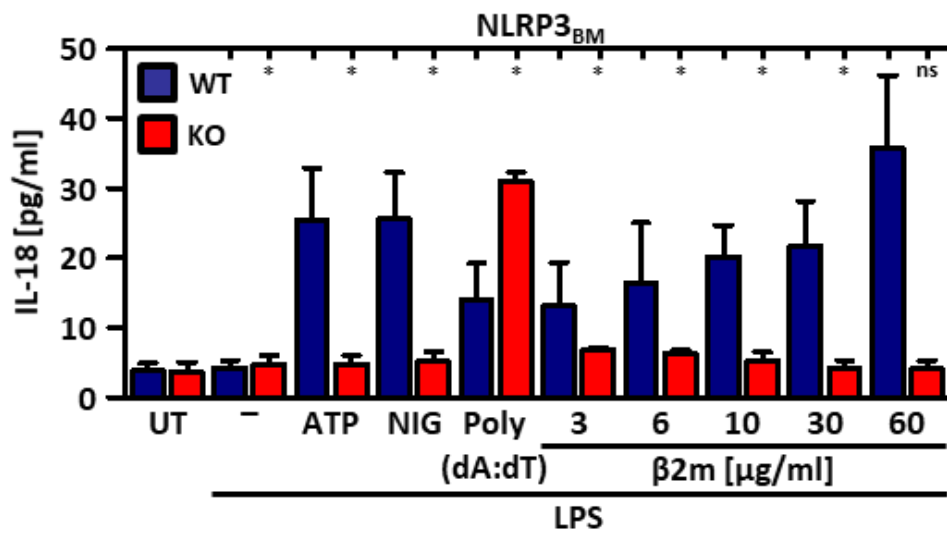
Supplementary Figure 2

β2m-induced IL-18 release from murine MΦs in a NLRP3-dependent matter. IL-18 release [pg/ml] from murine bone marrow cells of C57BL/6 (WT) (blue bars) and NLRP3-deficient (KO) (red bars) mice left untreated (UT) or primed with LPS (1 µg/ml, 3 h) and treated with ATP (5 mM, 30 min), NIG (10 µM, 30 min), poly(dA:dT) (1 µg/ml, 24 h) and increasing concentrations of β2m (3, 6, 10, 30, 60 µg/ml, 6 h) as measured by ELISA. Results are expressed as mean ± SEM. Data representative of at four independent experiments are shown. *P < 0.05, **P < 0.01, ***P < 0.001.
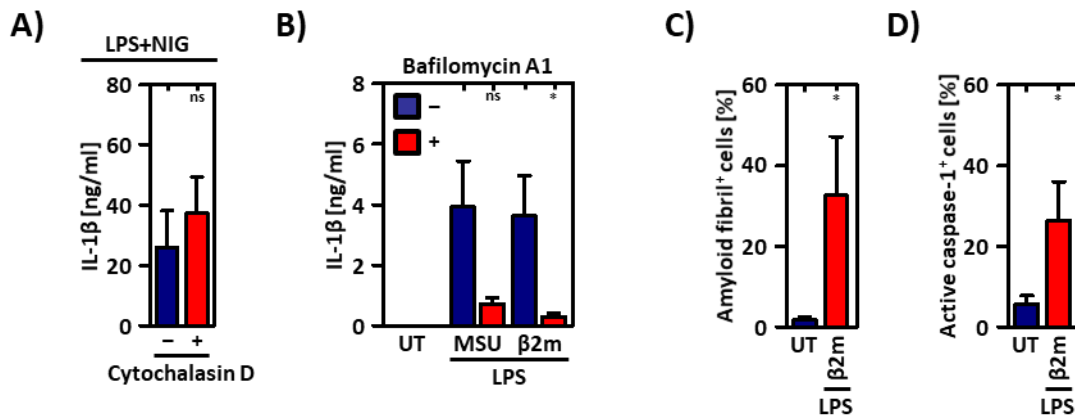
Supplementary Figure 3

Phagocytosis of β2m leading to formation of amyloid fibrils and lysosomal rupture. (**A**) IL-1β release [ng/ml] from MΦs primed with LPS (1 µg/ml, 3 h) and treated with Nigericin (NIG) (10 µM, 30 min) in the presence (red bar) and absence (blue bar) of phagocytosis inhibitor cytochalasin D (5 µM) as measured by ELISA. (**B**) IL-1β release [ng/ml] from MΦs left untreated (UT) or primed with LPS (100 ng/ml, 3 h) and treated with MSU (250 µg/ml, 6 h) and β2m (60 µg/ml, 6 h) in the presence (red bars) and absence (blue bars) of V-ATPase inhibitor bafilomycin A1 (3 µM) as measured by ELISA. Data representative of five independent experiments are shown. (**C**) Flow cytometry using AmyTracker™ 480 and FLICA® 660 to detect percentage [%] of (**C**) amyloid fibril+ and (**D**) active caspase-1+ MΦs LPS-primed (blue bars) and overnight-treated with β2m (60 µg/ml) (red bars). Results are expressed as mean ± SEM. Data representative of at six independent experiments are shown. *P < 0.05, **P < 0.01, ***P < 0.001.

Supplementary Figure 4

Distinct biophysical properties of β2m and β2m$_{W60G}$ as function of pH. (**A**) Kinetics of amyloid fibril formation of β2m and β2m$_{W60G}$. Fluorescence spectroscopy in the ThT binding assay to detect kinetics [AU] of amyloid fibril formation of β2m (solid lines) and β2m$_{W60G}$ (dash lines). (**B**) Folded fraction [%] of β2m (solid line, full circles) and of β2m$_{W60G}$ (dash line, empty circle) is represented as a function of pH. Data are representative of three independent experiments.

Supplementary Figure 5

Effect of β2m$_{W60G}$ on inflammasome induction. **(A)** Flow cytometry using LysoSensor™ Green to detect percentage [%] of lysosome– MΦs left untreated (UT) or primed with LPS (1 µg/ml, 3 h) and overnight-treated with MSU (250 µg/ml) (blue bars), β2m and β2m$_{W60G}$ (10 µg/ml) (red bars). **(B)** IL-18 release [pg/ml] from MΦs left untreated (UT) or primed with LPS (1 µg/ml, 3 h) and treated with β2m (blue bars) and β2m$_{W60G}$ (red bar) (10 µg/ml, 6 h) as measured by ELISA. Data representative of at five independent experiments are shown. *P < 0.05.
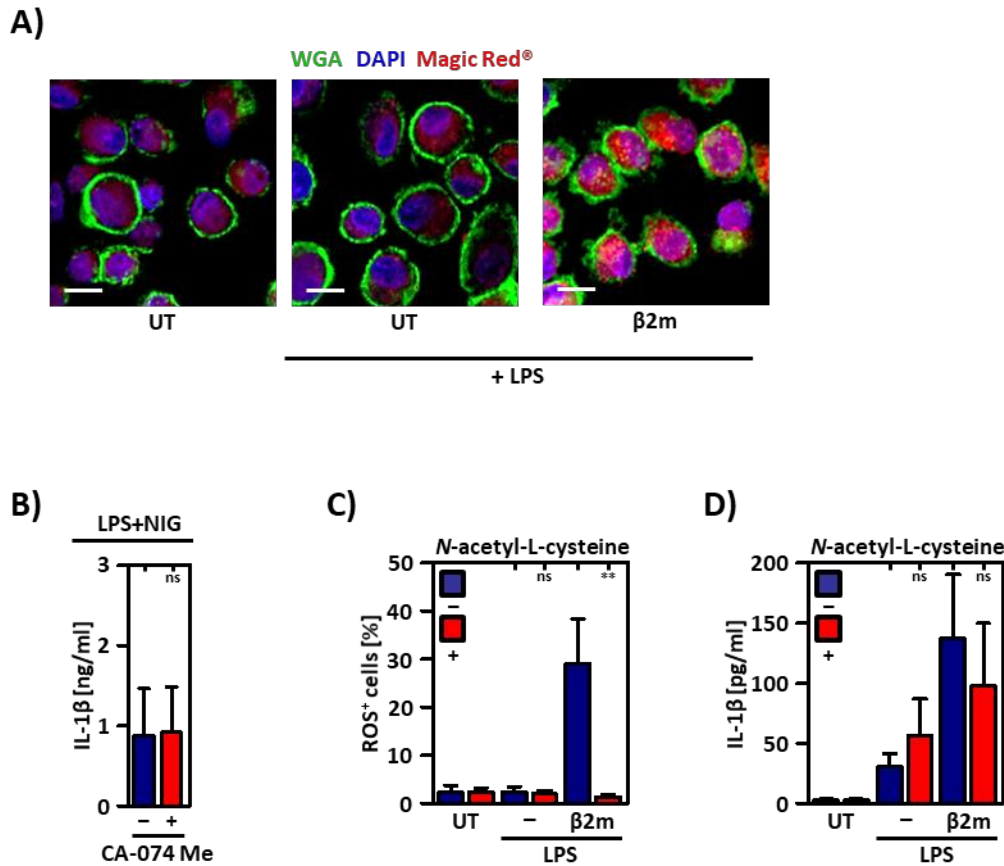
Supplementary Figure 6

Involvement of cathepsin-B and ROS in β2m-mediated NLRP3 inflammasome activation. (A) Confocal microscopy using MAGIC RED® (red) to detect cathepsin B in MΦs left untreated (UT) or primed with LPS (1 μg/ml, 3 h) and overnight-treated with β2m (60 μg/ml). Cell membranes and cell nuclei were stained using WGA (FITC, green) and DAPI (blue). Scale bar: 20 μm. Data representative of at three independent experiments are shown. (**B**) IL-1β release [ng/ml] from MΦs primed with LPS (100 ng/ml, 3 h) and treated with NIigericin (10 μM, 30 min) in the presence (red bar) and absence (blue bar) of cathepsin B-specific inhibitor CA-074 Me (10 μM) as measured by ELISAData representative of at least five independent experiments are shown. (**C**) Flow cytometry using CellROX® Deep Red to detect percentage [%] of ROS+ MΦs left untreated (UT) or primed with LPS (100 ng/ml, 3 h) and treated with β2m (60 μg/ml, 48 h) in the presence (red bars) and absence (blue bars) of anti-oxidant and free radical scavenger N-acetyl-l-cysteine (NAC) (5 mM). (**D**) IL-1β release [pg/ml] from MΦs left untreated (UT) or primed with LPS (100 ng/ml, 3 h) and treated with β2m (60 μg/ml, 6 h) in the presence (red bars) and absence (blue bars) of NAC (5 mM) as measured by ELISA. Results are expressed as mean ± SEM. Data representative of at four independent experiments are shown. *P < 0.05, **P < 0.01, ***P < 0.001.
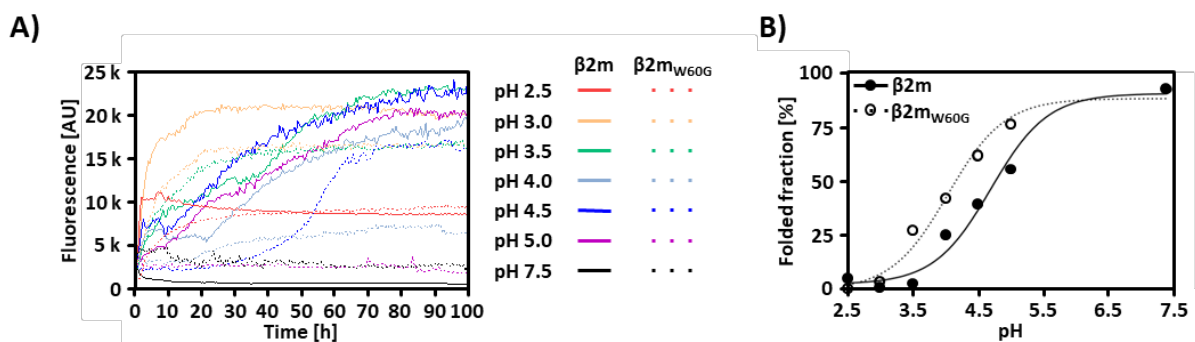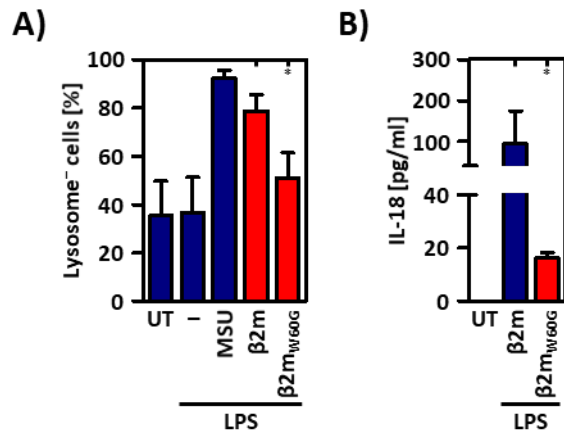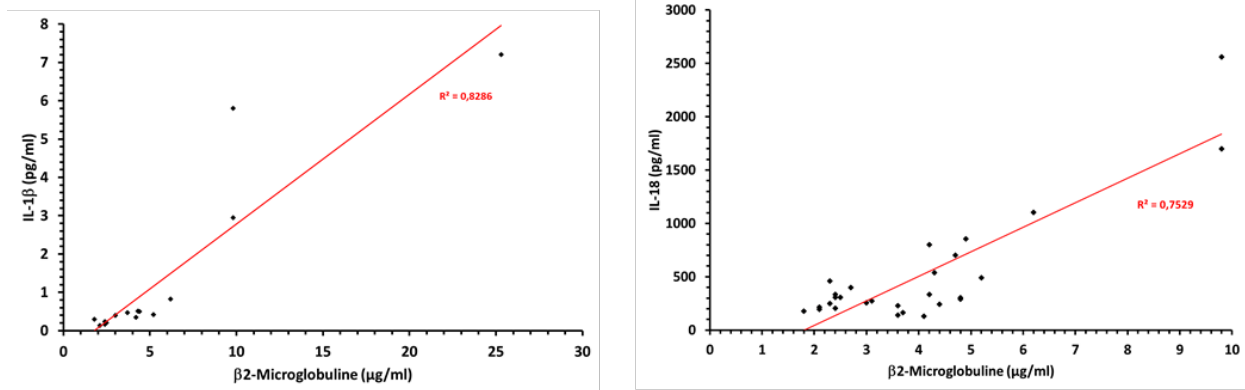
Supplementary Figure 7
Correlation of β2m level in human BM plasma of untreated MM patients with IL-1β or IL-18.
IL-1β [pg/ml] and IL-18 [ng/ml] levels in human BM plasma of untreated MM patients were
correlated with β2m plasma concentrations as measured by ELISA.
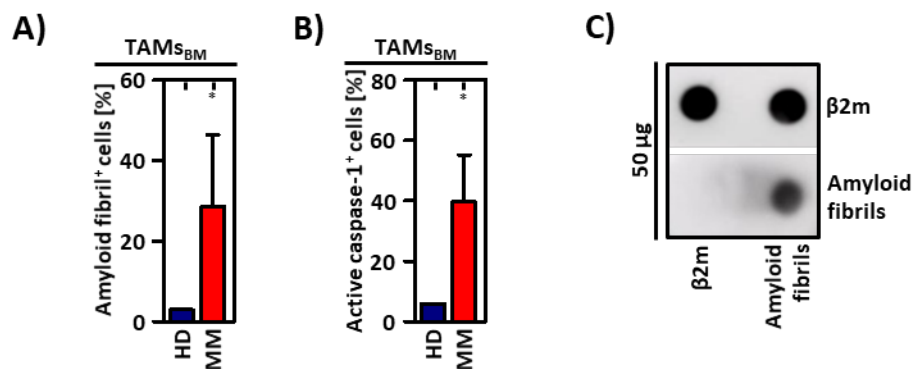
Supplementary Figure 8
Amyloid fibrils in isolated TAMs of HDs and untreated MM patients. (**A-B**) Flow cytometry using
AmyTracker™ 480 and FLICA® 660 to detect percentage [%] of (**A**) amyloid fibril+ and (**B**) active
caspase-1+ TAMs from human BM of HDs (blue bars) and untreated MM patients (red bars).
Data representative of five different MM patients and one HD are shown. (**C**) Dot blot analysis
of β2m and amyloid fibrils (total protein: 50 µg). Data representative of one experiment are
shown.
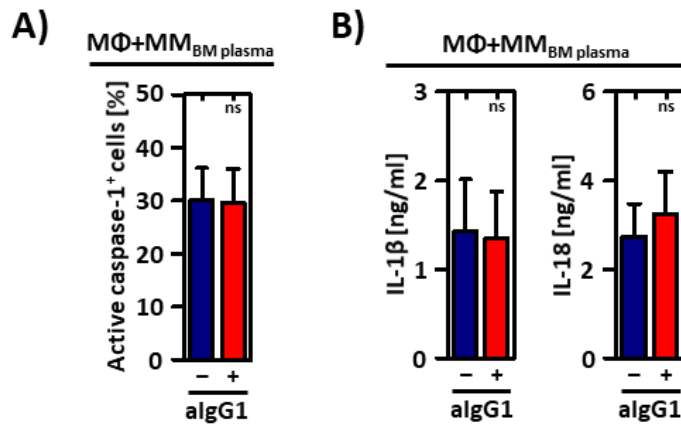
Supplementary Figure 9
(**A**) Flow cytometry using FLICA® 660 to detect percentage [%] of active caspase-1+ MΦs primed with LPS (100 ng/ml, 3 h) and overnight-co-cultured with human BM plasma of untreated MM patients (8 %) in the presence (red bar) and absence (blue bar) of a IgG1-neutralizing antibody (aIgG1) (10 µg/ml). (**B**) IL-1β and IL-18 release [ng/ml] from MΦs primed with LPS (100 ng/ml, 3 h) and overnight-co-cultured with human BM plasma of untreated MM patients (8 %) in the presence (red bars) and absence (blue bars) of a IgG1-neutralizing antibody (aIgG1) (10 µg/ml) as measured by ELISA. Results are expressed as mean ± SEM. Data representative of at least seven different MM patients are shown. Data representative of eleven (**A**) or eight (**B**) independent experiments are shown.
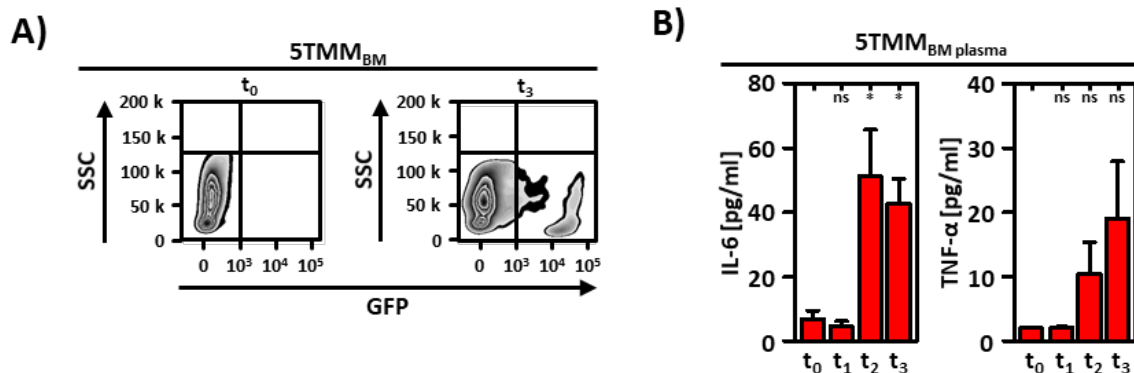
Supplementary Figure 10
Quantification of MM cells, IL-6 and TNF level in 5TMM mice. (**A**) Flow cytometry to detect murine GFP+ MM cells from BM of untreated 5TMM mice at different time points during MM progression (t0, t3). Data representative of four different 5TMM mice. (**B**) IL-6 and TNF-α levels [pg/ml] in murine BM plasma of untreated 5TMM mice at different time points during MM progression (t0, t1, t2, t3) as measured by LEGENDplex™. Data representative of four different 5TMM mice.
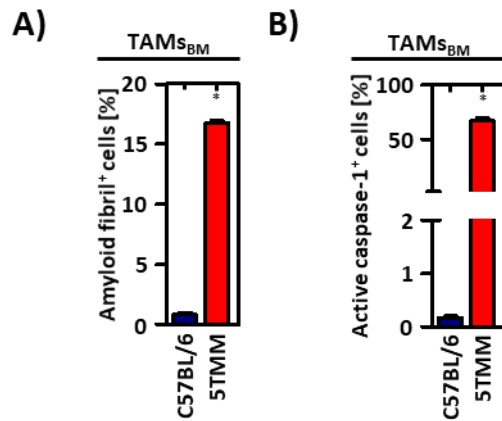
Supplementary Figure 11
Detection of amyloid fibrils in TAMs of 5TMM mice. (**A - B**) Flow cytometry using AmyTracker™ 480 and FLICA® 660 to detect percentage [%] of murine (**A**) amyloid fibril+ and (**B**) active caspase-1+ TAMs from BM of C57BL/6 (blue bars) and untreated 5TMM mice (red bars). Results are expressed as mean ± SEM. Data representative of at least three different 5TMM and C57BL/6 mice are shown.
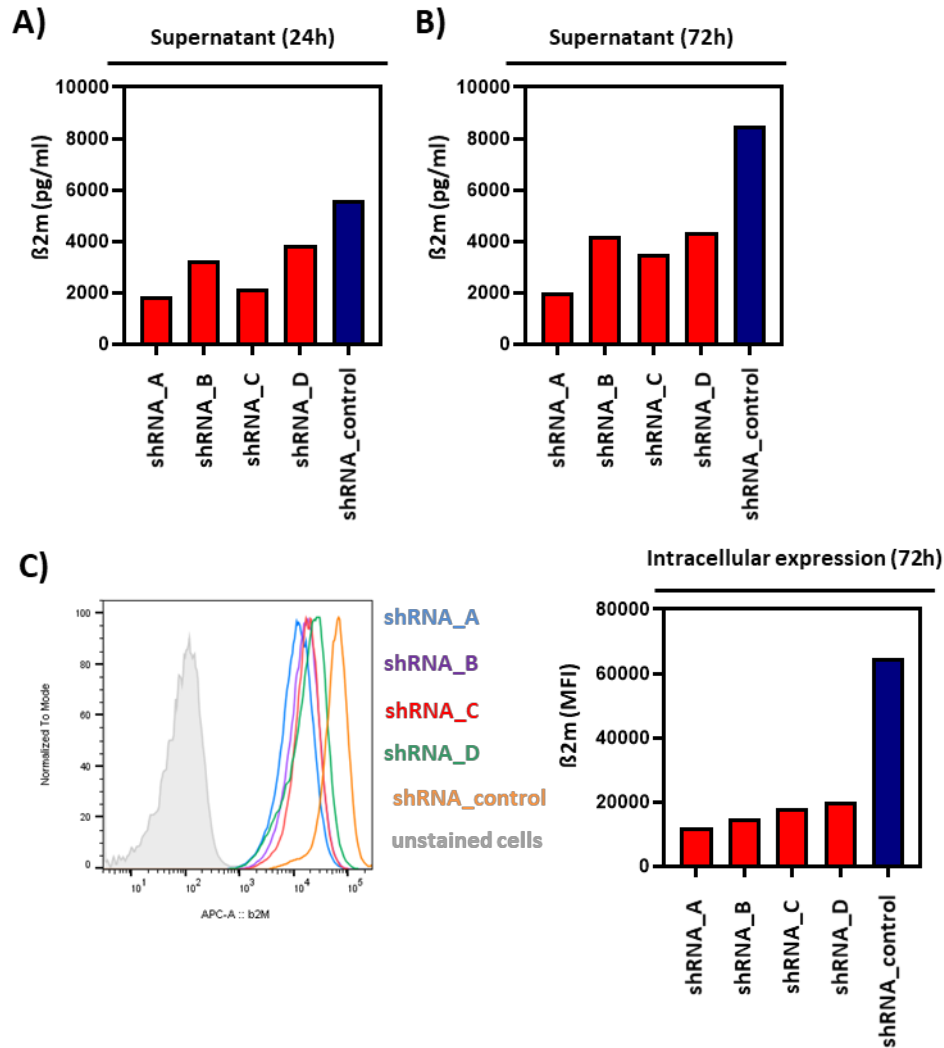
Supplementary Figure 12

Establishment of β2m-low expressing cell lines by shRNA. 5TGM1 cells were transduced with control shRNA (blue bars) or different shRNA variants against β2m (red bars). β2m secretion (A-B) or expression (C-D) was measured by ELISA or FACS respectively. The gray histogram indicates the unstained control (5TGM1 cells without anti-β2m-APC).
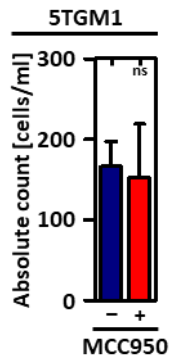
Supplementary Figure 13
Effect of MCC950 on 5TGM1 cells. Flow cytometry using 123count™ eBeads Counting Beads to detect growth [cells/ml] of murine 5TGM1 cells in the presence (red bar) and absence (blue bar) of NLRP3-specific inhibitor MCC950 (10 µM). Data representative of eight independent experiments are shown.
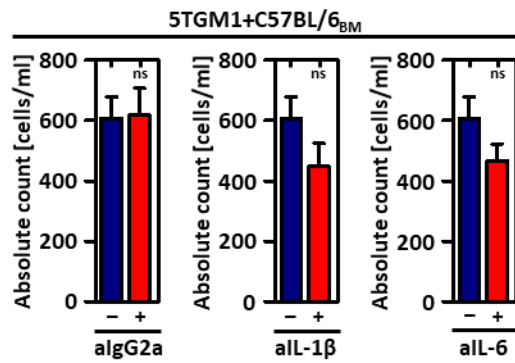
Supplementary Figure 14

Cell growth in the presence of IL-1b and IL-6 blocking antibodies. Flow cytometry using 123count™ eBeads Counting Beads to detect growth [cells/ml] of murine 5TGM1 cells co-cultured with murine BM cells (1:25, 96 h) from C57BL/6 mice in the presence (red bars) and absence (blue bars) of IgG2a, IL-1β and IL-6 neutralizing antibodies (aIgG2a, aIL-1β, aIL-6) (1 µg/ml). Data representative of eight different C57BL/6 mice are shown.
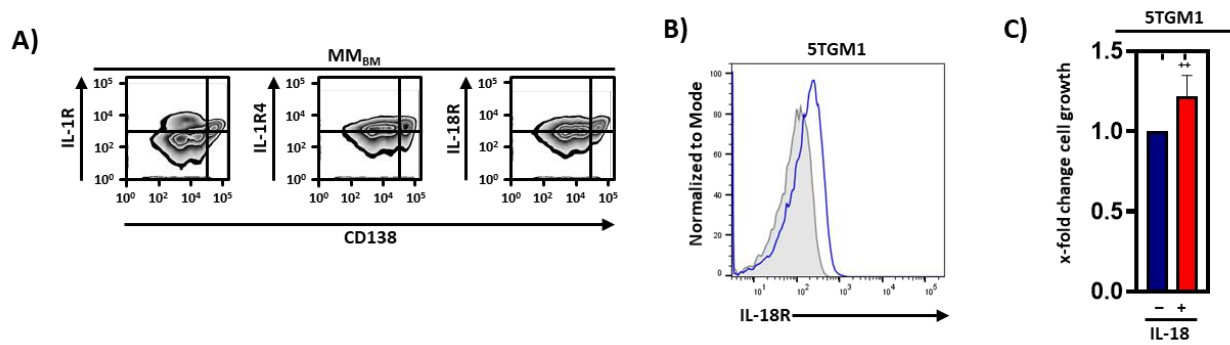
Supplementary Figure 15
(**A**) Flow cytometry to detect protein expression of IL-1R (FITC), IL-1R4 (APC) and IL-18R (PE) on the surface of human CD138 from BM of untreated MM patients. Data representative of eight different MM patients are shown. (**B**) Flow cytometry to detect protein expression of IL-18R (blue line) on the surface of 5TGM1 cells. Gray histogram indicated the isotype control. (**C**) 5TGM1 cells were stimulated with murine recombinant IL-18 (100ng/ml, 24h) and cell growth was measured by FACS. Data representative of four different experiments are shown, **P < 0.01.
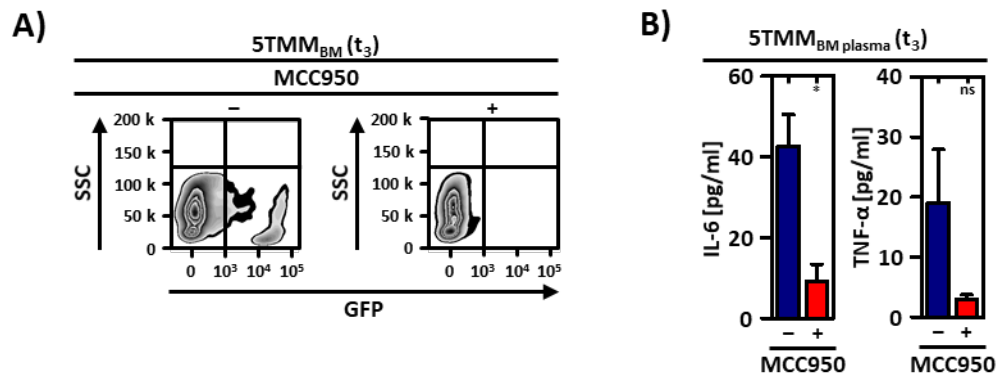
Supplementary Figure 16

Cell growth of MM cells and IL-6 and TNF level in MCC950 treated 5TMM mice. (**A**) Flow cytometry to detect murine GFP+ MM cells from BM of untreated and MCC950-treated (10 mg/kg) 5TMM mice during MM progression (t3). Results are expressed as mean ± SEM. Data representative of at least four different 5TMM mice. (**B**) IL-6 and TNF-α levels [pg/ml] in murine BM plasma of untreated (blue bars) and MCC950-treated (10 mg/kg) (red bars) 5TMM mice during MM progression (t3) as measured by LEGENDplex™. Results are expressed as mean ± SEM. Data representative of four different 5TMM mice. *P < 0.05.

4 NEUROSERPIN

Human neuroserpin (NS) is a secretory protein mainly expressed in neurons of the central and peripheral nervous systems. It belongs to the serine protease inhibitor superfamily and it shares with other serpins the unique fold and mechanism of action (86).

4.1 PHYSIOLOGICAL FUNCTIONS

The main physiological function of NS is the extracellular inhibition of tPA in the nervous system. NS directly controls the level of active tPA and thus provides a natural counter balance of its physiological activity (86).

tPA is a protease that cleaves plasminogen, yielding plasmin, a proteinase with a broad specificity whose roles in the central nervous system are not completely defined yet (135). Besides its role within the plasminogen cascade, the NS/tPA system is also involved in other complex brain functions. During brain development, NS and tPA are widely expressed in nervous tissues, in particular in the axonogenesis and synaptic connection stages (136). Furthermore, NS and tPA are found highly expressed in areas that retain synaptic plasticity, such as hippocampus, cerebellum, and amygdala, thus suggesting a direct role in controlling memory and learning processes (87,137). Finally, NS/tPA has been suggested to regulate the permeability between the vascular and nervous systems compartments during normal brain function and disease (135).

To sum up, NS is involved in a wide variety of functions within the nervous system. Therefore, alteration of NS activity can be detrimental for the processes the serpin is involved in, and gives rise to a series of neurodegenerative symptoms.

4.2 FAMILIAL ENCEPHALOPATHY WITH NEUROSERPIN INCLUSION BODIES

The NS metastable native state makes it susceptible to aberrant conformational changes upon mutations (67). Point mutations of NS are responsible for FENIB (familial encephalopathy with neuroserpin inclusion bodies), a severe neurodegenerative disease. FENIB is characterized by the accumulation of ordered polymers in inclusion bodies (known as Collins bodies) within the endoplasmic reticulum (ER) of neurons (138). It is an autosomal dominant disease that may present several different clinical phenotypes, including dementia, epilepsy, seizure, and loss of memory (30).

The accumulation of polymers composed of mutant NS in inclusion bodies leads to a gain of toxic function phenotype. However, loss of the normal function of NS within the nervous system may also contribute to the pathology. Thus, the pathogenesis in FENIB is likely to arise from these two mechanisms acting together (86).

To date, six NS mutations (Fig. 6) have been associated with FENIB: S49P, S52R, H338R, G392E, G392R and L47P (139). All the mutations are located around the β-sheet A and affect the stability of the region (Fig. 6). In particular, destabilization of the shutter region favours the opening of the β-sheet A and promotes the establishment of intermolecular interactions (86). For the first four mutations, a strong correlation between the tendency to polymerize and the number of Collins bodies and severity of FENIB was found, suggesting a gain of toxic function phenotype for NS polymers (30). Even though the accumulation of NS polymers fails to induce a classical unfolded protein response, the expression of a polymerization-prone variant led to an increase in oxidative stress and predisposed neurons to apoptotic cell death (140).
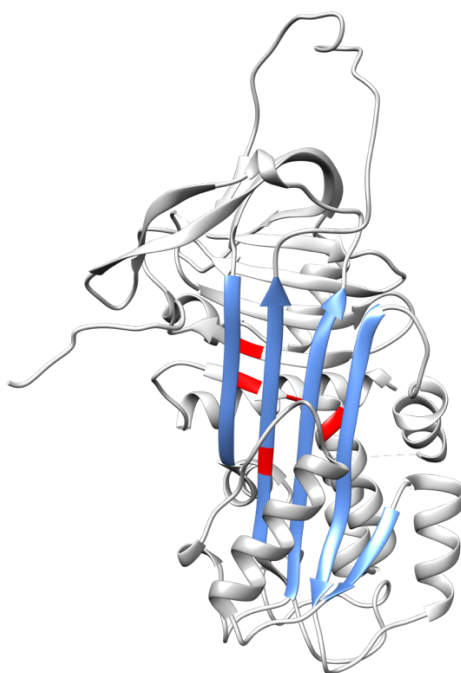
Figure 6. Mutations responsible for FENIB. The mutations associated with FENIB (red) are all localized around the β-sheet A (blue). They induce a destabilization and opening of the β-sheet A and subsequent establishment of intermolecular contacts (Native NS PDB ID 3F5N).

To date FENIB, like all the other serpinopathies, is still incurable. This is due to two main factors. On the one hand, the molecular bases of NS polymers toxicity are still not clearly understood; on the other hand, the lack of knowledge of the structure and elongation mechanism of serpin polymers prevents rational drug design to target the polymeric species. In conclusion, in order to develop tools to fight the serpinopathies, a detailed characterization of the molecular bases underlying the misfolding and polymerization events of serpin is pivotal.

4.3 PHD PROJECTS

This PhD project has been organized to study two different aspects of protein misfolding and aggregation using NS as model system.

Firstly, it was directed to assess the importance of glycosylation for NS stability and polymerization propensity.

Secondly, it focused on the identification of small molecules able to control the polymerization process.

4.3.1 Role of glycosylation in NS

As many other secreted proteins, NS is glycosylated and presents two (N)-linked glycosylation chains on asparagine residues N157 and N321 (141). Interestingly, a third glycosylation site, not used in the wild-type variant, has been described as partially glycosylated in position N401 for the pathological NS mutant G392E (139).

The presence of glycosylations at N157 and N321 has an important role in NS protein quality control and stability (86). In particular, the post-translational modifications are involved in protein recognition by ER chaperones and other lectins for quality control and folding, for selection of misfolded molecules, for degradation by ERAD, and for transport out of the ER (142). In addition, the glycan chains help NS to keep its physiological active and monomeric state (143). Indeed, if the glycosylation pattern is impaired by specific mutation of N157 or N321 residues, the handling of NS is similar to the pathological FENIB mutants and accumulation of NS polymers occurs (139). Thus, the sugars chains are essential to maintain NS in its physiological active state and to prevent aberrant intermolecular linkages that can lead to serpin polymers formation.

To date, all the biochemical and biophysical characterisations of NS have been done using recombinant protein purified from *E. coli* (137). However, the bacterially expressed NS not always reproduces its behaviour as observed in physiologic contexts. In order to get further details on the molecular properties of NS, we expressed, purified and characterized glycosylated NS (gNS). In particular, the biophysical and biochemical characterization of gNS highlighted the importance of glycan chains in stabilizing NS and in reducing its polymerization propensity.

Glycosylation Tunes Neuroserpin Physiological and Pathological Properties

Cristina Visentin, Luca Broggini, Benedetta Maria Sala, Rosaria Russo, Alberto Barbiroli, Carlo Santambrogio, Simona Nonnis, Anatoly Dubnovitsky, Martino Bolognesi, Elena Miranda, Adnane Achour and Stefano Ricagno*

I contributed to this work by helping in setting the conditions for expression and purification of gNS.

I was involved in the biochemical and biophysical characterization: in particular, I performed CD experiments, polymerization assays, and activity tests on both NS and gNS.

Article

Glycosylation Tunes Neuroserpin Physiological and Pathological Properties

Cristina Visentin [1], **Luca Broggini** [1], **Benedetta Maria Sala** [1,2,3], **Rosaria Russo** [4], **Alberto Barbiroli** [5], **Carlo Santambrogio** [6], **Simona Nonnis** [7], **Anatoly Dubnovitsky** [8], **Martino Bolognesi** [1], **Elena Miranda** [9], **Adnane Achour** [2] and **Stefano Ricagno** [1,*]

[1] Dipartimento di Bioscienze, Università degli Studi di Milano, Via Celoria, 26, 20133 Milan, Italy; cristina.visentin@unimi.it (C.V.); luca.broggini@unimi.it (L.B.); bmsala@kth.se (B.M.S.); martino.bolognesi@unimi.it (M.B.)

[2] Science for Life Laboratory, Department of Medicine Solna, Karolinska Institute, and Division of Infectious Diseases, Karolinska University Hospital, Solna, SE-17176 Stockholm, Sweden; adnane.achour@ki.se

[3] Department of Protein Science, School of Engineering Sciences in Chemistry, Biotechnology and Health, AlbaNova University Center, Royal Institute of Technology, SE-10691 Stockholm, Sweden

[4] Dipartimento di Fisiopatologia Medico-Chirurgica e dei Trapianti, Università degli Studi di Milano, Via Fratelli Cervi, 93, 20090 Segrate, Italy; rosaria.russo@unimi.it

[5] Dipartimento di Scienze per gli Alimenti, la Nutrizione e l'Ambiente, Università degli Studi di Milano, Via Celoria, 2, 20133 Milan, Italy; alberto.barbiroli@unimi.it

[6] Dipartimento di Biotecnologie e Bioscienze, Università degli Studi di Milano-Bicocca, Piazza dell'Ateneo Nuovo, 1, 20126 Milan, Italy; carlo.santambrogio@unimib.it

[7] Departimento di Medicina Veterinaria, Università degli Studi di Milano, Via dell'Università, 6, 26900 Lodi, Italy; Simona.Nonnis@unimi.it

[8] Science for Life Laboratory, Department of Medicine Solna, Karolinska Institutet, and Division of Rheumatology, Karolinska University Hospital, Solna, SE-17176 Stockholm, Sweden; anatoly.dubnovitsky@ki.se

[9] Dipartimento di Biologia e Biotecnologie 'Charles Darwin', and Istituto Pasteur - Fondazione Cenci-Bolognetti, Sapienza Università di Roma, Piazzale Aldo Moro, 5, 00185 Rome, Italy; mariaelena.mirandabanos@uniroma1.it

[*] Correspondence: stefano.ricagno@unimi.it

Abstract: Neuroserpin (NS) is a member of the serine protease inhibitors superfamily. Specific point mutations are responsible for its accumulation in the endoplasmic reticulum of neurons that leads to a pathological condition named familial encephalopathy with neuroserpin inclusion bodies (FENIB). Wild-type NS presents two N-glycosylation chains and does not form polymers in vivo, while non-glycosylated NS causes aberrant polymer accumulation in cell models. To date, all in vitro studies have been conducted on bacterially expressed NS, de facto neglecting the role of glycosylation in the biochemical properties of NS. Here, we report the expression and purification of human glycosylated NS (gNS) using a novel eukaryotic expression system, LEXSY. Our results confirm the correct N-glycosylation of wild-type gNS. The fold and stability of gNS are not altered compared to bacterially expressed NS, as demonstrated by the circular dichroism and intrinsic tryptophan fluorescence assays. Intriguingly, gNS displays a remarkably reduced polymerisation propensity compared to non-glycosylated NS, in keeping with what was previously observed for wild-type NS in vivo and in cell models. Thus, our results support the relevance of gNS as a new in vitro tool to study the molecular bases of FENIB.

Keywords: neuroserpin; protein polymerisation; glycosylation

1. Introduction

Neuroserpin (NS) is a human protein mainly expressed in the nervous system [1]. This protein is ascribed to the serine protease inhibitor (serpin) superfamily with which it shares the conserved serpin fold and mechanism of action [1,2]. Even though its physiological roles are not completely elucidated, NS activity is involved in memory, learning, and both synaptic and neurovascular compartment plasticity [3–5]. NS, as any member of the serpin superfamily, is characterised by the presence of a long and flexible loop, named the reactive centre loop (RCL), essential for its physiological function [6,7]. The RCL is recognized by the tissue plasminogen activator (tPA), the target protease [8]. Upon binding to NS, tPA hydrolyses the RCL loop at position Arg362 with the concomitant formation of acyl complex NS-tPA. The RCL cleavage triggers a major structural rearrangement in which the N-terminal portion of the cleaved RCL is inserted into the central ß-sheet A between strands 3A and 5A [9]. Typically, in serpins, such conformational change causes the disruption of the protease active site and prevents the hydrolysis of the acyl-complex, rendering this covalent complex extremely stable over time [10]. During the conformational change from the native to the RCL-cleaved form, a consistent stabilization of the serpin molecule takes place, yielding a cleaved form that is hyper-stable [11]. However, opposite to other serpin-protease pairs, the NS-tPA complex is short-living and rapidly dissociates at physiological pH, releasing free cleaved NS and active tPA [6,12,13]. Another serpin inhibitor of tPA, plasminogen activator inhibitor-1 (PAI1), is instead forming a long-living acyl-complex whose dissociation has never been observed [12]. Compared to PAI1, NS discriminates between tPA and uPA (urokinase-type plasminogen activator), and between the single- or double-chain tPA [12]. The pH also plays an important role in the stability of the NS-tPA complex [13]. Lee et al. demonstrated that strands sC1 and sC2 and helices hCD and hE contribute to the recruitment of tPA and to the stabilization of the NS-tPA complex [14]. Monomeric NS can access a third conformation, the latent fold, where the uncleaved RCL is inserted in the β-sheet A, similar to the cleaved conformation [2,11]. Both these NS conformations are extremely stable and unable to load, and consequently to inhibit, tPA.

NS mutations are responsible for the onset of familial encephalopathy with neuroserpin inclusion bodies (FENIB), a severe and fatal serpinopathy characterized by progressive neurodegeneration. Epilepsy, cognitive impairment and dementia are the main clinical symptoms reported for the patients. FENIB is a rare and autosomally dominant genetic disorder for which the age of onset and the severity of clinical manifestations are strictly correlated to the specific mutation carried by the patient [15]. There are six known point mutations related to FENIB: S49P, S52R, H338R, G392E, G392R, and L47P [16–19]. Mutated NS undergoes polymerization and deposits within the endoplasmic reticulum of neurons, where it accumulates as inclusion bodies [17,20] causing a poorly characterized neuronal toxicity that involves oxidative stress and apoptosis [21]. The structural features of polymeric NS are not completely understood yet. In all the polymerisation models reported for the prototypical serpin alpha-1 antitrypsin, the RCL loop exerts a crucial role and is thought to be inserted in β-sheet A of the neighbouring monomers as part of the intermolecular link [22,23], or intramolecularly to provide flexibility for the domain swap that links monomers into polymeric chains [23].

The monomeric and polymeric NS conformers can be discriminated using specific structural signatures in different spectroscopic techniques: the circular dichroism (CD) spectra of latent and polymeric NS show a more intense signal compared to native NS [24,25], and Noto et al. reported the possibility to profile each conformer using protein intrinsic fluorescence, i.e., the emission spectra of tryptophan or tyrosine residues within NS [25].

As many other secreted proteins, human NS is glycosylated in vivo and presents two N-linked glycosylation chains on asparagine residues N157 and N321. A third aberrant glycosylation chain added in N401 has been observed for the G392E pathological NS mutant and causes abundant polymer accumulation within the endoplasmic reticulum in cell models of FENIB [15,26–30]. The presence of the post-translational modifications is known to play an important role in the NS protein quality control [29] and stability [29,30]. In particular, Schipanski et al. [29] and Moriconi et al. [30] reported that the glycosylation plays a pivotal role in keeping NS in its physiological monomeric

state in HEK and COS-7 cells. When the physiologic glycosylation pattern is artificially impaired by the specific mutation of N157 and N321 residues, the behaviour of wild-type NS is reminiscent of the pathological FENIB mutants, and the accumulation of NS polymers was observed in the endoplasmic reticulum [30]. The effect was additive and the abrogation of both glycosylation sites caused an even more pronounced accumulation of NS polymers [30].

To date, only rat NS has been expressed glycosylated [31]; indeed, all the in vitro biochemical and biophysical studies on human NS have been conducted using recombinant protein purified from *E. coli* [8]. Curiously, in contrast to the studies conducted in vivo and in cell cultures models, purified NS efficiently polymerises in vitro even after short incubation times and at temperatures only slightly higher than the physiological 37 °C [24,25,32]. This suggests that, although technically convenient, bacterially expressed human NS does not reproduce the behaviour of this protein as observed in more physiologic contexts. These considerations highlighted the need to assess the role of the N-glycosylation in the molecular properties of the human wild-type NS in vitro. Thus, in order to shed light on this conundrum, we report here for the first time the expression, purification and characterisation of recombinant N-glycosylated human NS (gNS) produced using LEXSY® (*Leishmania tarentolae* expression system), an eukaryotic expression system based on *L. tarentolae* cells [33]. N-glycosylation by *Leishmania* spp. is more equivalent to the mammalian counterpart compared to other model organisms, e.g., insect cells or fungi [33]. For this reason, the use of LEXSY is particularly suitable for the expression of human glycosylated protein.

The presence of the correct glycosylation pattern and the conformational and biophysical properties of gNS were assessed in comparison with non-glycosylated bacterially purified NS, confirming the correct fold of the glycosylated variant (gNS). A marked reduction was observed in the heat-induced polymerisation propensity of gNS compared to NS. Finally, gNS displays a slightly increased efficiency in inhibiting tPA activity in vitro. Taken together, here, we produced a glycosylated version of NS that shares all molecular properties of native NS but, importantly, it better recapitulates NS polymerisation propensity, as observed in vivo and in cell models. Thus, gNS should be considered a valuable new in vitro tool to study NS polymerisation and its inhibition.

2. Results and Discussion

2.1. Expression and Purification of Glycosylated NS

In order to successfully express human NS in the LEXSY system, a *Leishmania*-optimised sequence of the NS gene was cloned into pLEXSY-sat2, an integrative plasmid for constitutive expression. The NS gene was cloned in frame with a 6-His tag engineered at the N-*terminus*. To improve the amount of secreted protein, the commercial secretion signal peptide was substituted with the modified sequence of the SP5 signal peptide (Figure 1A) [34]. Once stable expressing clones were obtained, protein expression was carried out for 60 h at 26 °C. NS expressed in LEXSY (thereafter named gNS) was purified from the growth medium after removing intact cells and cellular debris. Two steps of chromatography were performed to isolate the gNS monomer: an initial Ni-NTA affinity chromatography (AC) was followed by a size exclusion chromatography step (SEC) (Figure S1A). About 7 mg of highly pure monomeric gNS was obtained per litre of LEXSY culture, but, undesirably, nearly 80% of the purified protein was in the cleaved form (Figure 1B). The addition of cocktails of protease inhibitors in the medium did not ameliorate the proteolytic pattern (data not shown).

In vitro purified NS displayed a highly reproducible tendency to autoproteolysis over time, which is accelerated upon temperature increase (Figure S2). Thus, we hypothesise that the prolonged incubation of NS at 26 °C in LEXSY medium was responsible for this phenomenon. In order to minimize NS cleavage, the expression protocol was modified: after 60 h of culture, cells were collected, resuspended into fresh medium and incubated 16 h at 18 °C (Figure S1B). Next, purification steps were performed as reported above. The purification of gNS from such 16 h of growth resulted in a significantly increased amount of uncleaved native NS; however, the yield was reduced to 2 mg per litre of culture and a minor residual fraction of cleaved gNS was still present (Figure 1C).

A

MASRLVRVLAAAMLVAAAVSVAMAHHHHHHTDPTG
ATFPEEAIADLSVNMYNRLRATGEDENILFSPLSIALA
MGMMELGAQGSTQKEIRHSMGYDSLKNGEEFSFLK
EFSNMVTAKESQYVMKIANSLFVQNGFHVNEEFLQ
MMKKYFNAAVNHVDFSQNVAVANYINKWVENNTNN
LVKDLVSPRDFDAATYLALINAVYFKGNWKSQFRPE
NTRTFSFTKDDESEVQIPMMYQQGEFYYGEFSDGS
NEAGGIYQVLEIPYEGDEISMMLVLSRQEVPLATLEP
LVKAQLVEEWANSVKKQKVEVYLPRFTVEQEIDLKD
VLKALGITEIFIKDANLTGLSDNKEIFLSKAIHKSFLEV
NEEGSEAAAVSGMIAISRMAVLYPQVIVDHPFFFLIR
NRRTGTILFMGRVMHPETMNTSGHDFEEL

B

C

Figure 1. Human glycosylated NS (gNS) expression and purification in LEXSY. (**A**) Primary sequence of the construct used for gNS expression in LEXSY (UniProtKB - Q99574). The signal peptide sequence is colored in blue, the HisTag is green and the spacer in grey. The neuroserpin (NS) sequence is black, the glycosylation sites are in red and the triangle highlights the protease cleavage site. (**B**) SDS-PAGE analysis of gNS purification after AC and SEC chromatographic steps according to the protocol shown in Figure S1A. (**C**) SDS-PAGE analysis of optimized gNS purification after the AC and SEC chromatographic steps (see also Figure S1B). Abbreviations: Nat: native; CL: cleaved; AC: affinity chromatography; SEC: size exclusion chromatography.

2.2. gNS Is Properly Glycosylated

The presence of appropriate glycosylation on LEXSY-expressed gNS was verified using several complementary techniques. First, the migration of gNS in denaturing polyacrylamide gel electrophoresis (SDS-PAGE) was delayed compared to NS (Figure 6D). The increment of molecular mass was in agreement with the presence of N-glycan chains.

The presence of N-linked glycosylation was thereafter confirmed by enzymatic deglycosylation using peptide-N-glycosidase F (PNGaseF) and endoglycosidase H (EndoH). Both enzymes remove N-linked oligosaccharides, but with different specificities. The first enzyme is an amidase that removes all types of mammalian N-linked glycans, whereas EndoH removes only high-mannose and some hybrid types of N-linked glycans. As reported in Figure 2A, gNS was susceptible only to PNGaseF treatment, resulting in a faster migration in SDS-PAGE, whereas incubation with EndoH caused no reduction in molecular mass. Altogether, these results confirm the presence of N-glycosylation along the secretory pathway and the delivery of gNS with mature glycans to the growth medium. In agreement, previously identified N-glycans from an *L. tarentolae* recombinant glycoprotein consisted mostly of the mammalian complex biantennary and the paucimannose Man3GlcNAc2 structures [33]; such glycans are known to be effectively cleaved by PNGase F but not by Endo H [35].
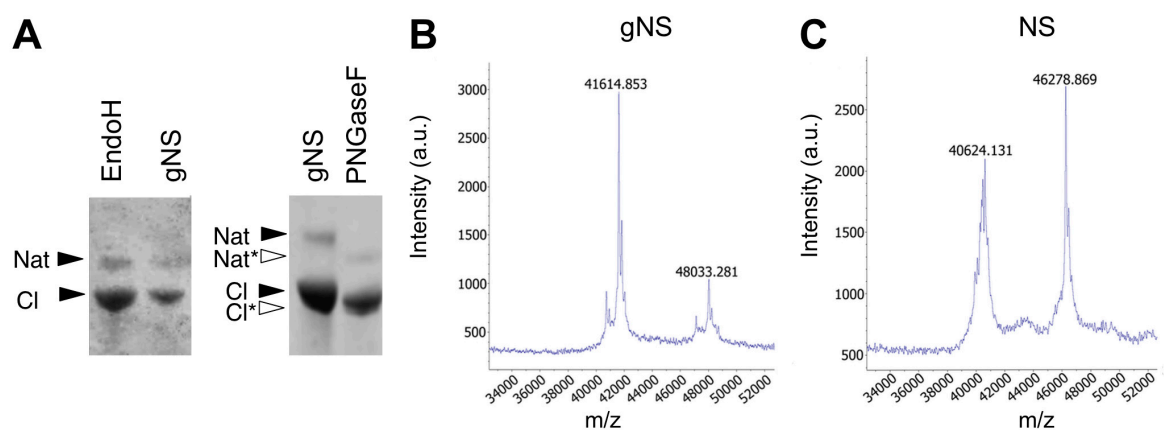
Figure 2. Assessment of N-glycosylation. (**A**) SDS-PAGE analysis of the enzymatic deglycosylation of gNS using EndoH or PNGaseF deglycosylases. All samples are a mixture of native and cleaved forms. Black and white arrows refer to lane 1 (gNS) and lane 2 (PNGaseF), respectively. (**B–C**) Matrix-assisted laser desorption ionisation-time of flight (MALDI-TOF) MS spectra of NS (**B**) and gNS. Abbreviations: Nat: native; Nat*: deglycosylated Nat; Cl: cleaved; Cl*: deglycosylated Cl.

In order to determine the precise protein molecular mass, matrix-assisted laser desorption ionisation-time of flight (MALDI-TOF) MS analyses under native conditions were performed both on gNS and NS proteins. As shown in Figure 2C, the masses of native and cleaved NS, detected at 46,279 and 40,624 Da, respectively, allow for clearly identifying the presence of the cleavage site at Arg362. Moreover, the masses of the gNS protein were detected at 48,033 Da and 41,615 Da for the native and cleaved protein forms, respectively (Figure 2B). The increment in the molecular mass of gNS compared to its theoretical mass unambiguously confirmed the presence of post-translational modifications in gNS.

In order to map the glycosylation sites, the peptides obtained by the tryptic in-gel digestion of gNS were analysed by UHPLC-MS/MS. The identified gNS peptides, which provided a sequence coverage of 74%, are listed in Table S1 in the Supplementary Material. Two glycopeptides were detected (Table ST1 and Figure 3), corresponding to glycosylation sites at positions N157 and N321. These glycopeptides were not present in a similar analysis performed on gNS deglycosylated by PNGaseF (data not shown).

Thus, the mass increment observed on gNS compared to NS was due to two occupied N-glycosylation sites. Further experiments would be required to elucidate the corresponding glycan structures.

Overall, these results confirmed that NS produced using the LEXSY expression system presents two N-glycosylations in the sites previously reported [30].
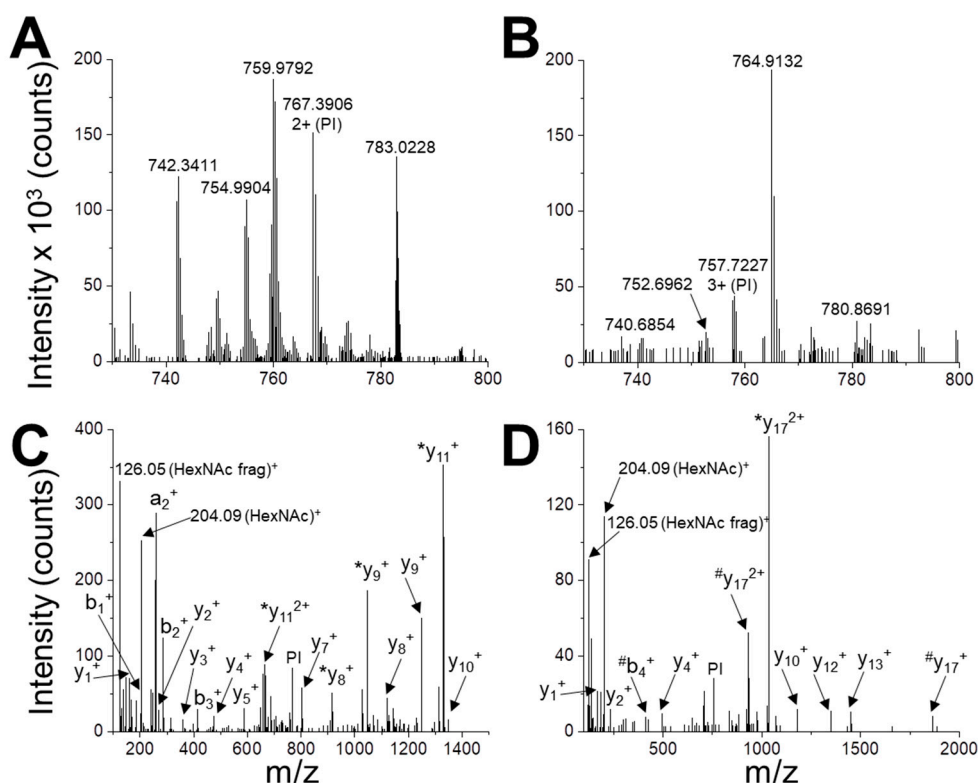
Figure 3. Identification of N-glycosylation sites. UHPLC-MS/MS analysis of glycopeptides WVENNTNNLVK (**A**,**C**) and DANLTGLSDNKEIFLSK (**B**,**D**). The peptides are detected in the MS spectrum as 2+ ion with m/z = 767.3906 (**A**) and 3+ ion with m/z = 757.7227 (**B**). These signals are selected and used as parent ions (PIs) for higher energy collision dissociation (HCD) fragmentation (**C**,**D**). Two glyco-diagnostic peaks are present in the fragmentation spectra (HexNAc, m/z 204.09; HexNAc fragment, m/z 126.05 Da), indicating that PIs are glycopeptides. Identified a-, b- and y-fragment ions are labelled (*, loss of HexNAc during fragmentation; #, loss of HexNAc2 during fragmentation).

2.3. Conformational Analysis of gNS

The potential impact of N-glycosylation at residues N157 and N321 on protein structure was evaluated by assessing the secondary structures content of gNS and NS by circular dichroism (CD) analyses. Comparison of the far-UV spectra of gNS and NS is presented in Figure 4A. The two CD spectra perfectly superpose, suggesting that the heterologous expression in LEXSY produces properly folded gNS and that its secondary structure is virtually identical to those of previously characterised NS [6,7]. Even if bacterially expressed NS is not glycosylated, it represents a good reference for NS folding since it was reported that the glycan is not required for the acquirement and maintenance of the serpin fold [30]. Next, the stability and potential conformational changes of gNS were monitored by molar ellipticity at 216 nm, along a temperature ramp from 20 to 95 °C. While bacterial NS undergoes two irreversible transitions at 56.6 and 87.0 °C (Figure 4B in accordance with [24]), the gNS temperature ramp displays two very minor increases (more negative) in CD signal at about 60 and 93 °C (Figure 4C). The conformational changes underlying such signals are irreversible, as the CD signal becomes even more negative when the sample was cooled down (Figure 4C). This typically indicates a gain of secondary structure, connected with latentisation and/or polymerisation reminiscent of what was observed for bacterial NS [24]. The comparison of Far-UV CD spectra recorded before and after the temperature ramp indicate that the latter shows a stronger CD signal (Figure 4D). The more regular structure of the RCL in the latent and polymeric conformers likely accounts for the increased CD signal, as previously reported [24].

It has been reported that intrinsic fluorescence can be informative of NS conformation [25]. For this reason, intrinsic tryptophan fluorescence was recorded to study gNS fold. The spectra of native or SEC-purified polymeric gNS are analysed and compared in Figure 4E. Native gNS presented a main peak at 330 nm, whereas, for the gNS polymers, a red shift and the quenching of the tryptophan signal were detected. These effects observed for polymeric gNS may be ascribed to an increased exposure of tryptophan residues in gNS polymers, similar to what has already been reported in the literature for bacterially expressed NS [7,25,36].

In conclusion, these data indicate that gNS is properly folded and that its overall structure closely resembles the one of bacterially expressed NS.
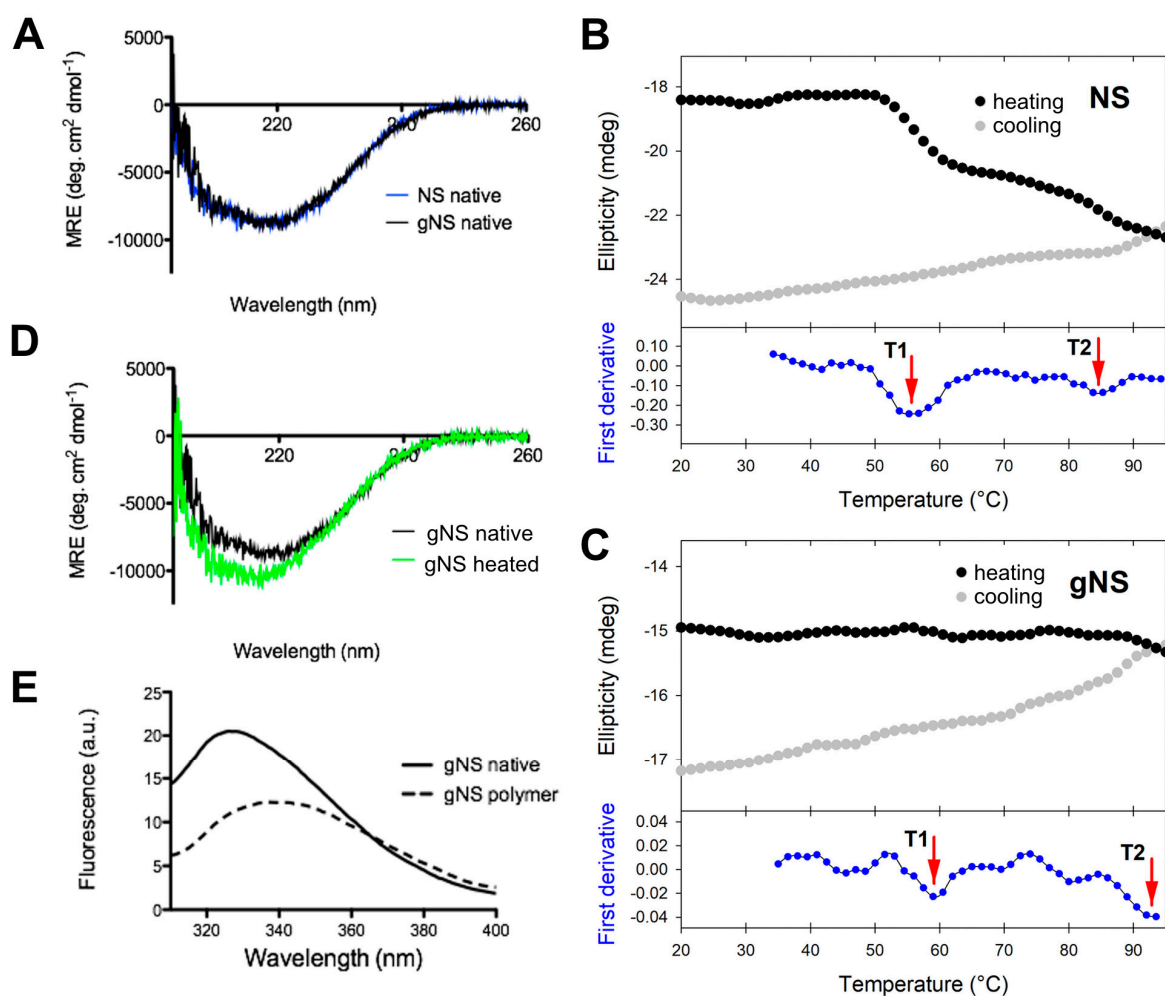
Figure 4. Conformational characterisation of gNS. (**A**) Far-UV circular dichroism (CD) spectra of native gNS and NS recorded at 20 °C. (**B,C**) Temperature ramp of NS (**B**) analogously reported in [24] and gNS (**C**) performed recording ellipticity at 216 nm during heating from 20 to 95 °C (black) and cooling down (grey). The first derivative is reported in the bottom (blue) and the two transitions T1 and T2 are highlighted by the red arrows. (**D**) Far-UV CD spectra of gNS recorded at 20 °C before (black) or after (green) heating the sample to 95 °C. (**E**) Intrinsic tryptophan fluorescence of native (solid line) and polymeric (dashed line) gNS recorded at 20 °C. The buffer 20 mM Tris-HCl pH 8, 50 mM KCl was used in all the measurements.

2.4. gNS Inhibits tPA In Vitro

Then the ability of gNS to inhibit tPA in vitro was assessed. The activity of tPA on its chromogenic substrate IPR-pNA was measured in the presence or absence of gNS or NS, monitoring absorbance at 405 nm. While in the absence of NS or gNS the absorbance due to IPR-pNA hydrolysis rapidly reached a plateau, in the presence of gNS and NS, the absorbance at 405 nm increased more

slowly and remained almost constant, indicating that both NS and gNS displayed similar inhibitory activity against tPA (Figure 5A). The inhibition of tPA by a sample of gNS incubated for 24 h at 45 °C was also tested and tPA was completely active when compared to the control reaction (Figure 5A), indicating that, during incubation, gNS has lost its inhibitory activity. This is likely due to the formation of the inactive polymer and latent forms and the concomitant disappearance of native gNS.
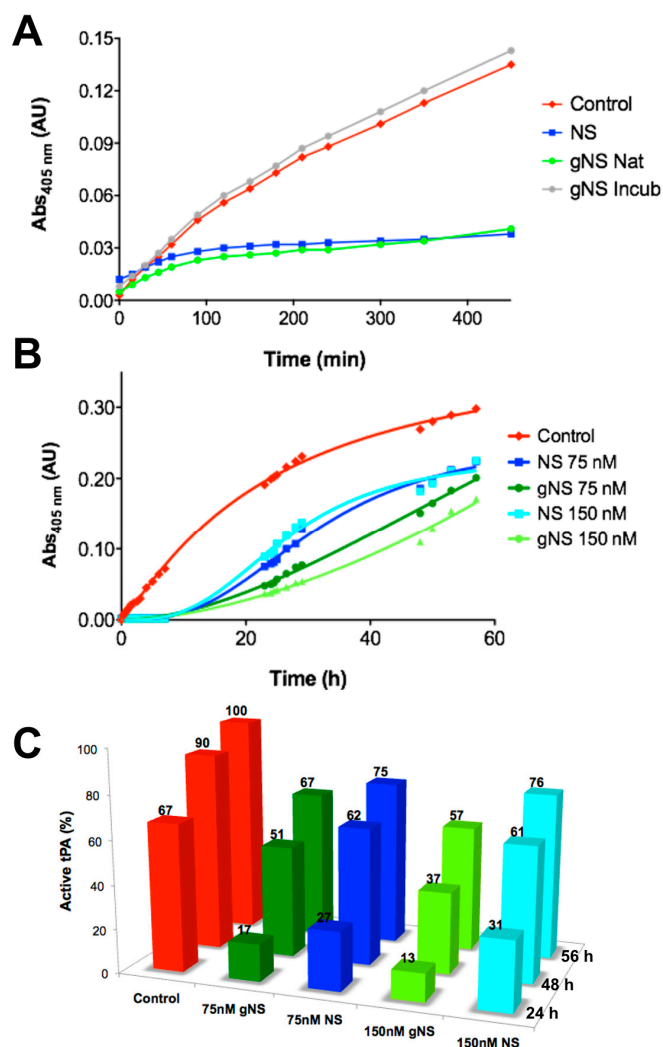
Figure 5. Comparison of tissue plasminogen activator (tPA) inhibition by NS and gNS. (**A**) tPA activity tests in the absence (red) and presence of 60 nM of NS (blue), native (green) or incubated for 24 h at 45 °C (grey) gNS. (**B**) The ability of gNS and NS to inhibit tPA at two different concentrations (75 and 150 nM) was compared. (**C**) The inhibitory efficiency of gNS or NS is reported in comparison to the control reaction. The activity of tPA in the positive control after 56 h is set to 100% and all other values have been normalised accordingly. In the control reaction, no gNS or NS was added.

The inhibition of tPA by gNS and NS was tested for longer times and at different concentrations (Figure 5B,C). It is apparent that gNS is a marginally more efficient inhibitor of tPA proteolytic activity since the substrate was hydrolysed more slowly in the presence of gNS than in the presence of NS (Figure 5B). Figure 5C shows more quantitively than panel 5B the different tPA inhibitions by NS and gNS. The percentage of active tPA at different times of incubation is reported in comparison with the control reaction without inhibitors. During the first 24 h of incubation time, the comparison of tPA activity in the presence of gNS or NS shows marked differences at both concentrations tested. In particular, curves in Figure 5B show that, after about 15 h, substrate hydrolysis by tPA is markedly increasing in the presence of NS, while, in the presence of gNS, tPA activity grows more slowly, displaying lower rate of hydrolysis for the first 50 h. At the end of the experiment (56 h), the difference

in inhibitory efficiency tends to level up even though gNS was still a marginally better inhibitor than NS (Figure 5B,C). These observations strongly suggest a higher stability—i.e., slower rate of hydrolysis—of the gNS-tPA covalent complex compared to the one formed by NS-tPA. Although the gNS-tPA complex remains transient, the presence of the two N-glycans seem to stabilise the tPA-gNS complex with a consequent slower deacylation rate [14]. The full description of this observation and the molecular bases of this stabilisation by the presence of the glyco-antennas will require further characterisation in a future work.

2.5. Glycosylation Reduces Heat-Induced Polymerisation of gNS

The role of glycosylation during the heat-induced polymerization process was next evaluated. Solutions of gNS and NS at a concentration of 63.8 μM were incubated at 45 °C and the presence of polymeric species was assessed at different time points using SEC and both non-denaturing and denaturing PAGE (Figure 6). Most of the bacterially purified NS was already assembled into large polymeric species after 3 h of incubation and only a minor peak corresponding to monomeric NS was visible (Figure 6A). Non-denaturing PAGE confirmed the presence of very large polymers, as they were barely entering in the non-denaturating PAGE (Figure 6C). The denaturing PAGE analysis of aliquots of the same samples assessed the SDS-solubility of these species (Figure 6D). Thus, as previously shown [24], at 45 °C, NS undergoes rapid conformational changes, leading to the formation of a great excess of polymers over the latent conformer.

In contrast, gNS displayed a remarkably different behaviour. First, even after 24 h of incubation, only a minor amount of polymeric form was detected by SEC (Figure 4B) and non-denaturing PAGE (Figure 4C). Moreover, polymers formed by gNS were eluted at 10–12 mL in SEC, in contrast to the large polymers formed by bacterially purified NS that were eluted into the dead volume of the column (Figure 6B). Analogously, in non-denaturating PAGE, gNS polymers displayed an apparent lower mass range (Figure 6C) compared to polymers formed by bacterially expressed NS. When analysed by denaturing PAGE, the gNS polymers dissolved and migrated as monomeric gNS, as observed for the bacterially purified counterpart (Figure 6D). It should be noted that, even though a small amount of polymers was observed upon incubation at 45 °C, most of the gNS remained monomeric, as shown in SEC and non-denaturating gel (Figure 6B,C). The different migration of gNS in the non-denaturating gel suggests that the native conformer disappears over time (Figure 6C). Overall, these data indicate that, in the presence of glycosylation, polymer formation is greatly reduced. Importantly, gNS polymerisation propensity is in line with previous observations in vivo and in cell models of FENIB where wild-type NS does not accumulate in polymeric deposits [26,37]. These results reinforce the hypothesis that the presence of glycan is crucial in preventing aberrant interaction between NS monomers [30].

The lack of inhibitory activity observed in vitro by incubated gNS (Figure 5A) suggests that the native gNS undergoes a conformational change resulting in the formation of the inactive latent conformation, as also suggested by Figure 6C.
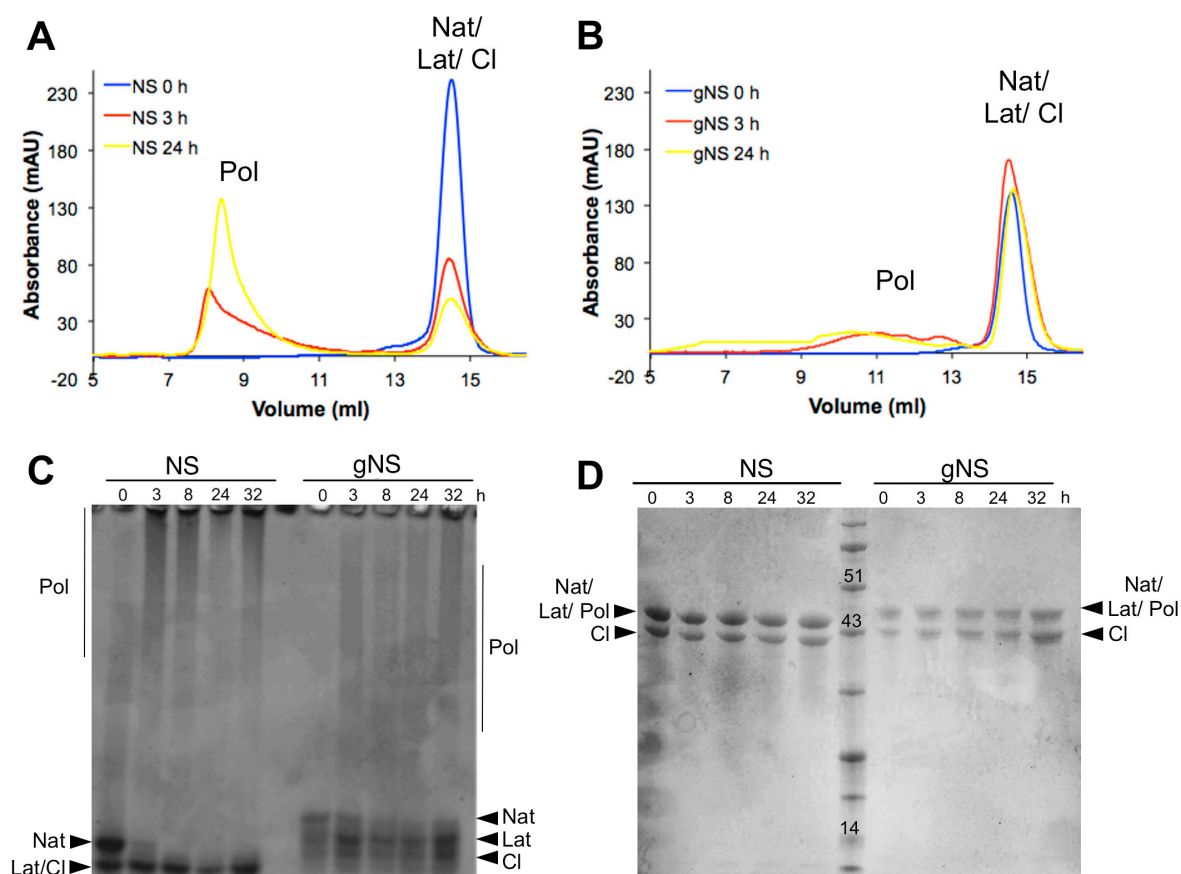
Figure 6. Heat-induced polymerisation of gNS. A solution of gNS or NS was incubated at 45 °C and analysed at different time points. SEC analysis of NS (**A**) or gNS (**B**) using an Increase Superdex 200 column. Aliquots of NS or gNS were analysed by non-denaturing (**C**) and denaturing (**D**) PAGE. Abbreviations: Nat: native; Cl: cleaved; Lat: latent; Pol: polymers.

3. Materials and Methods

3.1. LEXSY Plasmid and Strain

The cassette containing the sequence of the human NS gene optimized for *Leishmainia tarentolae* codon bias, in fusion at the N-terminus with the sequence for the secretion signal peptide (5'-ATGGCTAGCCGTCTCGTCCGGGTGCTCGCAGCGGCAATGCTGGTGGCAGCCGCTGTCTCCGT CGCAATGGCC-3') and the 6-His tag, was sub-cloned into the pLEXSY-sat2 plasmid (Jena Bioscience, Jena, Germany) using *NcoI* and *Kdel* restriction enzymes (New England Lab, NEB, Ipswich, MA, USA). pCloneGZ/NS and pLEXSY-sat2 were digested with *NcoI* and *Kdel*. The digestion products were gel-purified and ligated using the Quik Ligation kit (NEB). The resulting pLEXSY-sat2/NS plasmid was linearized with SwaI restriction enzyme (Thermo Fisher Scientific, Waltham, MA, USA). All the amplification steps were performed in *E. coli* XL1 cells (Invitrogen, Thermo Fisher Scientific, Waltham, MA, USA) at 30 °C for plasmid stability reasons. LEXSY host P-10 cells (Jena Biosciences) were transfected with linearized pLEXSY-sat2/NS plasmid and plated on freshly prepared agar plates (40 mM Hepes pH 7.4, 26 g/L brain heart infusion, 10% inactivated fetal calf serum, 1% bactoagar, 50 µg/mL hemin, 1 unit/mL penicillin and 0.1 mg/mL streptomycin, 100 µg/mL nourseothricin, NTC). After 2 weeks at 26 °C, colonies were inoculated into Brain Heart Infusion (BHI) medium supplemented with 50 µg/mL hemin, 1 unit/mL penicillin, 100 µg/mL streptomycin (BHI-complete medium) and 100 µg/mL NTC.

Protein expression was evaluated by dot-blot using monoclonal anti-NS(m19) primary antibody and HRP-coupled anti-rabbit IgG. Membranes were developed using Pierce ECL Western Blotting

substrate (Thermo Fisher Scientific, Waltham, MA, USA). All chemicals were purchased from Sigma Aldrich (St. Louise, MO, USA), and NTC was bought from Jena Bioscience.

3.2. gNS Expression and Purification

Transformed LEXSY cells were cultured at 26 °C in BHI complete medium, always added with NTC, in a ventilated tissue flask in static suspension in the dark. Cultures were split two times a week with a 1:20 dilution into fresh medium. For large-scale protein expression, cells were cultured 50 h under 220 rpm shaking at 26 °C in the dark and then collected by centrifugation during 15 min at 4500 *g*. The cell pellet was resuspended in the same volume of fresh BHI-complete medium and incubated for 16 h at 18 °C. Finally, cells were collected 15 min at 10,500 *g* and the supernatant was concentrated using an Amicon Millipore ultrafiltration system. Concentrated culture medium was dialyzed against buffer A (20 mM Tris-HCl pH 8.0, 10 mM imidazole, 300 mM NaCl) to remove hemin and loaded onto a 5-mL HiTrap Chelating HP Amersham column (GE Healthcare, Chicago, IL, USA) previously equilibrated with the same buffer. Proteins were eluted in buffer B (20 mM Tris-HCl pH 8.0, 250 mM imidazole, 300 mM NaCl) after a washing step at 10% of buffer B. Monomers were further isolated by gel filtration using an Hi Load 16/60 Superdex200 column (GE Healthcare) equilibrated in 10 mM Tris-HCl, 50 mM KCl, pH 8.0. All purifications steps were performed at 4 °C. All chemicals were purchased from Sigma-Aldrich, unless differently specified. NS concentration was measured by optical absorption using an extinction coefficient at 280 nm of 37,360 M^{-1} cm^{-1}. Due to the impossibility to obtain a completely native sample of gNS, all experiments comparing gNS and bacterially expressed NS were performed using a mix of native and cleaved NS in a ratio similar to gNS samples allowing reliable comparisons.

3.3. NS Expression and Purification

E. coli BL21 Rosetta (DE3) pLysS Competent Cells Novagen (Merck KGaA) transformed with pQE81L plasmid carrying the human NS gene with a N-terminus 6-His tag were used to express and purify NS as reported in [6]. Briefly, bacterial cells were grown in Superior Broth (Molecular Dimension) containing 100 μg/mL ampicillin, and protein expression was induced with 0.2 mM isopropyl-β-D-thiogalactopyranoside at 17 °C for 16 h. NS was purified from the soluble fraction. Buffer A supplemented with cOmplete protease inhibitor cocktail (Hoffmann-La Roche, Basel, Switzerland) was added, and the cell pellets were immediately sonicated. Crude extract was clarified by centrifugation and filtered before being loaded onto a 1-mL HiTrap Chelating HP column (GE Healthcare) previously equilibrated with buffer A. Protein was eluted in 100% buffer B. Monomers were further isolated by gel filtration using an Hi Load 16/60 Superdex200 column (GE Healthcare) equilibrated in 10 mM Tris-HCl, 50 mM KCl, pH 8.0. All purification steps were performed at 4 °C and all chemicals were purchased from Sigma-Aldrich, unless differently specified. NS concentration was measured by optical absorption using an extinction coefficient at 280 nm of 37,360 cm^{-1} M^{-1}.

3.4. NS Autoproteolysis Assay

A solution of 63.8 μM of NS in 10 mM Tris-HCl, 50 mM KCl, pH 8 or 7.6 was incubated at 26 °C or 37 °C. At different time of incubation, an aliquot was subjected to denaturing-PAGE. Gels were stained with Coomassie Brilliant Blue R-250. The experiment was repeated at least three times, and representative gel is reported.

3.5. Deglycosylation Assay

Deglycosylation was performed using a peptide-N Glycosydase F (PNGase) deglycosylation kit (NEB) in non-denaturing conditions or an endoglycosydase H (EndoH) deglycosylation kit (NEB). According to the manufacturer's instruction, 10 μg of gNS was diluted in GlycoBuffer and 2 μl of PNGaseF was added. Protein mix was incubated at 37 °C for 16 h before SDS-PAGE analysis. For EndoH digestion, 10 μg of gNS were diluted in Glycoprotein denaturing buffer and incubated 10 min at 80 °C prior to the addition of 2 μL of the enzyme. The mixture was incubated 5 h at 37 °C and

analysed by SDS-PAGE. In both assays, a solution of 10 µg gNS were prepared in the same experimental conditions but with no enzyme as a negative control. The experiment was repeated at least three times and representative gels are reported.

3.6. MALDI-TOF MS Analysis

Matrix-assisted laser desorption ionisation-time of flight (MALDI-TOF) mass analysis was carried out on concentrated NS or gNS solutions. NS and gNS constructs have slightly different Histag constructs: the theoretical mass is 46,271 and 45,810 Da, respectively. Purified protein samples were diluted with 0.1% trifluoroacetic acid in water (TFA) to a final concentration of 10 pmol/µL, prior protein precipitation with 50% trichloroacetic acid (TCA). Each sample was loaded onto a MALDI target plate using the dry droplet technique and sinapinic acid (SA) in 0.1% TCA:acetonitrile (2:1) as matrix. Mass spectrometry analysis was carried out by a Bruker Daltonics Reflex III instrument (Bruker Daltonics, Billerica, MA, USA) equipped with a nitrogen laser (337 nm), operating in linear positive mode. Each spectrum was accumulated for at least 200 laser shots and protein calibration standards II (Bruker Daltonics) were used for calibration [38]. The PeptideMass tool (http://www.expasy.org/tools/peptide-mass.html) was used to calculate the theoretical masses of native and cleaved NS and gNS proteins and for identifying NS cleavage site.

3.7. UHPLC-MS/MS Analysis

Ultra performance liquid chromatography-tandem mass spectrometry (UHPLC-MS/MS) analysis were performed on gNS and deglycosylated tryptic peptides obtained by a standard in-gel digestion protocol [39] applied on gel bands of gNS and gNS deglycosylated with PNGaseF. After digestion, the peptides were desalted by C18 Ziptips (Millipore, Burlington, MA, USA) and injected on an Orbitrap Fusion mass spectrometer equipped with a nano-UHPLC system EASY 1000 (Thermofisher). Peptides were separated by a 1-h gradient (aqueous phase: milliQ water, 0.1% formic acid; organic phase: 80% acetonitrile, 20% milliQ water, 0.1% formic acid), detected by the orbitrap analyzer, and subjected to a first fragmentation step by Higher energy Collision Dissociation (HCD). The corresponding HCD fragmentation spectra allowed the for identification of unmodified peptides by the software Proteome Discoverer (Thermo Fisher). In the case of glycopeptides, instead, HCD fragmentation mainly generates intense reporter ions of the glyco-antenna, e.g., HexNAc, 204.09 Da. This feature was exploited to selectively trigger a second fragmentation step by EThcD, a combination of HCD and Electron Transfer Dissociation (ETD), in order to better identify the peptide sequence and map the modification site [40].

3.8. Circular Dichroism Analysis

CD measurements were carried out on 4.5 µM NS or gNS in 10 mM Tris-HCl, 50 mM KCl, pH 8.0, by a J-810 spectropolarimeter (Jasco, Mary's Court Easton, MD, USA) equipped with a PFD-425S temperature controller module (Jasco), in a 0.1 cm path-length cuvette. Temperature ramps ware performed recording ellipticity at 216 nm during sample heating from 20 to 95 °C and following cooling from 95 to 20°C (temperature slope 1.0 °C/min). First, the derivative of the data has been calculated and plotted to determine the temperature of transitions.

3.9. Intrinsic Protein Fluorescence Assay

The intrinsic tryptophan fluorescence of 11 µM monomeric or polymeric gNS was measured in a FP-8200 spectro-fluorimeter (Jasco) at 20 °C. Emission spectra from 310 to 410 nm were recorded and 295 nm was used as an excitation wavelength. Each trace is the average of the accumulation of three spectra.

3.10. Polymerisation Assay

Solution of 63.8 µM NS or gNS in 10 mM Tris-HCl pH 8.0 and 50 mM KCl were incubated at 45 °C. Aliquots at different incubation time were collected and analysed by size exclusion

chromatography (SEC) using a Superdex 200 Increase 10/300 GL column (GE Healthcare Europe GmbH). An aliquot of each sample was subsequently subjected to non-denaturing polyacrylamide gel electrophoresis. The experiment was repeated at least three times and representative gels are reported.

3.11. Non-denaturing Polyacrylamide Gel Electrophoresis (PAGE)

Samples were prepared as previously reported [41]. Briefly, aliquots of gNS or NS at different times of incubation at 45 °C were collected and mixed at a 1:1 volume ratio with a non-denaturing loading buffer (250mM Tris-HCl, 50% glycerol, 0.5% bromophenol blue, pH 6.8). Samples were separated into 7.5 % non-denaturing polyacrylamide gels run at 90 V for 2 h at 4 °C to prevent sample denaturation and/or polymer dissociation. Gels were stained with Coomassie Brilliant Blue R-250. The experiment was repeated at least three times and representative gels are reported.

3.12. Inhibitory Activity Test

The inhibition of two-chain tissue plasminogen activator (2ctPA, American Diagnostica, Pfungstadt, Germany) by NS or gNS was determined in the presence of the chromogenic substrate H-D-Ile-Pro-Arg-p-nitroanilide (IPR-pNA; Chromogenix, Werfer, L'Hospitalet de Llobregat, Spain) by recording the pNA accumulation upon substrate cleavage. The reaction was prepared mixing 60, 75 or 150 nM NS, 250 μM IPR-pNA, 1 nM 2ctPA in 50 mM Tris-HCl pH 7.4, 10 mM Na_2HPO_4, 150 mM NaCl, and 0.1% Tween and incubated at 25 °C [42]. The reaction was monitored at 405 nm in an Ultraspec 2100 Pro spectrophotometer (Amersham Bio, Little Chalftont, UK). The curves shown are representative of all the performed experiments.

4. Conclusions

In summary, we report here the expression, purification and characterisation of human N-glycosylated NS. Recombinant gNS is properly glycosylated in the physiologic positions N154 and N321, which were previously identified [30]. Moreover, gNS is properly folded and it is a marginally better in vitro inhibitor of tPA activity than non-glycosylated NS. Crucially, the presence of the two N-glycosylation chains impacts gNS propensity to pathologic polymerisation. More specifically, while non-glycosylated NS efficiently forms polymers in vitro, the formation of gNS polymers is slow and marginal. Although the present data do not provide a detailed explanation for this observation, gNS low polymerisation propensity may be due to the steric hindrance of the two glycan chains and to the slight increase in gNS fold stability, as seen in Figure 4B,C. Here, we show that the artifactual polymerisation propensity observed for wild-type NS expressed in bacteria is due to the absence of a proper glycosylation, while gNS displays a behaviour closely resembling what has been observed in vivo and in cell systems. Thus, gNS may be seen as a valuable tool to properly characterise the polymerisation propensity of the FENIB mutants in vitro.

Abbreviations

AC	Affinity chromatography
CD	Circular dichroism
Cl	Cleaved neuroserpin
EndoH	Endoglycosidase H
FENIB	Familial encephalopathy with neuroserpin inclusion bodies
Frag	Proteolytic neuroserpin fragment
gNS	Glycosylated NS
Lat	Latent neuroserpin
LEXSY	Leishmania expression system
MALDI-TOF	Matrix Assisted Laser Desorption/Ionization - Time of Flight Mass
MS	Spectrometry
Nat	Native neuroserpin
NS	Neuroserpin
PNGaseF	Peptide -N-Glycosidase F
Pol	Polymeric neuroserpin
RCL	Reactive centre loop
SDS-PAGE	Sodium Dodecyl Sulphate - PolyAcrylamide Gel Electrophoresis
SEC	Size exclusion chromatography
SERPIN	Serine Protease Inhibitor
tPA	Tissue Plasminogen Activator
UHPLC MS/MS	Ultra high performance liquid chromatography - tandem mass spectrometer

References

1. Miranda, E.; Lomas, D.A. Neuroserpin: A serpin to think about. *Cell. Mol. Life Sci.* **2006**, *63*, 709–722. doi:10.1007/s00018-005-5077-4.

2. Whisstock, J.C.; Bottomley, S.P. Molecular gymnastics: Serpin structure, folding and misfolding. *Curr. Opin. Struct. Biol.* **2006**, *16*, 761–768. doi:10.1016/j.sbi.2006.10.005.

3. Hastings, G.A.; Coleman, T.A.; Haudenschild, C.C.; Stefansson, S.; Smith, E.P.; Barthlow, R.; Cherry, S.; Sandkvist, M.; Lawrence, D.A. Neuroserpin, a brain-associated inhibitor of tissue plasminogen activator is localized primarily in neurons. Implications for the regulation of motor learning and neuronal survival. *J. Biol. Chem.* **1997**, *272*, 33062–33067. doi:10.1074/jbc.272.52.33062.

4. Yepes, M.; Lawrence, D.A. Tissue-type plasminogen activator and neuroserpin: A well-balanced act in the nervous system? *Trends Cardiovasc. Med.* **2004**, *14*, 173–180. doi:10.1016/j.tcm.2004.03.004.

5. Galliciotti, G.; Sonderegger, P. Neuroserpin. *Front. Biosci.* **2006**, *11*, 33–45. doi:10.2741/1778.

6. Ricagno, S.; Caccia, S.; Sorrentino, G.; Antonini, G.; Bolognesi, M. Human neuroserpin: Structure and time-dependent inhibition. *J. Mol. Biol.* **2009**, *388*, 109–121. doi:10.1016/j.jmb.2009.02.056.

7. Takehara, S.; Onda, M.; Zhang, J.; Nishiyama, M.; Yang, X.; Mikami, B.; Lomas, D.A. The 2.1-A crystal structure of native neuroserpin reveals unique structural elements that contribute to conformational instability. *J. Mol. Biol.* **2009**, *388*, 11–20. doi:10.1016/j.jmb.2009.03.007.

8. Caccia, S.; Ricagno, S.; Bolognesi, M. Molecular bases of neuroserpin function and pathology. *Biomol. Concepts* **2010**, *1*, 117–130. doi:10.1515/bmc.2010.019.

9. Gooptu, B.; Lomas, D.A. Conformational pathology of the serpins: Themes, variations, and therapeutic strategies. *Annu. Rev. Biochem.* **2009**, *78*, 147–176. doi:10.1146/annurev.biochem.78.082107.133320.

10. Huntington, J.A.; Read, R.J.; Carrell, R.W. Structure of a serpin-protease complex shows inhibition by deformation. *Nature* **2000**, *407*, 923–926. doi:10.1038/35038119.

11. Onda, M.; Belorgey, D.; Sharp, L.K.; Lomas, D.A. Latent S49P neuroserpin forms polymers in the dementia familial encephalopathy with neuroserpin inclusion bodies. *J. Biol. Chem.* **2005**, *280*, 13735–13741. doi:10.1074/jbc.M413282200.

12. Barker-Carlson, K.; Lawrence, D.A.; Schwartz, B.S. Acyl-enzyme complexes between tissue-type plasminogen activator and neuroserpin are short-lived in vitro. *J. Biol. Chem.* **2002**, *277*, 46852–46857. doi:10.1074/jbc.M207740200.

13. Carlson, K.-S.B.; Nguyen, L.; Schwartz, K.; Lawrence, D.A.; Schwartz, B.S. Neuroserpin Differentiates Between Forms of Tissue Type Plasminogen Activator via pH Dependent Deacylation. *Front. Cell. Neurosci.* **2016**, *10*, 154. doi:10.3389/fncel.2016.00154.

14. Lee, T.W.; Yang, A.S.-P.; Brittain, T.; Birch, N.P. An analysis approach to identify specific functional sites in orthologous proteins using sequence and structural information: Application to neuroserpin reveals regions that differentially regulate inhibitory activity. *Proteins* **2015**, *83*, 135–152. doi:10.1002/prot.24711.

15. Miranda, E.; MacLeod, I.; Davies, M.J.; Pérez, J.; Römisch, K.; Crowther, D.C.; Lomas, D.A. The intracellular accumulation of polymeric neuroserpin explains the severity of the dementia FENIB. *Hum. Mol. Genet.* **2008**, *17*, 1527–1539. doi:10.1093/hmg/ddn041.

16. Davis, R.L.; Shrimpton, A.E.; Holohan, P.D.; Bradshaw, C.; Feiglin, D.; Collins, G.H.; Sonderegger, P.; Kinter, J.; Becker, L.M.; Lacbawan, F.; et al. Familial dementia caused by polymerization of mutant neuroserpin. *Nature* **1999**, *401*, 376–379. doi:10.1038/43894.

17. Coutelier, M.; Andries, S.; Ghariani, S.; Dan, B.; Duyckaerts, C.; van Rijckevorsel, K.; Raftopoulos, C.; Deconinck, N.; Sonderegger, P.; Scaravilli, F.; et al. Neuroserpin Mutation Causes Electrical Status Epilepticus of Slow-Wave Sleep. *Neurology* **2008**, *71*, 64–66. doi:10.1212/01.wnl.0000316306.08751.28.

18. Davis, R.L.; Shrimpton, A.E.; Carrell, R.W.; Lomas, D.A.; Gerhard, L.; Baumann, B.; Lawrence, D.A.; Yepes, M.; Kim, T.S.; Ghetti, B.; et al. Association between conformational mutations in neuroserpin and onset and severity of dementia. *Lancet* **2002**, *359*, 2242–2247. doi:10.1016/S0140-6736(02)09293-0.

19. Hagen, M.C.; Murrell, J.R.; Delisle, M.-B.; Andermann, E.; Andermann, F.; Guiot, M.C.; Ghetti, B. Encephalopathy with Neuroserpin Inclusion Bodies Presenting as Progressive Myoclonus Epilepsy and Associated with a Novel Mutation in the Proteinase Inhibitor 12 Gene. *Brain Pathol.* **2011**, *21*, 575–582. doi:10.1111/j.1750-3639.2011.00481.x.

20. Davis, R.L.; Holohan, P.D.; Shrimpton, A.E.; Tatum, A.H.; Daucher, J.; Collins, G.H.; Todd, R.; Bradshaw, C.; Kent, P.; Feiglin, D; et al. Familial encephalopathy with neuroserpin inclusion bodies. *Am. J. Pathol.* **1999**, *155*, 1901–1913. doi:10.1016/S0002-9440(10)65510-1.

21. Guadagno, N.A.; Moriconi, C.; Licursi, V.; D'Acunto, E.; Nisi, P.S.; Carucci, N.; De Jaco, A.; Cacci, E.; Negri, R.; Lupo, G.; et al. Neuroserpin polymers cause oxidative stress in a neuronal model of the dementia FENIB. *Neurobiol. Dis.* **2017**, *103*, 32–44. doi:10.1016/j.nbd.2017.03.010.

22. Lomas, D.A.; Evans, D.L.; Finch, J.T.; Carrell, R.W. The mechanism of Z alpha 1-antitrypsin accumulation in the liver. *Nature* **1992**, *357*, 605–607. doi:10.1038/357605a0.

23. Yamasaki, M.; Li, W.; Johnson, D.J.D.; Huntington, J.A. Crystal structure of a stable dimer reveals the molecular basis of serpin polymerization. *Nature* **2008**, *455*, 1255–1258. doi:10.1038/nature07394.

24. Ricagno, S.; Pezzullo, M.; Barbiroli, A.; Manno, M.; Levantino, M.; Santangelo, M.G.; Bonomi, F.; Bolognesi, M. Two latent and two hyperstable polymeric forms of human neuroserpin. *Biophys. J.* **2010**, *99*, 3402–3411. doi:10.1016/j.bpj.2010.09.021.

25. Noto, R; Santangelo, M.G.; Levantino, M.; Cupane, A.; Mangione, M.R.; Parisi, D.; Ricagno, S.; Bolognesi, M.; Manno, M.; Martorana, V. Functional and dysfunctional conformers of human neuroserpin characterized by optical spectroscopies and Molecular Dynamics. *Biochim. Biophys. Acta* **2015**, *1854*, 110–117. doi:10.1016/j.bbapap.2014.10.002.

26. Miranda, E.; Römisch, K.; Lomas, D.A. Mutants of neuroserpin that cause dementia accumulate as polymers within the endoplasmic reticulum. *J. Biol. Chem.* **2004**, *279*, 28283–28291. doi:10.1074/jbc.M313166200.

27. Davies, M.J.; Miranda, E.; Roussel, B.D.; Kaufman, R.J.; Marciniak, S.J.; Lomas, D.A. Neuroserpin polymers activate NF-kappaB by a calcium signaling pathway that is independent of the unfolded protein response. *J. Biol. Chem.* **2009**, *284*, 18202–18209. doi:10.1074/jbc.M109.010744.

28. Kroeger, H.; Miranda, E.; MacLeod, I.; Pérez, J.; Crowther, D.C.; Marciniak, S.J.; Lomas, D.A. Endoplasmic reticulum-associated degradation (ERAD) and autophagy cooperate to degrade polymerogenic mutant serpins. *J. Biol. Chem.* **2009**, *284*, 22793–22802. doi:10.1074/jbc.M109.027102.

29. Schipanski, A.; Oberhauser, F.; Neumann, M.; Lange, S.; Szalay, B.; Krasemann, S.; van Leeuwen, F.W.; Galliciotti, G.; Glatzel, M. Lectin OS-9 delivers mutant neuroserpin to endoplasmic reticulum associated degradation in familial encephalopathy with neuroserpin inclusion bodies. *Neurobiol. Aging* **2014**, *35*, 2394–2403. doi:10.1016/j.neurobiolaging.2014.04.002.

30. Moriconi, C.; Ordoñez, A.; Lupo, G.; Gooptu, B.; Irving, J.A.; Noto, R.; Martorana, V.; Manno, M.; Timpano, V.; Guadagno, N.A.; et al. Interactions between N-linked glycosylation and polymerisation of neuroserpin within the endoplasmic reticulum. *FEBS J.* **2015**, *282*, 4565–4579. doi:10.1111/febs.13517.

31. Hill, R.M.; Brennan, S.O.; Birch, N.P. Expression, purification, and functional characterization of the serine protease inhibitor neuroserpin expressed in Drosophila S2 cells. *Protein Expr. Purif.* **2001**, *22*, 406–413. doi:10.1006/prep.2001.1463.

32. Belorgey, D.; Sharp, L.K.; Crowther, D.C.; Onda, M.; Johansson, J.; Lomas, D.A. Neuroserpin Portland (Ser52Arg) is trapped as an inactive intermediate that rapidly forms polymers. *Eur. J. Biochem.* **2004**, *271*, 3360–3367. doi:10.1111/j.1432-1033.2004.04270.x.

33. Breitling, R.; Klingner, S.; Callewaert, N.; Pietrucha, R.; Geyer, A.; Ehrlich, G.; Hartung, R.; Müller, A.; Contreras, R.; Beverley, S.M.; et al. Non-pathogenic trypanosomatid protozoa as a platform for protein research and production. *Protein Expr. Purif.* **2002**, *25*, 209–218.

34. Klatt, S.; Konthur, Z. Secretory signal peptide modification for optimized antibody-fragment expression-secretion in Leishmania tarentolae. *Microb. Cell Factories* **2012**, *11*, 97. doi:10.1186/1475-2859-11-97.

35. Trimble, R.B.; Tarentino, A.L. Identification of distinct endoglycosidase (endo) activities in Flavobacterium meningosepticum: Endo F1, endo F2, and endo F3. Endo F1 and endo H hydrolyze only high mannose and hybrid glycans. *J. Biol. Chem.* **1991**, *266*, 1646–1651.

36. Noto, R.; Santangelo, M.G.; Ricagno, S.; Mangione, M.R.; Levantino, M.; Pezzullo, M.; Martorana, V.; Cupane, A.; Bolognesi, M.; Manno, M. The tempered polymerization of human neuroserpin. *PLoS ONE* **2012**, *7*, e32444. doi:10.1371/journal.pone.0032444.

37. Galliciotti, G.; Glatzel, M.; Kinter, J.; Kozlov, S.V.; Cinelli, P.; Rülicke, T.; Sonderegger, P. Accumulation of mutant neuroserpin precedes development of clinical symptoms in familial encephalopathy with neuroserpin inclusion bodies. *Am. J. Pathol.* **2007**, *170*, 1305–1313. doi:10.2353/ajpath.2007.060910.

38. Tedeschi, G.; Pagliato, L.; Negroni, M.; Montorfano, G.; Corsetto, P.; Nonnis, S.; Negri, A.; Rizzo, A.M. Protein pattern of Xenopus laevis embryos grown in simulated microgravity. *Cell Biol. Int.* **2011**, *35*, 249–258. doi:10.1042/CBI20100248.

39. Shevchenko, A.; Tomas, H.; Havlis, J.; Olsen, J.V.; Mann, M. In-gel digestion for mass spectrometric characterization of proteins and proteomes. *Nat. Protoc.* **2006**, *1*, 2856–2860. doi:10.1038/nprot.2006.468.

40. Yu, Q.; Wang, B.; Chen, Z.; Urabe, G.; Glover, M.S.; Shi, X.; Guo, L.W.; Kent, K.C.; Li, L. Electron-Transfer/Higher-Energy Collision Dissociation (EThcD)-Enabled Intact Glycopeptide/Glycoproteome Characterization. *J. Am. Soc. Mass Spectrom.* **2017**, *28*, 1751–1764. doi:10.1007/s13361-017-1701-4.

41. Irving, J.A.; Ekeowa, U.I.; Belorgey, D.; Haq, I.; Gooptu, B.; Miranda, E.; Pérez, J.; Roussel, B.D.; Ordóñez, A.; Dalton, L.E.; et al. The serpinopathies studying serpin polymerization in vivo. *Methods Enzymol.* **2011**, *501*, 421–466. doi:10.1016/B978-0-12-385950-1.00018-3.

42. Saga, G.; Sessa, F.; Barbiroli, A.; Santambrogio, C.; Russo, R.; Sala, M.; Raccosta, S.; Martorana, V.; Caccia, S.; Noto, R.; et al. Embelin binds to human neuroserpin and impairs its polymerisation. *Sci. Rep.* **2016**, *6*, 769. doi:10.1038/srep18769.

4.3.2 EMBELIN-LIKE COMPOUNDS AS NS POLYMERIZATION INHIBITORS

The absence of knowledge on the mechanism of serpin polymer formation as well as the lack of information on their three-dimensional structure make serpinopathies incurable (30). To date, no efficient treatments have been identified even though several approaches have been proposed, including the application of RCL-like peptides or small molecules (30).

Recently, a promising small molecule, embelin (EMB), was found to act as an antagonist of PAI-1, a serpin inhibitor of tPA (144). EMB is a natural occurring para-benzoquinone and it is the major active constituent of *Embelia ribes* fruits (145). It has a wide spectrum of biological activities, including anti-inflammatory, anti-oxidant and anti-tumor (145), and its ability to cross the blood brain barrier make it suitable for developments of treatments of central nervous system disorders (146). A structural characterization of PAI-1/EMB complex revealed that the small molecule binds in a pocket formed by helices B and D and by strands 1 and 2 of the β-sheet A (144). Interestingly, the same region was found to be a source of instability in α_1AT and the introduction of bulky hydrophobic residues filling this cavity resulted in stabilization and decreased polymerization trends (147).

Given the high structural homology between PAI-1, NS and α_1AT (30), EMB was recently tested as NS polymerization inhibitor (148). Notably, it was observed that EMB has the ability to prevent NS polymerization and to dissolve preformed NS polymers. Moreover, it binds to all the conformations of NS and leads to the formation of small and soluble oligomers (148). Nevertheless, the chemical properties of EMB prevent it from being a suitable candidate for further hit development. Indeed, its low polarity and high hydrophobicity account for its poor solubility in water; in addition, EMB elicits its anti-polymerization activity at relatively high concentration, suggesting the need to improve its potentiality.

In order to identify EMB analogues with increased ability to prevent NS polymerization and with an increased solubility in water, we performed a systematic chemical modification of the EMB scaffold. The efficacy of the compounds designed to hamper NS intermolecular assembly was eventually tested *in vitro* by polymerization assays. Our data indicated that none of the tested compound recapitulate the anti-polymerization properties of EMB, suggesting that the para-benzoquinone molecule is still the best candidate for the development of treatments against FENIB.

Embelin as Lead Compound for New Neuroserpin Polymerization Inhibitors

Cristina Visentin, Loana Musso, Luca Broggini, Francesca Bonato, Rosaria Russo, Claudia Moriconi, Martino Bolognesi, Elena Miranda, Sabrina Dallavalle, Daniele Passarella and Stefano Ricagno*

I contributed to this work by setting the protocols for NS expression and production. I produced the protein and assessed its quality and purity.
I also performed polymerization assays in presence and absence of EMB-like compounds and evaluate the results.

Embelin as Lead Compound for New Neuroserpin Polymerization Inhibitors

Cristina Visentin [1,†]**, Loana Musso** [2,†]**, Luca Broggini** [1] ⓘ**, Francesca Bonato** [3]**, Rosaria Russo** [4] ⓘ**,**
Claudia Moriconi [5]**, Martino Bolognesi** [1] ⓘ**, Elena Miranda** [5,6] ⓘ**, Sabrina Dallavalle** [2] ⓘ**,**
Daniele Passarella [3] ⓘ **and Stefano Ricagno** [1,*] ⓘ

[1] Dipartimento di Bioscienze, Università degli Studi di Milano, Via Celoria, 26, 20133 Milan, Italy;
   cristina.visentin@unimi.it (C.V.); luca.broggini@unimi.it (L.B.); martino.bolognesi@unimi.it (M.B.)

[2] Dipartimento di Scienze per gli Alimenti, la Nutrizione e l'Ambiente, Università degli Studi di Milano,
   Via Celoria, 2, 20133 Milan, Italy; loana.musso@unimi.it (L.M.); sabrina.dallavalle@unimi.it (S.D.)

[3] Dipartimento di Chimica, Università degli Studi di Milano, Via Golgi, 19, 20133 Milan, Italy;
   francesca.bonato@unimi.it (F.B.); daniele.passarella@unimi.it (D.P.)

[4] Dipartimento di Fisiopatologia Medico-Chirurgica e dei Trapianti, Università degli Studi di Milano,
   Via Fratelli Cervi, 93, 20090 Segrate, Italy; rosaria.russo@unimi.it

[5] DipartimPento di Biologia e Biotecnologie 'Charles Darwin', Sapienza Università di Roma, Piazzale Aldo
   Moro, 5, 00185 Rome, Italy; moriconi.cla@gmail.com (C.M.); mariaelena.mirandabanos@uniroma1.it (E.M.)

[6] Istituto Pasteur—Cenci Bolognetti Foundation, Sapienza Università di Roma, Piazzale Aldo Moro, 5,
   00185 Rome, Italy

[*] Correspondence: Stefano.ricagno@unimi.it; Tel.: +39-02-5031-4914

[†] These authors equally contributed to this work.

✓ check for updates

Abstract: Familial encephalopathy with neuroserpin inclusion bodies (FENIB) is a severe and lethal neurodegenerative disease. Upon specific point mutations in the *SERPINI1*gene-coding for the human protein neuroserpin (NS) the resulting pathologic NS variants polymerize and accumulate within the endoplasmic reticulum of neurons in the central nervous system. To date, embelin (EMB) is the only known inhibitor of NS polymerization in vitro. This molecule is capable of preventing NS polymerization and dissolving preformed polymers. Here, we show that lowering EMB concentration results in increasing size of NS oligomers in vitro. Moreover, we observe that in cells expressing NS, the polymerization of G392E NS is reduced, but this effect is mediated by an increased proteasomal degradation rather than polymerization impairment. For these reasons we designed a systematic chemical evolution of the EMB scaffold aimed to improve its anti-polymerization properties. The effect of EMB analogs against NS polymerization was assessed in vitro. None of the EMB analogs displayed an anti-polymerization activity better than the one reported for EMB, indicating that the EMB–NS interaction surface is very specific and highly optimized. Thus, our results indicate that EMB is, to date, still the best candidate for developing a treatment against NS polymerization.

Keywords: protein polymerization; drug design; neurodegeneration

1. Introduction

The serpinopathies are a group of conformational diseases characterized by the accumulation of a misfolded member of the serpin (serine protease inhibitor) superfamily into large inclusion bodies that cause cellular toxicity [1]. Familial encephalopathy with neuroserpin inclusion bodies (FENIB) is a member of this group of pathologies. FENIB is a rare and autosomal dominant genetic disease with fatal outcome [2], which presents as consequence of point mutations in the *SERPINI1*gene coding for neuroserpin (NS) [3–6]. Mutant NS accumulates within the endoplasmic reticulum of neurons causing

progressive neurodegeneration, with consequent epilepsy, cognitive impairment and dementia as clinical symptoms [2–6]. The amount of inclusions and the severity of the pathology, as well as the date of onset, depend on the specific mutation present in the patient [4,7]. To date, there are six reported mutations responsible for FENIB: S49P, L47P, S52R, H338R, G392E and G392R [2,4–6].

NS is mainly expressed in the central nervous system [8], where is involved in several cellular and developmental processes including synaptic and axonal plasticity, learning and memory [9–11]. As a serpin, NS mainly inhibits tissue plasminogen activator (tPA) [12]. Substrate recognition and inhibition are mediated by a long disordered loop, named reactive center loop (RCL), that is specifically recognized and cleaved by tPA. Upon cleavage, there is a transition from disorder to order in the N-terminal part of the RCL, which is inserted in beta-sheet A of NS and drags the tPA molecule to the opposite side of the NS molecule, before the hydrolysis of the acyl NS-tPA complex. The geometry of the protease's active site is distorted in this process preventing the completion of the proteolytic reaction [13]. Typically, such acyl–enzyme, serpin–protease, complexes are not hydrolysable thus very stable over time, on the contrary the NS-tPA complex is short-lived and is hydrolyzed within minutes [14,15]. After cleavage, the RCL, which is usually exposed in the native (Nat) conformation, gets inserted into the beta sheet A between strands 3A and 5A. This conformation is referred to as cleaved (Cl) NS and is inactive. NS shares the typical serpin fold with the other members of the superfamily. The exposure of the RCL loop makes the Nat fold metastable and this accounts for its intrinsic propensity to adopt more stable conformations such as the latent (Lat) and the polymeric forms (Pol). Lat is extremely stable, but inactive: in this monomeric conformation the RCL is uncleaved, but nevertheless inserted in the beta sheet A, as observed for Cl [16].

NS, as many secreted proteins, is glycosylated, presenting two N-glycosylation chains in positions N157 and N321 that decrease spontaneous polymerization in vitro and in vivo [17,18]. Indeed, alteration of the glycosylation pattern due to their removal or pathologic mutation leads to enhanced polymers (Pol) formation [17,18]. The molecular structure of serpin Pol is still under debate and several models have been proposed, mainly for alfa-1 antitrypsin and alfa-1 antithrombin, two prototypical serpins for molecular studies. In all such models, the transition of the RCL from the disordered exposed conformation to the highly structured beta conformation is a paramount step. Specifically, the RCL inserts in beta sheet A of neighboring monomers as part of the intermolecular link [19,20] or intramolecularly allowing a larger domain swap of the C-terminal stretch of the protein [21]. This latter model is gaining momentum. Like the ones formed by other serpins, NS polymers are long, flexible and unbranched [22], and spectroscopic data indicate that the Nat to Pol transition implies a gain in secondary structure content [23,24].

FENIB, as other serpinopathies, is an incurable disease and there are no active clinical trials for FENIB therapies. Several approaches have been proposed for the treatment of alfa-1 antitrypsin deficiency, the most common serpinopathy [16], but no cure for this conditions has been reported yet. Chemical chaperones, peptides related to the RCL and small molecules have been proposed, however a specific and efficient polymerization inhibitor has not been identified so far [16]. We recently reported the ability of embelin (EMB) to prevent NS polymerization and to dissolve preformed NS polymers [25]. In vitro, EMB binds to all NS conformations destabilizing both the Nat and Lat forms and resulting in the accumulation of small and soluble oligomers (Olig) [25]. EMB is the major active constituent of fruits from *Embelia ribes* and is chemically known as 2,5-dihydroxy-3-undecyl-1,4-benzoquinone. This molecule was long known in Asian traditional medicine [26], and its pharmaceutical potential against central nervous system pathologies has been extensively investigated in the literature [27]. It is particularly interesting for its capability to cross the blood brain barrier and to elicit its effect directly in the central nervous system [28].

Here we show that in presence of EMB concentrations lower than 0.75 mM NS forms increasingly bigger aggregates; however, at 0.12 mM—the lowest concentration tested—a residual effect is still detectable. Moreover we observed a reduction in NS polymeric accumulation in COS-7 cells treated with EMB, however our results suggest that this reduction was not related to the expected anti-aggregation

effect of the EMB molecule but was mainly due to the activation of the proteasome system. We thus we performed a systematic chemical modification of the EMB scaffold to identify EMB analogs with better anti-polymerization properties and tested the effects of each EMB analog against NS polymerization in vitro. Despite its simple structure, the chemical properties of EMB seem to be already optimal for NS polymerization inhibition, and no better molecule was identified. Thus, EMB remains the best starting point for the future development of a treatment against FENIB.

2. Materials and Methods

2.1. NS Expression and Purification

E. coli BL21 Rosetta (DE3) pLysS competent cells Novagen (Merck KGaA, Darmstadt, Germany) transformed with pQE81L plasmid carrying the human NS gene with a N-terminus 6-His tag were used to express and purify NS as reported in [15]. Briefly, bacterial cells were grown in Superior Broth (Molecular Dimension, Sheffield, UK) containing 100-μg/mL ampicillin and protein expression was induced with 0.2-mM isopropyl-β-D-thiogalactopyranoside at 17 °C for 16 h. NS was purified from the soluble fraction. Buffer A supplemented with cOmplete protease inhibitor cocktail (Hoffmann-La Roche, Basel, Switzerland) was added and the cell pellet was immediately sonicated. Crude extract was clarified by centrifugation and filtered before being loaded onto a 1 mL HiTrap Chelating HP column (GE Healthcare, Chicago, IL, USA) previously equilibrated with buffer A. Protein was eluted in 100% buffer B. Monomers were further isolated by gel filtration using a Hi Load 16/60 Superdex200 column (GE Healthcare, Chicago, IL, USA) equilibrated in 10-mM Tris-HCl, 50-mM KCl, pH 8.0. All purification steps were performed at 4 °C and all chemicals were purchased from Sigma-Aldrich (St. Louise, MO, USA), unless differently specified. NS concentration was measured by optical absorption using an extinction coefficient at 280 nm of 37,360 cm^{-1} M^{-1}.

2.2. Compounds Mix Preparation

EMB powder was directly dissolved in 10-mM Tris HCl, 50-mM KCl, pH 8.0 until reaching saturation conditions and the solution was immediately centrifuged at 4 °C for 10 min at 20,000× *g* in order to remove the excess of insoluble EMB. Absorbance at 325 nm was measured and EMB concentration was determined using an extinction coefficient of 24,000 cm^{-1} M^{-1} at pH 7.4. Supernatant was then used to dilute NS.

EMB analogs were dissolved as described above and used at saturation condition, but it was not possible to determine the precise concentration by optical absorbance.

2.3. Polymerization Assays

Solution of 85-μM native NS dissolved in 10-mM Tris-HCl, 50-mM KCl, pH 8.0 in the presence or absence of compounds prepared as described in Section 2.2 were incubated at 45 °C. Aliquots were collected after 0, 1 and 3 h of incubation and analyzed by SEC and non-denaturing-PAGE.

2.4. COS-7 cells Culture and DNA Transfection

COS-7 cells were cultured and transfected as described before [17]. Briefly, cells were maintained in DMEM (D6546) supplemented with 5% *v/v* FBS and Glutamax (Life Technologies, Carlsbad, CA, USA) at 37 °C and 5% *v/v* CO$_2$ in a humidified incubator. Transfections were performed in 6-well plates pretreated with 0.1-mg/mL poly L-lysine (Sigma-Aldrich, St. Louise, MO, USA). Typically, 4 μg plasmid DNA were introduced into each well mixed with 10 μL of Lipofectamine 2000 (Life Technologies, Carlsbad, CA, USA) in serum-free Opti-MEM I culture medium (Life Technologies, Carlsbad, CA, USA) following the manufacturer's protocol. The culture medium was replaced with fresh medium 16 h after transfection and DMSO as a control or 10-μM EMB alone or plus 2.5-μM MG132 were added to the fresh medium. Cells were incubated for another 24 h before collection of cell lysates and culture media as described in the next paragraph.

2.5. SDS and Non-Denaturing PAGE and Western Blot Analysis of Cellular Samples

The cell pellet from each well of 6-well plates was lysed in 100 µL of Nonidet lysis buffer [150 mM NaCl, 50 mM Tris-Cl, pH 7.5, 1% *v/v* Nonidet P-40, plus protease inhibitor mixture (cOmplete, Hoffmann-La Roche, Basel, Switzerland)]. The soluble protein fraction was collected in the supernatant after centrifugation at 12,000× *g*, 4 °C for 15 min, and proteins in the insoluble pellet were extracted by heating at 95 °C in loading buffer (Tris-HCl 125 mM pH 6.8, 10% *v/v* glycerol, 0.02% *w/v* bromo-phenol blue, 5% *v/v* beta-mercaptoethanol and 2% *w/v* SDS). Forty micrograms of total protein from each lysate and the equivalent volume of each culture medium were mixed with the same loading buffer (without SDS and beta-mercaptoethanol for non-denaturing PAGE) and analyzed in 10% *w/v* acrylamide SDS-PAGE or 7.5% *w/v* acrylamide non-denaturing PAGE and western blot as described before [29,30]. The horseradish peroxidase signal was developed using the LiteAblot PLUS and TURBO extra sensitive chemiluminescent substrates (EuroClone, Pero, Italy) and exposed to film or visualized on a ChemiDoc system (BioRad, Segrate, Italy). Unless stated otherwise, reagents, buffers, culture media and serum for cell cultures were purchased from Sigma-Aldrich (St. Louise, MO, USA). Rabbit polyclonal anti-NS antibody was made in-house [7]; rabbit polyclonal anti-GAPDH antibody was from Abcam (Cambridge, UK).

2.6. Non-Denaturing Polyacrylamide gel Electrophoresis

Samples were prepared as previously described [31]. Briefly, aliquots of NS in the presence or absence of compounds were collected and mixed at a 1:1 volume ratio with non-denaturing loading buffer (250-mM Tris-HCl, 50% glycerol, 0.5% bromophenol blue, pH 6.8). Samples were separated into 7.5% non-denaturing polyacrylamide gels run at 90 V for 2 h at 4 °C. Gels were stained with Coomassie brilliant blue R-250.

2.7. Size exclusion Chromatography

Analytical size exclusion chromatography runs were performed using a Superdex200 10/300 GL column (GE Healthcare, Chicago, IL, USA) or Superdex200 Increase 10/300 GL column (GE Healthcare, Chicago, IL, USA) previously equilibrated in 10-mM Tris HCl, 50-mM KCl, pH 8.0 buffer.

2.8. Synthesis of EMB Analogs

All reagents and solvents were reagent grade or were purified by standard methods before use. Melting points were determined in open capillaries by a SMP3 apparatus and are uncorrected. ^{1}H spectra were recorded on Bruker AMX 300 MHz (Bruker, Billerica, MA, USA) or Bruker AV600 (Bruker, Billerica, MA, USA) spectrometers at 298 K, using deuterated solvents commercially available. Chemical shifts were reported in parts per million (δ). The coupling constants (J) are reported in Hertz (Hz) and ^{13}C NMR spectra were recorded on Bruker AMX 300 MHz (Bruker, Billerica, MA, USA) or Bruker AV600 (Bruker, Billerica, MA, USA) spectrometers.

Solvents were routinely distilled prior to use; anhydrous tetrahydrofuran (THF) and ether (Et$_2$O) were obtained by distillation from sodium-benzophenone ketyl; dry methylene chloride was obtained by distillation from phosphorus pentoxide. All reactions requiring anhydrous conditions were performed under a positive nitrogen flow and all glassware was oven dried and/or flame dried.

Isolation and purification of the compounds were performed by flash column chromatography on silica gel 60 (230–400 mesh). Analytical thin-layer chromatography (TLC) was conducted on TLC plates (silica gel 60 F254, aluminum foil). Compounds on TLC plates were detected under UV light at 254 and 365 nm or were revealed using TLC stains as KMnO$_4$, iodine or 10% phosphomolybdic acid (PMA) in ethanol.

Silica treated with oxalic acid (referred to as oxalic acid-precoated silica) was prepared as follows: standard silica was suspended overnight in a 0.1 M oxalic acid (aq) solution; then was filtered under vacuum, then dried in oven.

Compound **4** was obtained as reported in literature [32].

Compounds **8** and **11** were obtained as reported in literature [33].

Compounds **9** was obtained as reported in literature [34].

Compounds **2a**, **3a**, **10a** and **1a** (embelin) were prepared as reported in literature [35].

3-(bromo-propyloxi)-tert-butyl-dimethyl-silane was prepared as reported in literature [36].

2.8.1. 3-allyl-2,5-dimethoxy-[1,4]benzoquinone (**2e**) and 3-allyl-2-hydroxy-5-methoxy-[1,4]benzoquinone (**3e**)

To a solution of compound **11** (82 mg, 0.36 mmol) in CH_3CN (3.5 mL), a solution of ceric ammonic nitrate (CAN, 502 mg, 0.89 mmol) in CH_3CN/H_2O 7/3 (4 mL) was added dropwise at $-10\ ^\circ C$. The reaction was stirred at room temperature for 2 h, diluted with Et_2O (20 mL) and washed with water (8 mL) and brine. The organic layer was dried over anhydrous Na_2SO_4 and concentrated in vacuo. The crude was purified by flash column chromatography on oxalic acid-precoated silica gel using ETP: ethyl acetate 85:15 as eluent, to give compounds **2e** (53 mg, 71%) and **3e** (12 mg, 17%) as bright yellow solids. R_f = 0.64 (**2e**) and 0.22 (**3e**) in ETP: ethyl acetate 85:15).

2e: mp: 90 °C; ^{1}H-NMR (300 MHz, $CDCl_3$): δ 5.86–5.73 (2H, m), 5.11–5.04 (1H, dq, J = 17.12, 1.59 Hz), 5.03–4.98 (1H, dq, J = 10.0, 1.36 Hz), 4.07 (3H, s), 3.81 (3H, s), 3.21–3.18 (2H, dt, J = 6.48, 1.45 Hz). ^{13}C-NMR (75 MHz, $CDCl_3$): δ 183.87, 182.24, 159.18, 156.42, 134.51, 128.01, 116.67, 105.87, 61.79, 56.80, 27.55.

3e: mp: 100 °C; ^{1}H-NMR (300 MHz, $CDCl_3$): 5b: δ 7.28 (1H, s), 5.90–5.76 (2H, m), 5.15–5.08 (1H, dq, J = 17.23, 1.58 Hz), 5.04–5.00 (1H, dq, J = 9.95, 1.28 Hz), 3.86 (3H, s), 3.22–3.19 (2H, dt, J = 6.56, 1.14 Hz). (in agreement with [37]).

2.8.2. 3-allyl-2,5-dihdroxy-1,4-benzoquinone (**1e**)

To a solution of **2e** (39 mg, 0.19 mmol) in EtOH (8.5 mL), 2-M NaOH (aq., 4.2 mL) was added. The reaction was heated at 70 °C for 2 h. The solution was cooled at room temperature, then was diluted with 2-M HCl (21 mL) and extracted with ethyl acetate (3 × 21 mL). The combined organic phases were washed with brine, dried over anhydrous Na_2SO_4 and concentrated in vacuo to give compound **1e** (34 mg) as a brown solid in quantitative yield. mp: 144–146 °C; ^{1}H-NMR (300 MHz, DMSO-d_6): δ 11.26 (2H, br s), 5.83–5.73 (2H, m), 5.03–4.94 (2H, m), 3.06 (1H, br s), 3.04 (1H, br s); ^{13}C-NMR (75 MHz, DMSO-d_6): δ 161.4 (× 2C), 135.00(× 2C), 115.8 (× 2C), 115.2, 104.51, 26.69.

2.8.3. 3-butyl-2,5-dimethoxy-[1,4] benzoquinone (**2d**) and 3-butyll-2-hydroxy-5-methoxy-[1,4] benzoquinone (**3d**)

To a solution of **10d** (70 mg, 0.27 mmol, 1 eq) in CH_3CN (2.75 mL) cooled to $-10\ ^\circ C$, ceric ammonium nitrate (CAN, 383 mg, 0.68 mmol) in CH_3CN: H_2O 7:3 (2.7 mL) was added dropwise. After the addition, the solution was stirred at room temperature for 2 h. The solution was diluted with Et_2O (15 mL) and washed with H_2O and brine. The organic layer was dried over anhydrous Na_2SO_4 and the solvent was evaporated. The resulting crude material was purified by preparative-TLC chromatography in hexane: ethyl acetate 8:2 to give compound **2d** (20 mg, 35%) as an orange solid and compound **3d** (18 mg, 29%) as a dark brown oil. **2d**: mp: 94 °C. ^{1}H-NMR (300 MHz, CD_3OH-d_4): δ 5.85 (1H, s), 3.87 (3H, s), 2.47 (2H, t, J = 7.2 Hz), 1.54–1.41 (2H, m), 1.40–1.25(2H, m), 0.93 (3H, t, J = 7.2 Hz). **3d**: ^{1}H-NMR (300 MHz, CD_3OH-d_4): 5.74 (1H, s), 4.07 (3H, s), 3.82 (3H, s), 2.45 (2H, t, J = 7.2 Hz), 1.48–1.36 (2H, m), 1.35–1.22 (2H, m), 0.93 (3H, t, J = 7.2 Hz). **2d** and **3d** are intermediates for the synthesis of **1d** and were not tested against NS polymerization.

2.8.4. 3-butyl-2,5-dihydroxy-1,4-benzoquinone (**1d**)

To a solution of **2d** (11 mg, 0.05 mmol) in EtOH (2.2 mL), 2-M NaOH (aq., 1.1 mL) was added. The reaction mixture was heated at 70 °C for 2 h.

The solution was cooled to room temperature, then was diluted with 2-M HCl (5.4 mL) and extracted with ethyl acetate (3×5 mL). The combined organic phases were washed with brine (10 mL), dried over anhydrous Na_2SO_4 and the solvent was evaporated to give compound **1d** (10 mg) as a red/brownish solid in quantitative yield. mp: 132–133 °C. ^{1}H-NMR (300 MHz, CH_3OH-d_4): δ 11.20 (2H, bs), 5.78 (1H, s), 2.46 (2H,t, *J* = 7.4 Hz); 1.45–1.18 (4H, m), 0.92 (3H, t, *J* = 7.1 Hz).

2.8.5. 3-heptyl-1,2,4,5-tetramethoxybenzene (**10b**)

To a solution of 1,2,4,5-tetramethoxybenzene **9** (130 mg, 0.66 mmol) in dry THF (6 mL), *n*-BuLi (1.6 M in hexane, 610 μL, 0.98 mmol) was added at room temperature. After 40 min. under stirring, 1-bromoheptane (154 μL, 0.98 mmol) was added dropwise, and the reaction mixture was stirred overnight. Then, a saturated solution of NH_4Cl was added, and the aqueous phase was extracted with ethyl acetate. The combined organic phases were dried over Na_2SO_4. The solvent was removed under vacuum and the crude mixture was purified by flash column chromatography with hexane: ethyl acetate 90:10, to give 88 mg of compound **10b** in 45% yield. Colorless oil. ^{1}H-NMR (300 MHz, $CDCl_3$): δ 6.41 (s, 1H), 3.84 (s, 3H), 3.77 (s, 3H), 2.65–2.55 (m, 2H), 1.59–1.45 (m, 2H), 1.43–1.21 (m, 8H), 0.87 (t, *J* = 7.5 Hz, 3H); ^{13}C-NMR (75 MHz, $CDCl_3$): δ 148.9 (× 2C), 141.2 (× 2C), 131.1, 96.8, 60.9 (× 2C), 56.3 (× 2C), 31.8, 30.7, 29.9, 29.1, 24.6, 22.5, 14.1.

2.8.6. 3-Heptyl-2,5-Dihydroxy-[1,4] Benzoquinone (**1b**)

To a solution of **10b** (70 mg, 0.24 mmol) in CH_3CN (2.3 mL) a solution of CAN (323 mg, 0.59 mmol) in CH_3CN: H_2O 7:3 (2.5 mL) was added dropwise at −10 °C (salt-ice bath) over 10 min. The reaction was allowed to stir at rt for 3 h, concentrated in vacuo and diluted with ethyl acetate. The organic layer was washed with water, brine, dried over anhydrous Na_2SO_4. The solvent was removed under vacuum and the residue was used in the next reaction without further purification. The crude was dissolved in ethanol (8 mL) and 2-M NaOH (aq., 4mL) was added, then the reaction was heated to reflux for 4 h. Then, the mixture was concentrated under vacuum and was diluted with 2-M HCl (10 mL). The precipitate was filtered under vacuum and washed with hexane, to give compound **1b** (17 mg, 30% yield) as an orange solid. ^{1}H-NMR (300 MHz, DMSO-d_6): δ 11.04 (brs, 2H), 5.76 (s, 1H), 2.26 (t, *J* = 6.9 Hz, 2H), 1.40–1.29 (m, 2H), 1.28–1.13 (m, 8H), 0.83 (t, *J* = 7.2 Hz, 3H). ^{13}C-NMR (75 MHz, DMSO-d_6): 117.35, 103.8, 31.2, 28.9, 28.4, 27.6, 22.0, 22.0, 13.9.

2.8.7. 3-nonyl-1,2,4,5-tetramethoxybenzene (**10c**)

To a solution of 1,2,4,5-tetramethoxybenzene **13** (160 mg, 0.81 mmol) in dry THF (7 mL), *n*-BuLi (1.6-M in hexane, 750 μL, 1.21 mmol) was added at room temperature. After 30 min. under stirring, 1-bromononane (231 μL, 1.21 mmol) was added dropwise, and the reaction mixture was stirred overnight. Then, a saturated solution of NH_4Cl was added, and the aqueous phase was extracted with ethyl acetate. The combined organic phases were dried over anhydrous Na_2SO_4. The solvent was removed under vacuum and the crude mixture was purified by flash column chromatography with hexane: ethyl acetate 95:5, to give 121 mg of compound **10c** in 46% yield. Colorless oil. ^{1}H-NMR (300 MHz, $CDCl_3$): δ 6.41 (1H, s), 3.84 (6H, s), 3.76 (6H, s), 2.65–2.56 (2H, m), 1.60–1.44 (2H, m), 1.43–1.26 (12H, m), 0.87 (3H, t, *J* = 6.9 Hz). ^{13}C-NMR (75 MHz, $CDCl_3$): δ 148.8(× 2C), 141.1 (× 2C), 131.1, 96.8, 60.9 (× 2C), 56.2 (× 2C), 31.9, 30.7, 30.0, 29.5, 29.4, 29.3, 24.6, 22.5, 14.1.

2.8.8. 3-nonyl-2,5-dihydroxy-[1,4] benzoquinone (**1c**)

To a solution of **10c** (82 mg, 0.25 mmol) in CH_3CN (2.5 mL) a solution of CAN (347 mg, 0.63 mmol) in CH_3CN: H_2O 7:3 (2.7 mL) was added dropwise at −10 °C (salt-ice bath) over 15 min. The reaction was allowed to stir at rt for 3 h, concentrated in vacuo and diluted with ethyl acetate. The organic layer was washed with water, brine, dried over anhydrous Na_2SO_4. The solvent was removed under vacuum and the residue was used in the next reaction without additional purification. The crude was dissolved in ethanol (8 mL) and 2 M NaOH aq. (4mL) was added, then the reaction was heated to

reflux for 4 h. Then mixture was concentrated under vacuum and was diluted with 2-M HCl (10 mL). The obtained precipitate was filtered under vacuum and washed with hexane, to give compound **1c** (27 mg, 40% yield) as a bright orange solid. ^{1}H-NMR (300 MHz, DMSO-d_6): δ 10.92 (brs, 2H), 5.66 (s, 1H), 2.25 (t, *J* = 7.7 Hz, 2H), 1.40–1.12 (m, 10H), 0.83 (t, *J* = 6.9 Hz, 3H). ^{13}C-NMR (75 MHz, CDCl$_3$): δ 117.0, 102.2, 31.8, 29.5, 29.5, 29.3, 27.9, 22.6, 22.5, 14.1.

2.8.9. Tert-butyldimethyl-[3-(2,3,5,6-tetramethoxyphenyl)-propoxy]-silane (**10f**)

A solution of 1,2,4,5-tetramethoxybenzene **9** (750 mg, 3.78 mmol) in anhydrous THF (4.7 mL), under nitrogen atmosphere, was cooled to 0 °C, then *n*-BuLi 1.6-M (2.4 mL, 3.78 mmol) was added dropwise. The reaction was warmed to room temperature and stirred for 2 h. Then, the reaction was cooled to −80 °C and a solution of 3-(bromopropyloxy)-tert-butyldimethylsilane (1.44 g, 5.68 mmol) in anhydrous THF (4.7 mL) was added dropwise. The reaction was slowly warmed to room temperature and stirred for 22 h. NH$_4$Cl sat. (20 mL) was added to the reaction and the solution was diluted and extracted with ethyl acetate. The combined organic phases were washed with H$_2$O, brine and dried on anhydrous Na$_2$SO$_4$. The crude (1.767 g) was purified by flash column chromatography in hexane: ethyl acetate 9:1, to give compound **10f** (488 mg, 35% yield) as yellow-pale oil.

^{1}H-NMR (300 MHz, CDCl$_3$): δ 6.41 (1H, s), 3.84 (6H, s), 3.76 (6H, s), 3.69 (2H, t, *J* = 7.2 Hz), 2.67 (2H, m), 1.84–1.66 (2H, m), 0.90 (9H, s), 0.06 (6H, s). ^{13}C-NMR (150 MHz, CDCl$_3$): δ 148.8 (× 2C), 141.0 (× 2C), 130.6, 96.7, 63.4, 60.9 (× 2C), 56.2 (× 2C), 33.9, 25.9 (× 3C), 21.2, 18.3, -5.2 (× 2C).

2.8.10. 2,5-dihydroxy-3-(3-hydroxy-propyl)-[1,4] benzoquinone (**1f**)

To a solution of **10f** (100 mg, 0.27 mmol, 1 eq) in CH$_3$CN (2.7 mL) cooled to −10 °C, a solution of CAN (376 mg, 0.67 mmol, 2.5) in CH$_3$CN: H$_2$O 7:3 (1.9 mL) was added dropwise. The reaction was warmed to room temperature and stirred for 2 h., then it was diluted with H$_2$O (10 mL) and extracted with ethyl acetate (2 × 15 mL). The combined organic phases were washed with H$_2$O, brine and then dried over anhydrous Na$_2$SO$_4$. The crude was used in the next step without additional purification. The residue was diluted with CH$_2$Cl$_2$ (2.7 mL) and HClO$_4$ (60% *v/v*, 4 drops) was added; the reaction was stirred at room temperature for 3 h. The mixture was diluted with CH$_2$Cl$_2$ (3 mL) and washed with water. The aqueous phase was further extracted with CH$_2$Cl$_2$ (3 × 4 mL). The combined organic phases were washed with brine, dried over anhydrous Na$_2$SO$_4$ and the solvent was evaporated under vacuum. The resulting crude was purified by preparative-TLC (CH$_2$Cl$_2$, 0.5% CH$_3$OH + 0.5% CH$_3$COOH) to give product **1f** (15 mg, 28% yield) as a brown solid, mp: 155 °C ^{1}H-NMR (600 MHz, CDCl$_3$): δ 5.94 (1H, s), 4.39–4.27 (2H, m), 2.53–2.40 (2H, m), 2.06–1.93 (2H, m). ^{13}C-NMR (150 MHz, CDCl$_3$): δ 182.1, 181.8, 155.9, 155.1, 114.5, 104.7, 68.2, 29.7, 29.3, 20.2, 17.3.

2.8.11. (E)-methyl–4-(2,3,5,6-tetramethoxyphenyl)-but-2-enoate (**12**)

To a stirred solution of **11** (180 mg, 0.80 mmol) in dry acetone (14 mL), K$_2$CO$_3$ (115 mg, 0.83 mmol, 1.04 eq) and CH$_3$I (57 μL, 0.91 mmol, 1.14 eq) were added under nitrogen atmosphere. The mixture was heated to reflux for 16 h. The solvent was evaporated, the crude was diluted with AcOEt (10 mL), washed with water (7 mL) and the aqueous layer was further extract with AcOEt (2 × 7 mL). The combined organic layers were washed with brine (15 mL), then dried over anhydrous Na$_2$SO$_4$ and concentrated in vacuo. The crude was purified by flash chromatography in hexane: ethyl acetate 9:1, to give 91 mg of 3-allyl-1,2,4,5-tetramethoxybenzene as brown oil (yield 48%, R$_f$ = 0.36 in hexane: ethyl acetate 9:1.

To a stirred solution of 3-allyl-1,2,4,5-tetramethoxybenzene (50 mg, 0.21 mmol) in DCM (4.3 mL), methyl acrylate (57 μL, 0.63 mmol) and UMICORE M73 SIMes (8 mg, 0.01 mmol) were added under nitrogen atmosphere. The mixture was stirred 6 h at room temperature. The solvent was evaporated, and the resulting crude was purified by flash chromatography in hexane: ethyl acetate 9:1, to give 25 mg of **12** as a yellow oil. (yield 40%, R$_f$ = 0.12 in hexane: ethyl acetate 9:1. ^{1}H-NMR (300 MHz,

CDCl$_3$): δ 7.12 (1H, dt, *J* = 6.2 Hz, 15.5 Hz); 6.47 (1H, s), 5.75 (1H, dt, *J* = 1.8 Hz, 15.5 Hz), 3.85 (6H, s), 3.75 (6H, s), 3.67 (3H, s), 3.56 (2H, dd, *J* = 1.8 Hz, 6.2 Hz).

2.8.12. (2E)-4-(2,5-dihydroxy-3,6-dioxocyclohexa-1,4-dienyl)-but-2-enoic acid (**5**)

To a solution of **12** (42 mg, 0.14 mmol) in CH$_3$CN (1.4 mL) cooled to −10 °C, a solution of CAN (195 mg, 0.35 mmol) in CH$_3$CN: H$_2$O 7:3 (1.4 mL) was added dropwise. The reaction was warmed to room temperature and stirred for 3 h., then it was diluted with H$_2$O (10 mL) and extracted with ethyl acetate (2 × 15 mL). The combined organic phases were washed with H$_2$O, brine and then dried over anhydrous Na$_2$SO$_4$. The crude was used in the next step without further purification. The residue was diluted with CH$_2$Cl$_2$ (2.5 mL) and HClO$_4$ (60% *v/v*, 4 drops) was added; the reaction was stirred at room temperature for 3 h. The mixture was diluted with CH$_2$Cl$_2$ (3 mL) and washed with water. The aqueous phase was further extracted with CH$_2$Cl$_2$ (3 × 4 mL). The combined organic phases were washed with brine, dried over anhydrous Na$_2$SO$_4$ and the solvent was evaporated under vacuum to give a mixture of (2*E*)-methyl 4-(2,5-dihydroxy-3,6-dioxocyclohexa-1,4-dienyl)-but-2-enoate (20 mg) as a brown solid used in the next step without further purification. ^{1}H-NMR (300 MHz, acetone-d_6): δ 6.93 (1H, dt, *J* = 6.6 Hz, 15.6 Hz); 5.95 (1H, s); 5.88 (1H, dt, *J* = 1.5 Hz, 15.6 Hz); 3.66 (3H, s); 3.31–3.37 (2H, m).

To a solution of the above quinone (15 mg, 0.06 mmol) in aq. 50% THF (2.6 mL), LiOH H$_2$O (13 mg, 0.32 mmol) was added and the mixture was stirred overnight at rt protected from light. The solvent was evaporated, and the crude was diluted with 2-N HCl (10 mL) then extracted with ethyl acetate and washed with brine. The organic phases were dried over anhydrous Na$_2$SO$_4$, the solvent was then removed in vacuo to give 9 mg (87%) of the product **5** as a brown solid.

^{1}H-NMR (300 MHz, CH$_3$OH-d_4): δ 6.92 (1H, dt, *J* = 6.4 Hz, 15.4 Hz); 5.95 (1H, s); 5.80 (1H, dt, *J* = 1.5 Hz, 15.4 Hz); 3.33–3.37 (2H, m).

2.8.13. 1,2,4,5-tetramethoxy-3-(pent-4-en-1-yl)benzene (**10g**)

1,2,4,5-tetramethoxybenzene **9** (0.77 g, 3.89 mmol) was dissolved in dry THF (20 mL) and HMPA (0.07 mL) was added. The solution was cooled down to −40 °C, then a 1.6-M solution of n-BuLi in hexane (3.8 mL, 6.08 mmol) was added dropwise. The reaction mixture was stirred for 40 min. while it was allowed to warm up to room temperature, then it was cooled down again to −40 °C and 5-bromo-1-pentene (1 mL, 8.44 mmol) was added dropwise. The reaction mixture was slowly warmed up to room temperature and stirred for 27 h, after which it was quenched with a saturated solution of NH4Cl (30 mL). The organic layer was extracted with ethyl acetate and the combined organic phases were washed with brine and dried over Na2SO4, then concentrated in vacuo. The crude product was purified by flash column chromatography using a hexane-ethyl acetate (85:15) solution, providing 498 mg (48% yield) of compound **10g** as a transparent oil. 1H-NMR (300 MHz, CDCl3): δ (ppm) = 6.41 (s, 1H); 5.84 (m, 1H); 5.01 (d, *J* = 14.7 Hz, 1H) 4.97 (d, *J* = 11.0 Hz, 1H); 3.84 (s, 6H); 3.76 (s, 6H); 2.63 (t, *J* = 7.7 Hz, 2H); 2.10 (dd, *J* = 14.3, 7.1 Hz, 2H); 1.63 (quint, *J* = 7.8 Hz, 2H). 13C-NMR (75 MHz, CDCl3): δ (ppm) = 148.84, 141.06, 138.89, 130.68, 114.28, 96.73, 60.94, 56.23, 33.97, 29.78, 24.15.

2.8.14. 2,5-dihydroxy-3-(pent-4-en-1-yl)cyclohexa-2,5-diene-1,4-dione (**1g**)

A solution of compound **10g** (147 mg, 0.55 mmol) in acetonitrile (5.5 mL) was cooled down to −7 °C with an ice and salt bath, and a solution of 0.25-M CAN (760.3 mg, 1.38 mmol) in a CH$_3$CN and H$_2$O solution (7:3) was added dropwise. The reaction mixture was stirred at room temperature for 2 h. At the end of the reaction Et$_2$O (25 mL) was added and the organic layer was washed with water and brine, then it was dried on Na$_2$SO$_4$ and concentrated in vacuo. The crude product of this first step was dissolved in ethanol (25 mL) and NaOH$_{aq}$ 2 M (12.2 mL) was added. The reaction mixture was warmed up to 70 °C and stirred for 3 h. After reaction completion the solution was cooled down to 0 °C and it was acidified to pH 1 with HCl 37%. The reaction mixture was then extracted with ethyl acetate, the combined organic phases were dried on Na$_2$SO$_4$ and concentrated in vacuo. Product **1g**

(80.7 mg, 71% yield) was obtained as a dark orange solid without any further purification. ^{1}H-NMR (300 MHz, CDCl$_3$): δ(ppm) = 6.00 (s, 1H); 5.77 (m, 1H); 4.99 (m, 2H); 2.46 (t, *J* = 7.8 Hz, 2H); 2.07 (m, 2H); 1.57 (quint, *J* = 7.6 Hz, 2H). ^{13}C-NMR (100 MHz, *d*[6]-DMSO): δ (ppm) = 139.54, 118.18, 115.94, 104.97, 34.24, 27.94, 22.76 (detected signals).

2.8.15. 3-allyl-2,5-bis-((2-(dimethylamino)ethyl)amino)-1,4-benzoquinone (**6**)

To a solution of benzoquinone **2e** (40 mg, 0.19 mmol) in CH$_2$Cl$_2$ (1.9 mL) at 0 °C, HClO$_4$ (60% *v/v*, 1.5 mL) was added dropwise. The reaction was stirred 6 h at 0 °C, then was diluted with CH$_2$Cl$_2$ (10 mL) and washed with H$_2$O and brine, dried over anhydrous Na$_2$SO$_4$ and evaporated. Compound **3e** (42 mg) was used in the next step without any further purification.

To a solution of **3e** (37 mg, 0.19 mmol) in EtOH (13 mL), NaHCO$_3$ (0.82 g, 51 eq) and *N*,*N*-dimethylethylenediamine (0.25 mL, 1.95 mmol, 97% *w/w*) were added dropwise under nitrogen atmosphere. The reaction was stirred at room temperature for 48 h. The solvent was evaporated and the crude mixture was purified with preparative-TLC (CH$_2$Cl$_2$: CH$_3$OH 9:1 + 1% H$_2$O) providing compound **6** (17 mg, 35% yield) as a purple solid. mp: 64 °C. ^{1}H-NMR (300 MHz, CDCl$_3$): δ 7.27–7.18 (m, 1H), 7.07–6.95 (m, 1H), 6.02–5.88 (1H, m), 5.26 (s, 1H), 5.04 (dq, *J* = 1.9 Hz, 10.3 Hz, 1H), 4.98 (dq, *J* = 1.9 Hz, 17.0 Hz, 1H), 3.61 (q, *J* = 5.8 Hz, 2H), 3.31(dt, *J* = 2.0 Hz, 5 Hz, 2H), 3.15 (q, *J* = 5.8 Hz, 2H), 2.55 (t, *J* = 6.1 Hz, 2H), 2.51 (t, *J* = 6.1 Hz, 2H), 2.25 (s, 3H), 2.24 (s, 3H).

2.8.16. (E)-1,8-bis(2,3,5,6-tetramethoxyphenyl)oct-4-ene (**13**)

To a solution of compound **10g** (106 mg, 0.40 mmol) in dry dichloromethane (4 mL) was added Hoveyda–Grubbs 2nd generation catalyst (14.3 mg, 0.02 mmol). The reaction mixture was stirred at reflux for 4 h., then the solvent was evaporated in vacuo. The crude product was purified by flash column chromatography with a hexane and ethyl acetate (8:2) solution, providing 85 mg (85% yield) of product **13** as a transparent oil. ^{1}H-NMR (300 MHz, CDCl$_3$): $\delta\delta$(ppm) = 6.40 (s, 2H); 5.45 (tt, *J* = 9.3, 5.2 Hz, 2H); 3.83 (s, 12H); 3.75 (s, 12H); 2.59 (m, 4H); 2.06 (m, 4H); 1.57 (brs, 4H).^{13}C NMR (100 MHz, CDCl$_3$): $\delta\delta$(ppm) = 148.82, 141.23, 130.96, 130.30, 96.98, 60.92, 56.31, 32.95, 30.59, 24.25.

2.8.17. 1,8-bis(2,3,5,6-tetramethoxyphenyl)octane (**14**)

Compound **13** (70.7 mg, 0.14 mmol) was dissolved in methanol (2.8 mL), then 10% $_w$ Pd/C (118 mg) was added. The reaction mixture was placed in H$_2$ atmosphere and stirred at room temperature for 24 h. After reaction completion, the catalyst was filtered on a double layer of Celite, paying attention to keep it wet, then the solvent was evaporated. The crude product was purified by flash column chromatography with a hexane and ethyl acetate (70:30) solution to afford 41.6 mg (59% yield) of product **14** as a crystalline transparent solid. ^{1}H-NMR (300 MHz, CDCl$_3$): $\delta\delta$(ppm) = 6.39 (s, 2H); 3.83 (s, 12H); 3.75 (s, 12H); 2.58 (m, 4H); 1.51 (m, 4H); 1.38 (brs, 4H); 1.33 (brs, 4H). ^{13}C NMR (100 MHz, CDCl$_3$): $\delta\delta$(ppm) = 148.91, 140.98, 128.54, 97.01, 60.42, 56.87, 31.74, 29.43, 29.02, 25.12.

2.8.18. (E)-3,3'-(oct-4-ene-1,8-diyl)bis(2,5-dihydroxycyclohexa-2,5-diene-1,4-dione) (**7a**)

A solution of compound **13** (94 mg, 0.19 mmol) in acetonitrile (1.9 mL) was cooled down to −7 °C with an ice and salt bath and a solution of 0.25-M CAN (510.9 mg, 0.93 mmol) in a CH$_3$CN/H$_2$O (7:3) mixture was added drop-by-drop. The reaction mixture was stirred at room temperature for 4 h, after which it was quenched with Et$_2$O (10 mL). The organic layer was washed with water and brine, then it was dried on a Na$_2$SO$_4$ and concentrated in vacuo. The crude product was employed in the next step without any further purification; it was dissolved in NaOH$_{aq}$ 2 M (8.36 mL), then the reaction mixture was warmed up to 70 °C and stirred for 4 h. After reaction completion, the solution was cooled down to 0 °C and it was acidified to pH 1 with HCl 37%. The reaction mixture was extracted with ethyl acetate, the combined organic phases were dried on Na$_2$SO$_4$ and concentrated in vacuo. The resulting brown solid was triturated in hexane, providing 58 mg of product **7a** (79% yield) as a brown powder. ^{1}H-NMR (300 MHz, CD$_3$OD): $\delta\delta$(ppm) = 6.44 (s, 2H); 5.42 (brs, 2H); 2.41–2.33 (m, 4H); 2.03 (brs, 4H);

1.61 (brs, 4H). ^{13}C NMR (100 MHz, d^6-DMSO): δδ(ppm) = 176.92, 170.57, 130.12, 123.99, 118.81, 32.27, 29.50, 29.02, 26.81 (detected signals).

2.8.19. 3,3′-(octane-1,8-diyl)bis(2,5-dihydroxycyclohexa-2,5-diene-1,4-dione) (**7b**)

A solution of compound **14** (39 mg, 0.08 mmol) in acetonitrile (1 mL) was cooled down to −7 °C with an ice and salt bath and a solution of 0.25-M CAN (274 mg, 0.5 mmol) in a CH_3CN/H_2O (7:3) mixture was added drop-by-drop. The reaction mixture was stirred at room temperature for 7 h. The reaction was quenched with Et_2O (5 mL) and the organic layer was washed with water and brine, then it was dried on Na_2SO_4 and concentrated in vacuo. The crude product was employed in the next step without any further purification; it was dissolved in ethanol (3.6 mL) and $NaOH_{aq}$ 2-M (3.5 mL) was added. The reaction mixture was then warmed up to 70 °C and stirred for 4 h. After reaction completion the solution was cooled down to 0 °C, acidified to pH 1 with HCl 37% and extracted with ethyl acetate. The combined organic phases were dried on anhydrous Na_2SO_4 and concentrated in vacuo. The resulting brown solid was triturated in a solution of hexane and ethyl acetate (8:2), providing 27 mg of product **7b** (87% yield) as a brown solid. ^{1}H-NMR (300 MHz, $CDCl_3$): δδ(ppm) = 8.06 (brs, 4H) 5.99 (s, 2H); 2.35 (t, *J* = 7.4 Hz, 4H); 1.62 (m, 4H); 1.29– 1.24 (m, 8H). ^{13}C NMR (100 MHz, d^6-DMSO): δδ(ppm) = 119.74, 110.56, 34.40, 30.12, 29.89, 25.54 (detected signals).

3. Results

3.1. NS Polymerization at Different Concentrations of EMB

In our previous study, embelin (EMB) was reported as the first molecule capable to interfere with the heat-induced in vitro polymerization of NS [25]. It was shown to destabilize Nat and Lat NS with a 1:1 EMB:NS binding ratio. All the experiments were performed in large excess of EMB (1.5 mM) compared to the concentration of NS (85 μM), but the effects of lower concentrations of EMB were not determined [25]. Here we test the effect of several dilutions of EMB on heat-induced in vitro polymerization of NS. A solution of 85-μM NS was incubated with EMB at concentrations ranging between 0 and 1.5 mM and NS polymerization was evaluated after 16 h of incubation at 45 °C by analytical size-exclusion chromatography (SEC, Figure 1)
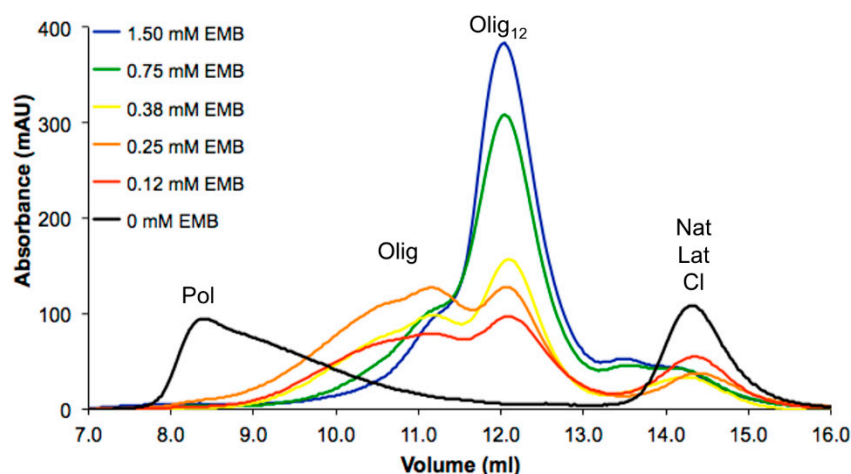
Figure 1. Effects of decreasing concentration of embelin (EMB) in heat-induced polymerization of neuroserpin (NS). Aliquots of 85-μM native NS were incubated 16 h at 45 °C in the absence (black) or presence of 1.5-mM (blue), 0.75-mM (green), 0.38-mM (yellow), 0.25-mM (orange) or 0.12-mM (red) EMB and analyzed by size-exclusion chromatography (SEC) using a Superdex 200 10/300 GL in 10-mM Tris HCl, 50-mM KCl, pH 8.0 buffer. Acronyms—Nat—native NS; Lat—latent NS; Cl—cleaved; Olig—oligomer; Pol—polymers.

In the absence of EMB, NS abundantly formed Pol which were eluted in the dead volume of the column (8.5 mL) as previously reported [25]; only a minor peak corresponding to monomeric Lat was eluted at 14.5 mL. In the presence of 1.5 mM EMB, the high-molecular weight Pol were not observed, but smaller oligomers eluted at 12.3 mL (Olig$_{12}$), in keeping with the effect we previously reported in Saga et al. [25]. A very similar result was observed in the presence of 0.75-mM EMB, where the typical peak at 12.3 mL was predominant, but the peak eluted at 11.2 mL—corresponding to larger oligomers—was slightly more intense. The peak corresponding to Olig$_{12}$ was present at all tested concentrations, but its intensity decreased proportionally to the amount of EMB added. The reduction of these species was paralleled by the appearance of larger aggregates as indicated by the appearance of two intense broad peaks eluting at 11.2 and 10.5 mL associated with larger oligomeric species (Olig).

3.2. EMB Promotes Proteasomal Degradation in Cell Lines Expressing NS

The effect of EMB on polymerization was assessed in COS-7 cells transiently transfected for expression of wild type (WT) and G392E NS. Electrophoresis and western blot analysis of cells cultured for 24 h after transfection showed that, in the absence of EMB, WT NS was efficiently expressed and secreted (Figure 2A, WT NS panel, lanes 1 and 4). A small part of the protein was found in the insoluble fraction (Figure 2B, first lane), but most of it was contained in the soluble cellular fraction and culture medium as a native monomeric conformation, as revealed by non-denaturing PAGE (Figure 2C, WT NS panel, lanes 1 and 4). In keeping with previous studies [7], in cells expressing G392E NS most of the protein accumulated in the intracellular fraction, both in the soluble lysate (Figure 2A, G392E NS panel, first lane) and as insoluble aggregates (Figure 2B, lane 4); soluble intracellular and secreted G392E NS proteins were found mostly in the polymeric conformation (Figure 2C, G392E NS panel, lanes 1 and 4).

In parallel wells, transfected cells were treated with 10-μM EMB, collected after 24 h of incubation and analyzed similarly by SDS and non-denaturing electrophoresis and western blot. EMB promoted a reduction in NS signal for both WT and G392E NS transfected cells (Figure 2A,C, WT NS and G392E NS panels, lanes 2 and 5 and corresponding histograms). Unexpectedly, the polymerization pattern remained similar to the one observed in the absence of EMB, but with a weaker signal (Figure 2C, G392E NS panel, compare lane 1 to lane 2 and 4 to 5 and histogram). Inhibiting the proteasome in cells treated with 10-μM EMB by treating them at the same time with 2.5-μM MG132 caused a recovery in protein signals, which were restored to control levels (Figure 2, A and 2C, WT NS and G392E NS panels, compare lanes 3 and 6 with the other lanes and histograms). Moreover, the simultaneous treatment with EMB and MG132 exerted a modest toxicity in cells expressing NS, as shown by the presence of a low amount of the loading control protein GAPDH in the culture medium of cells expressing WT NS under the double treatment (Figure 2A, WT NS-GAPDH panel, lane 6). When COS-7 cells were transfected with a non-related neuronal protein, neuroligin 3, a reduction in protein levels after SDS-PAGE and western blot analysis of the cell lysates was also observed upon EMB treatment, with recovery to control levels when cells were treated simultaneously with EMB and MG132 as described for NS (results not shown).
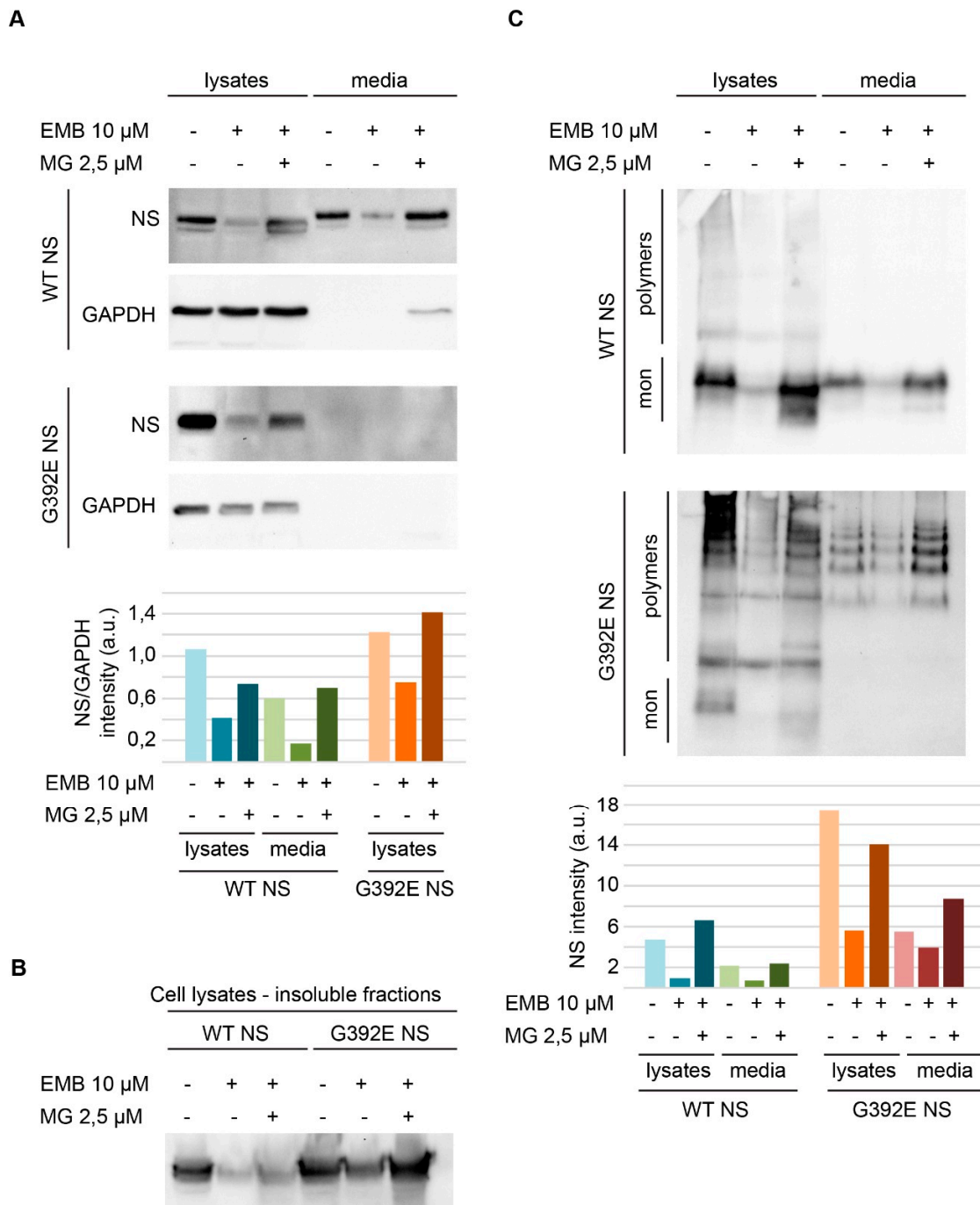
Figure 2. Embelin treatment results in a decreased level of wild type and polymerogenic G392E mutant NS that is reversed by proteasomal inhibition. (**A**) SDS-PAGE and western-blot analysis of lysates and culture media of cells transfected with wild type or G392E NS and treated with EMB (10 µM) alone or together with the proteasomal inhibitor MG132 (2.5 µM), as indicated in figure. GAPDH served as a loading control. Histogram shows the densitometric analysis of the western blot membranes, with NS intensity values normalized to GAPDH intensities for the corresponding lanes; (**B**) SDS-PAGE and western blot analysis of the insoluble proteins from post-nuclear pellets obtained from the same samples in A, extracted as described in the Methods section; (**C**) non-denaturing PAGE and western blot analysis of the same samples analyzed in A. The histogram shows the densitometric analysis of the western blot membranes; for the G392E NS samples, the value was calculated by addition of all the separate bands present in each lane.

3.3. Design and Synthesis of EMB Analogs

In order to ameliorate EMB pharmacological properties and to explore the structure-activity relationship, EMB analogs were designed and synthetized (Figure 3). The low water solubility of EMB prevented crystallographic or NMR studies on the NS–EMB complex thus both chemical moieties of EMB, the lipophilic chain and the quinone ring, were systematically modified.
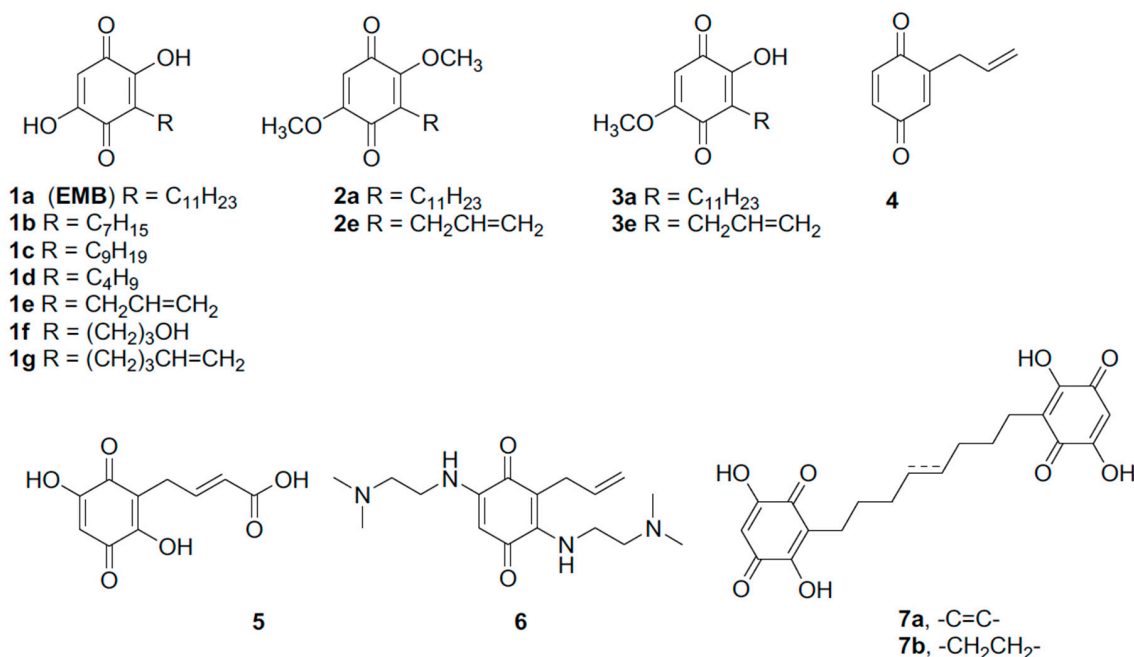
Figure 3. Structure of embelin (**1a**, EMB) and analogs (**1b–g**, **2a,e**, **3a,e**, **4–6**, **7a,b**).

The role of the n-alkyl residue in position 3 was first, evaluated by modulation its length. Initially, shorter chains were inserted to reduce the lipophilicity with respect to the lead compound. The synthesis of embelin (**1a**) and its analogs **1b–1d** started from the common precursor 1,2,4,5-tetramethoxybenzene (**9**) [34] which was subjected to an ortho-metalation reaction in the presence of *n*-BuLi (Figure 4). To obtain the intermediates **10a**, **10d** and **10g** the ortho-metalation reactions were carried out in presence of hexamethylphosphoramide (HMPA) at −40 °C [38]. On the contrary, the intermediates **10c** and **10b** were obtained carrying out the reaction at room temperature and without HMPA [39].

The analog bearing an allyl chain at position 3 (compound **1e**) was prepared following a different strategy, based on the treatment of the phenol **8** with allyl bromide and subsequent microwave-assisted Claisen rearrangement to obtain the alkylated compound **11** [33].

Once obtained compounds **10a–d**, **10g** and **11,** the substituted benzene rings were oxidized to the corresponding quinones. EMB **1a** and quinones analogs **1b**, **1c** and **1g** were obtained by treatment with CAN, followed by hydrolysis of the crude intermediates with 2-M NaOH.

To evaluate the role of the free hydroxy groups on the EMB benzoquinone core, 2,5-dimethoxy and 2-hydroxy-5-methoxy-1,4-benzoquinones **2a** and **3a**, formed by CAN–mediated oxidation of **10a**, were isolated and purified. Following the same procedure, the analogs **2e** and **3e** were obtained. Treatment of 2,5-dimethoxy-1,4-benzoquinones intermediates **2e** with 2-M NaOH (aq.) in ethanol, gave 2,5-dihydroxy-1,4-benzoquinones **1e** in quantitative yield.
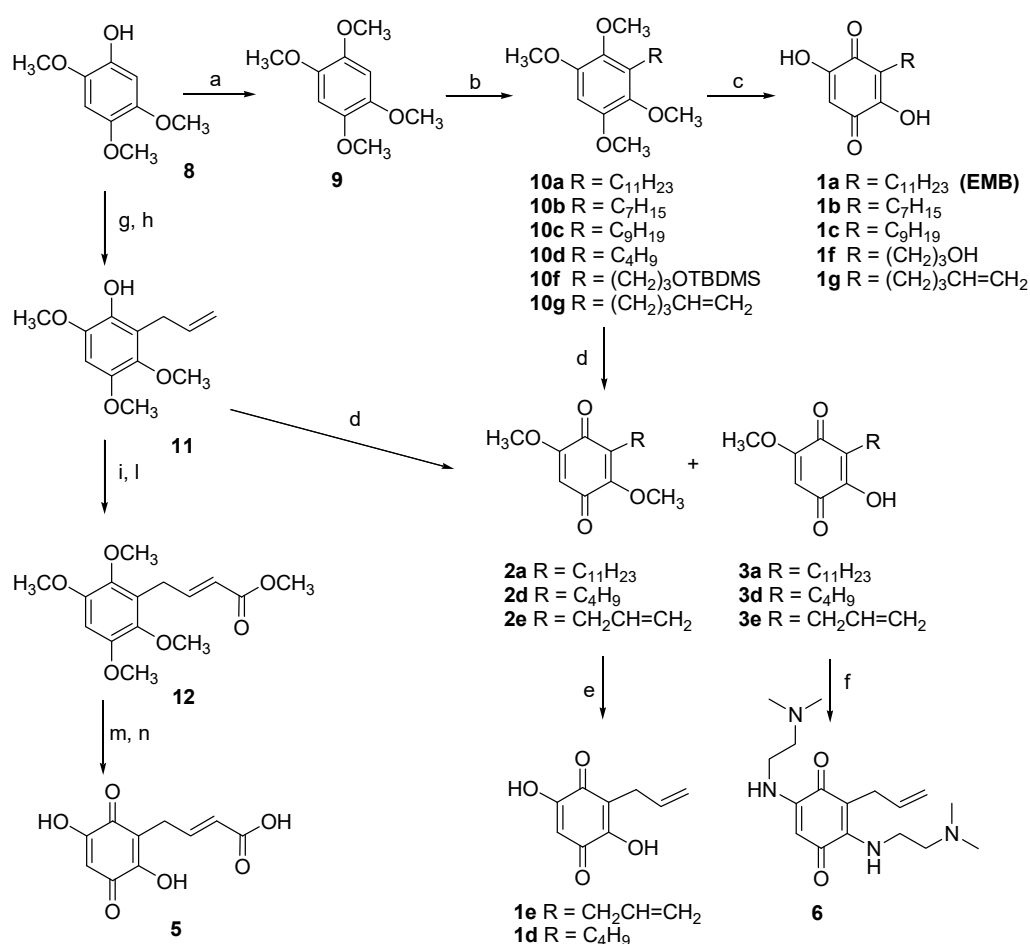
Figure 4. Synthesis of embelin (**1a**) and analogs **1b–1g**, **5** and **6**. Reagents and conditions: (a) CH$_3$I, K$_2$CO$_3$, acetone, reflux, 86%; (b) for **10a**: *n*-BuLi 1.6 M, HMPA, THF, −40 °C, 1 h, then 1-bromoundecane, −10 °C, overnight, 28%; for **10b**: *n*-BuLi 1.6 M, THF, rt, 40 min. then heptylbromide, rt, overnight, 45%; for **10c**: *n*-BuLi 1.6 M, THF, rt, 30 min. then nonylbromide, rt, overnight, 46%; for **10d**: *n*-BuLi 1.6 M, HMPA, THF, −40 °C, 1 h, then 1-bromobutane, −10 °C, overnight, 31%; for **10f**: *n*-BuLi 1.6 M, THF, 0 °C to rt, 2 h, then 3-(bromopropyloxi)-*tert*-butyldimethylsilane −80 °C to rt, 22 h, 35%; for **10g**: *n*-BuLi 1.6 M, HMPA, THF, −40 °C to rt, 40 min., then 5-bromo-1-pentene, −40 °C to rt, 27 h, 48%; (c) i. CAN, CH$_3$CN:H$_2$O 7:3, −10 °C, then rt; ii. 2-M NaOH (aq.), EtOH, 70 °C, 2 h, yields over two steps for **1a**: 67%, **1b**: 30%, **1c**: 40%; **1g**: 71%; for **1f**: i. CAN, CH$_3$CN: H$_2$O 7:3, −10 °C, 2 h, ii. HClO$_4$ 60%, CH$_2$Cl$_2$, rt, 3 h, 28% over two steps; (d) CAN, CH$_3$CN: H$_2$O 7:3, −10 °C then rt, yields **2a**: 36%, **3a**: 43%, **2e**: 71%, **3e**: 17%, **2d**: 35%, **3d**: 29%; (e) 2-M NaOH (aq.), EtOH, 70 °C, 2 h, **1e**: quant, **1d**: quant.; (f) NaHCO$_3$, (CH$_3$)$_2$NCH$_2$CH$_2$NH$_2$, EtOH, 48 h, rt **6**:35% (g) allyl bromide, K$_2$CO$_3$, acetone, 97%; (h) MW, 190 °C, 30 min, 92%; (i) CH$_3$I, K$_2$CO$_3$, acetone, 16 h, reflux, 48%; (l) methyl acrylate, UMICORE M73 SIMes, CH$_2$Cl$_2$, 6 h, rt, 55%; (m) i. CAN, CH$_3$CN: H$_2$O 7:3, −10 °C, then rt; ii. HClO$_4$ 70%, CH$_2$Cl$_2$, rt, 3 h, 61% over two steps; (n) LiOH·H$_2$OH, THF: H$_2$O 1:1, rt, overnight, 64%.

In order to increase the polarity and, hopefully, the water solubility with respect to the lead compound, a hydroxy group and a carboxylic group were introduced on the side chain, maintaining intact the 2,5-dihydroxy-1,4-benzoquinone scaffold.

With this purpose, (3-bromopropyloxy)-tertbutyldimethylsilane was used as electrophile after ortho lithiation substitution reaction, to obtain compound **10f** in 35% yield [40]. CAN-mediated oxidation and treatment with perchloric acid (60%) in dichloromethane of the resulting mixture of quinones gave the EMB analog **1f**.

To introduce a carboxylic group on the side chain, the allyl derivative **11** was methylated, then the resulting tetramethoxy intermediate was reacted with methyl acrylate in presence of the metathesis catalyst UMICORE M73 SIMes, to give compound **12** in 55% yield. CAN-mediated oxidation and treatment with perchloric acid (60%) in dichloromethane gave the corresponding quinone in 61% yield over two steps. Finally, hydrolysis of methyl ester with LiOH·H_2O gave the acid **5**.

To explore the role of the 2,5-substituents on the quinone ring, the hydroxy groups were replaced by a *N,N*-dimethylethylenediamino residue. Compound **3e** was thus reacted with NaHCO$_3$ and *N,N*-dimethylethyleneamine in ethanol for 48 h at room temperature [41], to give compound **6** in 35% yield.

Additionally, the quinone analog **4**, completely lacking substituents in position 2,5 on the ring, was prepared by CAN-mediate oxidation of 2-allyl-4-methoxyphenol [32].

Finally, dimeric analogs of EMB were synthetized, aiming at an enhanced biologic activity with respect to the monomeric species and to increase the aqueous solubility due to the presence of two quinone rings in the final compounds (Figure 5). An olefin cross-metathesis reaction with Hoveyda–Grubbs second-generation catalyst was performed on compound **10g**, resulting in the dimer **13** with an 85% yield. The double bond of the dimeric compound was then reduced by hydrogenolysis to give compound **14** in 59% yield and both **13** and **14** were transformed via CAN-mediated oxidation to the corresponding bisquinones **7a** and **7b**, as outlined in Figure 5.
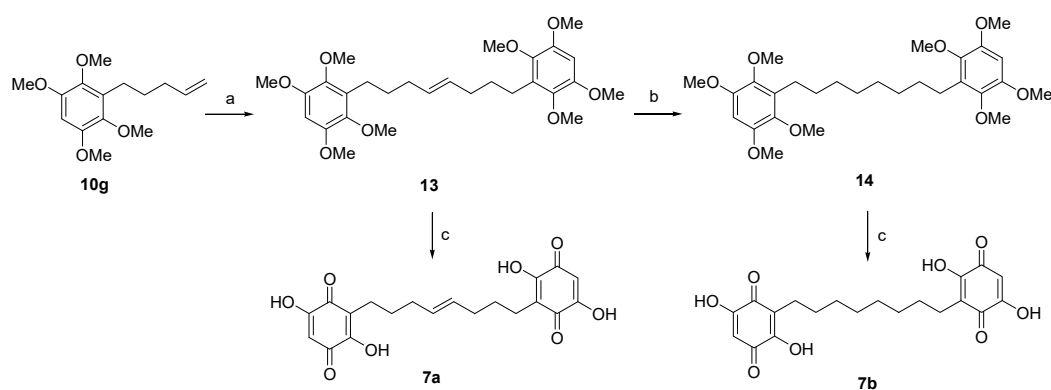
Figure 5. Synthesis of dimeric compounds **7a,b**. Reagents and conditions. (a) Hoveyda–Grubbs 2nd generation catalyst, dry CH$_2$Cl$_2$, reflux, 5 h, 85%; (b) H$_2$, Pd/C, MeOH, r.t., 24 h, 59%; (c) i. CAN, CH$_3$CN: H$_2$O 7:3, −10 °C to rt; 4 h ii. 2-M NaOH (aq.), EtOH, 70 °C, 4 h, yields over two steps for **7a**: 79%; for **7b**: 87%.

3.4. Effects of the EMB Analogs on NS Polymerization

All the EMB analogs synthetized were tested to assess their capability to interfere with heat-induced polymerization of NS. A solution of 85-μM NS was incubated at 45 °C in the presence or absence of each compound at saturating concentration. A solution of NS in the presence of EMB was used as an additional control. The effect of each compound after 3 h of incubation was assessed by SEC (Figure 6 and Table 1). After 1 or 3 h of incubation, an aliquot of the incubated mixture was taken and analyzed by non-denaturing PAGE (representative results are shown in Figure 7).
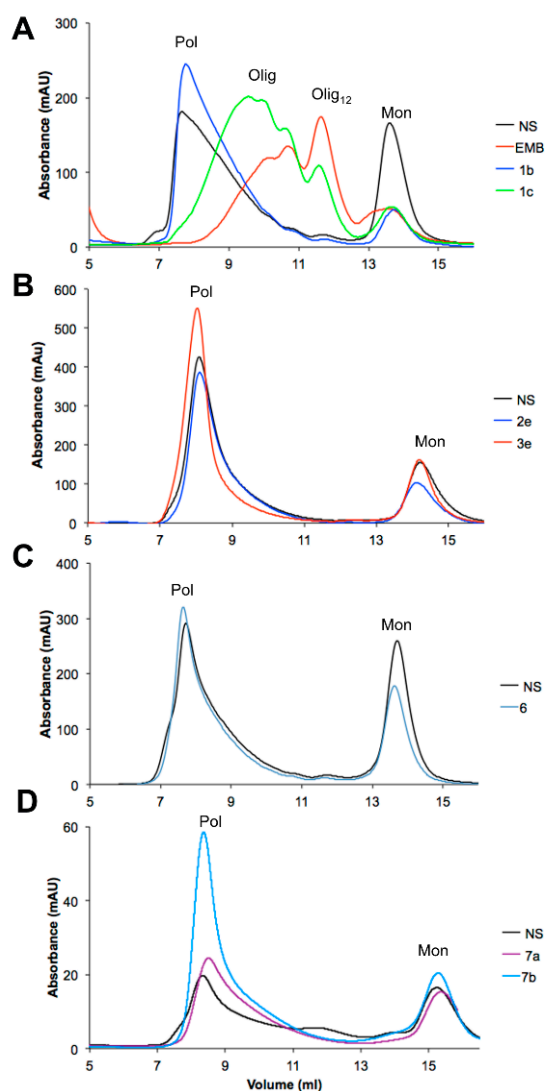
Figure 6. SEC analyses of EMB-analogs effect on heat-induced NS polymerization. Solutions of 85-μM NS was incubated 3 h at 45 °C in the presence or absence of EMB analogs at saturating concentration. The effect of representative compounds of (**A**) group 1, (**B**) group 2, (**C**) group 3, (**D**) group 3 is reported.

Table 1. EMB-analogs effect on NS heat-induced polymerization. The effect of EMB analogs on NS heat-induced polymerization at saturating concentration after 3 h of incubation at 45 °C was evaluated by SEC analysis and the amount of each species was calculated. Pol—NS polymers eluting in the dead column volume; Olig—oligomers eluting at 10–11 mL; Olig12—oligomers typically formed in presence of EMB eluting at 12.3 mL; Mon—monomeric NS eluted at 14–15 mL; Control—NS incubated in absence of potential inhibitors; All compounds were tested at saturating concentration.

	Pol	Olig	Olig12	Mon
Control	73%	0%	5%	22%
EMB, 1a	2%	37%	48%	14%
1b	80%	0%	3%	17%
1c	10%	50%	27%	13%
1d	54%	0%	0%	46%
1e	66%	0%	0%	34%
1f	69%	0%	0%	31%
1g	52%	0%	0%	48%

Table 1. *Cont.*

	Pol	Olig	Olig12	Mon
2a	3%	44%	23%	30%
3a	7%	35%	38%	20%
2e	79%	0%	0%	21%
3e	77%	0%	0%	23%
4	73%	0%	11%	16%
5	76%	0%	0%	24%
6	66%	0%	0%	34%
7a	56%	8%	0%	35%
7b	70%	06%	0%	24%
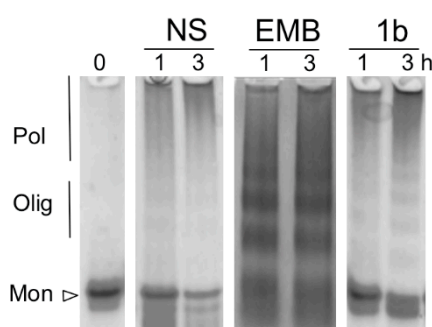
Figure 7. Non-denaturing PAGE analysis of EMB and 1b EMB analogs effect on heat-induced NS polymerization. Solutions of 85-μM NS were incubated for 3 h at 45 °C in presence or absence of EMB and analyzed by non-denaturing PAGE after 1 and 3 h of incubation.

The first group of modifications was intended to modify the length of the alkyl tail in position 3. The effect of two representative EMB analogs (**1b** and **1c**) is reported in Figure 6A in comparison with unmodified EMB. As previously reported [25], EMB promoted the formation of $Olig_{12}$ compared to the large polymers in its absence. Table 1 reports the distribution of different species in the presence or the absence of the compounds obtained by SEC analysis. In the presence of EMB almost no Pol were detectable, whereas 85% of the protein was in the oligomeric form (37% Olig and 48% $Olig_{12}$). In the absence of any compounds 73% of NS was present as Pol that eluted in the dead volume. The same incubated mixtures of NS alone or NS in the presence of EMB were analyzed by non-denaturing PAGE (Figure 7), which clearly highlighted the differences between the two samples: in the first case the high-molecular weight Pol poorly entered the gel, whereas in the presence of EMB it was possible to separate different oligomeric species. A similar effect was observed for compound **1c**, which promoted the formation of oligomers, even though they eluted at higher column volume compared to the species formed in the presence of EMB. EMB analogs **1b**, **1d**, **1e**, **1f**, **1g** and **5** instead did not exert any significant effects on NS polymerization as reported in Table 1. Indeed, in the presence of these EMB analogs $Olig_{12}$ were not present, whereas most of the protein formed Pol. **1c** on the contrary was still capable to prevent the formation of Pol but was less efficient compared to EMB to promote the formation of $Olig_{12}$. Figure 7 shows a representative gel of coincubation of NS with EMB-derivative **1b**. According to SEC analysis, this compound promoted the formation of Pol as most represented species.

Next the role of the free hydroxyl group in positions C2 and C5 was evaluated. To this aim, two compounds were synthesized with the substitution of hydroxyl group in position 5 (**3a** and **3e**) or both hydroxyl groups in position 2 and 5 (**2a** and **2e**). Moreover, in compounds **2e** and **3e** also the alkyl tail was modified, and their effect is reported as representative of this group. For analogs **2e** and **3e**, no anti-polymeric action was detected as reported in Figure 6B. Table 1 clearly shows that in the presence of analogs **2e** and **3e** NS predominantly formed Pol (79% and 77%, respectively). Residual anti-polymeric activity was observed in the presence of **2a** and **3a** in which Olig and $Olig_{12}$ were

present, but still in a percentage lower than that in the presence of EMB. EMB derivative **3e** was slightly more effective than **3a** with 38% and 23% of protein present as $Olig_{12}$, respectively (Table 1).

Compound **4**, completely lacking 2,5-hydroxy group on quinone scaffold with respect to compound **1e**, did not exert significant anti-polymeric activity, even though a slight amount of $Olig_{12}$ was detected (11%, Table 1).

Moreover, also the replacement of both hydroxy groups at C2 and C5 with N,N-dimethylethylenediamino residues (**6**), did not produce any anti-polymerization effect (Table 1).

Finally, two different EMB dimers were tested (Figure 6D). Even in this case, the presence of the EMB analogs **7a** or **7b** did not exert significant effects on NS polymerization: as reported in Figure 6D and Table 1, traces of Olig were detected, but 56% and 70% of the protein were forming Pol, thus indicating that the polymerization pathway was not altered.

4. Discussion

The serpinopathies are a group of protein misfolding diseases characterized by the accumulation of serpin polymers in the endoplasmic reticulum of serpin-expressing cells [1]. To date no pharmacological treatment against the polymerization of any serpin is available, due to several reasons. Serpins are very plastic molecules which undergo major conformational changes both in physiologic and pathologic conditions [1]. In particular, the structure of serpin polymers is still under debate [2,20–22] preventing a structure-based drug design strategy. Moreover, the localization within the endoplasmic reticulum protects the serpin polymers from pharmacological molecules not able to penetrate the cellular membranes [2,3,5–7]. In the case of FENIB, a potential anti-polymerization molecule should also be able to pass the blood brain barrier. In this context, EMB displays several important properties: (I) it binds to all NS conformers with a stoichiometry of 1:1; (II) it is the first molecule capable to prevent NS Pol formation; (III) it can dissolve preformed polymers in vitro [25]; and (IV) it can cross the blood brain barrier [28].

In previous work [25], only the aqueous saturated solution of EMB was used to characterize its anti-polymerization properties, while here we describe for the first time the dose–response effects of EMB against NS polymerization. Our data indicate that while even the lowest concentration of EMB tested (0.12 mM) perturbs NS polymerization, lowering the concentration of EMB results in increasingly bulkier NS oligomers (Figure 1). When cell lines expressing a polymerogenic variant of NS (G392E NS, [4]) were treated with EMB, lower Pol levels were observed, but this effect was also apparent for WT NS and for a non-related protein (neuroligin 3, results not shown), and was reverted by simultaneous treatment with the proteasome inhibitor MG132, suggesting that the decrease in NS and neuroligin 3 levels was mainly due to the activation of the proteasome system or maybe to a general decrease in protein synthesis caused by EMB, rather than to a specific anti-polymerization activity. In fact, an increase in monomeric or oligomeric G392E NS in the presence of EMB was not observed after non-denaturing electrophoresis and western blot analysis, nor did we observe an increase in G392E NS secretion as expected for the monomeric protein. In particular, this compound was reported to regulates the apoptosis pathway through the inhibition of NF-kB. Even though a positive effect was observed, it was not directly associated with the remodulation of NS polymerization.

These observations prompted us to search for other small molecules with enhanced specificity. The low water solubility of EMB, its tendency to form micelles and its ability to cause NS oligomerization hampered crystallographic and NMR experiments; in turn, the lack of structural data on NS–EMB complex prevented a structural-based drug design strategy. Furthermore, NS is a very complex protein for in silico docking of small molecules: the Nat conformation is metastable and displays highly flexible regions and, moreover, it does not present any obvious deep cavity where small molecules could be accommodated. Thus, in order to identify other molecules with anti-polymerization properties, a systematic chemical modification of EMB was undertaken: the two main EMB moieties—the quinone ring and the lipophilic tail—were modified. None of the synthesized EMB analogs displayed an anti-polymerization effect distinctly better than the one reported for the lead compound. Interestingly,

most of the modifications resulted in inactive compounds, indicating that the binding of EMB to NS is achieved by an already optimal interaction interface, and only a few minor chemical modification led to compounds that retained activity. All the chemical groups of EMB seem to be important for its interaction with NS, but the lipophilic tail seems to be crucial: the only tolerated modification is its shortening of two C atoms (**1c**), while all other modifications (shorter, more polar or longer tail, more rigid chain or dimeric structures) lead to inactive molecules.

The substitution of one or two hydroxyl groups on the quinone ring with *O*-methyl groups (compounds **2a** and **3a**, respectively) resulted in active compounds. In presence of compound **2a** NS forms smaller oligomers than the ones formed in presence of **3a**, but EMB remained better inhibitor compared with these two molecules. This observation indicates that compounds with hydroxyl groups in such positions have a higher anti-polymerization activity, thus in that respect EMB presents optimized substituent on the quinone ring. Moreover, the comparison of effects exerted by the couple **2a/3a** and **2e/3e** confirmed the importance of the alkyl tail in the inhibition process. Indeed, these couple of compounds differs only in the tail structure. In general, other modifications of the substituents on the quinone ring resulted in inactive molecules and, in particular, all analogs bulkier than EMB lost activity. Altogether, our results confirmed that, to date, EMB is the best inhibitor of NS polymerization in vitro.

EMB was reported to bind to PAI-1, PAI-2 and PN1, three members of the serpin family: EMB is an antagonist of the inhibitory abilities of these serpins against their target proteases, while no effects on polymerization were reported [42]. A study about EMB-derived molecules tested for PAI-1 identified the hydroxyl groups at C2 and C5 and the length of the alkyl chains at C3 as determinant for inhibitory potency and some EMB analogs displaying relevant inhibition properties were identified [43]. Still, in that study the effects of EMB and its analogs were tested with regards to modulation of serpin inhibitory activity against its target protease and polymerization was not addressed. In a different report [44], even very conservative modifications of the structure of EMB abolished its ability to interfere with α-glucosidase, a protein involved in diabetes mellitus, in analogy with what we observed in the present work.

In summary, in this work we show that the interaction between EMB and NS is already so specific that all the analogs produced were found to be either inactive or with a lower anti-polymerization activity than EMB itself. The activity of EMB decreased with decreasing concentration, however all tested EMB concentrations were able to reduce NS polymerization. Finally, the effect observed in a cell model was the reduction of NS protein level through a non-NS specific effect due to an increase in proteasomal degradation. Overall, the present data are encouraging; however, future strategies to better shuttle EMB into the endoplasmic reticulum of neurons to achieve high local concentrations will likely lead to stronger and more specific anti-polymerization effects.

References

1. Fra, A.; D'Acunto, E.; Laffranchi, M.; Miranda, E. Cellular Models for the Serpinopathies. *Methods Mol. Biol. Clifton NJ* **2018**, *1826*, 109–121. [CrossRef]
2. Davis, R.L.; Shrimpton, A.E.; Holohan, P.D.; Bradshaw, C.; Feiglin, D.; Collins, G.H.; Sonderegger, P.; Kinter, J.; Becker, L.M.; Lacbawan, F.; et al. Familial dementia caused by polymerization of mutant neuroserpin. *Nature* **1999**, *401*, 376–379. [CrossRef]

3. Davis, R.L.; Holohan, P.D.; Shrimpton, A.E.; Tatum, A.H.; Daucher, J.; Collins, G.H.; Todd, R.; Bradshaw, C.; Kent, P.; Feiglin, D.; et al. Familial encephalopathy with neuroserpin inclusion bodies. *Am. J. Pathol.* **1999**, *155*, 1901–1913. [CrossRef]

4. Davis, R.L.; Shrimpton, A.E.; Carrell, R.W.; Lomas, D.A.; Gerhard, L.; Baumann, B.; Lawrence, D.A.; Yepes, M.; Kim, T.S.; Ghetti, B.; et al. Association between conformational mutations in neuroserpin and onset and severity of dementia. *Lancet Lond. Engl.* **2002**, *359*, 2242–2247. [CrossRef]

5. Coutelier, M.; Andries, S.; Ghariani, S.; Dan, B.; Duyckaerts, C.; van Rijckevorsel, K.; Raftopoulos, C.; Deconinck, N.; Sonderegger, P.; Scaravilli, F.; et al. Neuroserpin Mutation Causes Electrical Status Epilepticus of Slow-Wave Sleep. *Neurology* **2008**, *71*, 64–66. [CrossRef] [PubMed]

6. Hagen, M.C.; Murrell, J.R.; Delisle, M.B.; Andermann, E.; Andermann, F.; Guiot, M.C.; Ghetti, B. Encephalopathy with Neuroserpin Inclusion Bodies Presenting as Progressive Myoclonus Epilepsy and Associated with a Novel Mutation in the Proteinase Inhibitor 12 Gene. *Brain Pathol. Zurich Switz.* **2011**, *21*, 575–582. [CrossRef] [PubMed]

7. Miranda, E.; MacLeod, I.; Davies, M.J.; Pérez, J.; Römisch, K.; Crowther, D.C.; Lomas, D.A. The intracellular accumulation of polymeric neuroserpin explains the severity of the dementia FENIB. *Hum. Mol. Genet.* **2008**, *17*, 1527–1539. [CrossRef] [PubMed]

8. Miranda, E.; Lomas, D.A. Neuroserpin: A serpin to think about. *Cell Mol. Life Sci. CMLS* **2006**, *63*, 709–722. [CrossRef] [PubMed]

9. Hastings, G.A.; Coleman, T.A.; Haudenschild, C.C.; Stefansson, S.; Smith, E.P.; Barthlow, R.; Cherry, S.; Sandkvist, M.; Lawrence, D.A. Neuroserpin, a brain-associated inhibitor of tissue plasminogen activator is localized primarily in neurons. Implications for the regulation of motor learning and neuronal survival. *J. Biol. Chem.* **1997**, *272*, 33062–33067. [CrossRef]

10. Yepes, M.; Lawrence, D.A. Tissue-type plasminogen activator and neuroserpin: A well-balanced act in the nervous system? *Trends Cardiovasc. Med.* **2004**, *14*, 173–180. [CrossRef]

11. Galliciotti, G.; Sonderegger, P. Neuroserpin. *Front. Biosci J. Virtual Libr* **2006**, *11*, 33–45. [CrossRef] [PubMed]

12. Caccia, S.; Ricagno, S.; Bolognesi, M. Molecular bases of neuroserpin function and pathology. *Biomol. Concepts* **2010**, *1*, 117–130. [CrossRef]

13. Huntington, J.A.; Read, R.J.; Carrell, R.W. Structure of a serpin-protease complex shows inhibition by deformation. *Nature* **2000**, *407*, 923–926. [CrossRef] [PubMed]

14. Barker-Carlson, K.; Lawrence, D.A.; Schwartz, B.S. Acyl-enzyme complexes between tissue-type plasminogen activator and neuroserpin are short-lived in vitro. *J. Biol. Chem.* **2002**, *277*, 46852–46857. [CrossRef] [PubMed]

15. Ricagno, S.; Caccia, S.; Sorrentino, G.; Antonini, G.; Bolognesi, M. Human neuroserpin: Structure and time-dependent inhibition. *J. Mol. Biol.* **2009**, *388*, 109–121. [CrossRef]

16. Gooptu, B.; Lomas, D.A. Conformational pathology of the serpins: Themes, variations, and therapeutic strategies. *Annu. Rev. Biochem* **2009**, *78*, 147–176. [CrossRef] [PubMed]

17. Moriconi, C.; Ordonez, A.; Lupo, G.; Gooptu, B.; Irving, J.A.; Noto, R.; Martorana, V.; Manno, M.; Timpano, V.; Guadagno, N.A.; et al. Interactions between N-linked glycosylation and polymerisation of neuroserpin within the endoplasmic reticulum. *FEBS J.* **2015**, *282*, 4565–4579. [CrossRef] [PubMed]

18. Visentin, C.; Broggini, L.; Sala, B.M.; Russo, R.; Barbiroli, A.; Santambrogio, C.; Nonnis, S.; Dubnovitsky, A.; Bolognesi, M.; Miranda, E.; et al. Glycosylation Tunes Neuroserpin Physiological and Pathological Properties. *Int. J. Mol. Sci.* **2020**, *21*, 3235. [CrossRef]

19. Lomas, D.A.; Evans, D.L.; Finch, J.T.; Carrell, R.W. The mechanism of Z alpha 1-antitrypsin accumulation in the liver. *Nature* **1992**, *357*, 605–607. [CrossRef]

20. Yamasaki, M.; Li, W.; Johnson, D.J.D.; Huntington, J.A. Crystal structure of a stable dimer reveals the molecular basis of serpin polymerization. *Nature* **2008**, *455*, 1255–1258. [CrossRef]

21. Yamasaki, M.; Sendall, T.J.; Pearce, M.C.; Whisstock, J.C.; Huntington, J.A. Molecular basis of α1-antitrypsin deficiency revealed by the structure of a domain-swapped trimer. *EMBO Rep.* **2011**, *12*, 1011–1017. [CrossRef] [PubMed]

22. Noto, R.; Santangelo, M.G.; Ricagno, S.; Mangione, M.R.; Levantino, M.; Pezzullo, M.; Martorana, V.; Cupane, A.; Bolognesi, M.; Manno, M. The tempered polymerization of human neuroserpin. *PLoS ONE* **2012**, *7*, e32444. [CrossRef]

23. Santangelo, M.G.; Noto, R.; Levantino, M.; Cupane, A.; Ricagno, S.; Pezzullo, M.; Bolognesi, M.; Mangione, M.R.; Martorana, V.; Manno, M. On the molecular structure of human neuroserpin polymers. *Proteins* **2012**, *80*, 8–13. [CrossRef]

24. Noto, R.; Santangelo, M.G.; Levantino, M.; Cupane, A.; Mangione, M.R.; Parisi, D.; Ricagno, S.; Bolognesi, M.; Manno, M.; Martorana, V. Functional and dysfunctional conformers of human neuroserpin characterized by optical spectroscopies and Molecular Dynamics. *Biochim. Biophys. Acta* **2015**, *1854*, 110–117. [CrossRef] [PubMed]

25. Saga, G.; Sessa, F.; Barbiroli, A.; Santambrogio, C.; Russo, R.; Sala, M.; Raccosta, S.; Martorana, V.; Caccia, S.; Noto, R.; et al. Embelin binds to human neuroserpin and impairs its polymerisation. *Sci. Rep.* **2016**, *6*. [CrossRef] [PubMed]

26. Radhakrishnan, N.; Gnanamani, A.; Prasad, N.R.; Mandal, A.B. Inhibition of UVB-induced oxidative damage and apoptotic biochemical changes in human lymphocytes by 2,5-dihydroxy-3-undecyl-1,4-benzoquinone (embelin). *Int. J. Radiat. Biol.* **2012**, *88*, 575–582. [CrossRef]

27. Kundap, U.P.; Bhuvanendran, S.; Kumari, Y.; Othman, I.; Shaikh, M.F. Plant Derived Phytocompound, Embelin in CNS Disorders: A Systematic Review. *Front. Pharmacol.* **2017**, *8*. [CrossRef]

28. Pathan, S.A.; Iqbal, Z.; Zaidi, S.; Talegaonkar, S.; Vohra, D.; Jain, G.K.; Azeem, A.; Jain, N.; Lalani, J.R.; Khar, R.K.; et al. CNS drug delivery systems: Novel approaches. *Recent. Pat. Drug Deliv. Formul.* **2009**, *3*, 71–89. [CrossRef]

29. Filosa, R.; Peduto, A.; Aparoy, P.; Schaible, A.M.; Luderer, S.; Krauth, V.; Petronzi, C.; Massa, A.; de Rosa, M.; Reddanna, P.; et al. Discovery and biological evaluation of novel 1,4-benzoquinone and related resorcinol derivatives that inhibit 5-lipoxygenase. *Eur. J. Med. Chem.* **2013**, *67*, 269–279. [CrossRef]

30. Filosa, R.; Peduto, A.; Schaible, A.M.; Krauth, V.; Weinigel, C.; Barz, D.; Petronzi, C.; Bruno, F.; Roviezzo, F.; Spaziano, G.; et al. Novel series of benzoquinones with high potency against 5-lipoxygenase in human polymorphonuclear leukocytes. *Eur. J. Med. Chem.* **2015**, *94*, 132–139. [CrossRef]

31. Martín-Acosta, P.; Haider, S.; Amesty, Á.; Aichele, D.; Jose, J.; Estévez-Braun, A. A new family of densely functionalized fused-benzoquinones as potent human protein kinase CK2 inhibitors. *Eur. J. Med. Chem.* **2018**, *144*, 410–423. [CrossRef]

32. Lamblin, M.; Sallustrau, A.; Commandeur, C.; Cresteil, T.; Felpin, F.-X.; Dessolin, J. Synthesis and biological evaluation of hydrophilic embelin derivatives. *Tetrahedron* **2012**, *68*, 4655–4663. [CrossRef]

33. Ogata, T.; Doe, M.; Matsubara, A.; Torii, E.; Nishiura, C.; Nishiuchi, A.; Kobayashi, Y.; Kimachi, T. Studies on the oxidative cyclization of 3-hydroxyalkyl-1,2,4-trialkoxynaphthalenes and synthetic application for the biologically active natural compound rhinacanthone. *Tetrahedron* **2014**, *70*, 502–509. [CrossRef]

34. Kwon, Y.-J.; Sohn, M.-J.; Kim, C.-J.; Koshino, H.; Kim, W.-G. Flavimycins A and B, Dimeric 1,3-Dihydroisobenzofurans with Peptide Deformylase Inhibitory Activity from Aspergillus flavipes. *J. Nat. Prod.* **2012**, *75*, 271–274. [CrossRef] [PubMed]

35. Mehta, G.; Pan, S.C. Total synthesis of the novel, biologically active epoxyquinone dimer (+/-)-torreyanic acid: A biomimetic approach. *Org. Lett.* **2004**, *6*, 3985–3988. [CrossRef] [PubMed]

36. Lin, Z.; Jensen, J.K.; Hong, Z.; Shi, X.; Hu, L.; Andreasen, P.A.; Huang, M. Structural insight into inactivation of plasminogen activator inhibitor-1 by a small-molecule antagonist. *Chem. Biol.* **2013**, *20*, 253–261. [CrossRef] [PubMed]

37. Chen, F.; Zhang, G.; Hong, Z.; Lin, Z.; Lei, M.; Huang, M.; Hu, L. Design, synthesis, and SAR of embelin analogues as the inhibitors of PAI-1 (plasminogen activator inhibitor-1). *Bioorg. Med. Chem. Lett.* **2014**, *24*, 2379–2382. [CrossRef] [PubMed]

38. Chen, X.; Gao, M.; Jian, R.; Hong, W.D.; Tang, X.; Li, Y.; Zhao, D.; Zhang, K.; Chen, W.; Zheng, X.; et al. Design, synthesis and α-glucosidase inhibition study of novel embelin derivatives. *J. Enzyme Inhib. Med. Chem.* **2020**, *35*, 565–573. [CrossRef]

39. Miranda, E.; Römisch, K.; Lomas, D.A. Mutants of neuroserpin that cause dementia accumulate as polymers within the endoplasmic reticulum. *J. Biol. Chem.* **2004**, *279*, 28283–28291. [CrossRef] [PubMed]

40. Belorgey, D.; Crowther, D.C.; Mahadeva, R.; Lomas, D.A. Mutant Neuroserpin (S49P) that causes familial encephalopathy with neuroserpin inclusion bodies is a poor proteinase inhibitor and readily forms polymers in vitro. *J. Biol. Chem.* **2002**, *277*, 17367–17373. [CrossRef]

41. Irving, J.A.; Ekeowa, U.I.; Belorgey, D.; Haq, I.; Gooptu, B.; Miranda, E.; Pérez, J.; Roussel, B.D.; Ordóñez, A.; Dalton, L.E.; et al. The serpinopathies studying serpin polymerization in vivo. *Methods Enzymol.* **2011**, *501*, 421–466. [CrossRef] [PubMed]

42. Mizuno, C.S.; Rimando, A.M.; Duke, S.O. Phytotoxic activity of quinones and resorcinolic lipid derivatives. *J. Agric. Food Chem.* **2010**, *58*, 4353–4355. [CrossRef] [PubMed]

43. Trapella, C.; Fischetti, C.; Lazzari, I.; Guerrini, R.; Rizzi, A.; Camarda, V.; Lambert, D.G.; McDonald, J.; Regoli, D.; Salvadori, S. Structure-activity studies on the nociceptin/orphanin FQ receptor antagonist 1-benzyl-N-{3-[spiroisobenzofuran-1(3H),4'-piperidin-1-yl]propyl} pyrrolidine-2-carboxamide. *Bioorg. Med. Chem.* **2009**, *17*, 5080–5095. [CrossRef] [PubMed]

44. Reinaud, O.; Capdevielle, P.; Maumy, M. Synthesis of New 3-(-2-Alkenyl)-2-hydroxy-5-methoxy-p-benzoquinones via Claisen Rearrangement of Original 5-Methoxy-4-(2-propenyloxy)-o-benzoquinones. *Synthesis* **1988**, *1988*, 293–300. [CrossRef]

5 DISCUSSION

Understanding the molecular bases underlying the conversion of soluble and active proteins into potentially toxic aggregates is pivotal to develop efficient treatments against conformational diseases. Indeed, due to the complexity and diversity of the factors involved in misfolding and aggregation processes, to date these pathologies are still incurable (5).

The data presented in this PhD thesis show that protein misfolding and aggregation processes are triggered by multifactorial causes. Nevertheless, the results here reported demonstrated that a complex ensemble of biophysical properties allows proteins to explore partially unfolded states, which is one of the main determinants leading to protein aggregation. In particular, we found that the tendency of proteins to achieve such conformations is regulated by several factors, including protein primary sequence, presence of post-translation modifications (PTMs), and chemical environment.

The primary mechanism of maintaining soluble and functional states of proteins is encoded in the sequence and involves the existence of intrinsic energy barriers that prevents the conversion into aggregation-prone states (149). Proteins have evolved structural and sequence-based strategies to maintain a functional state and prevent self-assembly (5). Thus, small changes, like the above presented D85V mutation in mβ2m (see paragraph 3.3.2), can alter the aggregation propensity of proteins and turn them into potentially pathological agents (150). Indeed, several conformational pathologies are linked to point mutations that disrupt folding equilibrium and favour the formation of polymeric states (24). This is the case of α1AT deficiency, caused by the E342K mutation (151), or the hereditary systemic amyloidosis linked to the D76N hβ2m mutant (34).

Modifications in the primary sequence can even favour or disadvantage misfolding and aggregation processes. As discussed above, the single substitution D85V in mβ2m switched the behaviour of the protein from non-amyloidogenic to amyloidogenic (see paragraph 3.3.2). This happens because the aminoacid 85 falls in an aggregation prone region and modifications within this sensitive segment drastically alter protein biophysical properties. Indeed, we observed that the mutation enhances the ability of the protein to form aggregation-prone species under physiological conditions that results in an increased propensity to form fibrils.

We found a similar outcome for D76N substitution in hβ2m (see paragraph 3.3.1). The higher amyloidogenicity of the natural mutant is generally ascribed to a general destabilization of the native state (117,119). Indeed, we found that the D76N substitution favours the formation of a malleable and expanded partially unfolded state that accounts for the establishment of intermolecular interactions. Our findings are in agreement with previous observations that linked the lower stability of D76N native fold to an increased tendency to form partially folded, typically amyloidogenic, states (119). In particular, the presence of an expanded partially unfolded ensemble in D76N further corroborates the hypothesis that exposure of hydrophobic domains is pivotal step in the fibrillation process (119).

Furthermore, the importance of primary sequence in dictating protein aggregation can also be inferred by the observation that some mutations reduce the tendency of protein to aggregate (121). In particular, we observed that the non-amyloidogenic W60G hβ2m possesses a higher stability towards environmental stresses, *e.g.*, low pH, than wt hβ2m (see paragraph 3.3.3). This results in a different behaviour of the two proteins: indeed, while wt hβ2m in lysosomal condition is mostly unfolded and aggregates abundantly, W60G hβ2m remains soluble and present a higher percentage of folded fraction.

Then, we observed that another important factor that tunes the ability of proteins to achieve aggregation-prone states is the presence of PTMs. Indeed, it is well know that PTMs are crucial regulators of protein activity, stability, and interactions (152). Our investigations

highlighted how glycosylation prevents NS misfolding and subsequent polymerization (see paragraph 4.3.1). Indeed, we found that the presence of two glycan chains drastically reduces protein propensity to polymerize without altering its physiological activity and conformation. However, the presence of PTMs is not necessarily always protective against misfolding: indeed, it is well documented that hyperphosphorylation of tau protein results in self-assembly and formation of amyloid fibrils in a series of pathologies (153) and that phosphorylation of Ser129 in α-synuclein promotes fibril formation and its deposition in Lewy bodies (154).

Lastly, we found that a major role is played by the protein chemical environmental. Within the crowded environment of the cell, proteins retains their functional states through a series of complex networks (5). However, environmental stresses, like extreme temperatures, change in pH or oxidative stress, can lead to misfolding and aggregation (155). In particular, we observed that chemical environment can finely tune the aggregation propensity of proteins. For example, experimental conditions that favour the achievement of an expanded denatured state, *e.g.*, low pH and low ionic strength, facilitate aggregation in D76N hβ2m (see paragraph 3.3.1). Equally, the drop in pH that wt hβ2m experiences upon internalization in MM cells lysosomes causes its misfolding and aggregation (see paragraph 3.3.3).

In summary, our findings added valuable data to the complex framework of misfolding and aggregation processes, providing new tools for their complete understanding. Indeed, all this information can be particularly useful for the development of therapeutics. For example, the identification of aggregation-prone regions within the primary sequence can be used to design small molecules or antibodies that prevent misfolding and aggregation. Indeed, this approach was successfully exploited for α1AT (mAb$_{4B12}$ monoclonal antibody (156)) and for structured-based peptides inhibiting Aβ aggregation (157). We applied the same approach on NS, using EMB as starting point for the development of novel inhibiting molecules (see paragraph 4.3.2). Our results indicated that EMB remains the best candidate for development of FENIB treatments (158). However, further investigations are required to identify EMB-modifications that increase its delivery efficiency within ER of neurons, thus improving the anti-NS polymerization activity.

In conclusion, the data here presented help depicting the intricate puzzle of protein misfolding and aggregation. Indeed, the only way to solve it is to gather as many pieces as possible and fit them all together.

6 SIDE PROJECT

Rational mutations of antigen-derived peptides to increase MHC-I stability

Luca Broggini, Cristina Paissoni, Sara Pellegrino, Alberto Barbiroli, Carlo Camilloni*, Adnane Achour*,

and Stefano Ricagno*

Manuscript in preparation.

I contributed to this work by preparing all the reported MHC-I complexes. This includes expression and purification of β2m variants (human and murine) and of heavy chain variants (human and murine).
I performed thermal denaturing experiments by circular dichroism of each complex.
I performed crystallization trials for 1Y3P9V, d3V, and d3P complexes. I collected X-ray data and then processed and analysed them. Finally, I solved the structures of the three complexes and performed the structure refinements to obtain high quality models.

Rational mutations of antigen-derived peptides to increase MHC-I stability

Luca Broggini[1], Cristina Paissoni[1], Sara Pellegrino[2], Alberto Barbiroli[3], Carlo Camilloni[1]*, Adnane Achour[4]*, and Stefano Ricagno[1]*

[1] Department of Biosciences, Università degli Studi di Milano, Milan 20133, Italy;

[2] DISFARM, Department of Pharmaceutical Sciences, University of Milan, Milan 20133, Italy;

[3] DeFENS, Department of Food Environmental and Nutritional sciences, University of Milan, Milan 20133, Italy;

[4] Science for Life Laboratory, Department of Medicine, Karolinska Institute, Stockholm, Sweden.

* Authors to whom correspondence should be addressed

Abstract

The ability of the MHC-I/TCR system to activate the immune system has been largely exploited in vaccines development. Indeed, the identification of MHC-I restricted epitopes for inclusion in peptide-based vaccines is used to design novel modified peptides that can increase the immune response against pathogens. However, stability and immunogenicity of MHC-I remain two great obstacles to the achievement of efficient and robust vaccines.

A powerful procedure to improve the effectiveness of the design is to increase the peptide-MHC binding affinity by substituting residues in key peptide anchor positions with others displaying more appropriate properties. Ideally, the substitution should be conservative not to alter MHC-I/TCR recognition.

Here, we report a structural and biophysical characterization of human and murine MHC-I bearing different NY-ESO-1$_{157-165}$ and gp100$_{25-33}$ peptides, respectively.

Our results revealed how our rationally designed peptides entail an increment in MHC-I stability, without altering its three-dimensional conformation. In addition, the structural analysis shed lights on the atomic details of the peptide/binding groove interactions, increasing our understanding of peptide binding and providing new tools for further developments.

Taken together, our data demonstrate the accuracy of the peptide-mutation strategy and provide new valuable information for further developments of peptide candidates.

Introduction

MHC-I is a heterotrimeric complex that displays on the cell surface peptides derived from exogenous proteins for the recognition by appropriate T cell lymphocytes (TCLs) (1). MHC-I/TCL interaction is a prerequisite for the activation of an immune response against virus infected or malignant cells. In particular, the TCLs recognition is mediated by T cell receptors (TCRs) that specifically interacts with the MHC-I binding groove where the antigenic peptide is accommodated (2).

Over the last years the potentialities of MHC-I/TCR system has been exploited for the development of vaccines (3). Indeed, the identification of MHC-I restricted epitopes for inclusion in peptide-based vaccines is used to design novel modified peptides that can increase the immune response against the expressing cells (4). To date, several peptide-based vaccines are at late stage development for a serious of diseases (including AIDS vaccine, gastric cancer vaccine and allergy vaccine) (3).

The use of peptides-based vaccines presents pros and cons: on the one hand, peptides are easy to produce, do not contain infectious material (unlike attenuated vaccines), can be easily modified to increase stability and immunogenicity and do not present particular safety issues; on the other hand, they are usually poorly immunogenic, especially when compared to other conventional vaccine strategies, and they show a reduced bio-availability upon administration (3).

Despite the recent developments, one of the main concern in the design of peptide-based vaccines regards the stability and the immunogenicity of MHC-I bearing the administrated peptide (5). Indeed, MHC-I must be displayed on the cell surface as long as required for the recognition to occur; at the same time, it needs to elicit a strong T cell response against the displaying cell (6).

A powerful procedure to improve the effectiveness of this strategy is to increase the peptide-MHC binding affinity by substituting residues in key peptide anchor positions with others displaying more appropriate properties (7). Optimally, the mutations should be conservative not to alter the structural features required for TCRs recognition and should lead to an increment in complex stability (8). Indeed, the stability of the MHC-I well correlates with its half-life on the cell membrane and with its ability to induce a robust immune response (5).

Here, we analysed human MHC-I (hMHC-I) bearing different NY-ESO-1$_{157-165}$ (9) modified peptides and, in parallel, we investigated the stability of murine MHC-I (mMHC-I) displaying variants of the gp100$_{25-33}$ antigen (10).

NY-ESO-1$_{157-165}$ is an antigenic peptide displayed by the MHC-I of many cancer cells (such as breast, prostate, ovarian cancer, and melanoma) but that is not present in healthy adult cells. Accordingly, it has been largely used for cancer vaccines development (6,11,12). Unfortunately, this peptide presents at the *C-terminus* a cysteine (Cys) residue that, due to cysteinylation and dimerization, affects vaccines formulation reducing their immunogenic efficacy (13). In addition, other non-optimal interactions between the peptide and the heavy chain have been found, opening the way to the design of modifications that could increase the binding efficacy (6). Thus, to identify NY-ESO-1-derived peptides that increase MHC-I stability we produced and characterized several NY-ESO-1/MHC-I variants (Table 1). In particular, NY-ESO-1$_{157-165}$ peptide was modified on residues 1, 3 and 9, which are the crucial sites for the interaction of the peptide with the heavy chain and for the interaction of MHC-I with TCRs (9) (Table 1). While mutations on N- and C- terminal residues are directly involved in stabilizing the complex, modifications on the third residue affect the conformation, and thus the spatial organization, of the peptide within the binding groove (9).

gp100[25-33] (gp33) is an immunodominant epitope found in mice infected with the lymphocytic choriomeningitis virus (LCMV) (14). Even though the exposition of gp33/MHC-I complex induces a robust TCL response, the virus is able to escape the recognition by introducing mutations on the gp33 sequence (10). In order to restore the recognition and to design novel peptides with increased immunogenicity, a series of peptides have been recently designed and analysed (10). In particular, insertion of a Pro in position 3 (yielding the MHC-I complex hereafter named V3P) modify the spatial organization of the peptide within the binding groove without altering TCR recognition. (10).

One of the strategies adopted to increase the delivery efficiency of peptides upon administration is to insert non-conventional aminoacid that are poorly recognized by proteases (3). Indeed, insertion of D-aminoacid prevents peptide hydrolysis, increasing peptide pharmacokinetics properties.

Thus, in order to study the effects of D-substitution on gp33/MHC-I stability, we performed a biophysical and structural characterization of two gp33/MHC-I variants bearing D-aminoacid (Table 1). In particular, we modified the wild-type gp33 epitope and its variant V3P by inserting a d-Phe in position 6, yielding the two complexes d3V and d3P (Table 2).

Our results revealed how rationally designed peptide mutations entail an increment in MHC-I stability; in addition, the structural characterizations identified the atomic details of the peptide/binding groove interactions, increasing our understanding of peptide binding.

In conclusion, our data confirmed the accuracy of the peptide-mutation strategy and paved the way for further characterizations aimed at the identification of peptide candidates for vaccine development.

Methods

MHC-I Purification. Human HLA-A2 heavy chain, murine H-2D$_b$ heavy chain, wt hβ2m and wt mβ2m proteins were expressed individually as inclusion bodies using the BL21 (DE3) *E.coli* strain, following previous published protocols (10,15).

The ternary MHC-I was obtained through dilution. The peptide (10 μM) and wt β2m (2 μM) were incubated in the refolding buffer (100 mM Tris pH 8, 450 mM L-Arginine, 5 mM L-Glutathione reduced, 0.5 mM L-Glutathione oxidized, 2 mM EDTA, 0.5 mM AEBSF) at 4°C under stirring for 30 minutes. The unfolded heavy chain solubilized in 6 M GdnHCl was then added to a final concentration of 1 μM.

The refolding was completed after 72 hours at 4°C under stirring. The solution was concentrated trough Stirred Ultrafiltration Cell (Millipore) and Amicon Ultra-15 Centrifugal Filters (EMD Millipore) up to approximately 3 mL. The sample was then purified by size exclusion chromatography using a Superdex 200 column (GE Healthcare) equilibrated in 20 mM Tris-HCl pH 8, 150 mM NaCl for hMCH-I or 20 mM Tris-HCl pH 7.4 for mMHC-I.

The eluted protein was analyzed by SDS-PAGE, frozen in liquid nitrogen and stored at -20°C.

Circular Dichroism. Thermal unfolding experiments were performed by circular dichroism (CD) in the far-UV region on a J-810 spectropolarimeter (JASCO Corp., Tokyo, Japan) equipped with a Peltier system for temperature control. Protein concentration was 0.2 mg/mL. For hMHC-I the buffer composition was in 20 mM Tris-HCl, pH 8.0, 150 mM NaCl, while mMHC-I were in 20 mM Tris-HCl pH 7.4.

The temperature ramp measurements were recorded from 20 to 95°C (temperature slope 60°C/hour) in a 0.1 cm path length cuvette and monitored at 218 nm wavelength. Tm was

calculated as the first-derivative minimum of the traces. Far-UV CD Spectra were recorded before and after unfolding ramp (260-190 nm).

1Y3P9V Crystallization. Crystallization experiments were performed at 293 K using sitting drop vapour diffusion method by mixing equal amount of MHC-I/NY-ESO-1$_{157-165}$ 1Y3P9V (6 mg/mL) in 20 mM Tris-HCl pH 8.0, 150 mM NaCl and reservoir solution. Best diffracting crystals were obtained in 1.5 M Ammonium Sulphate, 100 mM Tris-HCl, pH 8. Crystals were cryoprotected with 25 % glycerol and flash-frozen in liquid nitrogen. X-ray diffraction data were collected at the beam line ID-23-1 at ESRF (European Synchrotron Radiation Facility of Grenoble, France).

d3P and d3V Crystallization. Crystallization experiments were performed at 293 K using sitting drop vapour diffusion method by mixing equal amount of (7 mg/mL) in 20 mM Tris-HCl pH 7.4 and reservoir solution. Best diffracting crystals were obtained in 1.7 M Ammonium Sulphate, 100 mM Tris-HCl, pH 8.3. Crystals were cryoprotected with 20 % glycerol and flash-frozen in liquid nitrogen. X-ray diffraction data were collected at the beam line XRD-2 at Elettra (Trieste, Italy).

1Y3P9V Structure Determination. The crystal diffracted up to 2.54 Å and belongs to the space group P 21 3. The data collection statistics are shown in Table X.
The diffraction data were processed using XDS and the intensities were merged with AIMLESS. The structure was solved by molecular replacement using MolRep. WT NY-ESO-1 MHC-I (PDB code: 1S9W) (9) was used as searching model. One molecule was found in the asymmetric unit. The model molecule was firstly subjected to a rigid-body refinement and then to a restrained refinement using Refmac5 (16). Manual model building was then carried out using the COOT; figures were prepared with Chimera and PyMol software.

d3P Structure Determination. Crystal diffracted up to 2.43 Å and belongs to the space group C 2 1. The data collection statistics are shown in Table X.
The diffraction data were processed using Staraniso (17) and the intensities were merged with AIMLESS. The structure was solved by molecular replacement using PhaserMR (18) and PDB 5TIL (10) as searching model. Two subunits of the complex were found in the asymmetric unit. The model molecules were subjected firstly to a rigid-body refinement and then to a restrained refinement using phenix.phaser (19). Manual model building was then carried out using the COOT; figures were prepared with Chimera and PyMol softwares.

d3V Structure Determination. Crystal diffracted up to 2.45 Å and belongs to the space group C 2 1. The data collection statistics are shown in Table X.
The diffraction data were processed using Staraniso (17) and the intensities were merged with AIMLESS. The structure was solved by molecular replacement using PhaserMR (18) and PDB 5TJE (10) as searching model. Two subunits of the complex were found in the asymmetric unit. The model molecules were subjected firstly to a rigid-body refinement and then to a restrained refinement using phenix.phaser (19). Manual model building was then carried out using the COOT; figures were prepared with Chimera and PyMol software.

Results

Thermodynamic Stability measured by Circular Dichroism. In order to evaluate the effects of peptide mutations on the thermal stability of MHC-I, thermal unfolding ramps were recorded in the far-UV region (Fig. 1 and Fig.2). Notably, some complexes present a two-state transition (wt, 1H9V, 1F, 1N, 3P, 9V), while the remaining show a classical cooperative unfolding behaviour (Fig. 1 and Fig. 2). Most of the mutations largely increased the melting temperature of the complex (Table 2-3 and fig. 2 -3).

1Y3P9V crystal structure. In order to better understand the molecular interactions occurring in the peptide binding groove, the crystal structure of 1Y3P9V complex was determined to 2.41 Å resolution, providing an electron density of excellent quality (Table 4).
Comparison of the crystal structures of 1Y3P9V and NY-ESO-1 wt (20) revealed a high structural conservation between the two complexes (RMSD 0.28 Å, as calculated over the whole Cα backbone). Indeed, the modifications do not alter the spatial organization of the complex (Fig. 3). As expected, the peptide is located within the binding groove of the heavy chain and its position is perfectly superimposable to that of the NY-ESO-1 wt. In addition, the orientation of peptide side chains is identical in the two variants, apart from peptide residue Trp5 (Fig. 3). The different orientation of pW5 entails a structural rearrangement of Gln155 of the heavy chain (Fig. 3). Indeed, to accommodate the bulky aromatic ring of pW5, the Gln155 rotates and points toward the solvent.
Finally, the bulky Tyr in position 1 points directly towards the solvent. This orientation is predicted to be beneficial for TCRs binding: indeed, the hydroxyl group of the Tyr establishes Van der Waals and H-bond interactions with a Ser in the TCR binding region (20).

d3V crystal structures. The crystal structure of d3V was determined to 2.43 Å resolution (Table 4), providing an electron density of excellent quality (Fig. 4).
Comparison between the d3V and gp33 wt complex revealed minor changes in the three-dimensional architecture of the complex, in particular in the β2m region (RMSD of 0.785 Å, as calculated over the whole Cα backbone) (Fig. 4). The peptide conformation within the binding groove is conserved (Fig. 4) even though the orientation of pY4 and pF6 are different in the two complexes. Indeed, the introduction of a D-aminoacid entails the rotation of the two bulky residues. These rotations slightly modify the position of residues in the binding groove: in particular, residues R62 and E163 are the most affected. These residues are also involved in the recognition by TCRs: indeed, it is likely that their different orientations have repercussions on the binding affinity of d3V towards TCRs.

d3P crystal structures . The crystal structure of d3P was determined to 2.45 Å (Table 4) and the electron density was of excellent quality (Fig. 5).
Superimposition of d3P and gp33 V3P complexes revealed a conserved tertiary structure, despite minor changes in the β2m region (RMSD of 1.88 Å, as calculated over the whole Cα backbone). d3P peptide is loaded within the heavy chain binding groove and its conformation is identical to the gp33 V3P peptide (Fig. 5). The main differences lie in residues pY4 and pF6 which assume a different orientation in the two complexes (Fig. 5). In particular, their positions in d3P complex modify the spatial organization of residues R62 and H155 of the heavy chain (Fig. 5). Among them, the H155 is bended and orientation may alter the

recognition by TCRs: indeed, H155 is directly involved in the interaction with the TCRs binding region (10).

Discussion

While developing new and more efficient peptides for vaccination, it is pivotal to rationally design modifications that increase the MHC-I stability. Indeed, the stability of the complex is directly correlated to an increased half-life on the cell membranes which in turn increases the likelihood of TCRs recognition and TCLs activation (5).

Here, we rationally modified NY-ESO-1$_{157-165}$ and gp33 antigens and characterized the newly formed MHC-I complexes.

Most of the analysed peptides increased the thermal stability of the MHC-I (Fig. 1). However, it is worth noticing that in MHC-I/NY-ESO-1 the thermal ramps do not always follow a classic one-state unfolding profile. Indeed, in some cases a two-state transition is observed (Fig. 1). This outcome is likely to be attributed to an instability of the MHC-I: indeed, the first transition refers to the dissociation of the non-covalent complex between the heavy chain and β2m and the subsequent unfolding of the heavy chain. The second transition, instead, could represent either the aggregation of the heavy chain or the unfolding of β2m.

In any case, the first transition reflects the stability of the MHC-I and has been considered to derive melting temperature values.

However, despite being a useful tool to evaluate the effects of the peptide modifications, thermal stability experiments are not *per se* informative in predicting whether the mutated peptide will retain its antigenic properties (6).

Thus, we performed a structural characterization by X-crystallography to shed light into the interactions on the peptide binding groove. The understanding of the atomic details of peptide-heavy chain interactions are pivotal to determine the molecular determinants of the interaction and to guide future peptide optimizations.

The structural analyses were done for 1Y3P9V, d3V, and d3P complexes. In all the three cases, the peptide conformation within the α1 domain of the heavy chain was conserved. This confirmed the accuracy of the modification strategy as the mutations should not induce large rearrangement not to alter recognition by TCRs.

Then, the crystal structures revealed adjustments of several heavy chain residues side chain. Indeed, the presence, or the different orientation, of bulky aminoacids in the peptide sequence entail local bending or turns of heavy chain residues (e.g. His155 in d3P or Q155 in 1Y3P9V). Since that these heavy chain residues are involved in binding to the TCR, it is tempting to speculate that their different orientation may also affect TCR recognition.

Interestingly, the presence of d-Phe in d3V and d3P complex do not modify either the affinity toward the heavy chain or the stability. Indeed, introduction of non-conventional aminoacids should be considered to increase the delivery efficacy, especially when dealing with easily hydrolysable peptides.

In conclusion, this work provided useful information on accuracy of the design strategies for NY-ESO-1- and gp33-derived peptides.

Further characterizations, e.g. MHC-I/TCR affinity and MHC-I/TCR structural analysis, are needed to allow the selection of the best candidates for peptide-vaccine development.

References

1.   Wieczorek M, Abualrous ET, Sticht J, Álvaro-Benito M, Stolzenberg S, Noé F, et al. Major Histocompatibility Complex (MHC) Class I and MHC Class II Proteins: Conformational Plasticity in Antigen Presentation. Front Immunol [Internet]. 2017 Mar 17;8:292. Available from: https://pubmed.ncbi.nlm.nih.gov/28367149

2.   Liu QJ, Gao B. Manipulation of MHC-I/TCR interaction for immune therapy. Cell Mol Immunol [Internet]. 2008 Jun;5(3):171–82. Available from: https://pubmed.ncbi.nlm.nih.gov/18582398

3.   Purcell AW, McCluskey J, Rossjohn J. More than one reason to rethink the use of peptides in vaccine design. Nat Rev Drug Discov [Internet]. 2007;6(5):404–14. Available from: https://doi.org/10.1038/nrd2224

4.   Comber JD, Philip R. MHC class I antigen presentation and implications for developing a new generation of therapeutic vaccines. Ther Adv vaccines [Internet]. 2014 May;2(3):77–89. Available from: https://pubmed.ncbi.nlm.nih.gov/24790732

5.   Morón G, Dadaglio G, Leclerc C. New tools for antigen delivery to the MHC class I pathway. Trends Immunol. 2004 Feb;25(2):92–7.

6.   Chen J, Stewart-Jones G, Bossi G, Lissin NM, Wooldridge L, Choi EML, et al. Structural and kinetic basis for heightened immunogenicity of T cell vaccines. J Exp Med [Internet]. 2005;201(8):1243–55. Available from: http://www.pubmedcentral.nih.gov/articlerender.fcgi?artid=2213140&tool=pmcentrez&rendertype=abstract

7.   Borbulevych OY, Baxter TK, Yu Z, Restifo NP, Baker BM. Increased immunogenicity of an anchor-modified tumor-associated antigen is due to the enhanced stability of the peptide/MHC complex: implications for vaccine design. J Immunol [Internet]. 2005 Apr 15;174(8):4812–20. Available from: https://pubmed.ncbi.nlm.nih.gov/15814707

8.   Denkberg G, Klechevsky E, Reiter Y. Modification of a tumor-derived peptide at an HLA-A2 anchor residue can alter the conformation of the MHC-peptide complex: probing with TCR-like recombinant antibodies. J Immunol. 2002 Oct;169(8):4399–407.

9.   Webb AI, Dunstone MA, Chen W, Aguilar MI, Chen Q, Jackson H, et al. Functional and structural characteristics of NY-ESO-1-related HLA A2-restricted epitopes and the design of a novel immunogenic analogue. J Biol Chem. 2004;279(22):23438–46.

10.   Duru AD, Sun R, Allerbring EB, Chadderton J, Kadri N, Han X, et al. Tuning antiviral CD8 T-cell response via proline-altered peptide ligand vaccination. PLOS Pathog [Internet]. 2020 May 4;16(5):e1008244. Available from: https://doi.org/10.1371/journal.ppat.1008244

11.   Jäger E, Gnjatic S, Nagata Y, Stockert E, Jäger D, Karbach J, et al. Induction of primary NY-ESO-1 immunity: CD8+ T lymphocyte and antibody responses in peptide-vaccinated patients with NY-ESO-1+ cancers. Proc Natl Acad Sci U S A. 2000 Oct;97(22):12198–203.

12.   Jäger E, Chen YT, Drijfhout JW, Karbach J, Ringhoffer M, Jäger D, et al. Simultaneous humoral and cellular immune response against cancer-testis antigen NY-ESO-1: definition of human histocompatibility leukocyte antigen (HLA)-A2-binding peptide epitopes. J Exp Med. 1998 Jan;187(2):265–70.

13.   Chen W, Yewdell JW, Levine RL, Bennink JR. Modification of cysteine residues in vitro and in vivo affects the immunogenicity and antigenicity of major histocompatibility complex class I-restricted viral determinants. J Exp Med. 1999 Jun;189(11):1757–64.

14.   Moskophidis D, Zinkernagel RM. Immunobiology of cytotoxic T-cell escape mutants of lymphocytic choriomeningitis virus. J Virol. 1995 Apr;69(4):2187–93.

15. Halabelian L, Ricagno S, Giorgetti S, Santambrogio C, Barbiroli A, Pellegrino S, et al. Class I major histocompatibility complex, the Trojan Horse for secretion of Amyloidogenic β2-Microglobulin. J Biol Chem. 2014;289(6):3318–27.

16. Murshudov GN, Skubák P, Lebedev AA, Pannu NS, Steiner RA, Nicholls RA, et al. REFMAC5 for the refinement of macromolecular crystal structures. Acta Crystallogr D Biol Crystallogr [Internet]. 2011/03/18. 2011 Apr;67(Pt 4):355–67. Available from: https://pubmed.ncbi.nlm.nih.gov/21460454

17. Vonrhein C, Tickle IJ, Flensburg C, Keller P, Paciorek W, Sharff A, et al. Advances in automated data analysis and processing within {\it autoPROC}, combined with improved characterisation, mitigation and visualisation of the anisotropy of diffraction limits using {\it STARANISO}. Acta Crystallogr Sect A [Internet]. 2018 Jul;74(a1):a360. Available from: https://doi.org/10.1107/S010876731809640X

18. McCoy AJ, Grosse-Kunstleve RW, Adams PD, Winn MD, Storoni LC, Read RJ. Phaser crystallographic software. J Appl Crystallogr. 2007 Aug;40(Pt 4):658–74.

19. Afonine P V, Grosse-Kunstleve RW, Echols N, Headd JJ, Moriarty NW, Mustyakimov M, et al. Towards automated crystallographic structure refinement with {\it phenix.refine}. Acta Crystallogr Sect D [Internet]. 2012 Apr;68(4):352–67. Available from: https://doi.org/10.1107/S0907444912001308

20. Webb AI, Dunstone MA, Chen W, Aguilar M-I, Chen Q, Jackson H, et al. Functional and Structural Characteristics of NY-ESO-1-related HLA A2-restricted Epitopes and the Design of a Novel Immunogenic Analogue. J Biol Chem [Internet]. 2004 May 28;279(22):23438–46. Available from: http://www.jbc.org/content/279/22/23438.abstract

Figures and tables legends

Figure 1. NY-ESO-1 MHC-I thermodynamic stability. Thermal denaturation unfolding curves of hMHC-I bearing NY-ESO-1-derived peptides monitored in the Far-UV region by circular dichroism.

Figure 2. mMHC-I/gp33 unfolding profiles. Thermal denaturation unfolding curves of gp33-derived peptides monitored in the Far-UV region by circular dichroism.

Figure 3. 1Y3P9V crystal structure. A) Comparison between the crystal structures of 1Y3P9V (cyan) and NY-ESO-1 wt (grey, PDB entry: 1S9W). B) 1Y3P9V peptide with its electron density map. C) Comparison between 1Y3P9V (cyan) and NY-ESO-1 wt (grey) peptide orientation within the binding groove. D) Different spatial arrangement of Q155 in 1Y3P9V (cyan) and NY-ESO-1 wt (grey).

Figure 4. d3V crystal structure. A) Comparison between the crystal structures of d3V (green) and gp33 wt (yellow, PDB entry: 1S7U). B) d3V peptide with its electron density map. C) Comparison between d3V (green) and gp33 wt (yellow) peptide orientation within the binding groove. D) Different spatial arrangement of R62 and E163 in d3V (green) and gp33 wt (yellow).

Figure 5. d3P crystal structure. A) Comparison between the crystal structures of d3P (orange) and gp33 V3P (grey, PDB entry: 4NSK). B) d3P peptide with its electron density map. C) Comparison between d3P (orange) and gp33 V3P (yellow) peptide orientation within the binding groove. D) Different spatial arrangement of R62 and H155 in d3P (green) and gp33 V3P (yellow).

Table 1. **NY-ESO-1 $_{157-165}$ peptide modifications.** Modifications are highlighted in red.

Table 2. **gp33 peptide modifications.** Modifications are highlighted in red.

Table 3. Calculated melting temperature for MHC-I complexes bearing NY-ESO-1-derived peptides and gp33-derived peptides.

Table 4. Data collection and refinement statistics for 1Y3P9V, d3P and d3V. Values in parenthesis are for the highest resolution shell.

Figures and Tables

Figure 1. hMHC-I/NY-ESO-1 unfolding profiles.
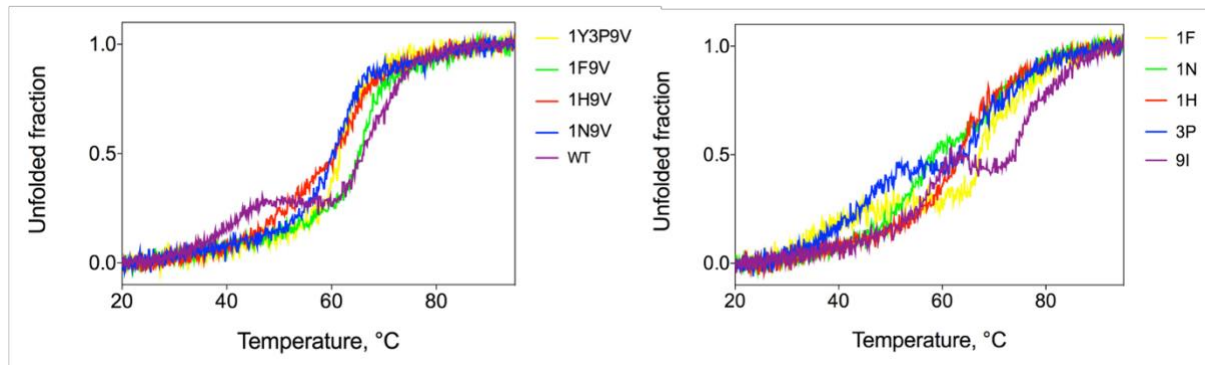
Figure 2. mMHC-I/gp33 unfolding profiles.
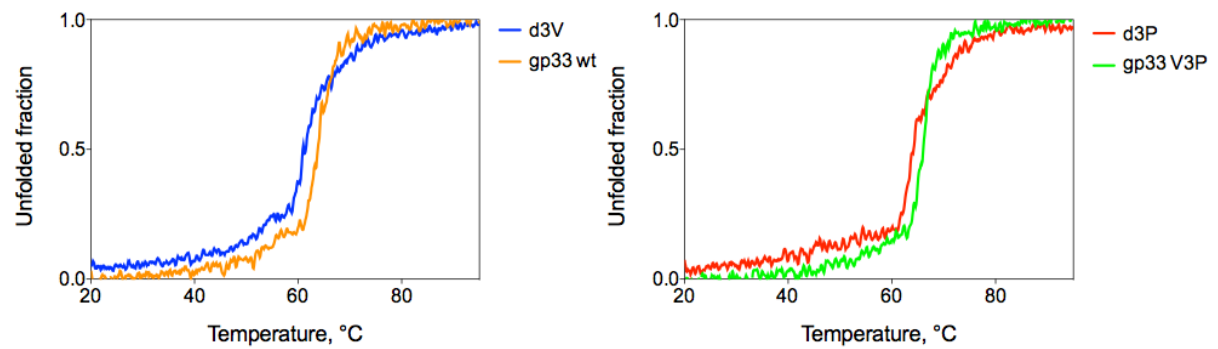
Figure 3. 1Y3P9V crystal structure.
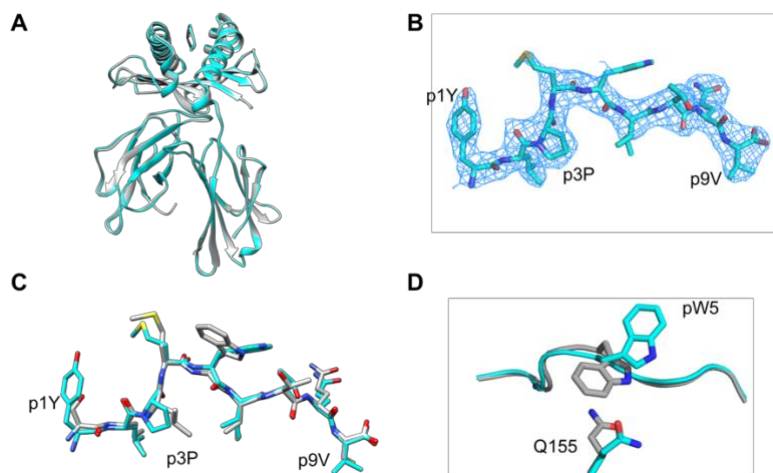
Figure 4. d3V crystal structure.
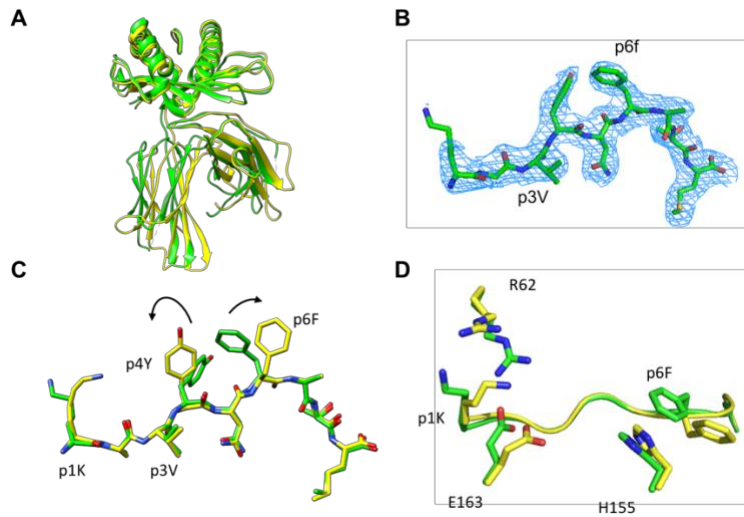
Figure 5. d3P crystal structure.
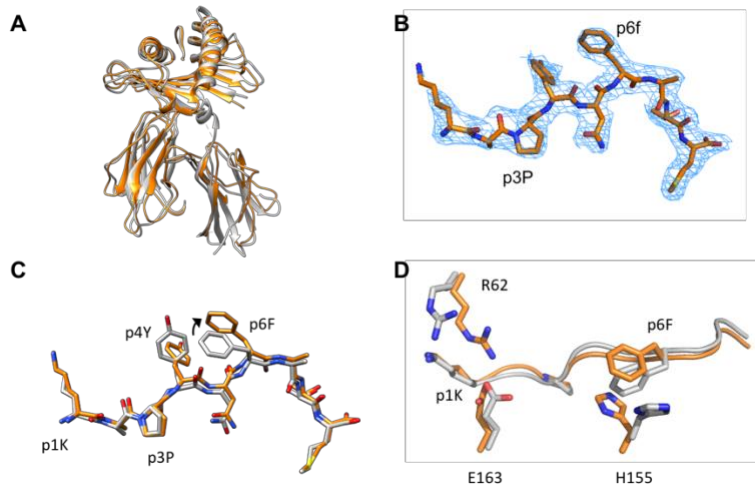
Table 1. NY-ESO-1 $_{157-165}$ peptide modifications.

Complex name	Type of complex	Peptide on MHC-I
NY-ESO-1 wt	hMHC-I/NY-ESO-1	SLLMWITQC
1Y3P9V	hMHC-I/NY-ESO-1	YLPMWITQV
1F9V	hMHC-I/NY-ESO-1	FLLMWITQV
1H9V	hMHC-I/NY-ESO-1	HLLMWITQV
1N9V	hMHC-I/NY-ESO-1	NLLMWITQV
9I	hMHC-I/NY-ESO-1	SLLMWITQI
3P	hMHC-I/NY-ESO-1	SLPMWITQC
1N	hMHC-I/NY-ESO-1	NLLMWITQC
1H	hMHC-I/NY-ESO-1	HLLMWITQC
1F	hMHC-I/NY-ESO-1	FLLMWITQC

Table 2. gp33 peptide modifications.

Complex name	Type of complex	Peptide on MHC-I
gp33 wt	mMHC-I/gp33	KAVYNFATM r
gp33 V3P	mMHC-I/gp33	KAPYNFATM
d3V	mMHC-I/gp33	KAVYNfATM *
d3P	mMHC-I/gp33	KAPYNfATM *

* f stands for D-Phe

Table 3. Calculated melting temperature for MHC-I complexes bearing NY-ESO-1-derived peptides and gp33-derived peptides.

Complex	T_m / °C
NY-ESO-1 wt	39.1
1Y3P9V	61.4
9I	55.2
3P	42.7
1F9V	65.4
1H9V	50.2
1N9V	60.5
1N	52.7
1H	63.5
1F	35.7
gp33 wt	63.5
gp33 V3P	66.0
gp33 d3V	61.5
gp33 d3P	64.0

Table 4. Data collection and refinement statistics for 1Y3P9V, d3P and d3V.

Structure	1Y3P9V	d3P	d3V
Beam Line	ID-23-1 (ESRF)	XRD-2 (Elettra)	XRD-2 (Elettra)
Space group	P 2_1 3	C 2	C 2
Unit cell dimensions			
a (Å)	118.7	120.6	120.5
a (Å)	118.7	125.9	124.6
a (Å)	118.7	92.9	92.9
b (°)	90	126.6	126.8
Resolution (Å)	83.94 - 2.41 (2.54 - 2.41)	76.76 - 2.43 (2.68 - 2.43)	76.24 - 2.45 (2.72 - 2.45)
R_{merge} (%)[a]	9.4 (87.8)	6.0 (102.3)	7.2 (126.4)
I/sI	15.0 (2.9)	22.1 (2.0)	13.9 (1.5)
Completeness (%)	100.0 (100.0)	sperichal: 98.9 (16.7)	sperichal: 64.4 (11.9)
		elipsoidal: 98.9 (60.8)	elipsoidal: 92.4 (59.9)
Multiplicity	14.2 (14.3)	5.6 (7.0)	6.6 (6.6)
Unique reflections	20710	30284	25964
Refinement			
R_{work} (%)[b]	20.21	21.4	21.4
R_{free} (%)	25.86	25.8	26.9
Number of atoms	6366	6158	6323
Protein	6288	6158	6323
Waters	56	65	64
Heteroatoms	22	37	39
Ramachandran plot, *n* (%)			
Most favoured region	368 (98.40)	678 (95.4%)	699 (96.15%)
Allowed region	5 (1.34)	30 (4.2%)	26 (3.58%)
Outliers	1 (0.27)	3 (0.4%)	2 (0.28%)

[a] $R_{merge} = \Sigma_{hkl} \Sigma_j |I_{hkl,j} - \langle I_{hkl} \rangle| / \Sigma_{hkl}\Sigma_j I_{hkl,j}$ where I is the observed intensity and $\langle I \rangle$ is the average intensity.

[b] $R_{work} = \Sigma_{hkl}|F_O - F_C| / \Sigma_{hkl}|F_O|$ for all data except 5–10%, which were used for the R_{free} calculation.

7 BIBLIOGRAPHY

1. Anfinsen CB. Principles that govern the folding of protein chains. Science (80-) [Internet]. 1973 Jul 20;181(4096):223 LP – 230. Available from: http://science.sciencemag.org/content/181/4096/223.abstract

2. Mayor U, Guydosh NR, Johnson CM, Grossmann JG, Sato S, Jas GS, et al. The complete folding pathway of a protein from nanoseconds to microseconds. Nature. 2003 Feb;421(6925):863–7.

3. Schaeffer RD, Daggett V. Protein folds and protein folding. Protein Eng Des Sel [Internet]. 2010/11/03. 2011 Jan;24(1–2):11–9. Available from: https://pubmed.ncbi.nlm.nih.gov/21051320

4. Onuchic JN, Wolynes PG. Theory of protein folding. Curr Opin Struct Biol. 2004;14(1):70–5.

5. Chiti F, Dobson CM. Protein Misfolding, Amyloid Formation, and Human Disease: A Summary of Progress Over the Last Decade. Annu Rev Biochem. 2017 Jun;86:27–68.

6. Soto C. Unfolding the role of protein misfolding in neurodegenerative diseases. Nat Rev Neurosci [Internet]. 2003;4(1):49–60. Available from: https://doi.org/10.1038/nrn1007

7. Zhou H-X. Influence of crowded cellular environments on protein folding, binding, and oligomerization: biological consequences and potentials of atomistic modeling. FEBS Lett [Internet]. 2013/02/05. 2013 Apr 17;587(8):1053–61. Available from: https://pubmed.ncbi.nlm.nih.gov/23395796

8. Díaz-Villanueva JF, Díaz-Molina R, García-González V. Protein Folding and Mechanisms of Proteostasis. Int J Mol Sci [Internet]. 2015 Jul 28;16(8):17193–230. Available from: https://pubmed.ncbi.nlm.nih.gov/26225966

9. Knowles TPJ, Vendruscolo M, Dobson CM. The amyloid state and its association with protein misfolding diseases. Nat Rev Mol Cell Biol [Internet]. 2014;15(6):384–96. Available from: https://doi.org/10.1038/nrm3810

10. Dobson CM. Protein folding and misfolding. Nature. 2003 Dec;426(6968):884–90.

11. Hartl FU, Bracher A, Hayer-Hartl M. Molecular chaperones in protein folding and proteostasis. Nature [Internet]. 2011;475(7356):324–32. Available from: https://doi.org/10.1038/nature10317

12. Hartl FU, Hayer-Hartl M. Molecular chaperones in the cytosol: from nascent chain to folded protein. Science. 2002 Mar;295(5561):1852–8.

13. Wang L, Wang X, Wang C. Protein disulfide-isomerase, a folding catalyst and a redox-regulated chaperone. Free Radic Biol Med. 2015 Jun;83:305–13.

14. Ali Khan H, Mutus B. Protein disulfide isomerase a multifunctional protein with multiple physiological roles. Front Chem [Internet]. 2014 Aug 26;2:70. Available from: https://pubmed.ncbi.nlm.nih.gov/25207270

15. Ross CA, Poirier MA. Protein aggregation and neurodegenerative disease. Nat Med. 2004 Jul;10 Suppl:S10-7.

16. Varshavsky A. The ubiquitin system, an immense realm. Annu Rev Biochem. 2012;81:167–76.

17. Stolz A, Wolf DH. Endoplasmic reticulum associated protein degradation: a chaperone assisted journey to hell. Biochim Biophys Acta. 2010 Jun;1803(6):694–705.

18. Nakatogawa H, Suzuki K, Kamada Y, Ohsumi Y. Dynamics and diversity in autophagy mechanisms: lessons from yeast. Nat Rev Mol Cell Biol. 2009 Jul;10(7):458–67.

19. Kroemer G, Mariño G, Levine B. Autophagy and the integrated stress response. Mol

Cell. 2010 Oct;40(2):280–93.

20. Ghosh DK, Ranjan A. The metastable states of proteins. Protein Sci. 2020 Mar;

21. Gamblin SJ, Skehel JJ. Influenza hemagglutinin and neuraminidase membrane glycoproteins. J Biol Chem [Internet]. 2010/06/10. 2010 Sep 10;285(37):28403–9. Available from: https://pubmed.ncbi.nlm.nih.gov/20538598

22. Law RHP, Zhang Q, McGowan S, Buckle AM, Silverman GA, Wong W, et al. An overview of the serpin superfamily. Genome Biol [Internet]. 2006/05/30. 2006;7(5):216. Available from: https://pubmed.ncbi.nlm.nih.gov/16737556

23. Baldwin AJ, Knowles TPJ, Tartaglia GG, Fitzpatrick AW, Devlin GL, Shammas SL, et al. Metastability of Native Proteins and the Phenomenon of Amyloid Formation. J Am Chem Soc [Internet]. 2011 Sep 14;133(36):14160–3. Available from: https://doi.org/10.1021/ja2017703

24. Surguchev A, Surguchov A. Conformational diseases: Looking into the eyes. Brain Res Bull [Internet]. 2010;81(1):12–24. Available from: http://www.sciencedirect.com/science/article/pii/S036192300900313X

25. Winklhofer KF, Tatzelt J, Haass C. The two faces of protein misfolding: gain- and loss-of-function in neurodegenerative diseases. EMBO J [Internet]. 2008 Jan 23;27(2):336–49. Available from: https://pubmed.ncbi.nlm.nih.gov/18216876

26. Girnius S. Overview of systemic and localized amyloidosis. Rev Heal Care. 2013;4(4):231–47.

27. Murphy MP, LeVine H. Alzheimer's disease and the amyloid-beta peptide. J Alzheimers Dis [Internet]. 2010;19(1):311–23. Available from: https://pubmed.ncbi.nlm.nih.gov/20061647

28. Milani P, Merlini G, Palladini G. Light Chain Amyloidosis. Mediterr J Hematol Infect Dis [Internet]. 2018 Mar 1;10(1):e2018022–e2018022. Available from: https://pubmed.ncbi.nlm.nih.gov/29531659

29. Davies MJ, Lomas DA. The molecular aetiology of the serpinopathies. Int J Biochem Cell Biol. 2008;40(6–7):1273–86.

30. Gooptu B, Lomas DA. Conformational pathology of the serpins: themes, variations, and therapeutic strategies. Annu Rev Biochem. 2009;78:147–76.

31. Carrell RW, Lomas DA. Conformational disease. Lancet [Internet]. 1997;350(9071):134–8. Available from: http://www.sciencedirect.com/science/article/pii/S0140673697020734

32. Chiti F, Dobson CM. Amyloid formation by globular proteins under native conditions. Nat Chem Biol. 2009 Jan;5(1):15–22.

33. Höppener JWM, Ahrén B, Lips CJM. Islet Amyloid and Type 2 Diabetes Mellitus. N Engl J Med [Internet]. 2000 Aug 10;343(6):411–9. Available from: https://doi.org/10.1056/NEJM200008103430607

34. Valleix S, Gillmore JD, Bridoux F, Mangione PP, Dogan A, Nedelec B, et al. Hereditary Systemic Amyloidosis Due to Asp76Asn Variant β2-Microglobulin. N Engl J Med [Internet]. 2012 Jun 13;366(24):2276–83. Available from: http://dx.doi.org/10.1056/NEJMoa1201356

35. Kovacs GG. Concepts and classification of neurodegenerative diseases [Internet]. 1st ed. Vol. 145, Handbook of Clinical Neurology. Elsevier B.V.; 2018. 301–307 p. Available from: http://dx.doi.org/10.1016/B978-0-12-802395-2.00021-3

36. Ruberg FL, Berk JL. Transthyretin (TTR) cardiac amyloidosis. Circulation [Internet]. 2012 Sep 4;126(10):1286–300. Available from: https://pubmed.ncbi.nlm.nih.gov/22949539

37. Wechalekar AD, Gillmore JD, Hawkins PN. Systemic amyloidosis. Lancet [Internet]. 2016 Jun 25;387(10038):2641–54. Available from: https://doi.org/10.1016/S0140-6736(15)01274-X

38. Nelson R, Sawaya MR, Balbirnie M, Madsen AØ, Riekel C, Grothe R, et al. Structure of the cross-beta spine of amyloid-like fibrils. Nature [Internet]. 2005 Jun 9;435(7043):773–8. Available from: https://pubmed.ncbi.nlm.nih.gov/15944695

39. Swuec P, Lavatelli F, Tasaki M, Paissoni C, Rognoni P, Maritan M, et al. Cryo-EM structure of cardiac amyloid fibrils from an immunoglobulin light chain AL amyloidosis patient. Nat Commun [Internet]. 2019;10(1):1269. Available from: https://doi.org/10.1038/s41467-019-09133-w

40. Knowles TP, Fitzpatrick AW, Meehan S, Mott HR, Vendruscolo M, Dobson CM, et al. Role of intermolecular forces in defining material properties of protein nanofibrils. Science. 2007 Dec;318(5858):1900–3.

41. Sunde M, Blake C. The structure of amyloid fibrils by electron microscopy and X-ray diffraction. Adv Protein Chem. 1997;50:123–59.

42. Khurana R, Coleman C, Ionescu-Zanetti C, Carter SA, Krishna V, Grover RK, et al. Mechanism of thioflavin T binding to amyloid fibrils. J Struct Biol. 2005 Sep;151(3):229–38.

43. Qiang W, Yau W-M, Lu J-X, Collinge J, Tycko R. Structural variation in amyloid-β fibrils from Alzheimer's disease clinical subtypes. Nature. 2017 Jan;541(7636):217–21.

44. Petkova AT, Leapman RD, Guo Z, Yau W-M, Mattson MP, Tycko R. Self-propagating, molecular-level polymorphism in Alzheimer's beta-amyloid fibrils. Science. 2005 Jan;307(5707):262–5.

45. Dobson CM, Knowles TPJ, Vendruscolo M. The Amyloid Phenomenon and Its Significance in Biology and Medicine. Cold Spring Harb Perspect Biol. 2020 Feb;12(2).

46. Jackson MP, Hewitt EW. Why are Functional Amyloids Non-Toxic in Humans? Biomolecules [Internet]. 2017 Sep 22;7(4):71. Available from: https://pubmed.ncbi.nlm.nih.gov/28937655

47. Chiti F, Webster P, Taddei N, Clark A, Stefani M, Ramponi G, et al. Designing conditions for in vitro formation of amyloid protofilaments and fibrils. Proc Natl Acad Sci U S A. 1999 Mar;96(7):3590–4.

48. Kollmer M, Close W, Funk L, Rasmussen J, Bsoul A, Schierhorn A, et al. Cryo-EM structure and polymorphism of Aβ amyloid fibrils purified from Alzheimer's brain tissue. Nat Commun [Internet]. 2019;10(1):4760. Available from: https://doi.org/10.1038/s41467-019-12683-8

49. Tycko R. Solid-state NMR studies of amyloid fibril structure. Annu Rev Phys Chem [Internet]. 2011;62:279–99. Available from: https://pubmed.ncbi.nlm.nih.gov/21219138

50. Morris AM, Watzky MA, Finke RG. Protein aggregation kinetics, mechanism, and curve-fitting: a review of the literature. Biochim Biophys Acta. 2009 Mar;1794(3):375–97.

51. Ruggeri FS, Šneideris T, Vendruscolo M, Knowles TPJ. Atomic force microscopy for single molecule characterisation of protein aggregation. Arch Biochem Biophys [Internet]. 2019/02/08. 2019 Mar 30;664:134–48. Available from: https://pubmed.ncbi.nlm.nih.gov/30742801

52. Arosio P, Knowles TPJ, Linse S. On the lag phase in amyloid fibril formation. Phys Chem Chem Phys. 2015 Mar;17(12):7606–18.

53. Scarpioni R, Ricardi M, Albertazzi V, De Amicis S, Rastelli F, Zerbini L. Dialysis-related

amyloidosis: challenges and solutions. Int J Nephrol Renovasc Dis [Internet]. 2016 Dec 7;9:319–28. Available from: https://pubmed.ncbi.nlm.nih.gov/27994478

54. Merlini G, Bellotti V. Molecular Mechanisms of Amyloidosis. N Engl J Med [Internet]. 2003;349(6):583–96. Available from: http://www.nejm.org/doi/abs/10.1056/NEJMra023144

55. Eakin CM, Berman AJ, Miranker AD. A native to amyloidogenic transition regulated by a backbone trigger. Nat Struct Mol Biol. 2006 Mar;13(3):202–8.

56. Törnquist M, Michaels TCT, Sanagavarapu K, Yang X, Meisl G, Cohen SIA, et al. Secondary nucleation in amyloid formation. Chem Commun [Internet]. 2018;54(63):8667–84. Available from: http://dx.doi.org/10.1039/C8CC02204F

57. Vetri V, Canale C, Relini A, Librizzi F, Militello V, Gliozzi A, et al. Amyloid fibrils formation and amorphous aggregation in concanavalin A. Biophys Chem [Internet]. 2007;125(1):184–90. Available from: http://www.sciencedirect.com/science/article/pii/S0301462206002481

58. Fusco G, Chen SW, Williamson PTF, Cascella R, Perni M, Jarvis JA, et al. Structural basis of membrane disruption and cellular toxicity by α-synuclein oligomers. Science. 2017 Dec;358(6369):1440–3.

59. Herling TW, Levin A, Saar KL, Dobson CM, Knowles TPJ. Microfluidic approaches for probing amyloid assembly and behaviour. Lab Chip [Internet]. 2018;18(7):999–1016. Available from: http://dx.doi.org/10.1039/C7LC01241A

60. Guo JL, Lee VMY. Cell-to-cell transmission of pathogenic proteins in neurodegenerative diseases. Nat Med. 2014 Feb;20(2):130–8.

61. Lorenzen N, Nielsen SB, Buell AK, Kaspersen JD, Arosio P, Vad BS, et al. The role of stable α-synuclein oligomers in the molecular events underlying amyloid formation. J Am Chem Soc. 2014 Mar;136(10):3859–68.

62. Merlini G. AL amyloidosis: from molecular mechanisms to targeted therapies. Hematol Am Soc Hematol Educ Progr [Internet]. 2017 Dec 8;2017(1):1–12. Available from: https://pubmed.ncbi.nlm.nih.gov/29222231

63. Labbadia J, Morimoto RI. The biology of proteostasis in aging and disease. Annu Rev Biochem. 2015;84:435–64.

64. Knowles TPJ, Waudby CA, Devlin GL, Cohen SIA, Aguzzi A, Vendruscolo M, et al. An analytical solution to the kinetics of breakable filament assembly. Science. 2009 Dec;326(5959):1533–7.

65. Gath J, Bousset L, Habenstein B, Melki R, Böckmann A, Meier BH. Unlike twins: an NMR comparison of two α-synuclein polymorphs featuring different toxicity. PLoS One. 2014;9(3):e90659.

66. Gettins PGW. Serpin structure, mechanism, and function. Chem Rev. 2002 Dec;102(12):4751–804.

67. Law RHP, Zhang Q, McGowan S, Buckle AM, Silverman G a, Wong W, et al. An overview of the serpin superfamily. Genome Biol. 2006;7(5):216.

68. Elliott PR, Lomas DA, Carrell RW, Abrahams JP. Inhibitory conformation of the reactive loop of alpha 1-antitrypsin. Nat Struct Biol. 1996 Aug;3(8):676–81.

69. Huntington JA. Shape-shifting serpins--advantages of a mobile mechanism. Trends Biochem Sci. 2006 Aug;31(8):427–35.

70. Ye S, Cech AL, Belmares R, Bergstrom RC, Tong Y, Corey DR, et al. The structure of a Michaelis serpin-protease complex. Nat Struct Biol. 2001 Nov;8(11):979–83.

71. Carrell RW, Owen MC. Plakalbumin, alpha 1-antitrypsin, antithrombin and the

mechanism of inflammatory thrombosis. Nature. 1985 Oct;317(6039):730–2.

72. Devlin GL, Bottomley SP. A protein family under "stress" - serpin stability, folding and misfolding. Front Biosci. 2005 Jan;10:288–99.

73. Fjellström O, Deinum J, Sjögren T, Johansson C, Geschwindner S, Nerme V, et al. Characterization of a small molecule inhibitor of plasminogen activator inhibitor type 1 that accelerates the transition into the latent conformation. J Biol Chem. 2013 Jan;288(2):873–85.

74. Mottonen J, Strand A, Symersky J, Sweet RM, Danley DE, Geoghegan KF, et al. Structural basis of latency in plasminogen activator inhibitor-1. Nature. 1992 Jan;355(6357):270–3.

75. Pearce MC, Powers GA, Feil SC, Hansen G, Parker MW, Bottomley SP. Identification and characterization of a misfolded monomeric serpin formed at physiological temperature. J Mol Biol. 2010 Oct;403(3):459–67.

76. Irving JA, Ekeowa UI, Belorgey D, Haq I, Gooptu B, Miranda E, et al. Chapter Eighteen - The Serpinopathies: Studying Serpin Polymerization In Vivo. In: Whisstock JC, Bird PIBT-M in E, editors. Serpin Structure and Evolution [Internet]. Academic Press; 2011. p. 421–66. Available from: http://www.sciencedirect.com/science/article/pii/B9780123859501000183

77. Schulze AJ, Baumann U, Knof S, Jaeger E, Huber R, Laurell CB. Structural transition of alpha 1-antitrypsin by a peptide sequentially similar to beta-strand s4A. Eur J Biochem. 1990 Nov;194(1):51–6.

78. Yamasaki M, Whisstock JC, Pearce MC, Huntington JA, Sendall TJ. Molecular basis of α1-antitrypsin deficiency revealed by the structure of a domain-swapped trimer. EMBO Rep [Internet]. 2011;12(10):1011–7. Available from: http://dx.doi.org/10.1038/embor.2011.171

79. Yamasaki M, Li W, Johnson DJD, Huntington JA. Crystal structure of a stable dimer reveals the molecular basis of serpin polymerization. Nature [Internet]. 2008;455(7217):1255–8. Available from: https://doi.org/10.1038/nature07394

80. Belorgey D, Hägglöf P, Karlsson-Li S, Lomas DA. Protein misfolding and the serpinopathies. Prion [Internet]. 2007/01/06. 2007;1(1):15–20. Available from: https://pubmed.ncbi.nlm.nih.gov/19164889

81. Roussel BD, Irving JA, Ekeowa UI, Belorgey D, Haq I, Ordóñez A, et al. Unravelling the twists and turns of the serpinopathies. FEBS J. 2011 Oct;278(20):3859–67.

82. Ekeowa UI, Freeke J, Miranda E, Gooptu B, Bush MF, Pérez J, et al. Defining the mechanism of polymerization in the serpinopathies. Proc Natl Acad Sci [Internet]. 2010 Oct 5;107(40):17146 LP – 17151. Available from: http://www.pnas.org/content/107/40/17146.abstract

83. Lomas DA, Evans DL, Finch JT, Carrell RW. The mechanism of Z alpha 1-antitrypsin accumulation in the liver. Nature. 1992 Jun;357(6379):605–7.

84. Chambers JE, Dickens JA, Marciniak SJ. Measuring the effects of α_1-antitrypsin polymerisation on the structure and biophysical properties of the endoplasmic reticulum. Biol Cell [Internet]. 2018;44(0). Available from: http://doi.wiley.com/10.1111/boc.201800023

85. Fregonese L, Stolk J. Hereditary alpha-1-antitrypsin deficiency and its clinical consequences. Orphanet J Rare Dis [Internet]. 2008 Jun 19;3:16. Available from: https://pubmed.ncbi.nlm.nih.gov/18565211

86. Miranda E, Lomas DA. Neuroserpin: A serpin to think about. Cell Mol Life Sci.

2006;63(6):709–22.

87. Reumann R, Vierk R, Zhou L, Gries F, Kraus V, Mienert J, et al. The serine protease inhibitor neuroserpin is required for normal synaptic plasticity and regulates learning and social behavior. LearnMem. 2017;24(1549-5485 (Electronic)):650–9.

88. Roussel BDBD, Lomas DADA, Crowther DCDC. Progressive myoclonus epilepsy associated with neuroserpin inclusion bodies (neuroserpinosis). DoiOrg [Internet]. 2016;18(S2):103–10. Available from: http://www.ncbi.nlm.nih.gov/pubmed/27618835

89. Ricagno S, Caccia S, Sorrentino G, Antonini G, Bolognesi M. Human Neuroserpin: Structure and Time-Dependent Inhibition. J Mol Biol [Internet]. 2009;388(1):109–21. Available from: http://dx.doi.org/10.1016/j.jmb.2009.02.056

90. Ricagno S, Pezzullo M, Barbiroli A, Manno M, Levantino M, Santangelo MG, et al. Two latent and two hyperstable polymeric forms of human neuroserpin. Biophys J [Internet]. 2010;99(10):3402–11. Available from: http://dx.doi.org/10.1016/j.bpj.2010.09.021

91. Takehara S, Zhang J, Yang X, Takahashi N, Mikami B, Onda M. Refolding and polymerization pathways of neuroserpin. J Mol Biol [Internet]. 2010;403(5):751–62. Available from: http://dx.doi.org/10.1016/j.jmb.2010.07.047

92. Huntington JA, Sendall TJ, Yamasaki M. New insight into serpin polymerization and aggregation. Prion [Internet]. 2009/01/16. 2009;3(1):12–4. Available from: https://pubmed.ncbi.nlm.nih.gov/19372754

93. Elliston ELK, Lomas DA, Irving JA. In Vitro Approaches for the Assessment of Serpin Polymerization. Methods Mol Biol. 2018;1826:87–107.

94. Noto R, Santangelo MG, Ricagno S, Mangione MR, Levantino M, Pezzullo M, et al. The tempered polymerization of human neuroserpin. PLoS One. 2012;7(3):1–12.

95. Xue Y, Björquist P, Inghardt T, Linschoten M, Musil D, Sjölin L, et al. Interfering with the inhibitory mechanism of serpins: crystal structure of a complex formed between cleaved plasminogen activator inhibitor type 1 and a reactive-centre loop peptide. Structure. 1998 May;6(5):627–36.

96. Skinner R, Chang WS, Jin L, Pei X, Huntington JA, Abrahams JP, et al. Implications for function and therapy of a 2.9 A structure of binary-complexed antithrombin. J Mol Biol. 1998;283(1):9–14.

97. Carrell RW, Evans DLI. Serpins: Mobile conformations in a family of proteinase inhibitors. Curr Opin Struct Biol [Internet]. 1992;2(3):438–46. Available from: http://www.sciencedirect.com/science/article/pii/0959440X9290236Z

98. Huntington JA, Whisstock JC. Molecular contortionism - On the physical limits of serpin "loop-sheet" polymers. Biol Chem. 2010;391(8):973–82.

99. Trelle MB, Pedersen S, Østerlund EC, Madsen JB, Kristensen SR, Jørgensen TJD. An Asymmetric Runaway Domain Swap Antithrombin Dimer as a Key Intermediate for Polymerization Revealed by Hydrogen/Deuterium-Exchange Mass Spectrometry. Anal Chem. 2017 Jan;89(1):616–24.

100. Miranda E, Pérez J, Ekeowa UI, Hadzic N, Kalsheker N, Gooptu B, et al. A novel monoclonal antibody to characterize pathogenic polymers in liver disease associated with α1-antitrypsin deficiency. Hepatology. 2010;52(3):1078–88.

101. Behrens MA, Sendall TJ, Pedersen JS, Kjeldgaard M, Huntington JA, Jensen JK. The shapes of Z-α1-antitrypsin polymers in solution support the c-terminal domain-swap mechanism of polymerization. Biophys J [Internet]. 2014;107(8):1905–12. Available

from: http://dx.doi.org/10.1016/j.bpj.2014.08.030

102. Faull S V, Elliston ELK, Gooptu B, Jagger AM, Aldobiyan I, Redzej A, et al. The structural basis for Z α(1)-antitrypsin polymerization in the liver. Sci Adv [Internet]. 2020 Oct 21;6(43):eabc1370. Available from: https://pubmed.ncbi.nlm.nih.gov/33087346

103. Güssow D, Rein R, Ginjaar I, Hochstenbach F, Seemann G, Kottman A, et al. The human beta 2-microglobulin gene. Primary structure and definition of the transcriptional unit. J Immunol. 1987 Nov;139(9):3132–8.

104. Li L, Dong M, Wang XG. The implication and significance of beta 2 microglobulin: A conservative multifunctional regulator. Chin Med J (Engl). 2016;129(4):448–55.

105. Hee C-S, Beerbaum M, Loll B, Ballaschk M, Schmieder P, Uchanska-Ziegler B, et al. Dynamics of free versus complexed β2-microglobulin and the evolution of interfaces in MHC class I molecules. Immunogenetics [Internet]. 2013;65(3):157–72. Available from: https://doi.org/10.1007/s00251-012-0667-4

106. Hee C-S, Fabian H, Uchanska-Ziegler B, Ziegler A, Loll B. Comparative biophysical characterization of chicken β2-microglobulin. Biophys Chem. 2012 Jun;167:26–35.

107. Chen W, Gao F, Chu F, Zhang J, Gao GF, Xia C. Crystal Structure of a Bony Fish β2-Microglobulin. J Biol Chem [Internet]. 2010 Jul 16;285(29):22505–12. Available from: http://www.jbc.org/content/285/29/22505.abstract

108. Christianson GJ, Brooks W, Vekasi S, Manolfi EA, Niles J, Roopenian SL, et al. Beta 2-microglobulin-deficient mice are protected from hypergammaglobulinemia and have defective antibody responses because of increased IgG catabolism. J Immunol [Internet]. 1997 Nov 15;159(10):4781 LP – 4792. Available from: http://www.jimmunol.org/content/159/10/4781.abstract

109. York IA, Rock KL. Antigen processing and presentation by the class I major histocompatibility complex. Annu Rev Immunol. 1996;14:369–96.

110. Floege J, Ehlerding G. Beta-2-Microglobulin-Associated Amyloidosis. Nephron [Internet]. 1996;72(1):9–26. Available from: https://www.karger.com/DOI/10.1159/000188801

111. Hansen TH, Bouvier M. MHC class I antigen presentation: learning from viral evasion strategies. Nat Rev Immunol [Internet]. 2009;9(7):503–13. Available from: https://doi.org/10.1038/nri2575

112. Hewitt EW. The MHC class I antigen presentation pathway: strategies for viral immune evasion. Immunology [Internet]. 2003 Oct;110(2):163–9. Available from: https://pubmed.ncbi.nlm.nih.gov/14511229

113. Otten GR, Bikoff E, Ribaudo RK, Kozlowski S, Margulies DH, Germain RN. Peptide and beta 2-microglobulin regulation of cell surface MHC class I conformation and expression. J Immunol. 1992 Jun;148(12):3723–32.

114. Niwa T. β2-Microglobulin Dialysis Amyloid and Its Formation: Role of 3-Deoxyglucosone and Advanced Glycation End Products. Nephron [Internet]. 1997;76(4):373–91. Available from: https://www.karger.com/DOI/10.1159/000190218

115. Gejyo F, Yamada T, Odani S, Nakagawa Y, Arakawa M, Kunitomo T, et al. A new form of amyloid protein associated with chronic hemodialysis was identified as β2-microglobulin. Biochem Biophys Res Commun [Internet]. 1985;129(3):701–6. Available from: http://www.sciencedirect.com/science/article/pii/0006291X85919485

116. Esposito G, Michelutti R, Verdone G, Viglino P, ÁNdez HH, Robinson C V., et al. Removal of the N-terminal hexapeptide from human β2-microglobulin facilitates protein aggregation and fibril formation. Protein Sci [Internet]. 2000;9(5):831–45. Available

from: http://doi.wiley.com/10.1110/ps.9.5.831

117. Le Marchand T, de Rosa M, Salvi N, Sala BM, Andreas LB, Barbet-Massin E, et al. Conformational dynamics in crystals reveal the molecular bases for D76N beta-2 microglobulin aggregation propensity. Nat Commun [Internet]. 2018;9(1):1658. Available from: https://doi.org/10.1038/s41467-018-04078-y

118. Leri M, Bemporad F, Oropesa-Nuñez R, Canale C, Calamai M, Nosi D, et al. Molecular insights into cell toxicity of a novel familial amyloidogenic variant of β2-microglobulin. J Cell Mol Med [Internet]. 2016;20(8):1443–56. Available from: https://doi.org/10.1111/jcmm.12833

119. Mangione PP, Esposito G, Relini A, Raimondi S, Porcari R, Giorgetti S, et al. Structure, folding dynamics, and amyloidogenesis of D76N β2-microglobulin roles of shear flow, hydrophobic surfaces, and α-crystallin. J Biol Chem. 2013;288(43):30917–30.

120. Mittag T, Forman-Kay JD. Atomic-level characterization of disordered protein ensembles. Curr Opin Struct Biol. 2007 Feb;17(1):3–14.

121. Camilloni C, Sala BM, Sormanni P, Porcari R, Corazza A, De Rosa M, et al. Rational design of mutations that change the aggregation rate of a protein while maintaining its native structure and stability. Sci Rep [Internet]. 2016 May 6;6:25559. Available from: http://dx.doi.org/10.1038/srep25559

122. Disease R. Dialysis-related amyloidosis : challenges and solutions. 2016;319–28.

123. Ivanova MI, Sawaya MR, Gingery M, Attinger A, Eisenberg D. An amyloid-forming segment of beta2-microglobulin suggests a molecular model for the fibril. Proc Natl Acad Sci U S A [Internet]. 2004/07/12. 2004 Jul 20;101(29):10584–9. Available from: https://pubmed.ncbi.nlm.nih.gov/15249659

124. Min R, Li Z, Epstein J, Barlogie B, Yi Q. Beta2-microglobulin as a negative growth regulator of myeloma cells. Br J Haematol. 2002 Aug;118(2):495–505.

125. Kumar SK, Rajkumar V, Kyle RA, van Duin M, Sonneveld P, Mateos M-V, et al. Multiple myeloma. Nat Rev Dis Prim [Internet]. 2017;3(1):17046. Available from: https://doi.org/10.1038/nrdp.2017.46

126. Wang H, Hu W-M, Xia Z-J, Liang Y, Lu Y, Lin S-X, et al. High numbers of CD163+ tumor-associated macrophages correlate with poor prognosis in multiple myeloma patients receiving bortezomib-based regimens. J Cancer [Internet]. 2019 Jun 2;10(14):3239–45. Available from: https://pubmed.ncbi.nlm.nih.gov/31289595

127. Hope C, Ollar SJ, Heninger E, Hebron E, Jensen JL, Kim J, et al. TPL2 kinase regulates the inflammatory milieu of the myeloma niche. Blood [Internet]. 2014/04/10. 2014 May 22;123(21):3305–15. Available from: https://pubmed.ncbi.nlm.nih.gov/24723682

128. Masters SL, Dunne A, Subramanian SL, Hull RL, Tannahill GM, Sharp FA, et al. Activation of the NLRP3 inflammasome by islet amyloid polypeptide provides a mechanism for enhanced IL-1β in type 2 diabetes. Nat Immunol [Internet]. 2010/09/12. 2010 Oct;11(10):897–904. Available from: https://pubmed.ncbi.nlm.nih.gov/20835230

129. Halle A, Hornung V, Petzold GC, Stewart CR, Monks BG, Reinheckel T, et al. The NALP3 inflammasome is involved in the innate immune response to amyloid-beta. Nat Immunol. 2008 Aug;9(8):857–65.

130. He Y, Hara H, Núñez G. Mechanism and Regulation of NLRP3 Inflammasome Activation. Trends Biochem Sci [Internet]. 2016/09/23. 2016 Dec;41(12):1012–21. Available from: https://pubmed.ncbi.nlm.nih.gov/27669650

131. Bataille R, Grenier J, Sany J. Beta-2-microglobulin in myeloma: optimal use for staging, prognosis, and treatment--a prospective study of 160 patients. Blood. 1984

Feb;63(2):468–76.

132. Ricagno S, Colombo M, Rosa M de, Sangiovanni E, Giorgetti S, Raimondi S, et al. DE loop mutations affect β2-microglobulin stability and amyloid aggregation. Biochem Biophys Res Commun [Internet]. 2008;377(1):146–50. Available from: http://www.sciencedirect.com/science/article/pii/S0006291X08018664

133. Santambrogio C, Ricagno S, Colombo M, Barbiroli A, Bonomi F, Bellotti V, et al. DE-loop mutations affect β2 microglobulin stability, oligomerization, and the low-pH unfolded form. Protein Sci [Internet]. 2010 Jul 17;19(7):1386–94. Available from: http://www.ncbi.nlm.nih.gov/pmc/articles/PMC2974830/

134. Esposito G, Ricagno S, Corazza A, Rennella E, Gümral D, Mimmi MC, et al. The Controlling Roles of Trp60 and Trp95 in β2-Microglobulin Function, Folding and Amyloid Aggregation Properties. J Mol Biol [Internet]. 2008;378(4):887–97. Available from: http://www.sciencedirect.com/science/article/pii/S0022283608002805

135. Yepes M, Lawrence DA. Tissue-type plasminogen activator and neuroserpin: a well-balanced act in the nervous system? Trends Cardiovasc Med. 2004 Jul;14(5):173–80.

136. Osterwalder T, Contartese J, Stoeckli ET, Kuhn TB, Sonderegger P. Neuroserpin, an axonally secreted serine protease inhibitor. EMBO J. 1996 Jun;15(12):2944–53.

137. Caccia S, Ricagno S, Bolognesi M. Molecular bases of neuroserpin function and pathology. Biomol Concepts. 2010 Aug;1(2):117–30.

138. Miranda E, Römisch K, Lomas DA. Mutants of neuroserpin that cause dementia accumulate as polymers within the endoplasmic reticulum. J Biol Chem. 2004 Jul;279(27):28283–91.

139. Moriconi C, Ordoñez A, Lupo G, Gooptu B, Irving JA, Noto R, et al. Interactions between N-linked glycosylation and polymerisation of neuroserpin within the endoplasmic reticulum. FEBS J. 2015 Dec;282(23):4565–79.

140. Guadagno NA, Moriconi C, Licursi V, D'Acunto E, Nisi PS, Carucci N, et al. Neuroserpin polymers cause oxidative stress in a neuronal model of the dementia FENIB. Neurobiol Dis [Internet]. 2017;103:32–44. Available from: http://dx.doi.org/10.1016/j.nbd.2017.03.010

141. Miranda E, MacLeod I, Davies MJ, Pérez J, Römisch K, Crowther DC, et al. The intracellular accumulation of polymeric neuroserpin explains the severity of the dementia FENIB. Hum Mol Genet [Internet]. 2008/02/11. 2008 Jun 1;17(11):1527–39. Available from: https://pubmed.ncbi.nlm.nih.gov/18267959

142. Moriconi C, Ordoñez A, Lupo G, Gooptu B, Irving JA, Noto R, et al. Interactions between N-linked glycosylation and polymerisation of neuroserpin within the endoplasmic reticulum. FEBS J. 2015;282(23):4565–79.

143. Schipanski A, Oberhauser F, Neumann M, Lange S, Szalay B, Krasemann S, et al. Lectin OS-9 delivers mutant neuroserpin to endoplasmic reticulum associated degradation in familial encephalopathy with neuroserpin inclusion bodies. Neurobiol Aging. 2014 Oct;35(10):2394–403.

144. Lin Z, Jensen JK, Hong Z, Shi X, Hu L, Andreasen PA, et al. Structural Insight into Inactivation of Plasminogen Activator Inhibitor-1 by a Small-Molecule Antagonist. Chem Biol [Internet]. 2013;20(2):253–61. Available from: http://www.sciencedirect.com/science/article/pii/S1074552113000033

145. Kundap UP, Bhuvanendran S, Kumari Y, Othman I, Shaikh MF. Plant Derived Phytocompound, Embelin in CNS Disorders: A Systematic Review. Front Pharmacol [Internet]. 2017 Feb 27;8:76. Available from:

https://pubmed.ncbi.nlm.nih.gov/28289385

146. Pathan SA, Iqbal Z, Zaidi SMA, Talegaonkar S, Vohra D, Jain GK, et al. CNS drug delivery systems: novel approaches. Recent Pat Drug Deliv Formul. 2009 Jan;3(1):71–89.

147. Parfrey H, Mahadeva R, Ravenhill NA, Zhou A, Dafforn TR, Foreman RC, et al. Targeting a Surface Cavity of α1-Antitrypsin to Prevent Conformational Disease. J Biol Chem [Internet]. 2003 Aug 29;278(35):33060–6. Available from: http://www.jbc.org/content/278/35/33060.abstract

148. Saga G, Sessa F, Barbiroli A, Santambrogio C, Russo R, Sala M, et al. Embelin binds to human neuroserpin and impairs its polymerisation. Sci Rep [Internet]. 2016;6(1):18769. Available from: http://www.nature.com/articles/srep18769

149. De Simone A, Dhulesia A, Soldi G, Vendruscolo M, Hsu S-TD, Chiti F, et al. Experimental free energy surfaces reveal the mechanisms of maintenance of protein solubility. Proc Natl Acad Sci [Internet]. 2011 Dec 27;108(52):21057 LP – 21062. Available from: http://www.pnas.org/content/108/52/21057.abstract

150. Monsellier E, Chiti F. Prevention of amyloid-like aggregation as a driving force of protein evolution. EMBO Rep [Internet]. 2007 Aug;8(8):737–42. Available from: https://pubmed.ncbi.nlm.nih.gov/17668004

151. Strnad P, McElvaney NG, Lomas DA. Alpha1-Antitrypsin Deficiency. N Engl J Med [Internet]. 2020 Apr 8;382(15):1443–55. Available from: https://doi.org/10.1056/NEJMra1910234

152. Christopher T. Walsh R& CP. Posttranslational modification of proteins: Expanding nature's inventory. Greenwood Village, CO, 2005, 576 pp., ISBN 0-9747077-3-2, $98.00. Biochem Mol Biol Educ [Internet]. 2006 Nov 1;34(6):461–2. Available from: https://doi.org/10.1002/bmb.2006.494034069996

153. Alonso A, Zaidi T, Novak M, Grundke-Iqbal I, Iqbal K. Hyperphosphorylation induces self-assembly of tau into tangles of paired helical filaments/straight filaments. Proc Natl Acad Sci U S A [Internet]. 2001/05/29. 2001 Jun 5;98(12):6923–8. Available from: https://pubmed.ncbi.nlm.nih.gov/11381127

154. Oueslati A. Implication of Alpha-Synuclein Phosphorylation at S129 in Synucleinopathies: What Have We Learned in the Last Decade? J Parkinsons Dis [Internet]. 2016;6(1):39–51. Available from: https://pubmed.ncbi.nlm.nih.gov/27003784

155. Weids AJ, Ibstedt S, Tamás MJ, Grant CM. Distinct stress conditions result in aggregation of proteins with similar properties. Sci Rep [Internet]. 2016;6(1):24554. Available from: https://doi.org/10.1038/srep24554

156. Motamedi-Shad N, Jagger AM, Liedtke M, Faull S V., Nanda AS, Salvadori E, et al. An antibody that prevents serpin polymerisation acts by inducing a novel allosteric behavior. Biochem J. 2016;473(19):3269–90.

157. Lu J, Cao Q, Wang C, Zheng J, Luo F, Xie J, et al. Structure-Based Peptide Inhibitor Design of Amyloid-β Aggregation [Internet]. Vol. 12, Frontiers in Molecular Neuroscience . 2019. p. 54. Available from: https://www.frontiersin.org/article/10.3389/fnmol.2019.00054

158. Saga G, Sessa F, Barbiroli A, Santambrogio C, Russo R, Sala M, et al. Embelin binds to human neuroserpin and impairs its polymerisation. Sci Rep [Internet]. 2016 Jan 6;6:18769. Available from: https://pubmed.ncbi.nlm.nih.gov/26732982